



UNIVERSITAT DE
BARCELONA

Vortex Dynamics in Superconducting Thin Films under Microwave Fields

Pedro-de-Jesús Cuadra-Solís



Aquesta tesi doctoral està subjecta a la llicència **Reconeixement- Compartlqual 3.0. Espanya de Creative Commons.**

Esta tesis doctoral está sujeta a la licencia **Reconocimiento - Compartirlqual 3.0. España de Creative Commons.**

This doctoral thesis is licensed under the **Creative Commons Attribution-ShareAlike 3.0. Spain License.**

Vortex Dynamics in Superconducting Thin Films under Microwave Fields



Pedro-de-Jesús Cuadra-Solís
Department de Física Fonamental
Universitat de Barcelona

A thesis submitted for the degree of

*Doctor en Física*s

Barcelona, July 2015

Vortex Dynamics in Superconducting Thin Films under Microwave Fields

Thesis submitted by

Pedro de Jesús Cuadra Solís

in order to complete the requirements to be granted the degree of

Doctor en Física

Supervisors: **Prof. Javier Tejada Palacios Ph.D.**

and

Assistant Prof. Antoni García Santiago Ph.D.

Tutor: **Assistant Prof. Antoni García Santiago Ph.D.**

Programa de Doctorat de Física Avançada

Bienni 1999–2001

Departament de Física Fonamental

Facultat de Física

Universitat de Barcelona

This thesis is dedicated to the memory of my mother

Acknowledgements

There are three persons I am particularly grateful to. Javier Tejada Palacios, one of my thesis supervisor, for accepting me as a Ph.D student at his laboratory and for the academic freedom. Antoni García Santiago, my second thesis supervisor and tutor, for his continuous advise, support and patience during this rather long time. For his positive, constructive and stimulating criticism, and for his time and availability. And finally, Joan Manel Hernández Ferràs, for his support and help at the lab, his stimulating discussion on experimental and fundamental physics. To all of them, I'm thankful for his great human qualities.

I specially want to express my gratitude to Johan Vanacken at KU Leuven, for his collaboration, advice and help, and without whom it would not have been possible to make part of this thesis. Thanks for hosting me at the Pulsed Field Group. I'm also indebted to Miroslav Grajcar from Comenius University in Bratislava for his collaboration. I also thanks to Paulo V. Santos for his invitation to the Paul-Drude Institut in Berlin.

I would like to show gratitude to Antoni Fernández Martínez, for his stimulating discussion on microwaves and superconductivity, and for his comradeship, time and team-working. I express also my gratitude to all my colleagues at the grup de magnetisme, the past, Marc Duran, Francesc Torres, Carla Carbonell, Neus Domingo, Anna Julià, Marta Jordi, Critina Seco, Saü Vèlez, Victor..., and the present one, Gianluca, Ferran, Diego, Ricardo, Sergi, Martí, Nahuel..., for the company and help. My very special thanks go the Alberto Hernández Mínguez and Roger Amigó for their great comradeship and support.

I am most grateful to Xavier Batlle for scientific collaboration on magnetism in the early stage of my doctoral studies at the University of Barcelona.

I would like to acknowledge to my colleagues from the CEIR-ARCO and Esteve Terradas VET schools for their interest and support on my studies and investigations.

I owe a great debt to Fernando Arnal and Guillermo Toruño for their wise words in maths and physics during my secondary and high school studies. My thanks also go to my friends, Toni Travieso, Toni Pérez, Manel Domingo, Gabriella Tihon, Gabi Dietz, Juanjo Pérez, Aintzane Ezenarro, and many others, who have supported me during these years.

My thankfulness to my brothers, Jorge Alberto, José René and his family, Barbara Marustha and her family, Sofía Yolanda and her family, and my father Pedro Joaquín, for being always there, despite the distance.

As a marathon, this has been a rather long way to run. Many things have happened, in personal life also. I would like to express my deepest gratitude to my ex-wife, Begoña, for her understanding, support, and sensitivity, and for the all years and moments of life shared.

I gratefully acknowledge to my couple Riitta, for her patience, company, and wise pieces of advice.

Travel grants to participate in conferences, congresses, and workshops on superconductivity from University of Barcelona are also gratefully acknowledged.

Contents

Contents	v
List of Figures	viii
Nomenclature	x
1 Introduction	1
2 Theoretical aspects of superconductivity	7
2.1 Superconductivity	7
2.1.1 Historical overview	7
2.1.2 London equations	10
2.1.3 The Ginzburg-Landau theory	11
2.1.4 Characteristic length scales ξ and λ	13
2.1.5 Type-1, type-2 and type-1.5 superconductors	14
2.2 Vortex matter in superconductors	18
2.2.1 The structure of an isolated vortex	18
2.2.2 The vortex lattice	20
2.2.3 Flux motion	22
2.2.4 Flux pinning	25
2.3 Thin film magnetization in perpendicular geometry	26
2.3.1 Bean model	26
2.3.2 Effective penetration depth	28
2.3.3 Demagnetization effects	29
2.3.4 Field and current profile	30

2.4	Superconductivity at microwave frequency	31
2.4.1	Complex conductivity	31
2.4.2	Maxwell’s equation and superconductors	34
2.4.3	Surface resistance and surface reactance	38
3	Experimental techniques	40
3.1	Introduction	40
3.2	Thin film preparation	40
3.2.1	$\text{La}_{1.82}\text{Sr}_{0.18}\text{CuO}_4$	40
3.2.2	Patterned Pb	43
3.2.3	MgB_2	45
3.3	SQUID magnetometry	46
3.3.1	dc magnetization	46
3.3.2	ac magnetic susceptibility	49
3.4	Microwave experimental techniques	50
3.4.1	Introduction	50
3.4.2	Basic microwave layout	52
3.4.3	Sweeping mode	54
3.4.4	Pulsed mode	56
3.4.5	Power reflected mode	58
3.4.6	rf-coil modeling	60
4	Vortex instabilities driven by microwave fields	63
4.1	Introduction	63
4.2	Dynamic effects in type-2 superconductors	66
4.2.1	Magnetic-flux jumps	66
4.2.2	Dendritic instability	69
4.3	Vortex dynamics under Sweeping Microwave Mode	72
4.3.1	Frequency-driven instability: $\text{La}_{1.82}\text{Sr}_{0.18}\text{CuO}_4$	72
4.3.2	Frequency-driven instability: patterned Pb	79
4.3.3	Frequency-driven instability: MgB_2	80
4.3.4	Microwave-frequency-driven vortex instabilities	87
4.4	Vortex dynamics under pulsed microwave mode	94

4.4.1	Avalanche-like vortex penetration: $\text{La}_{1.82}\text{Sr}_{0.18}\text{CuO}_4$	94
4.4.1.1	Magnetic field dependence	95
4.4.1.2	Temperature dependence	98
4.4.1.3	Pulse duration dependence	100
4.4.1.4	Power dependence	100
4.4.1.5	MW-pulse-induced instabilities: $\text{La}_{1.82}\text{Sr}_{0.18}\text{CuO}_4$	103
4.4.2	Avalanche-like vortex penetration: MgB_2	104
4.4.2.1	Temperature and pulse duration dependences	104
4.4.2.2	Magnetic field and pulse duration dependencies	106
4.4.2.3	MW-pulse-induced instabilities: MgB_2	108
4.4.3	Vortex instabilities driven by pulsed microwave fields	110
4.5	Summary	112
 5 Commensurability effects in ac and microwave power reflection mode experiments		114
5.1	Introduction	114
5.2	Commensurability effects	116
5.3	Patterned thin Pb film	117
5.4	ac magnetic susceptibility under MW irradiation	119
5.5	Magnetic field-dependent power reflection	124
5.5.1	MW power reflection as a function of temperature and frequency	124
5.5.2	Commensurability effects in MW reflection spectrometry	127
5.5.3	MW power reflection as a function of MW power	132
5.6	Summary	135
 6 Conclusions		137
 Appendix A: ac magnetic susceptibility		152
 Bibliography		154
 Publications and contributions		178
 Curriculum Vitae		184

List of Figures

1.1	The critical surface	2
2.1	The $H - T$ phase diagram of the different types of superconductors	16
2.2	$M(H)$ response for the different types of superconductors	17
2.3	Structure of an isolated vortex	18
2.4	Vortex-vortex interactions in the different types of superconductors	21
2.5	Triangular and square vortex lattices	22
2.6	Bean critical state model	27
2.7	Field and current profile for long cylinder and thin film	32
2.8	Equivalent circuit depicting complex conductivity in superconductors	34
3.1	The procedure to fabricate patterned film	43
3.2	The MPMS measuring setup	47
3.3	Layout of the detection circuit of the rf-SQUID-magnetometer	48
3.4	Microwave experimental setup	53
3.5	Sweeping mode experimental setup	55
3.6	Pulsed mode experimental setup	57
3.7	Power reflected mode experimental setup	59
3.8	Spatial distribution of the parallel and perpendicular components of the MW electric and magnetic fields	61
3.9	Low-temperature frequency spectrum	62
4.1	Magnetic-optical images of a dendritic instability	70
4.2	$\text{La}_{1.82}\text{Sr}_{0.18}\text{CuO}_4$. Temporal evolution in logarithmic scale of the magnetic moment registered as a function of MW frequency	73

LIST OF FIGURES

4.3	La _{1.82} Sr _{0.18} CuO ₄ . Substrate contribution to the magnetic moment registered as a function of MW frequency	74
4.4	La _{1.82} Sr _{0.18} CuO ₄ . Magnetic moment registered as a function of MW frequency in decreasing way and remnant mode	75
4.5	La _{1.82} Sr _{0.18} CuO ₄ . Magnetic moment registered as a function of MW frequency at different temperatures	76
4.6	La _{1.82} Sr _{0.18} CuO ₄ . Magnetic moment registered as a function of MW frequency for different MW powers	78
4.7	La _{1.82} Sr _{0.18} CuO ₄ . Magnetic moment registered as a function of MW frequency for different dc magnetic fields	79
4.8	Patterned Pb. Magnetic moment registered as a function of MW frequency for different MW powers	81
4.9	MgB ₂ . Time-dependent MW-free magnetic moment	81
4.10	MgB ₂ . Magnetic moment registered as a function of MW frequency and time with MW power of -5 dBm	83
4.11	MgB ₂ . Magnetic moment registered as a function of MW frequency with MW power of 0 dBm	84
4.12	MgB ₂ . Magnetic moment registered as a function of MW frequency with MW power of 5 dBm	86
4.13	MgB ₂ . Magnetic moment registered as a function of MW frequency with MW power of 10 dBm	87
4.14	La _{1.82} Sr _{0.18} CuO ₄ . Time evolution of the rf-SQUID output voltage signal variation under pulsed MW mode for different values of the dc magnetic fields	96
4.15	La _{1.82} Sr _{0.18} CuO ₄ . Magnetic-field dependence of the rf-SQUID output voltage signal variations under pulsed MW mode	97
4.16	La _{1.82} Sr _{0.18} CuO ₄ . rf-SQUID output voltage signal variation under pulsed MW mode at different values of temperatures	99
4.17	La _{1.82} Sr _{0.18} CuO ₄ . rf-SQUID output voltage signal variation under pulsed MW mode for different values of the pulse duration	101
4.18	La _{1.82} Sr _{0.18} CuO ₄ . rf-SQUID output voltage signal variation under pulsed MW mode for different values of the nominal MW powers	102

LIST OF FIGURES

4.19 MgB ₂ . Time dependence of the rf-SQUID output signal variation for different temperature values under pulsed MW mode	105
4.20 MgB ₂ . Temperature dependence of the total averaged rf-SQUID output signal variation under pulsed MW mode for different values of pulse duration	107
4.21 MgB ₂ . Magnetic field dependence of the total averaged rf-SQUID output signal variation under pulsed MW mode	107
4.22 MgB ₂ . Magnetic field dependence of the total averaged rf-SQUID output signal variation under pulsed MW mode for different values of pulse duration	108
4.23 MgB ₂ . Remnant part of MW-free isothermal magnetic hysteresis cycle	110
5.1 Layout of the Pb film with a composite array of square antidots .	118
5.2 Patterned Pb. ac susceptibility as a function of the reduced dc magnetic field under MW irradiation	120
5.3 Patterned Pb. ac susceptibility as a function of the nominal MW power	124
5.4 Patterned Pb. ΔS_{11} as a function of the reduced dc magnetic field at different temperature values, under a MW power of -10 dBm and a MW frequency of 2.01 GHz	125
5.5 Patterned Pb. ΔS_{11} as a function of the reduced dc magnetic field at different temperature values, under a MW power of -10 dBm and a MW frequency of 3.98 GHz	126
5.6 Patterned Pb. ΔS_{11} as a function of the reduced dc magnetic field at different temperature values, under a MW power of -10 dBm and a MW frequency of 1.86 GHz	127
5.7 Patterned Pb. S_{11} as a function of the reduced dc magnetic field at $T = 7.05$ K, under different MW power values and at MW frequency of 1.86 GHz	133
5.8 Patterned Pb. S_{11} as a function of the reduced dc magnetic field at $T = 7.10$ K, under different MW power values and at MW frequency of 2.01 GHz	134

Chapter 1

Introduction

Superconductivity is characterized by three hallmarks. The first one shows that superconductors, as opposed to conventional conductors, have the ability to conduct electrical current with very small resistance, no power loss, no generation of heat, and greatly reduced levels of noise. The resistance is small, but finite at microwave frequency and truly zero at dc magnetic fields. The second one implies that as the material enters the superconducting state, currents will develop to exclude the magnetic field from the interior. Finally, macroscopic quantum effects arise from the quantum mechanical nature of the superconducting correlated electron state. This particular state of matter is limited by three critical parameters: temperature T_c , dc magnetic field H_c , and current density J_c , which define the critical surface that separates the superconducting from the normal state in the space spanned by these parameters (Fig. 1.1). Thus, one of the main challenges in physics and material science of superconductors is to expand this surface as far as possible in order to look for technological applications.

Since 1986 [1], a new class of hole-doped cuprates that are superconductive at temperatures as high as 134 K has been identified (nowadays referred as high- T_c superconductors). The materials discovered up to that time, which had critical temperature lower than 23 K, are commonly known as low- T_c superconductors. These novel materials belong to the so-called type-2 superconductors, which exclude dc magnetic fields weaker than a lower critical field ($\simeq 10^{-2}$ tesla) from which the magnetic flux penetrates in the form of quantized flux lines or vortices [2]. The behavior of vortices dominates the physical properties of such supercon-

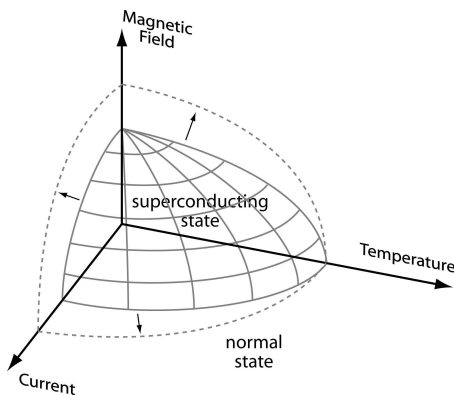


Figure 1.1: Sketch of the critical surface that separates the superconducting from the normal state in the space span by temperature, magnetic field and current.

ductors up to the upper critical field ($\simeq 10^2$ tesla), where superconductivity gives way to normal behavior and magnetic fields penetrate uniformly.

In the last decades, much interest has been devoted to the research of these high- T_c superconductors in order to extract fundamental physical information about the dynamics and the structure of the vortices but also to exploit their intrinsic characteristics for widespread application. The investigation implies also studies of their properties in dc and time-varying magnetic fields since most of the applications involve ac currents or require very low surface impedance in the presence of strong magnetic fields. Actually, the low power dissipation [3], the frequency independent penetration depth [4], the steep transition between the superconducting and normal state, and the more accessible working temperature regime [liquid nitrogen cooling (77 K), rather than liquid helium (4.2 K)], together with high values of J_c ($\sim 3\text{--}6 \times 10^6$ A/cm² at 65 K) of high quality thin films [5, 6] support and provide sufficient ground to consider good perspectives for the implementation and realization of this new class of superconductors in high-performance radio-frequency and superconductor-based microwave devices. As a matter of fact, superconducting materials have been preferred to normal metals for assembling low-loss electronic devices such as filters, antennas, resonators, etc. [7, 8, 9, 10, 11, 12, 13, 14], due to their low surface resistance ($R_s \sim 100\text{--}500$ $\mu\Omega$ between 4.2 and 77 K) [15, 16]. Moreover, the non-dispersive nature of superconductor makes them suitable for microwave wireless and satellite

communication systems where the information can be transmitted without separation of frequencies [8]. The list of applications includes electrical transmission cables, motors, generators, fault current limiters, superconductor magnetic energy storage systems, superconducting magnetic levitation transportation system (Superconducting Maglev), Terahertz imaging, and high-speed computing [17]. A considerable increase of the critical current in these high- T_c superconductors has been achieved through confining the vortices in columnar defects introduced by heavy-ion irradiation [18]. An additional contribution to the critical current in thickness-modulated thin films made of low- T_c superconductors was observed in magnetic fields (the so-called matching field) having vortex densities commensurate with the modulation [19]. To date, the combination of thin film growth techniques [20] and submicron lithography [21, 22, 23] has opened up the opportunity to fabricate not only nanostructured superconductors but also arrangements of ultrafine objects with well-defined geometries over macroscopic areas. Low- and high- T_c superconducting thin films with regular arrays of pinning sites have shown periodic local maxima in the critical current when an integer or rational value of the matching fields exists [22, 24, 25]. As an alternative to lithographic patterning, has been the use of anodized aluminum oxide membranes as a substrate for deposition of low- T_c superconducting thin films. This relatively dense hexagonal array of pores has revealed enhancements in the critical current that were commensurate with the underlying array [26, 27]. More recently, an increment of this current has been reported in high- T_c superconducting thin films containing self-assembled columnar defects [28].

On the other hand, the metallic thin film compounds made of MgB_2 are very attractive for potential uses exploiting their intrinsic properties, such as relatively high upper critical fields ($\sim 20\text{--}49$ T) [29, 30], extremely high J_c ($\sim 10^7$ A/cm² in thin films) [31], and rather good microwave properties at low temperature [32]. With reasonably high T_c (39 K) [33] and large energy gaps (6.8 and 1.8 meV for the σ and π bonds, respectively) [34], this system promises higher working temperatures and potentially higher operating speeds than common Nb-based integrated circuits. Moreover, the two-component character of MgB_2 [35, 36], has opened remarkable possibilities for new fundamental research topics, e.g., semi-Meissner state [37], the violation of the London law and Onsager-Feynman

quantization [38], noncomposite vortices [39], intrinsic Josephson effect [40], two-condensate Bose systems [41], etc. Additionally, the presence in this compound of two nearly independent order parameters may lead to a novel type-1.5 superconductivity [42, 43, 44].

However, the applicability of high- T_c superconductors is strongly conditioned by the high vortex mobility that results from their high T_c , small coherence length and strong anisotropy, that causes flux creep phenomena even for current densities much smaller than the critical one [45]. Additionally, it has been reported that under certain conditions these materials develop a thermoelectromagnetic instabilities [46, 47, 48, 49, 50, 51, 52], which consists of an abrupt propagation of a superconductor-normal interface, leaving behind a trail of overheated material. This interface rushes deep into the sample in an attempt to establish the lowest-energy state, for which the flux distribution should be smooth everywhere. Similar chaotic behavior for flux penetration has been observed in MgB_2 [53, 54, 55, 56, 58], and Pb [59, 60, 61, 62, 63, 64], as noise in magnetic hysteresis loops, jumps and finger-like or tree-like structures. These vortex instabilities represent a serious drawback and an important limitation on the value of the critical current, the use of these materials for high-field applications and the potential development of devices based on them.

My interest in superconductivity started soon after I attended in 1989 a course on the theory of superfluidity and superconductivity lectured by Prof. G. I. Salitra during my undergraduate studies at the Department of Theoretical Physics in Odessa State University. Then, the recent discovery high- T_c superconductors called considerable attention for both basic experimental and theoretical researches and applications. Particularly, the resonating-valence-bond theory of high- T_c superconductivity [65] attracted a lot of interests to some researchers at the department. I decided to join this group and to carry out my Master's thesis on **The Localization of Bose Excitation in High- T_c superconductors** under the supervision of Prof. V. A. Fedorin and the guidance of Prof. V. M. Adamyan (chairman of the department of theoretical physics). My first experience in *cryogenic world* and *superconductivity experiments* started during my short staying at the laboratory of Prof. O. Rapp in the School of Engineering Physics at the Royal Institute of Technology in Stockholm in autumn 1990.

This *experimental world* was enhanced later on, when I followed some courses on superconductivity under the postgraduate program in material sciences at the Universitat Autònoma de Barcelona between 1995 and 1997.

Afterwards, just before finishing the doctoral courses under the program in advanced physics at the Universitat de Barcelona in 2001, I met Prof. Javier Tejada-Palacios and Ph.D. Antoni García-Santiago from Grup de Magnetisme. As a junior postdoctoral García-Santiago was then focused on the *pinning of vortices* in a high- T_c superconductor by magnetic domain structure [66], meanwhile Prof. Tejada was interested on *microwave studies* in both magnetic and superconducting materials. The opportunity and possibility to work in a recognized worldwide experimental group and to carry out microwave studies on superconducting materials supposed an interesting challenge I accepted. Nevertheless, as it is well known in the science world, there is a feedback loop between question and answer, which is continuously opening new way for further investigation. Something similar has happened with the development of this thesis which started with the intention to stimulate the emission of coherent electromagnetic radiation from superconductors. The early-stage results opened new questions that together with the collaboration from other research groups drove us to the possibilities to investigate commensurability and vortex instability effects in superconducting thin films under microwave fields.

The main objective of this thesis is to study vortex dynamics in type-2 superconducting thin films made of $\text{La}_{1.82}\text{Sr}_{0.18}\text{CuO}_4$, patterned Pb and MgB_2 , by means of the combination of microwave, dc and ac measurements. In particular, we explore first the magnetic moment response in real time under continuous and pulsed microwave mode, and second commensurability effects both in presence of microwave fields under ac susceptibility mode and using microwave reflection spectrometry.

This work is organized as follows:

- **Chapter 2** is intended to give a brief historical overview of superconductivity and a short introduction to some *theoretical aspects* as the London equations and the Ginzburg-Landau theory. The different types of superconductors and the main aspects of vortex matter such as the vortex structure, vortex lattice, flux motion and flux pinning are also addressed. We

expose the effects of the finite size of the *thin film geometry* on the measured quantities. Finally, we make a short review of two fundamental microwave concepts, namely the *complex conductivity* and the *surface impedance* of a superconductor.

- **Chapter 3** gives an overview of the experimental techniques used to prepare the superconducting samples and of the SQUID-based magnetometry utilized. We also describe the low-temperature *microwave setup* and the different microwave measurement modes applied, namely *sweeping*, *pulsed* and *power reflected*. Finally, we sketch the proposed *theoretical model* to obtain an estimation of the characteristic frequencies and the electric and magnetic fields of the resonant structure formed by a multi-turn coil with a sample loaded in its core.
- **Chapter 4** presents the results on vortex dynamics of superconducting thin films made of $\text{La}_{1.82}\text{Sr}_{0.18}\text{CuO}_4$, Pb with a periodic array of microholes and MgB_2 under *continuous* and *pulsed microwave modes*. In the first set of experiments, the *temporal- and frequency-dependent magnetic moment* is investigated at different values of the temperature, dc magnetic fields, and nominal microwave power in the three samples. In the second set of experiments, the *temporal evolution of the sample magnetization* is recorded when single microwave pulses are applied at fixed values of temperature, dc magnetic fields, pulse duration and nominal power in the $\text{La}_{1.82}\text{Sr}_{0.18}\text{CuO}_4$ and MgB_2 samples.
- **Chapter 5** exposes the results obtained for a thin film of Pb with a periodic array of microholes under *ac susceptibility* and *microwave power reflection* techniques. The in-phase and out-of-phase components of the ac susceptibility are measured under the combination of crossed dc and microwave magnetic fields at different fixed values of microwave power and frequency for temperature close to T_c . The *magnetic field dependence of the microwave backward reflection coefficient* is studied in a wide range of temperature (from 6.80 K to 7.20 K) at different fixed microwave resonant modes and powers.

Chapter 2

Theoretical aspects of superconductivity

In this chapter, we first give a brief overview from the breakthrough and early history of superconductivity until the discovery of a new class of superconducting materials, and second we address theoretical aspects of superconductivity that will provide important arguments to explain the phenomena observed and described in the next chapters.

2.1 Superconductivity

2.1.1 Historical overview

Superconductivity is a macroscopic quantum phenomenon whose special physical properties have attracted the attention of many physicists and engineers, since it was discovered in 1911 by H. Karmarlingh Onnes [67], just three years after he first liquified helium. Later on, he found that the electrical resistance of some metals, such as lead, mercury, tin, and aluminum, disappeared completely (*perfect conductivity*) in a narrow temperature range at the so-called superconducting critical transition temperature, T_c , specific to each metal. Three years later, in 1914, he also discovered that a strong enough dc magnetic field or high enough electrical current restore the resistance in the sample.

In 1933, Meissner and Ochsenfeld [68] elucidated the interface between the trans-

2. Theoretical aspects of superconductivity

port and magnetic properties of superconductors when they found the more essential feature of superconductivity, the *perfect diamagnetism* or the ability to expel an external magnetic field below T_c (the *Meissner effect*). The thermal properties of the superconducting material were investigated by Gorter and Casimir in 1934 [69]. By introducing a phenomenological two-fluid model (TFM) they vaticinated a temperature dependence of the superconducting carriers. In 1935, the two remarkable electrodynamic properties of superconductivity were neatly described by the phenomenological theory of F. and H. London [70]. H. London also observed the anomalous skin effect, and F. London was the first to suggest that the flux in a superconductor is quantized [71].

The major theories of superconductivity were accomplished in the 1950s. In the spring of 1950, Maxwell [72], and independently Reynolds, Serin, Wright and Nesbitt [73], experimentally discovered that the mass of the isotope of mercury depends on T_c : $T_c M^{1/2} \approx \text{const}$. This *isotope effect* associated the mass and movement of the ions, and therefore the vibration of the crystal structure (phonons), with the mechanism of the superconductivity. Relying upon this effect, Fröhlich [74] and Bardeen [75] introduced the concept of phonon-mediated electron-electron attraction to establish the basic forces responsible for the superconductivity phenomenon. Ginzburg and Landau (1950) introduced a phenomenological theory, commonly called *macroscopic theory of superconductivity* [76]. This theory, based on the Landau's theory for second-order phase transition [77], introduces the density of superconducting electrons as an order parameter for describing the thermodynamic properties and basic lengths that characterize these materials via the expansion of the free energy in power terms of this parameter combined with temperature-dependent coefficients.

In 1953, Pippard [78] proposed a non-local electrodynamic model which studies the influence of the applied magnetic field on the superconducting electrons and introduces the coherence length concept, ξ . Later on, in 1956, Corak, Goodman, Satterthwaite and Wexler [79], experimentally discovered the existence of a superconducting energy gap. Cooper studied in 1956 the problem of two electrons interacting via an attractive effective potential above a frozen Fermi sea and deduced the condensate state of strongly-correlated conductivity electron pairs. In 1957, A. Abrikosov [2] used the Ginzburg–Landau theory to predict

2. Theoretical aspects of superconductivity

the existence of a new quantum state, the so-called *mixed state* in type-2 superconductors (see subsection 2.1.5), where magnetic field penetrates the superconductor in quantized flux lines, which interact in a repulsive way. The same year, Bardeen, Cooper and Schrieffer (BCS) proposed a complete microscopic theory that explains the mechanism of superconductivity [80]. In 1958, Bogoliubov proposed a new theoretical method for the superconductivity based on the canonical transformation approach developed by himself to explain theoretically the superfluidity phenomenon [81]. Both theories show that even a weak attractive phonon-mediated electron-electron interaction can bind electrons into the so-called *Cooper pairs*. Moreover, BCS and Bogoliubov theories provide a microscopic foundation to the phenomenological London and Ginzburg-Landau theories, as it was later on demonstrated by Gor'kov [82]. In 1962, Josephson [83] postulated the existence of the *quantum tunneling effect* that occurs when a supercurrent goes through a extremely thin film of an insulating material.

Superconducting materials research was rejuvenated by the discovery by Bednorz and Müller in 1986 of new a class of hole-doped cuprate (HDC) high-temperature superconductors (HTS) [1], some of which have a T_c in excess of 100 K. This vast class of layered copper oxide compounds with perovskite-like structures comprises more than 200 superconductor belonging to different families [84] with T_c values up to 134 K at ambient pressure, and is the only class of materials with confirmed T_c above liquid nitrogen temperature (77 K). The T_c in these materials has a dome-shaped dependence as a function of carrier concentration. The material that is both ferromagnetic and superconducting UGe₂ was first discovered in 2000, and remain of special interest since the coexistence of these two phases could be exploited for spintronic-type applications [85]. In 2001, it was found out superconductivity in magnesium diboride (MgB₂) at about 40 K [33]. MgB₂ is a simple compound of two abundant, inexpensive elements that belongs to the so-called conventional superconductors for which the superconductivity is based on the well-known electron-phonon interaction. Moreover, the presence of two gaps in MgB₂ makes this material a good candidate to demonstrate a new superconducting phase showing the coexistence of type-1 and type-2 behavior [44]. In 2008 new interesting iron-based superconductors with high T_c up to 55 K were discovered [86].

2.1.2 London equations

The two basic electrodynamic properties of superconductors (perfect conductivity and diamagnetism) were described by Fritz and Heinz London. By considering that the material is composed only of superconducting electron pairs and combining the expressions that describe the force exerted on this pair and the current density, the *first London equation* is obtained [45],

$$\mathbf{E} = \Lambda \frac{d\mathbf{J}}{dt}. \quad (2.1)$$

Here \mathbf{E} is the applied electric field, \mathbf{J} is the current density for paired electrons and $\Lambda = m/(n_s e^2)$, where e and m are the charge and mass of an electron, respectively, and n_s is the density of superconducting electrons per unit volume. Performing the rotor operation of both sides of Eq. (2.1) and using the Faraday's law leads to the *second London equation* [45],

$$\nabla^2 \mathbf{B} = \mathbf{B}/\lambda^2, \quad (2.2)$$

where $\lambda^2 = \Lambda/\mu_0$. This equation implies that the magnetic field and the currents are screened from the interior of a sample over a distance λ , thus accounting for the *Meissner effect*. The first London equation can be rewritten in a compact way using the vector potential \mathbf{A} of a local magnetic field ($\mathbf{B} = -\nabla \times \mathbf{A}$),

$$\mathbf{J} = -\frac{\mathbf{A}}{\mu_0 \lambda^2}. \quad (2.3)$$

The superconducting electron density n_s depends on the temperature, starting from zero at $T = T_c$ and increasing continuously up to the total density of the conduction electrons n when $T \rightarrow 0$. If the upper limit n is taken into account in Eq. (2.3), the frequency-independent skin depth, the so-called *London penetration depth*, is achieved:

$$\lambda_L^2(0) = \left(\frac{m}{ne^2 \mu_0} \right). \quad (2.4)$$

It is worth noting that the decrease of n_s as $T \rightarrow T_c$ causes the divergence of $\lambda_L(T)$ at T_c . It was found that $\lambda_L(T)$ diverges roughly as $[1 - (T/T_c)^4]^{-1/2}$ [45].

2.1.3 The Ginzburg-Landau theory

Ginzburg and Landau extended the London phenomenological model by using the Landau's theory of second-order phase transitions. They introduced as an order parameter, a complex scalar "wave function of the superconducting electrons", $\psi(\mathbf{r}) = |\psi(\mathbf{r})|e^{i\varphi(r)}$, such that $n_s \propto |\psi(\mathbf{r})|^2$. The order parameter equals zero above T_c and becomes infinite below T_c . The free energy functional F_s in absence of a magnetic field can be expanded in a power series of ψ in the vicinity of the phase transition [45],

$$F_s = F_n + \alpha|\psi|^2 + \frac{\beta}{2}|\psi|^4 + \dots, \quad (2.5)$$

where F_n is the free energy of the normal state, and α and β are phenomenological constants. The parameter β must be positive, otherwise the lowest energy would occur for arbitrarily large values of $|\psi|^2$, where the expansion is not longer adequate. On the other hand, the parameter α can be positive or negative. In the first case, α gives rise to a minimum in the free energy at $|\psi|^2 = 0$, which corresponds to the normal state. If $\alpha < 0$, the minimum in the free energy occurs when

$$|\psi|^2 = |\psi_\infty|^2 = -\frac{\alpha}{\beta}. \quad (2.6)$$

Here ψ_∞ designates the bulk value of the order parameter, corresponding to the maximum concentration of Cooper pairs that can exist in an infinitely large superconducting sample at a given temperature in absence of magnetic fields or currents. Using this expression in the free energy definition, yields

$$F_n - F_s = \frac{\alpha^2}{\beta}, \quad (2.7)$$

where $\alpha^2/\beta = \mu_0 H_c^2/2$ is the condensation energy of the superconducting state and H_c is the *thermodynamic critical field*. The condensation energy reflects an ordered superconductor state as compared with the normal one, and represents the available energy reservoir sustaining the superconducting state.

2. Theoretical aspects of superconductivity

In presence of a magnetic field h the free energy is modified as

$$F_s = F_n + \alpha|\psi|^2 + \beta|\psi|^4 + \frac{1}{2m^*}|(-i\hbar\nabla - 2e\mathbf{A})|^2 + \frac{\mu_0 h^2}{2}. \quad (2.8)$$

Here $m^* \approx 2m_e$ is the effective mass of the Cooper pair, \hbar is Planck's constant, and \mathbf{A} is the vector potential which corresponds to the field $\mathbf{h} = \nabla \times \mathbf{A} / \mu_0$. The fourth term represents the kinetic energy of the Cooper pairs, whereas the last term is the magnetic field energy density. Minimizing this free energy with respect to ψ and \mathbf{A} yields a set of coupled nonlinear Ginzburg–Landau (GL) differential equations [87]:

$$\frac{1}{2m^*} (-i\hbar\nabla - 2e\mathbf{A})^2 \psi + \beta|\psi|^2 = -\alpha\psi, \quad (2.9)$$

$$\mathbf{J} = \nabla \times \mathbf{h} = \frac{e}{m^*} [\psi^* (-i\hbar\nabla - 2e\mathbf{A}) \psi + \psi (i\hbar\nabla - 2e\mathbf{A}) \psi^*]. \quad (2.10)$$

These equations provide complete information on the superconducting state, namely the spatial variation of the order parameter (ψ), and the local distribution of the magnetic field inside the superconductor (\mathbf{A}). The nonlinear term acts like a repulsive potential of ψ on itself, thereby restricting strongly any variation of ψ in space. In the limiting case of $|\psi| = \text{constant}$, Eq. (2.10) reduces to the solution of the first London equation, thus the London approach appears as a frontier case of the GL equations as a result of rigid ψ .

For a finite superconductor one must provide boundary conditions. At a vacuum-superconductor frontier, no current can cross the insulating surface. Therefore, the momentum operator should satisfy [88]

$$(-i\hbar\nabla - 2e\mathbf{A}) \psi \cdot \mathbf{n} = 0, \quad (2.11)$$

where \mathbf{n} is the unit vector normal to the boundary. For a superconductor-normal metal interface this condition changes to

$$(-i\hbar\nabla - 2e\mathbf{A}) \psi \cdot \mathbf{n} = -\frac{i\hbar}{b} \psi, \quad (2.12)$$

where b is the so-called extrapolation length, accounting for the finite length over which the order parameter penetrates into the normal metal.

2. Theoretical aspects of superconductivity

Cooper pairs can tunnel into the normal metal (or a superconductor with a lower T_c) over a specific distance ξ_n and doing so induce superconducting properties in the normal metal. This phenomenon is known as the *proximity effect*. In the dirty limit (see below), ξ_n can be estimated as [89]

$$\xi_n = \sqrt{\frac{\hbar D}{2\pi k_B T}}, \quad (2.13)$$

where D is the diffusion constant of the normal metal which is proportional to the elastic mean free path of the electrons. Conversely, normal electrons diffuse into the superconductor and consequently reduce the order parameter, lowering T_c [90]. In the case of a magnetic metal, the T_c reduction is even more pronounced due to the strong pair breaking effect of the magnetic moments.

2.1.4 Characteristic length scales ξ and λ

From the first GL equation it is possible to determine the typical length scale over which the superconducting order parameter ψ can vary. In the simplest case where $\mathbf{A} = 0$ and T is very close to T_c such that the nonlinear term in ψ can be neglected, we obtain [89]

$$\nabla^2 \psi + \frac{1}{\xi^2} \psi = 0, \quad (2.14)$$

where $\xi(T) = \hbar/[2m^* \alpha(T)]^{1/2}$ is the coherence length. Since $\alpha(T) \propto (T - T_c)$ it follows

$$\xi(T) = \frac{\xi(0)}{\sqrt{1 - T/T_c}}. \quad (2.15)$$

The coherence length rises with increasing temperature and diverges at T_c . The relation between the temperature dependence coherence length $\xi(T)$ and the BCS-intrinsic coherence length ξ_0 depends on the purity of the material, which is given by the elastic mean free path l . In the clean limit ($l \gg \xi_0$) and dirty limit ($l \ll \xi_0$), $\xi(T)$ is given by [45]

$$\xi(T) = \frac{0.74 \xi_0}{\sqrt{1 - T/T_c}} \quad (l \gg \xi_0), \quad (2.16)$$

2. Theoretical aspects of superconductivity

$$\xi(T) = \frac{0.85\sqrt{\xi_0 l}}{\sqrt{1 - T/T_c}} \quad (l \ll \xi_0). \quad (2.17)$$

The magnetic penetration depth $\lambda(T)$ characterizes the distance over which the magnetic field is screened by the superconducting currents. The relations between the temperature dependent GL penetration depth $\lambda(T)$ and the London penetration depth $\lambda_L(0)$ for the clean and dirty limits are respectively [45]

$$\lambda(T) = \frac{\lambda_L(0)}{\sqrt{2(1 - T/T_c)}} \quad (l \gg \xi_0), \quad (2.18)$$

$$\lambda(T) = 0.64\lambda_L(0) \frac{\sqrt{\xi_0/l}}{\sqrt{1 - T/T_c}} \quad (l \ll \xi_0). \quad (2.19)$$

Zero-temperature values of the coherence length and penetration depth, $\xi(0)$ and $\lambda(0)$, respectively, depend strongly on the microscopic properties of the superconductor and the amount of impurities it contains.

It is useful to introduce the dimensionless Ginzburg–Landau parameter κ , which is defined as the ratio of the two characteristic lengths

$$\kappa \equiv \frac{\lambda(T)}{\xi(T)}, \quad (2.20)$$

which in this approximation turns to be temperature independent.

2.1.5 Type-1, type-2 and type-1.5 superconductors

Superconductors can be classified on the basis of their response to an external applied magnetic field accordingly to the sign of the surface energy of a boundary between normal and superconducting regions, which is roughly proportional to the difference $(\xi - \lambda)$. Hence, *type-1* superconductors are those with $\xi > \lambda$ and positive surface energy, while *type-2* superconductors have $\xi < \lambda$ and negative surface energy, which favors the formation of superconducting-normal boundaries and magnetic flux penetration. By considering the GL parameter, the breakpoint between the positive and negative surface energy was found to occur at $\kappa = 1/\sqrt{2}$ [2]. Very close to this point a long-range attraction of vortices appears, which

2. Theoretical aspects of superconductivity

is responsible for the new patterns where the Meissner and Abrikosov-lattice domains coexist. This case has been recently referred to as *type-1.5* superconductor [44, 91, 92, 93].

The $H - T$ phase diagram for a bulk type-1 and type-2 superconductor is represented in panels (a) and (b) in Fig. 2.1, respectively. Long cylinders [without demagnetization effect (see below)] of type-1 superconductors ($\kappa < 1/\sqrt{2}$) are in the Meissner state for applied fields up to H_c , given by

$$H_c(T) = \frac{\Phi_0}{2\sqrt{2}\pi\mu_0\lambda(T)\xi(T)}, \quad (2.21)$$

where Φ_0 is the superconducting flux quantum (see below). In the Meissner state, the superconductor behaves as a perfect diamagnetic material so that all magnetic flux is expelled from the interior of the sample ($B = 0$). At $H_c(T)$ a discontinuous breakdown of superconductivity in a first-order transition occurs and the sample turns to the normal state [Fig. 2.1(a)]. Long cylinders of type-2 superconductors ($\kappa > 1/\sqrt{2}$) are in the Meissner state for fields smaller than the *first critical field*

$$H_{c1}(T) = \frac{\Phi_0}{4\pi\mu_0\lambda^2(T)} \ln \kappa. \quad (2.22)$$

For fields $H > H_{c1}(T)$, there is a continuous increase in flux penetration until the magnetic flux overlaps at the so-called second critical field and the system becomes normal [Fig. 2.1(b)]. This *second critical field* can be expressed as

$$H_{c2}(T) = \frac{\Phi_0}{2\pi\mu_0\xi^2(T)}. \quad (2.23)$$

Because of the partial flux penetration, the diamagnetic energy cost of holding the field out is less, so H_{c2} can be much greater than H_c , making high-field superconducting magnets possible. In the so-called *mixed state* or *Schubnikov phase*, between H_{c1} and H_{c2} , the flux should not penetrate in laminar domains but rather in a regular array of flux tubes or *vortices*, each bearing a quantized amount of flux, the so-called *superconducting flux quantum* $\Phi_0 = h/2e = 2.07 \times 10^{-15} \text{ Tm}^2$ [2].

In the field and temperature region $H_{c2} < H < H_{c3}$, superconductivity only exists

2. Theoretical aspects of superconductivity

in a thin sheet at the surface, while the rest of the material is in the normal state. Above H_{c3} , superconductivity is completely destroyed and the whole sample is in the normal state. A very special case coined as intermediate–mixed state can be found in close vicinity to the crossover point at $\kappa = 1/\sqrt{2}$, where the Meissner (typical for type-1) and vortex states (typical for type-2) can coexist in the same sample [43, 94, 95, 96]. Finally, in type-1.5 superconductors, besides the Meissner and mixed states, a new vortex state exists in between, the vortex cluster or vortex clumps phase, where vortex-rich (vortex clusters) areas are separated by Meissner areas [Fig. 2.1(c)].

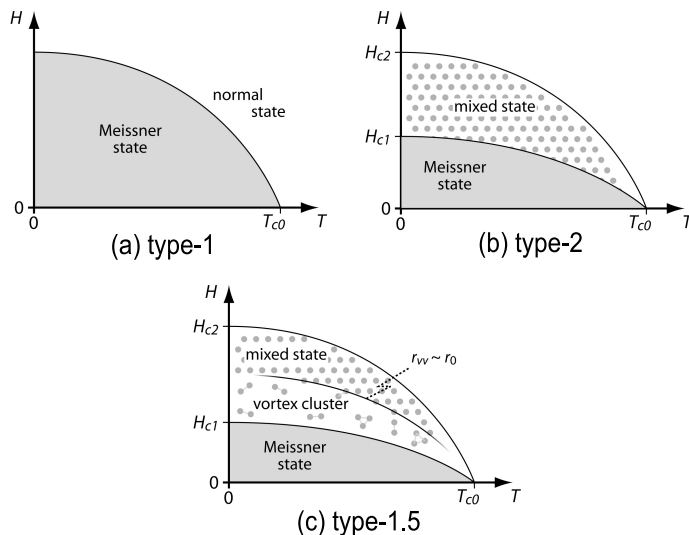


Figure 2.1: The $H - T$ phase diagram of (a) type-1 and (b) type-2 superconductors, and (c) a tentative schematic $H - T$ phase diagram of a type-1.5 superconductor [24].

By considering the equilibrium magnetization expression,

$$\mu_0 \mathbf{M} = \mathbf{B} - \mu_0 \mathbf{H}, \quad (2.24)$$

the different phases, namely Meissner, mixed, vortex cluster and normal, can be distinguished. The $M(H)$ response in type-1, type-2 and type-1.5 superconductors is shown in Fig. 2.2. Without taking into account demagnetization

2. Theoretical aspects of superconductivity

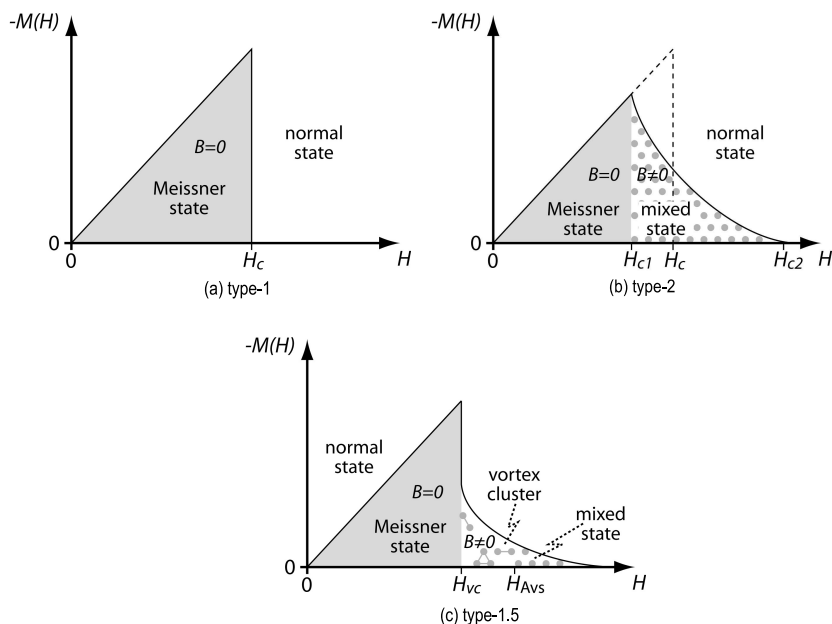


Figure 2.2: Reversible magnetization, without considering demagnetization fields, as a function of the applied magnetic field $[-M(H)]$ for (a) an ideal homogeneous type-1 superconductor, (b) a type-2 superconductor, and (c) a type-1.5 superconductor [24].

fields, type-1 superconductors have an abrupt first-order phase transition from the Meissner to the normal state at $H = H_c$. In type-2 superconductors, the transition from the Meissner to the mixed state leads to the appearance of a magnetization kink at $H = H_{c1}$. For $H > H_{c1}$, the type-2 superconductors are in the mixed state and the magnetization decreases in a smooth way as the magnetic flux penetrates the sample going down to zero at H_{c2} where the normal state is recovered. Type-1.5 materials are predicted to be just half way between type-1 and type-2 [37]: the formation of the vortex clusters surrounded by the Meissner phase results in the $M(H)$ drop at $H = H_{vc}$ (vc stands for vortex cluster). As the field increases above H_{vc} , vortex clusters grow, but the vortex-vortex distance r_{vv} in the clusters remains unchanged, $r_{vv} \approx r_{opt}$, where r_{opt} is the optimal vortex-vortex separation in the clusters caused by the competition of the vortex-vortex repulsion and the vortex-vortex attraction in type-1.5 materials [37, 97].

2.2 Vortex matter in superconductors

2.2.1 The structure of an isolated vortex

When flux first enters a type-2 superconductor, it is carried in an array of vortices sparsely distributed through the material. While the separation is large compared to λ , there will be negligible overlap or interaction of the vortices, so that each one can be treated as isolated. A single vortex consists of a normal core of radius ξ , around which shielding currents circulate. Fig. 2.3 shows a schematic representation of a vortex. The local magnetic field $h = |\mathbf{h}|$ and the superconducting electron density n_{sc} as a function of the distance r from the vortex center are also depicted in this figure. The superconducting order parameter vanishes in the center of the vortex core. The local field h is highest in the normal core and decays, due to the screening currents, over a distance given by the penetration depth λ .

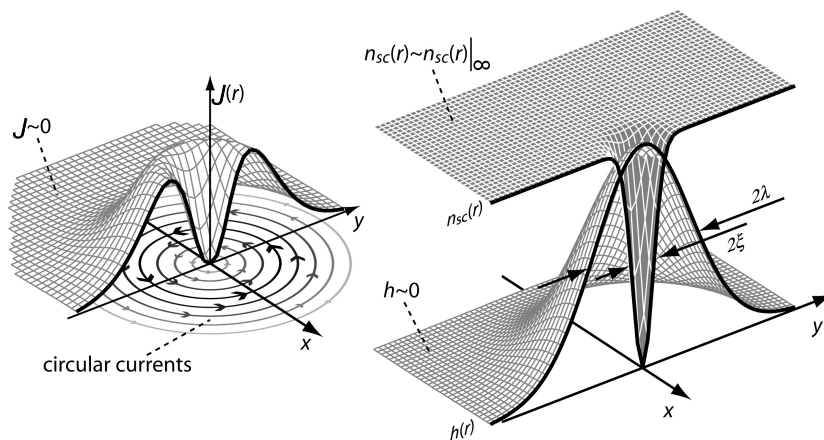


Figure 2.3: Structure of an isolated vortex, showing the radial distribution of the local field $h(r)$, the circulating supercurrents $J(r)$, and the density of the superconductor electrons $n_{sc}(r)$ [24].

The local magnetic field and current distribution in the mixed state ($H_{c1} < H < H_{c2}$) of a type-2 superconductor can be obtained by using the London model [70], which is valid provided that $\kappa \gg 1$ and the order parameter (ψ or n_{sc}) is nearly constant in space. In the London limit, the free energy per unit length (the line

2. Theoretical aspects of superconductivity

energy) can be expressed as [45, 88]

$$E_l = \frac{1}{2\mu_0} \int_{\text{volume}} (\mathbf{h}^2 + \lambda_L^2 |\nabla \times \mathbf{h}|^2) d\mathbf{r}, \quad (2.25)$$

where the first and second terms are the magnetic and the kinetic energy, respectively, and the integration volume does not include the hard cores of the vortices. Minimization of E_l with respect to the local field \mathbf{h} yields the London equation for the local field distribution outside the vortex core:

$$\mathbf{h} + \lambda_L^2 \nabla \times \nabla \times \mathbf{h} = 0. \quad (2.26)$$

This equation can also be derived from the GL theory by setting $\nabla\psi(\mathbf{r})$ to zero. To take into account the vortex core, this equation may be adjusted to

$$\mu_0 (\mathbf{h} + \lambda_L^2 \nabla \times \nabla \times \mathbf{h}) = \Phi_0 \delta_2(\mathbf{r}), \quad (2.27)$$

where the small core is represented by a two-dimensional delta-function and Φ_0 follows the local field direction. The local field distribution around a vortex can be expressed as [45, 88]

$$\mu_0 h(r) = \frac{\Phi_0}{2\pi\lambda^2} K_0\left(\frac{r}{\lambda}\right), \quad (2.28)$$

where K_0 is the zero-order Bessel function which decreases as $\exp(-r/\lambda)$ at large distances and diverges logarithmically as $\ln(\lambda/r)$ as $r \rightarrow 0$. By performing the derivative of the local field with respect to the radial dependence, the current distribution of a single vortex can be calculated [98]:

$$J(r) = \frac{\Phi_0}{2\pi\mu_0\lambda^2} K_1\left(\frac{r}{\lambda}\right). \quad (2.29)$$

Here, K_1 is the first order Bessel function which decreases as $1/r$ at short distances and diverges as $\exp(-r/\lambda)$ at large distances. The line energy is the sum of the field and the kinetic energy of the currents and a small core contribution [45, 88]:

$$E_l = \frac{1}{4\pi\mu_0} \left(\frac{\Phi_0}{\lambda}\right)^2 \left[\ln\left(\frac{\lambda}{\xi}\right) + \epsilon \right]. \quad (2.30)$$

2. Theoretical aspects of superconductivity

The constant $\epsilon \simeq 0.12$ describes the contribution of the normal core. Since E_l is a quadratic function of the magnetic flux, it is energetically unfavorable in a homogenous superconductor to form multiquanta vortices, carrying more than one flux quantum.

2.2.2 The vortex lattice

The interaction energy between two parallel vortices is easy to treat under the approximation $\kappa \gg 1$, since in this approach the medium is linear and a superposition (including an extra normal vortex core) may be used. Due to the repulsive electromagnetic interaction between vortices in superconductors, they tend to be positioned as far away from each other as possible, resulting in the well-known Abrikosov vortex lattice [2]. The repulsive interaction energy per unit length between two vortices i and j at a mutual distance r_{ij} is given by [45, 88],

$$U_{ij}(r_{ij}) = \frac{\Phi_0^2}{2\pi\mu_0\lambda^2} K_0 \left(\frac{r_{ij}}{\lambda} \right), \quad (2.31)$$

which decreases exponentially at large distances ($r_{ij} \gg \lambda$), and diverges at short distances ($\xi < r_{ij} \ll \lambda$). The repulsive force between two vortices f_{ij} can be estimated from the energy U_{ij} :

$$f_{ij}(r_{ij}) = -\frac{\partial U_{ij}}{\partial r_{ij}} = \frac{\Phi_0^2}{2\pi\mu_0\lambda^3} K_1 \left(\frac{r_{ij}}{\lambda} \right). \quad (2.32)$$

Vortices in superconductors consist of a normal core of size ξ and supercurrents flowing over a distance λ . If two vortices are generated in a type-1 superconductor, the normal core would overlap first, due to the larger values of ξ with respect to λ , thus leading to a gain in the condensation energy and, consequently, to vortex-vortex attraction [99] [Fig. 2.4(a)]. Two vortices in a type-2 superconductor, however, would have first their supercurrents overlapping, in view of the bigger λ , leading to vortex-vortex repulsion [Fig. 2.4(b)]. An attractive vortex-vortex interaction results in the formation of macroscopic normal domains in the intermediate state [94], while vortex-vortex repulsion leads to the appearance of the Abrikosov lattice [2]. For the case of type-1.5 superconductor the

2. Theoretical aspects of superconductivity

vortex-vortex interaction is the result of the competing interaction between the short-range repulsion and long-range attraction [Fig. 2.4(c)].

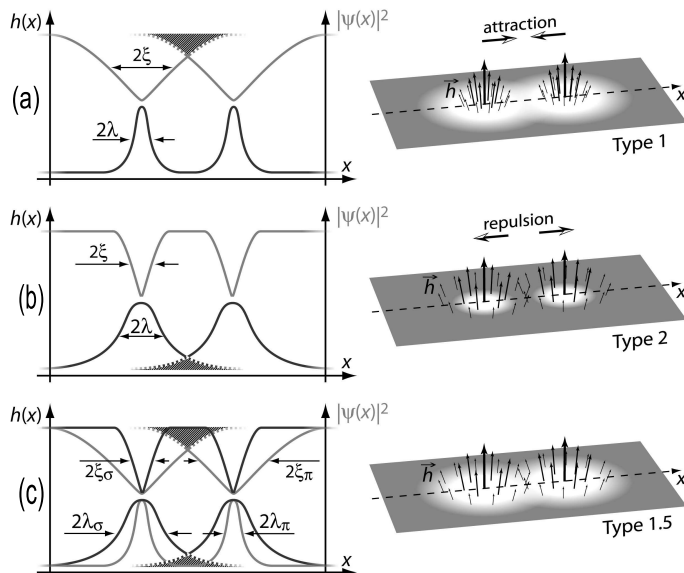


Figure 2.4: Sketches of the vortex-vortex interactions. In type-1 superconductors, vortex cores are overlapping first, thus causing an attraction between vortices (a). In type-2 superconductors, the first to overlap are the local fields $h(x)$, which leads to vortex-vortex repulsion (b). Type-1.5 superconductors combine both the vortex-vortex attraction and repulsion, since type-1 and type-2 conditions are formally fulfilled for the subcomponents of the order parameter simultaneously. Tentative and simplified picture is shown in (c) [24].

For a given vortex density, the maximum mutual distance between vortices is obtained for a triangular arrangement, which is the most favorable vortex configuration [Fig. 2.5(a)]. The density of vortices n_v increases with increasing field. The distance a_v between nearest neighbor vortices in the triangular lattice is related to the induction B through the relation

$$B(\Delta) = \Phi_0 n_v = \frac{2}{\sqrt{3}} \frac{\Phi_0}{a_v^2(\Delta)}. \quad (2.33)$$

The second most favorable configuration, with only a slightly higher energy, is a square vortex lattice [Fig. 2.5(b)]. The distance between nearest neighbor vortices

2. Theoretical aspects of superconductivity

in a square lattice depends on the induction B as

$$B(\square) = \Phi_0 n_v = \frac{\Phi_0}{a_v^2(\square)}. \quad (2.34)$$

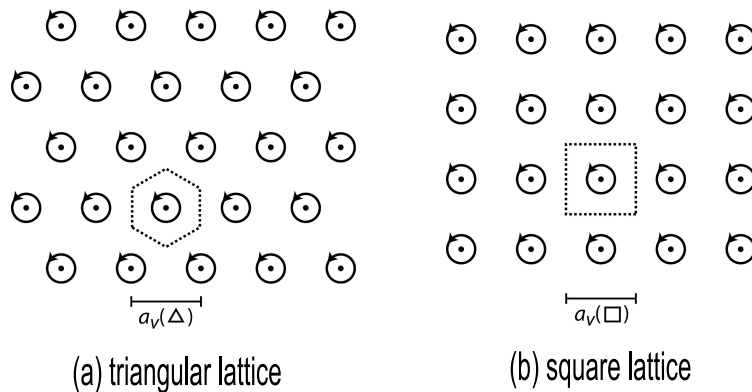


Figure 2.5: Schematic drawing of (a) a triangular and (b) a square vortex lattice with period $a_v(\Delta)$ and $a_v(\square)$, respectively. The dashed lines indicate the unit cells [24].

2.2.3 Flux motion

From a practical point of view, the most useful aspect of type-2 superconductors to date has been the ability to make superconducting solenoids which can supply steady fields of over 10 tesla without dissipation of energy because of the resistanceless persistent current. For making such magnets the superconducting material must not only have a critical field substantially higher than the field to be produced, but it must also be able to carry a high current in that field without resistance. High values for the critical current density in an applied field can be reached if the flux lines are prevented from moving, since a moving vortex induces an electric field parallel to the current density and hence dissipates energy. The origin of the flux motion is the Lorentz force that results from the action of the current density \mathbf{J} on the flux lines:

$$\mathbf{F}_L = \mathbf{J} \times \Phi_0. \quad (2.35)$$

2. Theoretical aspects of superconductivity

The Lorentz force tends to move the vortices transversely to the current. In order to suppress the motion of vortices, \mathbf{F}_L should be neutralized by a pinning force \mathbf{F}_P associated with the introduction of a pinning center into the superconductor. As long as every individual vortex is prevented from moving, $\mathbf{F}_L + \mathbf{F}_P = 0$. From this static scenario, an estimation of the pinning force of an individual pinning center and of J_c can be obtained. The total force acting on the flux line per unit length is the sum of several contributions [100]:

$$\mathbf{F} = \mathbf{F}_L - \mathbf{F}_P - \eta \mathbf{v}_v - \mathbf{F}_M, \quad (2.36)$$

where $-\eta \mathbf{v}_v$ is a small friction-like contribution (the viscous damping force) proportional to the vortex velocity \mathbf{v}_v , and \mathbf{F}_M is the Magnus force, which is usually negligible as well as the vortex mass [101]. A general formula for \mathbf{F}_P cannot be given, since it strongly depends on the specific type of the pinning centers. The average macroscopic pinning force per unit volume is related to the critical current density by the expression

$$F_P = J_c B. \quad (2.37)$$

In a steady state, the vortex velocity \mathbf{v}_v will achieve a constant value. In the limit of a pinning-free superconductor ($\mathbf{F}_P = 0$), \mathbf{v}_v is determined entirely by the viscosity of the medium, yielding $\mathbf{v}_v = (\mathbf{J} \times \Phi_0) / \eta$. The dissipative electric field in the core of the vortices (normal area) induced by the vortex motion is

$$\mathbf{E} = \mathbf{B} \times \mathbf{v}_v = (\mathbf{B} \times (\mathbf{J} \times \Phi_0)) / \eta. \quad (2.38)$$

\mathbf{E} induces a resistive voltage and an amount of energy is dissipated in order to maintain the applied current \mathbf{J} . From this expression, it is possible to define the *flux flow resistivity* [45]

$$\rho_f = E / J = \Phi_0 B / \eta, \quad (2.39)$$

which arises exclusively from the viscous flow of vortices. ρ_f is a linear function of B , so that $\rho_f = 0$ for $B = 0$, and $\rho_f = \rho_n$ for $B = \mu_0 H_{c2}(T = 0)$, where ρ_n is the normal state resistivity. From this, the flux flow resistivity can be redefined

2. Theoretical aspects of superconductivity

as

$$\rho_f = \rho_n B / H_{c2}(0). \quad (2.40)$$

This expression reflects that the concept of flux flow resistivity is clearly referred to an electrical resistivity which would be observed in the mixed state of a pinning-free type-2 superconductor. In the presence of pinning, this formulation is expected to be modified. A determination of the $E(J)$ relationship should prove very useful to extract information about the vortex motion. In practice, this is done by measuring voltage-current, $V(I)$, characteristics in transport measurements.

As opposed to what the resistive flux flow regime might suggest, criteria such as pinning and $J < J_c$ do not warrant for the complete absence of vortex motion. Thermal excitations can provide enough energy for vortices to hop from one pinning site to another at finite temperatures. This type of vortex motion is called *flux creep* and generates a resistive voltage proportional to the average creep velocity, which is usually much smaller than the velocity caused by the resistive flux flow. The electric field generated by the flux-creep-assisted vortex motion is given by [45]

$$E = vB = \omega_0 a_\omega B e^{-\frac{F_a}{k_B T}} \sinh\left(\frac{W}{k_B T}\right), \quad (2.41)$$

where v is the creep velocity, ω_0 is the attempt frequency, a_ω is the jump width, W is the difference in potential energy between two neighboring pinning sites, and $F_a = F_a(T, B, J)$ is the activation energy or barrier energy, *i.e.* the height of the potential barrier between two adjacent pinning sites. For small currents, the system is in the so-called *thermally assisted flux flow (TAF F)* regime:

$$E_{TAF F} \propto J e^{-\frac{F_a}{k_B T}} \quad \text{for } J \ll J_c \frac{k_B T}{F_a}. \quad (2.42)$$

When $J \approx J_c$, $E_{TAF F} \propto \exp[-F_a/(k_B T)]$, and for $J \gg J_c$, $E_{TAF F} \propto \sqrt{J^2 - J_c^2} \approx J$. For conventional type-2 superconductors, the activation energy is expressed as [102] $F_a(T, H, J) = F_0(1 - J/J_c)$. That is to say, the pinning strength decreases as the current increases.

2.2.4 Flux pinning

Vortex can be pinned by any spatial inhomogeneity of the material causing a local minimum in the free energy landscape. Crystalline imperfections as grain boundaries, twin boundaries, or stoichiometric deviations, amongst others, can act as pinning centers. The pinning can also be induced artificially by irradiation, ion implantation, film thickness modulation, doping, etc. Theoretically, these pinning mechanisms are accounted by local variations of T_c or κ which reduce the free energy if the vortex core is located at the position of the (normal) defect or pinning sites. Among the different possible mechanisms to pin vortices, the pinning can be core or electromagnetic type depending on the interaction between the vortex and the pinning center.

Core pinning. Vortices prefer to sit at any defect which produces a depression of the order parameter. At that place the free energy per unit length of the vortex is lowered since it is no longer necessary to fully generate the normal core of the vortex. The relevant distance in this kind of pinning is the coherence length ξ .

Electromagnetic pinning [103] takes place when the vortex-defect separation is smaller than the penetration depth λ . This kind of pinning occurs when the flux line is near a superconductor/normal boundary. This boundary imposes a condition on the supercurrents encircling the vortex core to flow parallel to the border. Theoretically, this effect can be modeled by assuming an image antivortex located at the normal phase which interacts attractively with the flux line.

Magnetic pinning [104, 105, 106]. In a model system consisting of a superconductor and a magnetic dipole at a fixed distance and with fixed magnetization, the interaction energy between the dipole and the screening currents is constant. In this specific case, any variation of the free energy of the system in the presence of vortices, either induced by the dipole or by an external field, can be attributed to rearrangements of the vortex pattern. The part of the interaction energy that is proportional to the magnetization of the dipole and sensitive to the vortex positions is usually referred to as the magnetic pinning energy.

2.3 Thin film magnetization in perpendicular geometry

Thin superconducting films in perpendicular magnetic fields would exhibit a mixed-state structure analogous to the Abrikosov state, even if the κ value of the film was less than $1/\sqrt{2}$ [107]. In this so-called perpendicular geometry, distinctive vortex properties from those observed in the bulk case arise in thin film samples.

2.3.1 Bean model

When a type-2 superconductor is cooled down below its T_c in zero applied field and an external magnetic field above H_{c1} is subsequently set, the flux-bearing vortices created at the surface layer start to invade the material pushed by the Meissner shielding currents, until their motion is terminated by available defects that tend to pin any vortex that passes by. The flux gradient in the regions where the vortices penetrate is determined by the maximum circulating dissipationless screening current $J_c(T)$. This critical current flows perpendicular with respect to the vortex lines and induces a Lorentz force on the vortices that is equal and opposite to the pinning force [108, 109]. The basic assumption of the *critical state model* [109] is that, as the vortices enter the sample, every pinning site that catches a vortex will hold onto it up to a certain maximum pinning force per unit vortex length. In this way the local balance between the two competing forces (the Lorentz and the pinning forces), creates a metastable equilibrium state, where the current density adjusts itself to a maximum magnitude, $|\mathbf{J}_{\max}| \equiv J_c$, the *critical current density*. From Ampère's law it follows that the flux density distribution $\mathbf{B}(\mathbf{r})$ in the critical state is given by

$$|\nabla \times \mathbf{B}(\mathbf{r})| = \mu_0 J_c. \quad (2.43)$$

The magnetization curve for an ideal, homogeneous superconductor without pinning centers is totally reversible, as it is shown in Fig. 2.2(a). However, the presence of pinning centers for the flux lines results in a strongly irreversible be-

2. Theoretical aspects of superconductivity

havior of the magnetization. Actually, the system achieves an inhomogeneous flux distribution with a higher density near the border that decreases linearly towards the center of the sample, whose slope is $\mu_0 J_c$, as illustrated in Fig. 2.6(a). Fig. 2.6(b) shows a set of B profiles that occur at different stages during an increase (left) and subsequent decrease (right) of the applied field. In the regions

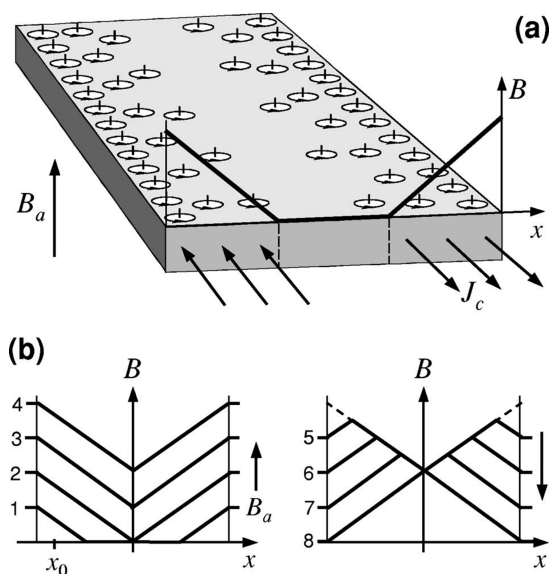


Figure 2.6: Bean critical state model. (a) Distribution of vortices, internal field, and current in a superconductor placed in a external magnetic field B_a . (b) Internal field profiles for increasing (left) and decreasing (right) B_a [110].

where vortices do not enter, smaller Meissner currents screen the external field. Upon increasing field, vortices fill the entire superconductor with maximum density at the boundaries and minimum in the center of the sample, and the critical current flows all over the sample volume, forming loops enclosed in the sample boundaries. With decreasing field, vortices exit the sample and form a negative flux gradient, so the critical currents invert polarity starting from the edge of the sample and extending to the center as the field drops to zero [109]. This intuitive and very physical Bean critical state scenario, sometimes modified to account for the field dependence of $J_c(T)$, has been used extensively to quantitatively explain the magnetization loops in superconducting samples. From the illustration it is evident that this strongly hysteretic process is quite analogous to what happens

2. Theoretical aspects of superconductivity

to a box of sand in which sand is added near the side walls (left), and then the walls are gradually lowered to zero height (right).

2.3.2 Effective penetration depth

So far we have been considering the properties of a bulk superconductor. However, the results shown here deal with films of finite size whose small thickness has important consequences for the vortex structure. First at all, when a magnetic field is applied perpendicular to the ab -plane of a thin film sample, vortices can be considered as straight lines with a normal core of size $\xi(T)$ in an almost two-dimensional vortex lattice [111], whereas the screening currents of the vortex are confined to the thickness of the film, t , giving a weakened screening capacity [88]. Hence, the field of the vortex is more spread out compared with that in a bulk superconductor, which results in a larger effective penetration depth [45, 88]

$$\Lambda(T) = \lambda(T)^2/t, \quad (2.44)$$

where $\lambda(T)$ is the bulk value of the penetration.

Second, the field around a single vortex in a thin film is less effectively screened at larger distances. The radial distribution of the local field around a vortex is given by [45, 88]:

$$\mu_0 h(r) = \frac{\Phi_0}{4\pi\Lambda(T)r} \quad \text{for } \xi < r \ll \Lambda, \text{ and} \quad (2.45)$$

$$\mu_0 h(r) = \frac{2\Phi_0\Lambda(T)}{\pi r^3} \quad \text{for } r \gg \Lambda. \quad (2.46)$$

Instead of the exponential decrease of the local magnetic field obtained at large distances from the vortex core in a bulk superconductor, the local field around a single vortex in thin films decreases as $1/r^3$.

Third, the current decreases within Λ as $1/r$, but even at large distances it decays only as $1/r^2$ [45, 88]:

$$j(r) = \frac{\Phi_0}{2\pi\Lambda(T)r} \quad \text{for } x < r \ll \Lambda, \text{ and} \quad (2.47)$$

2. Theoretical aspects of superconductivity

$$j(r) = \frac{\Phi_0}{\pi r^2} \quad \text{for } r \gg \Lambda. \quad (2.48)$$

Finally, the repulsive energy between two vortices decreases as $1/r$, so that the repulsive interaction between vortices in thin films is of larger range than in bulk superconductors.

Moreover, the presence of holes or antidots forming periodic pinning sites in a thin film leads to a renormalization of the penetration depth, where superconducting volume corrections have to be considered. Films with an artificial array of holes present a much easier flux-line penetration through the antidot with respect to a reference plain film, where $\Lambda(T)$ should be used [112]. In this case, the penetration depth is modified in the following way [103, 113]:

$$\Lambda_a(0) = \frac{\lambda(0)}{\sqrt{(1 - 2S_a/S_t)}}, \quad (2.49)$$

where S_a is the area occupied by the antidots and S_t is the total area of the film. The factor 2 is obtained from calculations in the London limit.

2.3.3 Demagnetization effects

For an infinite long cylinder, an applied magnetic field along its axis induces shielding currents flowing only in the lateral surface, with a constant value along the cylinder, and thus creates a spatially uniform magnetic field along the superconductor. However, at the top and bottom end surfaces of finite sample size the tangential magnetic field is not continuous and extra shielding currents are also induced there. Actually, in thin superconducting films the flux lines are forced to bend around the film resulting in an inhomogeneous current distribution and a sharp rise of the local magnetic field at the edges which is much larger than the applied field. As a result, higher values of current are necessary to shield the applied magnetic field, yielding larger values of the magnetization. Additionally, it has been shown that the thinner the sample, the larger this effect [114].

For an elliptically-shaped sample, the total effective field inside the sample H_{eff} , is given by $H_{\text{eff}} = H - H_d$, where H is the applied field and H_d is the demag-

2. Theoretical aspects of superconductivity

netization field. The demagnetization field is defined as $H_d = -NM$, where N is a shape-dependent demagnetization factor and M is the magnetization of the material. For a long thin sample in a parallel field $N = 0$, since field lines are not distorted, while for a short flat sample in a perpendicular field the demagnetization correction can be enormous. In the case of a superconductor M is negative so that H_d will be positive, which means that the demagnetization field actually increases H_{eff} inside the sample. The value of N has a range $0 \leq N \leq 1$ in SI units. For the superconducting thin films studied here, $N \rightarrow 1$, so that an effective field higher than the applied one is expected. A direct consequence of this demagnetization factor is that H_{c1} will be strongly reduced [115].

2.3.4 Field and current profile

The flux distribution of a thin type-2 superconductor in a perpendicular applied magnetic field higher than H_{c1} is expected to be, due to strong demagnetization effects, very different from that in a long cylinder in the parallel geometry described by the Bean critical state model [109]. The penetration of magnetic flux into thin type-2 superconducting strips of infinite length was first described in the framework of a critical state theory [116], which was later used for thin superconducting disks [117, 118, 119, 120].

The field and current distributions for a type-2 superconducting long cylinder in a parallel geometry and for a thin superconducting film in a perpendicular geometry are shown schematically in Fig. 2.7. The magnetic field lines and the vortices are given for both cases in the mixed state [Fig. 2.7(a)]. It is observed that contrary to the behavior in a long cylinder where the induced current flows only at the edge, the surface of the thin film is exposed to magnetic field lines that bend around the film, thereby inducing currents everywhere, and not only at the surface. In addition, for a finite applied magnetic field higher than H_{c1} , the region where the current density achieves J_c never fills the entire film but rather there is a region of the sample for which $0 < |\mathbf{J}| < J_c$ [Fig. 2.7(c)]. As a consequence, there is a flux-free central zone, where the profile of the flux density in the critical state never penetrates. This thin film characteristic strongly contrasts with that in the infinitely long cylinder.

2. Theoretical aspects of superconductivity

It is worthwhile mentioning that to calculate J_c from the magnetization, the characteristic dimension for a bulk cylinder is its radius R whereas for a superconducting thin film is its thickness t . Indeed, for a cylinder or film with finite width $2W_x$, infinite length L_y and exposed to a magnetic field H_z , the current-density vector turns out to have only one component [121]:

$$J_y = \frac{\partial H_x}{\partial z} - \frac{\partial H_z}{\partial x}. \quad (2.50)$$

For a thin film, the first term in Eq. (2.50) dominates over the second one (approximately by the factor radius/thickness), since the strong demagnetization effects force the external magnetic field to wrap around the sample. This results in tangential components H_x of opposite sign at the top and bottom of the film [$H_x(x, z = -t/2) = -H_x(x, z = t/2)$], thus requiring a large gradient of $\partial H_x/\partial z$ across the thickness. This in turn gives rise to a characteristic field for thin films, the so-called full penetration field, $H_p = J_c t/2$, at which the vortices penetrate to the center of the film [119, 121]. On the other hand, for an infinite cylinder with radius R and a magnetic field applied along its axis, the second term in Eq. (2.50) dominates over the first one leading to $H_p = J_c R$ [119, 121].

2.4 Superconductivity at microwave frequency

In this section we introduce the electrodynamics needed to understand the basic concept of surface impedance of superconductors. The treatment is kept on a phenomenological level. The physical concepts of the surface resistance and the surface reactance (or, equivalently, the penetration depth) are subsequently illustrated in terms of the energy dissipated and stored, respectively.

2.4.1 Complex conductivity

Superconductivity is a consequence of paired and unpaired electrons travelling within the lattice of a solid. The paired electrons travel, under the influence of an electric field, without resistive loss. In addition, due to thermal energy present in the solid, some of the electron pairs are split, so that some normal

2. Theoretical aspects of superconductivity

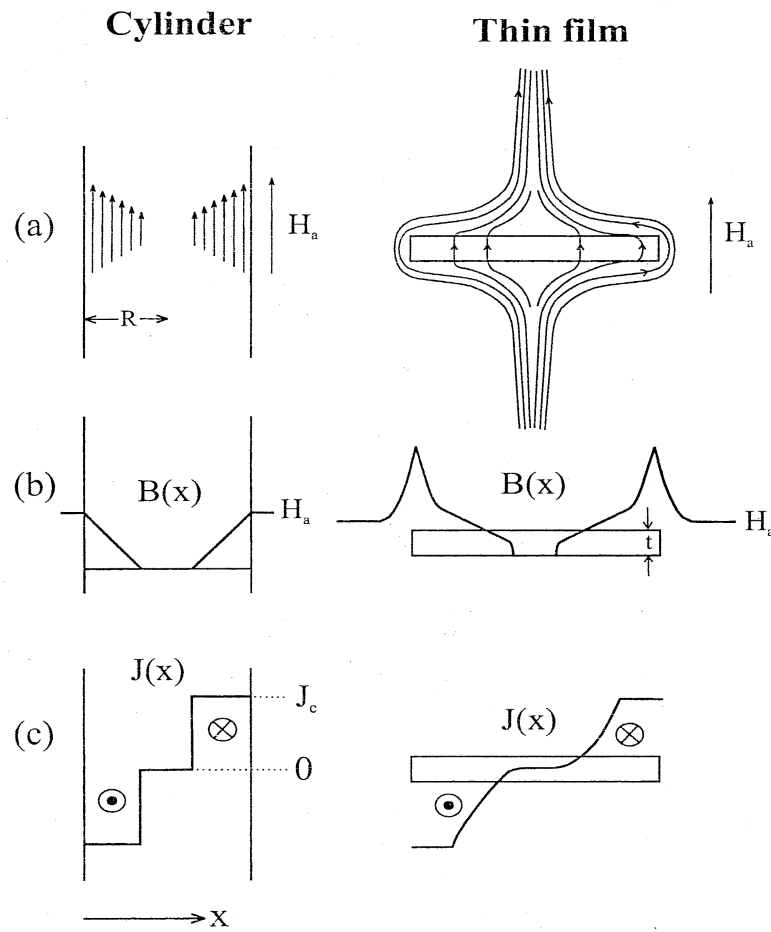


Figure 2.7: Current and field distributions in a type-2 superconducting long cylinder (left column) and thin film (right column). (a) Magnetic field lines, (b) field profile $B(x)$, and (c) current distribution $J(x)$ [122].

2. Theoretical aspects of superconductivity

electrons are always present at temperature above absolute zero. We will now use the picture of the TFM to form some fundamental expression and ideas of the complex conductivity introduced by Gorter and Casimir [69], and applied by the London brothers, to describe the finite conductivity of superconductors at microwaves frequencies [70]. The equations of motion of normal electrons (index "n") and Cooper pairs (index "s") are [4]

$$m \frac{d\mathbf{v}_n}{dt} + m \frac{\mathbf{v}_n}{\tau} = -e\mathbf{E}, \quad \text{and} \quad 2m \frac{d\mathbf{v}_s}{dt} = -2e\mathbf{E}. \quad (2.51)$$

Here \mathbf{v}_n and \mathbf{v}_s are the velocities of normal electrons and Cooper pairs, respectively, and in the normal case, damping, which results from scattering at time intervals τ , is taken into account. τ results solely from collisions between electrons and phonons (free electrons gas scenario), and independent of frequency. In contrast, Cooper pairs behave like free charges, due to their quantum-statistical bosonic nature. In an electric field, both kinetic contributions add to the total velocity $\mathbf{v} = \mathbf{v}_n + \mathbf{v}_s$. The current densities due to normal electrons and the electron pairs can be written as

$$\mathbf{J}_n = -n_n e \mathbf{v}_n, \quad \text{and} \quad \mathbf{J}_s = -n_s e \mathbf{v}_s. \quad (2.52)$$

Here n_n and n_s are the normal and the paired electron densities, respectively. Let us now assume that all the electromagnetic fields vary in a sinusoidal manner. Hence,

$$\mathbf{J}_n = \mathbf{J}_{n0} e^{j\omega t}, \quad \mathbf{J}_s = \mathbf{J}_{s0} e^{j\omega t}, \quad \text{and} \quad \mathbf{E} = \mathbf{E}_0 e^{j\omega t}. \quad (2.53)$$

Using these sinusoidal time dependencies in the previous expressions of the density and considering the equation of motion, we obtain expressions for the superconducting and normal current densities,

$$\mathbf{J} = \mathbf{J}_n + \mathbf{J}_s = (\sigma_1 - j\sigma_2)\mathbf{E}, \quad (2.54)$$

where σ_1 and σ_2 are

$$\sigma_1 = \frac{n_n e^2 \tau}{m(1 + \omega^2 \tau^2)}, \quad (2.55)$$

2. Theoretical aspects of superconductivity

$$\sigma_2 = \frac{n_s e^2}{\omega m} + \frac{\omega n_n e^2 \tau^2}{m(1 + \omega^2 \tau^2)}. \quad (2.56)$$

This concept of complex conductivity, fundamental to the microwave range of frequency, can be described in a simple equivalent circuit shown in Fig. 2.8. The total current in the circuit is split between the reactive inductance and the resistance which represents dissipation in the system. As the frequency decreases, the reactance becomes lower and more of the current flows through the inductance. When the current is constant this inductance completely shorts the resistance, allowing resistance-free current flow. The inductive part of the circuit becomes highly reactive at high frequencies and then losses occur due to current flowing through the resistor.

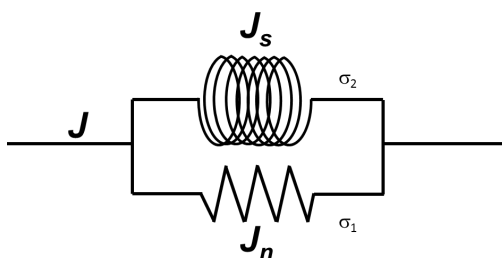


Figure 2.8: Equivalent circuit depicting complex conductivity in superconductors.

2.4.2 Maxwell's equation and superconductors

The wave equation for superconductors, useful to deduce the main propagation characteristics in the range of microwaves, can be derived from Maxwell's equations [4, 123],

$$\nabla^2 \mathbf{E} = \mu_0 \frac{\partial \mathbf{J}}{\partial t} + \epsilon \epsilon_0 \mu_0 \frac{\partial^2 \mathbf{E}}{\partial t^2}, \quad (2.57)$$

where ϵ and ϵ_0 are, respectively, the permittivity of the material and of vacuum. By combining the expression for the current density pointed out above and the London's first equation, and considering the case of sinusoidal time variations,

2. Theoretical aspects of superconductivity

the wave equation for the electric field is obtained,

$$\nabla^2 \mathbf{E} = j\omega\mu_0(\sigma + j\omega\epsilon\epsilon_0)\mathbf{E}. \quad (2.58)$$

A similar expressions can be obtained for the magnetic field. This is a very general form of the wave equation which can apply to both superconductors and normal conductors. To get understanding of the propagation of electromagnetic waves in superconductors a plane wave is assumed. For a plane wave travelling in the z direction, the simplest expressions for the electromagnetic fields are

$$E_x = E_0 e^{-\gamma z}, \quad \text{and} \quad H_y = H_0 e^{-\gamma z}. \quad (2.59)$$

Here the electric field is directed in the x direction and the magnetic field follows the y direction. By substituting these expressions into the wave equation, the propagation constant is obtained:

$$\gamma = \sqrt{j\omega\mu_0(\sigma + j\omega\epsilon\epsilon_0)} = \alpha + j\beta. \quad (2.60)$$

The real and imaginary parts of the propagation constant (termed as α and β) represent the attenuation and the phase, respectively, of the travelling wave. It is interesting to note that \mathbf{E} and \mathbf{H} are not independent for the plane waves under consideration, and are connected through the Faraday's law ($\nabla \times \mathbf{E} = -\partial \mathbf{B} / \partial t$). For plane waves, such becomes

$$-j\omega\mu_0 H_y = \frac{\partial E_x}{\partial z}. \quad (2.61)$$

Substituting E_x and H_y by their expressions in Eq. (2.60) gives

$$Z_s = \frac{E_x}{H_y} = \frac{j\omega\mu_0}{\gamma} = \sqrt{\frac{j\omega\mu_0}{\sigma + j\omega\epsilon\epsilon_0}}. \quad (2.62)$$

This is the intrinsic or surface impedance of the material. Intrinsic impedance is used for any material, while the surface impedance is usually used for good conductors. By replacing σ by $\sigma_1 - j\sigma_2$, the propagation constant and the surface

2. Theoretical aspects of superconductivity

impedance of a superconductor can be written, respectively, as

$$\gamma = \sqrt{j\omega\mu_0(\sigma_1 - j\sigma_2)}, \quad \text{and} \quad Z_s = \sqrt{\frac{j\omega\mu_0}{\sigma_1 - j\sigma_2}}. \quad (2.63)$$

In both cases, it is assumed that the conduction current in a superconductor is much larger than any displacement current ($\sigma \gg \omega\epsilon\epsilon_0$). For the case that the temperature is not too close to T_c , so that the supercurrent dominates the normal current ($\sigma_2 \gg \sigma_1$), an approximated expression for γ can be given

$$\gamma \approx \sqrt{\omega\mu_0\sigma_2} \left(1 + j\frac{\sigma_1}{2\sigma_2}\right). \quad (2.64)$$

The real part of this is the attenuation coefficient, α , which can be written as

$$\alpha = \text{Re}(\gamma) = \sqrt{\omega\mu_0\sigma_2} \quad (2.65)$$

This represents an exponential decay of the electric and magnetic field as the wave propagates in the z direction. A characteristic depth (λ) can be defined such that the wave is attenuated by e^{-1} of its initial value, which may be at the surface of the superconductor

$$\lambda = \frac{1}{\text{Re}(\gamma)} = \frac{1}{\sqrt{\omega\mu_0\sigma_2}}. \quad (2.66)$$

The characteristic depth λ is the same as the London penetration when σ_2 is considered in the TFM, and is governed by the properties of the electron pairs. It represents a depth to which electromagnetic fields penetrate superconductors and defines the extent of a region near the surface in which currents can be induced. A distinction must be made between the microwave and the dc penetration depth. The former is always $1/\text{Re}(\gamma)$ and using the first expression of Eq. (2.64) gives actual depth irrespective of the values σ_1 and σ_2 . This depth will change from the value given by the Eq. (2.66) when $\sigma_2 \gg \sigma_1$ (low temperature) to the normal state skin depth (see below) when $\sigma_2 = 0$ (at and above T_c). The dc superconducting penetration depth, the London depth, varies from a low-temperature value to an infinitely deep value as the superconductor becomes normal. In this case the

2. Theoretical aspects of superconductivity

normal carriers do not need to be considered as they have no effects on field penetration at dc. The imaginary part of the propagation constant is

$$\beta = \sqrt{\frac{\omega\mu_0\sigma_1}{4\sigma_2}}. \quad (2.67)$$

The intrinsic impedance, using the same approximation as given above ($\sigma_2 \gg \sigma_1$), becomes

$$Z_s = \sqrt{\left(\frac{\omega\mu_0}{\sigma_2}\right) \left(\frac{\sigma_1}{2\sigma_2} + j\right)}. \quad (2.68)$$

By looking at the real and imaginary parts of this expression, the surface resistance R_s , and surface reactance X_s , of the superconductor can be extracted:

$$R_s = \frac{\sigma_1}{2\sigma_2} \sqrt{\frac{\omega\mu_0}{\sigma_2}}, \quad \text{and} \quad X_s = \sqrt{\frac{\omega\mu_0}{\sigma_2}}. \quad (2.69)$$

Continuing with the derivation, σ_2 as defined previously can be substituted into the last equation, giving

$$R_s = \frac{\omega^2\mu_0^2\sigma_1\lambda^3}{2}, \quad \text{and} \quad X_s = \omega\mu_0\lambda. \quad (2.70)$$

For the TFM, provided σ_1 and λ are independent of frequency, R_s increases as ω^2 .

Finally, the derivation for the equations for normal conductors follows exactly the same steps as described above for superconductors by simply substituting $\sigma_2 = 0$, so that the imaginary and real parts of the propagation constant are equal:

$$\alpha = \beta = \sqrt{\frac{\omega\mu_0\sigma_n}{2}}. \quad (2.71)$$

Here σ_n is now the conductivity of a normal conductor and is purely real. The characteristic depth, known as the *skin depth*, is defined by

$$\delta = \sqrt{\frac{2}{\omega\mu_0\sigma_n}}. \quad (2.72)$$

In the limit of the frequency-independent conductivity, the skin depth is a func-

2. Theoretical aspects of superconductivity

tion of frequency ($\propto \omega^{1/2}$), while for the superconductor, the penetration depth is independent of ω (when $\sigma_2 \gg \sigma_1$). For a normal conductor, the surface resistance and surface reactance are equal:

$$R_n = X_n = \sqrt{\frac{\omega\mu_0}{2\sigma_n}} \quad (2.73)$$

2.4.3 Surface resistance and surface reactance

On the basis of the Poynting's theorem we can now give the physical meaning of the surface resistance and surface reactance [123]. The propagation of an electromagnetic wave in a lossy medium provokes an electric field \mathbf{E} along the path of current density \mathbf{J} ,

$$P_{\text{diss}} = \frac{1}{2} \text{Re} \left\{ \int_{\text{volume}} \mathbf{J} \cdot \mathbf{E} d^3\mathbf{r} \right\}. \quad (2.74)$$

Applying the local current-field relation ($\mathbf{J} = \sigma\mathbf{E}$), this expression reduces to the volume integral of $\sigma_1 \cdot |\mathbf{E}|^2$. Since the electric field decays exponentially into the superconductor, the integral can be split into a surface integral and an integration along the propagation in the z direction. Evaluating the latter integral, and using the expression of the surface impedance Z_s , we obtain

$$P_{\text{diss}} = \frac{1}{4} \int_{\text{surface}} (\sigma_1 \lambda |Z_s|^2) \cdot |\mathbf{H}(\mathbf{r})|^2 d\mathbf{r}. \quad (2.75)$$

The factor in parentheses equals $2R_s$. Accordingly, the average surface resistance quantifies the power dissipated by the electromagnetic wave in the superconductor,

$$P_{\text{diss}} = \frac{1}{2} \bar{R}_s \int_{\text{surface}} |\mathbf{H}(\mathbf{r})|^2 d^2\mathbf{r}. \quad (2.76)$$

The physical meaning of the surface reactance can be similarly illustrated by evaluating the electromagnetic energy W_s stored in the superconductor. Two mechanisms contribute to W_s : the magnetic field inside the superconductor, and the kinetic energy associated with the friction motion of the charge carriers,

$$W_s = \frac{1}{2} \int_{\text{volume}} [\mu_0 |\mathbf{H}(\mathbf{r})|^2 + \text{Im}(\mathbf{J} \cdot \mathbf{E})] d^3\mathbf{r}. \quad (2.77)$$

2. Theoretical aspects of superconductivity

By treating this expression in analogous way as in the previous case, $\mathbf{J} \cdot \mathbf{E}$ can be identified with $|\mathbf{E}|^2/\omega\sigma_2$. After splitting the integral as before, we arrive at

$$W_s = \frac{1}{4\omega} \int_{\text{surface}} \mu_0\omega\lambda \left(1 + \frac{\sigma_2|Z_s|^2}{\mu_0\omega} \right) \cdot |\mathbf{H}(\mathbf{r})|^2 d^2\mathbf{r}. \quad (2.78)$$

which can be simplified in the framework of the TFM to obtain

$$\omega W_s = \frac{1}{2} \bar{X}_s \int_{\text{surface}} |\mathbf{H}(\mathbf{r})|^2 d^2\mathbf{r}. \quad (2.79)$$

We conclude that the average surface reactance quantifies the energy stored in the superconductor during one microwave cycle $1/\omega$.

Chapter 3

Experimental techniques

3.1 Introduction

The samples investigated in this thesis are all thin superconducting films of different systems: lanthanum-strontium-based cuprate ($\text{La}_{2-x}\text{Sr}_x\text{CuO}_4$), lead (Pb), and magnesium diboride (MgB_2). A description of the preparation techniques and the experimental methods used for performing magnetization and microwave measurements are given in this chapter. The fabrication of $\text{La}_{2-x}\text{Sr}_x\text{CuO}_4$ and nanostructured Pb was carried out in the Institute for Nanoscale Physics and Chemistry at the Katholieke Universiteit Leuven (Flanders, Belgium), while MgB_2 was prepared in the Department of Experimental Physics at the Univerzita Komenského (Bratislava, Slovak Republic). All measurements were performed in the laboratories of the Group of Magnetism at the Universitat de Barcelona.

3.2 Thin film preparation

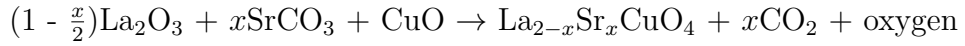
3.2.1 $\text{La}_{1.82}\text{Sr}_{0.18}\text{CuO}_4$

Epitaxial overdoped $\text{La}_{1.82}\text{Sr}_{0.18}\text{CuO}_4$ thin films were grown *in situ* by DC sputtering from stoichiometric targets on SrTiO_3 substrates. A complete explanation of the fabrication procedure is given in Liesbet Weckhuysen's dissertation [124]. We only consider here the main aspects of the processes. An ultra high vacuum (UHV) of 10^{-9} bar was performed to avoid contamination

3. Experimental techniques

in the deposition chamber by using a turbo molecular pump in combination with a rotational pump. The chamber was afterward filled with pure oxygen at a pressure of 2×10^{-3} bar. The chamber is provided with an inconel block which can heat up to 1000°C in a 100% oxygen environment. The temperature is monitored with a temperature controller and a Ni/NiCr thermocouple. Two needle valves are used to control the pressures of oxygen and another gas (argon, nitrogen) during the sputtering conditions. The pressure is monitored with four different counters.

The $\text{La}_{2-x}\text{Sr}_x\text{CuO}_4$ targets are made using the following stoichiometric reaction:



All separate components have to be warmed up to 400°C to expel the water and to avoid contamination. An amount of 0.05 mol should be used to have 20 g of $\text{La}_{2-x}\text{Sr}_x\text{CuO}_4$ target powder. They are all mixed in acetone, which evaporates without infecting the target. Hereafter, the target is annealed (heated in an oxygen atmosphere) for 12 hours at 900°C and mixed again. This procedure is also done at 950°C and 1000°C . Afterwards, the powders are mixed for the last time and then pressed (5 tons) in a circular shape and put into the furnace at 1000°C for 12 hours. Then the target is slowly cooled down for approximately 24 h, and mounted in a copper holder with silver paint. This block is heated up to 200°C to harden the silver paint and the holder is placed inside the deposition chamber later on.

The sputtering process comprises four steps:

1. The target is exposed to a high negative voltage (300 V), which excites the electrons and propels them to leave it.
2. These electrons collide with bound electrons from the oxygen and form a positively charged oxygen atom plus 2 electrons, which collide with other oxygen atoms.
3. The positively charged oxygen atoms are attracted to the target and impact on it.
4. Separate atoms and molecules from the target are in this way scattered in all directions. The substrate is then turned to the flow of scattered atoms.

3. Experimental techniques

To ensure quality thin films, it is necessary to perform a long pre-sputtering in order to achieve a steady-state (different atoms have different sputtering rates) and obtain a constant concentration. Moreover, to avoid possible collision of oxygen ions with the substrate, which can destroy the already deposited film, a magnetic field can be applied around the target. To make epitaxial thin films, a subtle combination of all parameters (oxygen pressure, target voltage, magnetic field intensity...) should be optimized.

The sample deposition has 4 different steps:

1. **Sample mounting.** The substrate (SrTiO_3) is mounted using silver paint on an inconel holder and surrounded by 4 sapphire substrates, to have a homogeneous temperature over the surface. The sample holder is then heated up to 600°C to harden the silver paint. It is then mounted in the deposition chamber and pumped up to 10^{-9} bar.
2. **Pre-sputtering.** The pressure inside the chamber is raised up to 1.9×10^{-3} bar with pure oxygen. The current source is connected with the target and the voltage is increased to ~ 300 V. The temperature of the substrate is gradually increased up to 840°C , which takes about one hour.
3. **Sputtering.** The pressure and the voltage over the target stay the same, but the substrate is turned in front of the target during about two hours, producing an epitaxial thin film of around 200 nm.
4. **Annealing.** The substrate is turned away from the target and the temperature is changed to 600°C for one hour. The sputter source is turned off. Then the pressure is increased up to 1 bar O_2 . The substrate is cooled down in the same pressure.

For the studies presented here, superconducting $\text{La}_{1.82}\text{Sr}_{0.18}\text{CuO}_4$ thin films with dimensions of $3 \times 3 \text{ mm}^2$ and 200 nm thickness were selected. These samples show a $T_c \sim 27$ K. This value was determined from the temperature dependence of the low-magnetic field (10 Oe) magnetization measured in a rf-SQUID magnetometer (see description below), by first cooling the sample in zero field [zero-field cooling (zfc) mode] from above T_c to the desired temperature well below T_c , then selecting the magnetic field and subsequently recording the magnetic moment in the

warming up process. Afterwards, the magnetic moment was registered meanwhile the sample was cooled down from above T_c under the same field [field cooling (fc) mode].

3.2.2 Patterned Pb

The Pb thin film with a composite antidot lattice was obtained by electron-beam lithography (EBL) through a lift-off technique. We only sketch here the sample preparation. More details can be found in Sophie Raedts' dissertation [122].

EBL was used to define the desired structure onto an electron sensitive resist bilayer of polymethyl metacrylate/methyl metacrylate (PMMA/MMA), which was deposited on top of a SiO_2 substrate. The use of two different layers is necessary to obtain an overhang profile which eventually facilitates the lift-off procedure and helps to avoid any contact between the material deposited directly onto the substrate and the material on top of the resist mask.

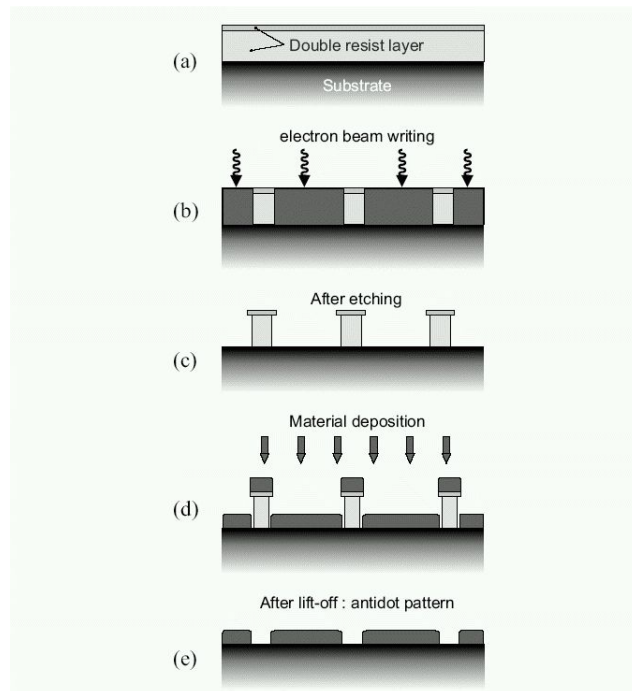


Figure 3.1: Schematic representation of the subsequent steps for preparing sub-micrometer structures by electron-beam lithography [122].

3. Experimental techniques

The procedure to fabricate the patterned film is plotted in Fig. 3.1.

- (a) The double resist layer of PMMA/MMA is spun onto the Si/SiO₂ substrate.
- (b) The desired mask is designed in the resist by mean of a scanning electron beam.
- (c) The regions exposed to the electron beam will be etched away in the next step such that only the resist pattern is left on the substrate.
- (d) The material is deposited on top in a UHV Varian molecular bean epitaxy system.
- (e) The resist mask together with the material deposited above the resist is removed by a lift-off procedure in warm acetone and shuddered in an ultrasonic bath for about 10 seconds.

Finally, the sample is immersed in isopropanol and dried in a flow of nitrogen gas to avoid condensation. The thickness of the deposited layer is limited by the thickness of the resist mask (~ 150 nm).

The UHV environment is obtained by subsequent pumping with a turbo pump and seven ion pumps, that guarantee a base pressure of the order of 10^{-12} to 10^{-11} bar. The evaporation chamber is equipped with a liquid nitrogen cooling shield (cryopanel) which provides extra pumping prior to evaporation. Substrates can be inserted into the chamber without interrupting the vacuum by a load-lock and cooled down to 77 K by a liquid nitrogen (LN₂) reservoir which is in thermal contact with the copper sample holder.

The chamber has an electron gun of 10 kW and 6 kW for the evaporation of germanium (Ge) and Pb, respectively. The structure and quality of the Pb layer strongly depend on the evaporation conditions and parameters as the surface roughness of the substrate, the substrate temperature, the evaporation rate, the working pressure in the evaporation chamber and the purity of the used source material. The evaporation rate together with the substrate temperature determine the diffusion of the Pb atoms onto the substrate and thus the structure of the resulting film. A thin Ge layer of ~ 20 nm is evaporated a few seconds before the main Pb deposition in order to facilitate the fabrication of a flat continuous

3. Experimental techniques

Pb layer without clustering. Thicker Ge layers (700 nm) are used to protect the Pb films against oxidation. The Ge is electron-beam evaporated from a source material with a purity of 99.99% and with an evaporation rate of approximately 20 nm/s.

The sample investigated here had a rectangular cross-section of $6 \times 4 \text{ mm}^2$ and a thickness of 50 nm. The total thickness including the substrate is $13.5 \text{ }\mu\text{m}$. The zero-field T_c was determined to be close to 7.20 K from the thermal dependence of the magnetization measured in the rf-SQUID following zfc and fc processes.

3.2.3 MgB₂

Superconducting MgB₂ thin films were deposited on sapphire (Al₂O₃) substrates by magnetron sputtering and by *ex-situ* annealing in argon atmosphere. The deposition process was performed by using two independent circular magnetrons (dc magnetron for magnesium and rf-magnetron for boron) on a rotating substrate holder. Prior to deposition the chamber was evacuated by turbomolecular pump to an overall pressure of 8×10^{-10} bar and then filled with argon to a working pressure of 8×10^{-6} bar. In order to control the growth and composition of the film, a suitable shield with apertures between the target and the holder was located.

To deposit Mg-B precursor films, Mg and B were simultaneously sputtered by using the balanced magnetrons of 2 inches of diameter. By feeding the dc (Mg target) and rf (B target) magnetrons during 40 minutes with powers of 27.2 – 38.0 W, and 200 or 275 W, respectively, films around 200-nm-thick were obtained. After deposition, the samples were transferred to another high-vacuum chamber, that includes annealing equipment. A Boraletic heater was located horizontally above the sample holder, which was cooled by fluent water. The *ex-situ* annealing procedure was performed at a pressure of 1×10^{-11} bar and a temperature of 680°C, which was kept constant for the range of annealing dwell times, between 120 and 180 seconds. The resulting films have dark brown color with silvery reflection. Additional information related with the sample preparation can be found in Gregor *et al* [125], and Mičunek *et al* [126].

The sample of MgB₂ used here is square in shape with cross-section dimensions

of $3 \times 3 \text{ mm}^2$ and a thickness of 200 nm, and has a critical temperature around 30 K and a transition width usually less than 1 K [125].

3.3 SQUID magnetometry

3.3.1 dc magnetization

Magnetization measurements have been carried out by using a commercial Quantum Design MPMS (Magnetic Property Measurement System), based on a rf-SQUID (radio frequency Superconducting QUantum Interference Device), which works at 20 MHz and acts as a magnetic flux-to-voltage converter (see Fig. 3.2). The MPMS setup is formed by a ^4He cryostat (a cylinder around 128 cm long and of 8 mm of diameter) and is equipped with a superconductor solenoid which can create dc magnetic fields between -5 T and 5 T . This equipment allows measuring magnetic moments with a high precision up to 10^{-6} emu ($1 \text{ emu} = 10^{-3} \text{ Am}^2$) as a function of the dc magnetic field, H_{dc} , temperature, T , and time, t , and enables to establish accurately the critical temperature, T_c , of the superconducting samples. The system permits a sweep rate of $5 \times 10^{-5} \text{ T}$. It is also provided with a continuous low temperature control and enhanced thermometry control that guarantees a low-temperature stability better than 10 mK. The temperature can be stabilized between 1.8 and 350 K. During measurements the sample is surrounded by a low-pressure helium gas bath ($7 \times 10^{-4} \text{ bar}$).

The sample holder consists of a transparent plastic straw which contains the sample, connected to a long metal rod. The sample is normally fixed inside the straw using a $25.4\text{-}\mu\text{m}$ -thick dielectric polytetrafluoroethylene (teflon) sheet, which does not contribute to the magnetic signal and reduces scratching. The probe is then brought inside the cryostat and attached to a stepper motor. The measurements were performed by using an extraction magnetometer option, in which the sample is moved through pick-up coils at constant velocity over a certain distance, the so-called *scan length*, whereas the signal from the pick-up coils is integrated to calculate the magnetic moment of the sample.

A schematic representation of the detection circuit is shown in Fig. 3.3. The pick-



Figure 3.2: The MPMS measuring setup.

up coils, wound in a second derivative detection circuit with the double inner coil in the opposite direction to the two outer coils, are located in the center of the magnet with the field direction along their axis. The detected signal in the coils is inductively coupled via the signal coil to the rf-SQUID, which produces an *output voltage signal* V between -10 V and 10 V as a function of the position z , as it is shown in Fig. 3.3, that is processed by an amplifier. The value of the magnetic moment is obtained by fitting the resulting $V(z)$ curve with the theoretically calculated response function of an ideal magnetic dipole, taking into account the constant offset, linear drift, and possible vertical displacement of the sample from the center of the pick-up coils.

When the superconducting magnet is used in the *no overshoot* mode, it creates a very uniform magnetic field over the entire sample region and the pick-up coils. Nevertheless, great care was taken due to the presence of demagnetization effects in thin film superconductors in perpendicular magnetic fields (see

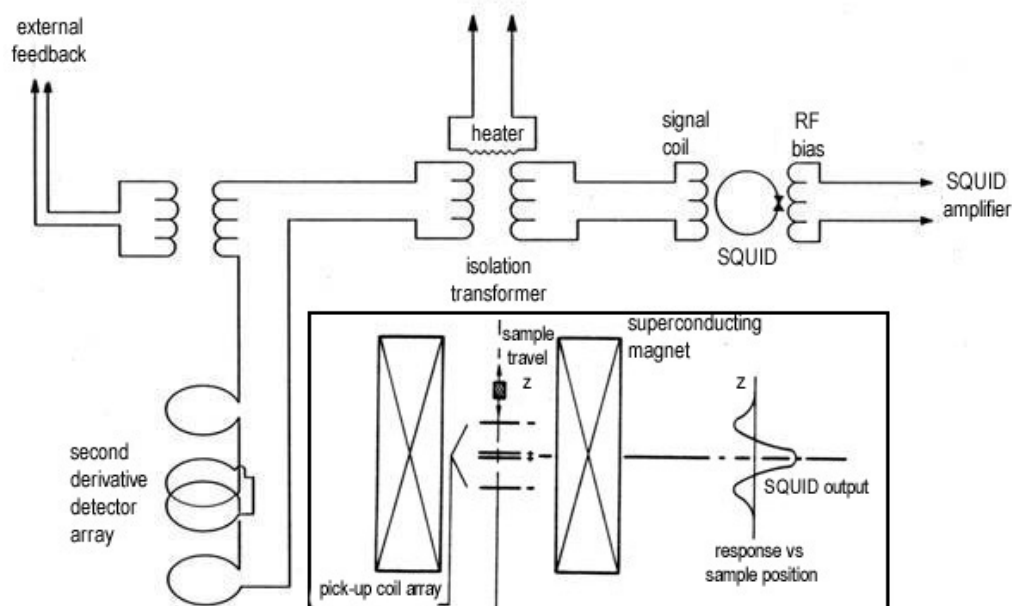


Figure 3.3: Layout of the detection circuit of the rf-SQUID-magnetometer.

subsection 2.3.3) [127]. To ensure good field homogeneity on the sample, all magnetization measurements were done by choosing small scan lengths (0.5 – 3.0 cm). Furthermore, the remnant field which appears as a parasitic magnetic signal was minimized by making a series of subsequent positive and negative field cycles from high field to zero with decreasing amplitude.

By using the extraction method, only stable or slow evolving magnetic field during the measuring time (that lasts some seconds) can be calculated. For a magnetic moment that evolves very fast in time, for example in milliseconds, it is better to extract the signal from the amplifier before numerical calculation. In this way, if a sample is kept fixed in the central part of the pick-up coils, the variation of the magnetic moment as a function of time induces a change of magnetic flux in the pick-up coils. Therefore, the rf-SQUID transforms the alteration of the magnetization into deviation of voltage as a function of time, which can be measured by using an external instrument like an oscilloscope or a multimeter. This measurement method is very sensitivity, since in a short interval of time it is the

variation of magnetization in the sample that is measured instead of the magnetization itself.

Finally, it is worth mentioning that due to the fact that the rf-SQUID can detect small shifts in the magnetic flux, this method can only be performed when the applied dc magnetic field in the superconducting magnet is stable. This point is critical and very important since otherwise the pick-up coils will detect a big flux deviation due to the change of the dc magnetic field that will saturate continuously the output signal from the amplifier, screening any other contribution coming from the sample.

3.3.2 ac magnetic susceptibility

The MPMS is both a dc magnetometer and an ac susceptometer. The difference between the two types of measurement is that the dc magnetization is measured as an absolute magnetic moment in an applied magnetic field at a specific temperature whereas ac susceptibility measurements register a change in the magnetic moment.

The ac susceptibility option allows ac measurements of a sample magnetic moment with a resolution of 5×10^{-9} emu (10^{-12} Am²), with an amplitude of the ac magnetic field, H_{ac} , from 0.1 mOe to 3.84 Oe and a frequency, f_{ac} , changing from 0.001 to 1000 Hz with loss of sensitivity occurring only at frequency below 0.01 Hz. A copper drive coil (which generates the ac field in the sample space), is situated in the helium gas bath between the dc magnet and the gradiometer detection coils, concentric with the dc MPMS superconducting magnet, thus providing a parallel configuration of the ac and dc fields. All three components are combined into a rigid structure to minimize changes in coil geometry as the sample temperature and dc magnetic field are varied.

During ac susceptibility measurements, a small ac drive magnetic field is superimposed on the dc magnetic field, causing a time-dependent moment in the sample. The field of this moment induces a current in the pick-up coils, allowing measurement without sample motion. The detection circuitry is configured to detect only in a narrow frequency band, normally at the fundamental frequency (that of the ac drive field). The differential or ac susceptibility, $\chi = dM/dH_{dc}$ (which

is actually the slope of the $M(H_{\text{dc}})$ curve), obtained from these measurements is described as having both in-phase or real component χ' and out-of-phase or imaginary component χ'' . ac measurements were performed as a function of T , H_{dc} , and nominal microwave power. A physical interpretation of the ac susceptibility is given in Appendix A.

3.4 Microwave experimental techniques

3.4.1 Introduction

A wide variety of microwave (MW) techniques are available for evaluating and characterizing thin superconducting films, among which the cavity resonant-based method [128] is perhaps the most broadly used in both applications and basic-physics studies at high frequencies [12, 129, 130, 131, 132, 133, 134, 135, 136, 137]. Basically, a cavity resonator is a structure that is able to contain an oscillating electromagnetic field and has a number of distinct resonant frequencies which depend upon the geometry of the cavity. When an oscillating field is set up within the cavity it decays gradually because of losses due mainly to (i) the finite conductivity of the walls of the cavity, (ii) the presence of any dielectric material within the cavity, or (iii) radiation out of any apertures in the walls. There are many ways to perform cavity perturbation but the principle of operation is similar in all cases [138]: the sample is immersed in a large electromagnetic cavity in a region of uniform electric and magnetic field, and from the resulting variation in the resonant frequency and bandwidth, the quality factor, which is defined as $Q = \omega U/P_c$, where U is the stored energy and P_c is the power dissipated in the resonant system, and the distribution of the electric and magnetic fields in the cavity are obtained. From this, sample properties as the surface impedance, Z_s , which account for the absorption and reflection of the electromagnetic waves at the sample surface (see section 2.4), are derived by using numerical simulations or reference experiments. The dynamic response of the vortex system is then described in terms of the superconducting penetration depth and the electric conductivity [130, 131, 139, 140, 141, 142, 143].

Other resonant techniques have been developed for the investigation of thin-film

3. Experimental Techniques

superconducting materials. These include the parallel-plate, in which two congruent films form a transmission line resonator with a length scale of the order of the MW wavelength [144, 145]. The parallel-plate dielectric resonator, formed by a sapphire that is sandwiched by two HTS films, is also sensitive to thin-film surface impedance but the latter is averaged over an area of the order of the wavelength [146]. Despite resonant techniques can potentially provide a very sensitive means for studying Z_s as a function of T or H_{dc} , they are necessarily limited to a few discrete frequencies at most and therefore require the use of many separate experiments in order to reveal the frequency spectrum. On the other hand, it is difficult to obtain precise absolute values of the complex sample properties, in contrast to relative changes as a function, for instance, of T or H_{dc} [147]. Different options to the cavity technique are the bolometric [148, 149] and Corbino [150, 151, 152, 153] approaches that cover a large frequency range continuously and have been successfully applied in the studies of the properties of different superconducting materials. In the former case, the MW absorption of the sample is determined by monitoring its temperature increase. Actually, for any conductor, the power absorbed per unit volume and averaged over a period of an ac cycle is proportional to the surface resistance, R_s . Thus, measuring the temperature enhancement in a weakly thermally anchored sample exposed to a known MW electromagnetic field gives R_s straightforwardly. In the case of the Corbino setup, the sample terminates the coaxial cable and, as in any other broadband technique, great care has to be taken with the calibration procedure in order to avoid undesired contributions in the reflected signal, namely directivity (the signal reaches the detector right away without interacting with the sample), source match (the signal coming from the sample is reflected again and adds to the signal approaching the sample), and reflection tracking (damping and phase shift in the transmission line). Other alternatives to perform frequency-dependent measurements are based on implementing the resonator in a transmission line structure, namely helical [133, 154, 155] and stripline or microstrip [156, 157, 158] resonators, on dielectric and superconducting materials.

3.4.2 Basic microwave layout

The present project is devoted to the study of the vortex dynamics in thin superconductor films under three different MW techniques, namely *sweeping*, *pulsed* and *power reflected* modes. Here we will focus on the MW frequency, f , range from 0.1 to 10.0 GHz, and MW nominal power, P , range from -20 to 20 dBm [159] (0.01 – 100 mW).

Some of the typical issues one has to face when designing a sample probe for an experiment in the rf and the lower MW ranges are the following. First, along with the thermometry-related and conventional dc wiring, the probe should be equipped with coaxial cables for handling signals with a frequency up to a few tens of GHz. Second, in the case of low- T_c superconductors, the probe should be suitable for measurements from room down to helium temperatures. Third, since measurements of the mixed state assume a magnetic field, the sample space is usually limited by the solenoid inner hole diameter or the coil diameter. At the same time, the thinner the coaxial cables employed, the higher is the attenuation for a given frequency. And, last but not least, the heat leakage due to the transmission line should be minimized.

The schematic drawing of the experimental layout is shown in Fig. 3.4. A common probe formed by a semi-rigid coaxial cable terminated in a multi-turn rf-coil with the sample under study loaded in its core, from now on the rf-coil-sample (cs), has been used. The rf-coil is formed by a 10-turn, 1.55-mm-long solenoid handmade by winding a 0.1-mm-thick, 99.9%-pure copper wire around a hollow plastic straw with an ellipsoidal cross-section of around 12 mm^2 . The cs is inserted in the aforementioned magnetometer, in the center of the superconductor magnet. Great care was taken for filling the cross-section of the coil with the sample and properly orienting the latter with respect to H_{dc} . Concerning the filling, the plastic straw was adjusted so that the sample would occupy as much of the entire section of the coil as possible. As for the orientation, the sample wrapped in teflon was inserted and glued with GE varnish inside the coil, so that its largest surface (ab -plane) was parallel to the axis of the coil and perpendicular to H_{dc} . The ends of the two terminals of the rf-coil are respectively soldered to

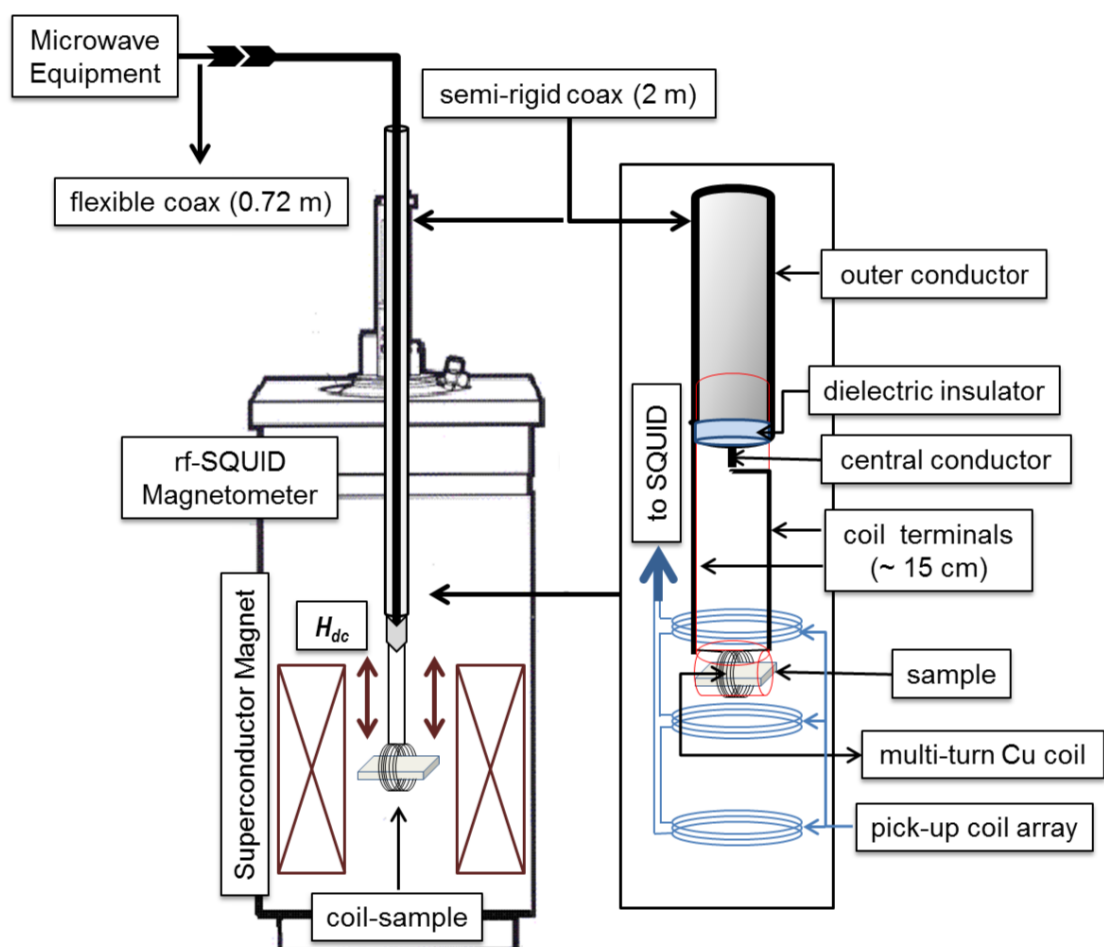


Figure 3.4: Illustration of the experimental setup inside the rf-SQUID magnetometer.

the 0.51-mm-thick central conductor pin and the 2.20-mm-wide outer conductor of a 2-m-long semi-rigid stainless steel coaxial cable, with a characteristic impedance of $50.0 \pm 1.5 \Omega$ and a physical cutoff frequency at 60 GHz. A distance of around 15 cm between the cs and the conductor pin of the transmission line was kept in order to avoid perturbation effects of the stainless steel coaxial cable when magnetization measurements were performed. The coaxial cable came into the magnetometer from outside, where it was connected via a 72-cm-long flexible coaxial cable to different MW equipments depending on the technique used. All the measurements were controlled by a computer via a General Purpose Interface Bus (GPIB).

A full calibration of the low temperature probe could not be performed at the working temperatures since the coil could not be accessed during the experiments and because of the lack of calibration standards at these temperatures. Nevertheless, previous to performing any measurements and in order to filter the signal reflected by the flexible coaxial cable, an appropriate one-port calibration procedure was first done over the frequency range 0.1–10.0 GHz, by consecutively placing three calibration standards [160] at the end of this cable. The power at the resonator, registered at room temperature by using a network analyzer (NA) [161] was found to be approximately four orders of magnitude less than the nominal applied power at the generator output, to which all values of P , refer. This reduction is due to losses in the rather long semi-rigid coaxial cable, at the connection between this cable and the flexible one, and at the soldering points at the terminals of the coil. This substantial decreasing in P may reduce the emergence of some effects as strong-driving nonlinearities and heating. The significance of these effects on the sample loaded in the core of the coil will be clarified later.

3.4.3 Sweeping mode

A schematic illustration of the experimental arrangement for performing the frequency-dependent measurements is shown in Fig. 3.5. A continuous MW signal was fed via the flexible coaxial cable to the semi-rigid coaxial cable with the cs by connecting the former either to a HP 83651B synthesized sweeper, SS, [162] or to the port of an external power supply (signal generator, SG) [163]. The SS

3. Experimental Techniques

and SG operate in step sweep mode and synthesize individually every frequency point, which results in noise reduction and ensures phase coherence. This setup allows measuring the sample magnetic moment under a continuous sweep of f or the relaxation of the magnetic moment over a wide range of fixed experimental parameters, including T , H_{dc} , f and P .

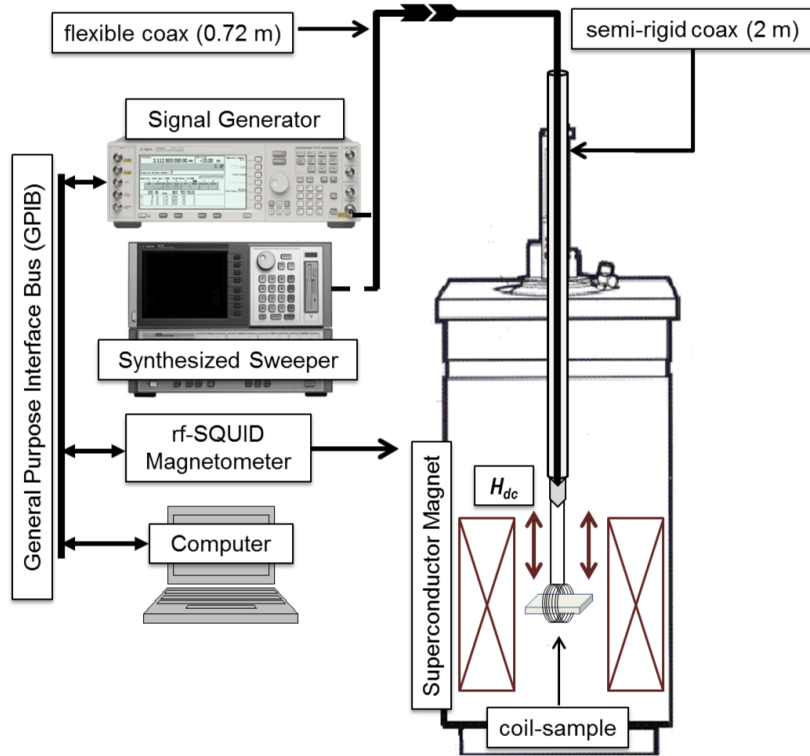


Figure 3.5: Diagram of the sweeping mode experimental setup.

To register the frequency-dependent magnetic moment response of the sample embedded in the coil, a zfc process was first performed from the normal state down to the working temperature below T_c , then a dc magnetic field was set, and thereafter both T and H_{dc} were kept constant. A dc measure command activates the MW equipment to start radiating at a fixed value of P . In sweeping mode the magnetic moment was recorded after every frequency step, from 0.10 to 4.00 GHz in steps of 0.02 GHz. The measurement of each point lasted

around 24 seconds so the sweeping rate of the frequency, df/dt , was about 0.8 MHz. Once the frequency had been swept, the dc magnetic field was switched off and the sample was then heated up to the normal state. In order to compute any possible contribution from the resonator and the substrate and discriminate between their inputs to the sample magnetic moment, identical measurements with the substrate placed inside the resonator and with the sample in the normal state were performed. The relaxation of the sample magnetic moment without radiation was also registered as a reference for that measured with radiation.

For performing dc and ac measurements as a function of P , the SG was used in sweeping mode. In both cases the sample followed a zfc protocol from the normal state down to temperature values below T_c , then a H_{dc} was applied and the dc or ac magnetization was measured after a dc or an ac measurement command activates the MW equipment to start radiating at fixed value of f . The magnetization was obtained in the range from -20.0 to 20.0 dBm in steps of 0.5 or 1.0 dBm. Finally, the magnetization under continuous radiation at fixed values of f , P , T , and H_{dc} , was recorded during around 1 hour after a zfc process was done.

3.4.4 Pulsed mode

Fig. 3.6 shows a sketch of the experimental setup used to carry out magnetization measurements under pulsed microwave fields. In this case the cs, joined to the coaxial cable, was inserted in the above mentioned cryostat and kept fixed at the central region of the magnetometer. In order to produce a controlled perturbation on the metastable critical state of the superconducting sample, the cs was excited by a single MW pulse provided by the internal source of a SG and modulated by a waveform generator [164]. To guarantee the temporal stability of the magnetic field during the measurements, the superconducting magnet was operated by an external sourcemeter [165].

The magnetic response of the sample to a single MW pulse was measured after either a zfc or fc mode by taking the output voltage signal from the rf-SQUID, V , in steps of 0.5 or 0.1 milliseconds (ms) during 200 or 1000 ms, and at different fixed values of H_{dc} , T , and MW perturbation parameters (pulse duration, t_{pulse} , f and P). The temporal variation of V with respect to the first registered value

3. Experimental Techniques

which is used as a reference, $\Delta V(t)$, was collected from the rf-SQUID either directly or through a high pass filter, and plotted in the time domain scale of an oscilloscope [166]. The reproducibility of the experiment and results was confirmed by remeasuring at different times and under the same initial conditions. To certify the presence of stochastic process each measurement was performed several time under the same initial conditions. The resulting data were then averaged.

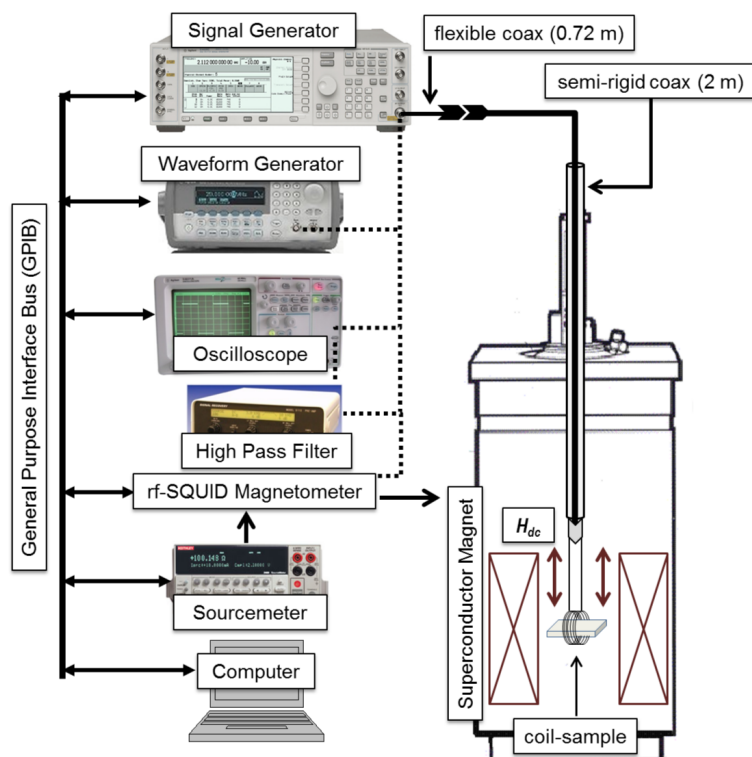


Figure 3.6: Diagram of the pulsed mode experimental setup.

It is worth mentioning that in the pulse regime the MW signal is modulated by a square wave pulse that is sufficiently short to eliminate or significantly reduce MW heating effects. One important drawback in interpreting the vortex instability phenomenon by using conventional magnetometry is the pause time before each data point is recorded (between 3 and 30 seconds). Although during this time the

magnetic field remains unchanged, the flux inside the superconductor continues evolving as a relaxation process (between 2 and 30 seconds), causing additional heating. Part of this heat is removed by the coolant, while the remainder compels the temperature of the superconductor to increase, leading to the occurrence of an avalanche. The present method has proven to be effective in the reduction of this pause time.

3.4.5 Power reflected mode

A schematic drawing of the experimental setup for making power reflected measurements is shown in Fig. 3.7. The cs was connected via semi-rigid and flexible coaxial cables to a performance network analyzer (PNA) [167] to measure the MW scattering parameters, which for a one-port measurement like the one performed here is the modulus of the complex reflection coefficient, $|S_{11}(f)| = 10 \log_{10}[P_{\text{ref}}(f)/P_{\text{in}}(f)]$, where $P_{\text{in}}(f)$ and $P_{\text{ref}}(f)$ are respectively the incident and reflected powers at the resonator. This experimental setup allows to make magnetic-field-dependent measurements of $|S_{11}|$ at one resonance mode under fixed values of P and T .

The reflection spectrum as measured here at the PNA is affected by losses in the cable, phase stability of the cable itself and the standing wave in the long MW line connecting the rf-coil in the magnetometer to the external PNA. However, in order to filter the signal reflected by the semi-rigid coaxial cable and collect only the signal that comes from the resonant setup, a Fourier transform (from the frequency to the time domain) was performed on the $|S_{11}(f)|$ spectra of interest after the calibration procedure. The time-domain signal was then filtered to remove undesired reflection contributions, and finally an inverse Fourier transform (from time domain to frequency) was made. The working resonant frequencies of the cs were then selected among the peaks that resulted from the ratio of the inverse Fourier transform obtained in the superconducting and normal states in that frequency range. Furthermore, the measurements of the reflection coefficient were performed over a narrow integration filter (50–150 Hz bandwidth) in the PNA and an averaging factor of 21 was used to reduce noise as well as to enhance the measurement accuracy.

3. Experimental Techniques

For measuring $|S_{11}|$ as a function of the dc magnetic field at constant values of temperature, first a zfc process was performed down to the working temperature with the cs fixed in the central homogeneous zone of H_{dc} . Then, as the dc magnetic field was swept in steps of 25 or 50 mOe with the help of the external sourcemeter and a continuous irradiation was applied at the selected f , P and T values, $|S_{11}(f)|$ was simultaneously recorded. Additionally, and in order to establish the thermal limitations of the setup and to evaluate the possible influence of MW heating on the cs, $|S_{11}|$ was measured as a function of H_{dc} for different values of P and at fixed T . The nominal power used here ranged from -20 to 0 dBm ($0.01-1$ mW).

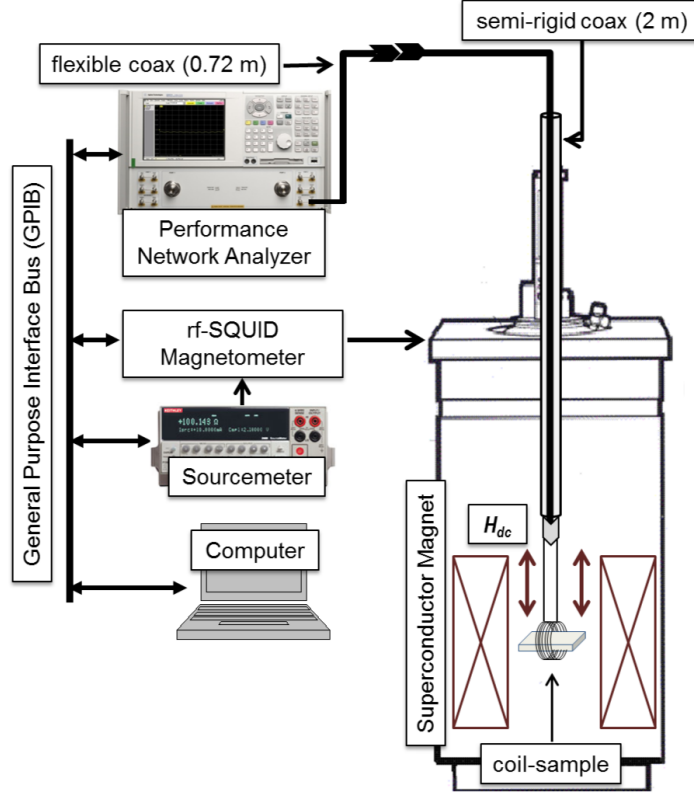


Figure 3.7: Diagram of the power reflected mode experimental setup.

3.4.6 rf-coil modeling

In order to search for the characteristics of the resonant structure formed by the cs, a theoretical approximation was proposed and the low-temperature frequency spectrum was registered, placing a thin film made of Pb with a square antidot array in the coil core [168]. We refer here only the most relevant finding that help to give an interpretation of the results when using the layout under different MW measurement techniques. Under the framework of the helical resonator approach [169], the spatial distribution of the MW electric (E_{\parallel} and E_{\perp}) and magnetic (H_{\parallel} and H_{\perp}) fields inside the resonant structure in the directions parallel (\parallel) and perpendicular (\perp) to the sample surface was estimated (see Fig. 3.8). The fields inside the coil space filled by the thin film were found to be practically homogeneous and considerably small in a large area through the coil except at the coil-sample edge, where they achieved a periodical behavior with sharp and deep local maxima for all cases but for E_{\parallel} , whose maxima appeared broad and shallow.

Additionally, the resonant frequency values by considering the coil alternatively as a $\lambda/4$ or a $\lambda/2$ resonator, $f_{th}(\lambda/4)$ and $f_{th}(\lambda/2)$, were theoretically obtained. The low-temperature frequency response of the cs resonator, given by the return loss $|S_{11}(f)|$, is shown in Fig. 3.9. The spectrum, obtained at $T = 4.00$ K, $H_{dc} = 10$ Oe and $P = -10$ dBm, presents resonant peaks at some defined frequency values f_{exp} in the whole range and decays slowly as f increases due to the presence of frequency-dependent losses in the coaxial cable. Such peaks are particularly significant at certain f_{exp} values, to wit $|S_{11}| \simeq 25, 21, 14, 16,$ and 12 dB at $f_{exp} \simeq 0.16, 1.12, 2.00, 3.05,$ and 3.17 GHz, respectively. The f_{exp} values and their number in this figure match fairly well those theoretically estimated for $f_{th}(\lambda/4)$ and $f_{th}(\lambda/2)$, which are respectively plotted as solid squares and open rhombuses in the same figure. The display of the resonant frequencies appears conditioned by the long terminal of the coil (which acts as bifilar transmission line), the coil and the sample itself.

By applying the 3 dB method [132, 138] to $|S_{11}(f)|$, for values of f_{exp} that match the theoretical estimated, numbers between 30 and 500 were obtained for the Q factor. This nonmonotonous behavior can be understood considering that the

3. Experimental Techniques

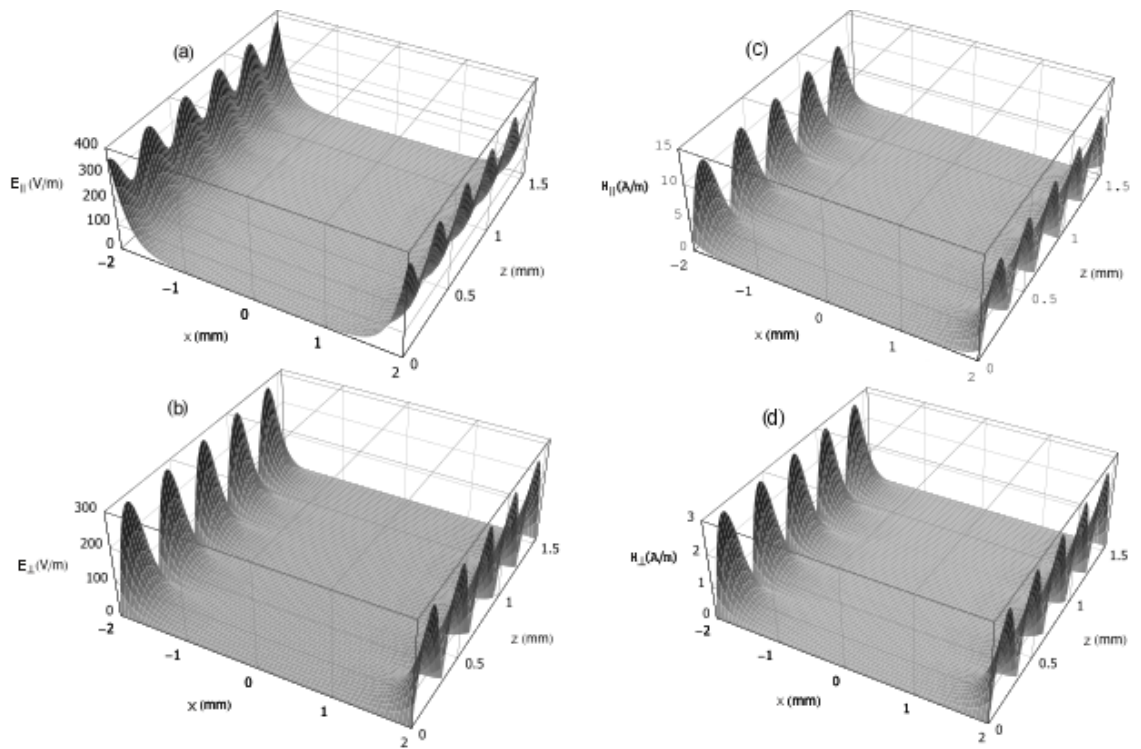


Figure 3.8: Spatial distribution of the parallel [E_{\parallel} (a) and H_{\parallel} (c)] and perpendicular [E_{\perp} (b) and H_{\perp} (d)] components of the MW electric and magnetic fields inside the coil space filled by the Pb thin film.

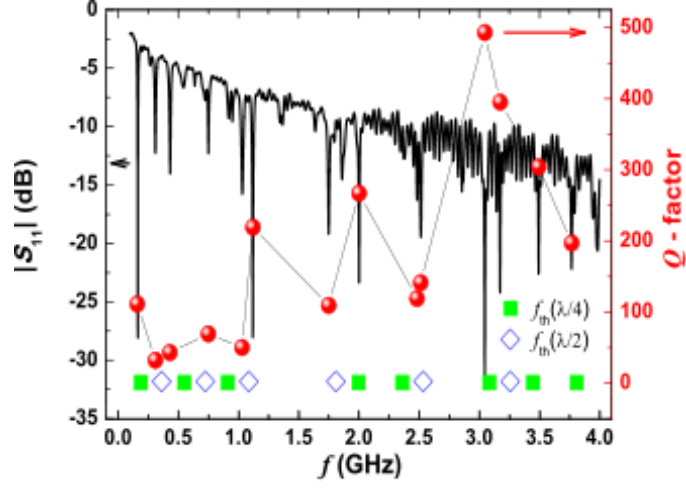


Figure 3.9: Low-temperature frequency spectrum obtained at $P = -10$ dBm for the cs setup. Theoretical estimates for the resonant frequencies made in the framework of the $\lambda/4$ and $\lambda/2$ models are shown respectively as solid squares and open rhombuses. The Q factor obtained from those f_{exp} values that match the theoretical model is also presented (solid circles). The lines connecting the points are only a guide to the eye.

shape of the resonant peaks can be affected by the contributions introduced by the coaxial cable and the coupling structures. Additionally, $|S_{11}(f)|$ can be influenced by the electromagnetic properties of the sample as the complex conductivity and the penetration depth of the superconductor, and the dielectric losses in the substrate. Another factor that affects strongly the resonance curves (via the shift of the center frequency and varying the bandwidth of the resonance mode), and reduces the Q factor, is the local Joule heating within one or more localized defects in the superconducting film. Those thermally induced effects have been registered in the MW frequency range in continuous and pulsed mode as a function of the MW power [170, 171, 172, 173, 174, 175, 176], and are characterized by relatively long time scales [172]. Finally, at the edge of the cs, $E_{\parallel} \simeq 10^2$ V/m, $E_{\perp} \simeq 850$ V/m, and $H_{\parallel} \simeq H_{\perp} \simeq 100$ mOe were calculated by using $P = 0$ dBm, $f = 1.06$ GHz and $Q = 50$. The significance of these values will be discussed later.

Chapter 4

Vortex instabilities driven by microwave fields

4.1 Introduction

The formation of spatial structures is a quite general property of complex physical systems. The development of an inhomogeneous state in these systems is, under certain conditions, thermodynamically more favorable than a homogeneous one. Spatially inhomogeneous magnetic structures can vary in a wide range, from a few lattice parameters to the dimensions of macroscopic samples. Macroscopic magnetic structures containing a large number of Abrikosov vortices are observed in both high- and low-temperature type-2 superconductors.

Vortices can move, change shape and scale, and transform the sample from one phase or state into another. Such dynamic effects can occur spontaneously or due to changes in the temperature, dc magnetic field, or mechanical stresses. An important role in the dynamics of vortices belongs to dissipative processes, which can control not only the relaxation but, frequently, also the topology of the inhomogeneous state. The vortex structures in type-2 superconductors can manifest instabilities of various natures being the best known the *thermoelectromagnetic instability* (TEMI), also known as *magnetic-flux jumps* or *vortex avalanches* [177]. We note that precisely TEMI restricts the non-dissipative current-carrying capacity of commercial superconductors. Therefore, the physical picture of the flux

4. Vortex instabilities driven by microwave fields

jumps, and particularly their nucleation and propagation, is of great interest for both fundamental physics, related with the vortex dynamics, and a successful development of thin film superconducting devices such as quantum circuits [178], detectors operating at MW frequency [179, 180, 181, 182], nonlinear instruments [183], and qubit readout [184], among others.

High-resolution magnetic-optical imaging (MOI) technique based on the Faraday effect [185, 186], has shown that a large number of type-2 superconducting thin films in perpendicular dc magnetic fields, e.g., Nb [187, 188], Nb₃Sn [189], NbN [190, 191], MgB₂ [56, 192, 193, 194], YNi₂B₂C [195], Pb [62], a-MoGe [196], a-MoSi [197], and also YBa₂Cu₃O_{7- δ} [46, 49], become unstable when exposed to time-varying moderate magnetic fields (increasing or decreasing) for material-dependent threshold values in temperature [58, 198, 199], applied magnetic field [53, 54, 55, 57, 190, 194, 200, 201], and transport current [202], as well as in sample dimensions [55, 200]. MOI reveals that the vortex lines move with a very high velocity (from 150 km/s at the very early stages down to 18 km/s at the latest [49]), inside spontaneously created channels. In fact, the vortices propagate forming numerous dendrites appearing sequentially and in a high intermittent way so that the magnetic flux in a superconductor forms a complex fractal structure. The fingerprints of these vortex avalanches have been also observed in isothermal experiments in the form of steps or jumps in the magnetic hysteresis loops [48, 53, 54, 55, 57, 194, 200, 201, 203], reentrance in ac susceptibility measurements [63], and noise response of the susceptibility components [204]. Recently, TEMI in Pb and Nb superconducting films, induced respectively by vortex depinning [60] and ac magnetic fields [205], have been reported. In the former, the avalanches were triggered at the edge by rising the temperature locally, while in the latter they appear as a result of a train of ac field cycles.

In HDC, the granularity limits the relevant size scale over which screening currents flow, and as a consequence the critical size predicted by the adiabatic flux jump theory [206] has been rarely exceeded and TEMI has been scarcely observed. Nevertheless, with nowadays ability to grow quality large single crystals and large grained polycrystalline HDC compounds, flux jumps have been also registered in these materials [46, 47, 48, 49, 50, 51, 52, 203, 207, 208, 209, 210, 211, 212]. By combining MOI and femtosecond pulsed laser technique on films of YBa₂Cu₃O_{7- δ} ,

4. Vortex instabilities driven by microwave fields

it has been possible to record a snapshot of the evolving flux distribution during the vortex avalanche [50, 207]. Flux jumping has been also visualized when ramping an external perpendicular magnetic field up in a similar sample [46]. TEMI appears also in magnetic hysteresis loops of highly textured polycrystalline samples of $\text{Bi}_2\text{Sr}_2\text{CaCu}_2\text{O}_{8+\delta}$ [48, 203], and in both magnetostriction and magnetization loops of single crystals made of $\text{La}_{2-x}\text{Sr}_x\text{CuO}_4$ [47, 52, 203, 209, 210]. It has been shown that the heat exchange conditions as well as the sweep rate strongly influence the appearance of flux instability in these materials [47]. Moreover, it was reported that the magnetic flux jumps last several microseconds and their dynamics is governed by the magnetic flux diffusivity, which is proportional to the flux flow resistivity [203]. Interestingly, these materials are often susceptible to flux creep, a phenomenon which can stabilize the critical state against flux jumping [51, 211], making thus HDC more resistant to TEMI than conventional superconductors.

On the other hand, MgB_2 -based applications are hindered by the presence of pronounced instabilities in the magnetic flux penetration that destroy the critical state and appear as noise in magnetic hysteresis loops at temperatures below certain threshold value, $T_{th} = 10$ K, and dc magnetic fields smaller than 2000 Oe [53, 54, 55, 56], or up to $T_{th} = 14$ K in nonhomogeneous microstructured areas [213]. TEMI has been also observed in the form of finger-like or tree-like structures in MOI experiments [56, 57, 58] or in the MW response of MgB_2 resonators as jumps in the resonance curves of the frequency-dependent complex transmission coefficient [214, 215].

The stability of the vortex structure depends on how strongly vortices are pinned by inhomogeneities created naturally during the material synthesis or made intentionally at a later stage. Making holes of proper size in superconducting films is a well-know approach for arresting the motion of individual vortices [24, 25]. Indeed, it has been demonstrated in superconductor-based devices, e.g., rf-SQUID and MW resonators, that noise can be reduced significantly by adding holes in the film structure [216, 217]. However, a flux-jump regime has been observed in type-2 Pb thin films with a periodic array of antidots [61, 62, 63], Pb plain samples [60, 64] and Pb-porous glass nanocomposite [59]. One way to suppress TEMI has been to coat the superconductor with a thin layer of metal [218, 219],

which provides an additional heat sink. Investigations on whether holes or morphologies at the nanoscale can have a stabilizing effect on the thermoelectromagnetic avalanches [196, 220, 221], have demonstrated that the region of TEMI in the field-temperature diagram can be suppressed, delimited or controlled by the presence of pinning landscapes.

In this chapter, we first describe shortly two dynamic effects in type-2 superconductors, namely magnetic-flux jumps and dendritic instabilities, and then we present experimental results that evidence the occurrence of vortex instabilities in the measurements of the magnetic moment under a continuous sweep of the MW frequency, and in the magnetization signal obtained from the SQUID magnetometer under MW pulses.

4.2 Dynamic effects in type-2 superconductors

4.2.1 Magnetic-flux jumps

The nature of magnetic-flux jumps is related to the positive feedback between electromagnetic and thermal processes in superconductors. The density of the superconducting current J , which shields the external magnetic field, decreases with increasing the sample temperature T_s by a small perturbation δT_s arising due to a certain initial heat release δQ_0 . Because of the decrease in the shielding current, the magnetic flux penetrates deeper into the superconductor. The motion of the magnetic flux into the sample induces an electric-field perturbation δE_0 , and consequently, the appearance of additional Joule heat, i.e., further heating δQ_1 , an additional temperature rise δT_1 , and therefore, an additional reduction of J . Under certain conditions, such a process takes an avalanche-like character, leading to the transition of a part of the sample (or even of the entire sample) to the normal state.

TEMI in superconductors appears only at low temperatures, when the local critical current density is high and the Lorentz force is large enough to drive vortices along the sample. Another significant reason is that both the thermal conductivity and the heat transfer from the superconducting film to the substrate are small at low temperature [200], so the heat produced by the vortex motion propagates

4. Vortex instabilities driven by microwave fields

faster than the heat conduction to the outside, and the positive feedback can be thus realized [177].

The commonly accepted theory of TEMI predicts that magnetic-flux jumps develop more or less homogeneously, occupying a significant part of the sample volume, while the front of the propagating magnetic flux remains smooth. The pattern of this front depends on the shape of the sample surface and the form of the region affected by the external perturbation, which is transformed into a flux jump. In other words, the spatial scale of the instability is limited only by the size of the sample, and small-scale perturbations are stabilized due to heat conductivity and external cooling.

The key dimensionless parameter of the model is the ratio of the magnetic ($t_{mag} = 1/D_{mag} = \mu_0\sigma$) and thermal ($t_{th} = 1/D_{th} = C/\kappa$) diffusion time constants [177]:

$$\tau = \frac{t_{mag}}{t_{th}} = \frac{D_{th}}{D_{mag}} = \frac{\mu_0\kappa\sigma}{C}. \quad (4.1)$$

Here D_{mag} and D_{th} are the magnetic and thermal diffusivity, respectively, κ is the heat conductivity, σ is the electric conductivity and C is the heat capacity. The magnetic diffusivity related to the viscous motion of vortices can be expressed in terms of flux-flow resistivity as, $D_{mag} = \rho_f/\mu_0$. For $\tau \ll 1$ ($t_{mag} \ll t_{th}$ or $D_{mag} \gg D_{th}$), rapid propagation of flux is accompanied by adiabatic heating of the superconductor, i.e., there is not time enough to redistribute and remove the heat released due to flux motion. For $\tau \gg 1$ ($t_{mag} \gg t_{th}$ or $D_{mag} \ll D_{th}$), the spatial distribution of flux remains fixed during the stage of rapid heating. These adiabatic ($\tau \ll 1$) and dynamic ($\tau \gg 1$) approximations are the basis of the approach to the flux jumping problem, and the flux-jump scenario significantly depends on the relation between the values of κ , C , and σ .

In a magnetization experiment where the external magnetic field is ramped at a rate much smaller than 1 T/s, a background electrical-field, $E_b < 10^{-4}$ V/m, induced by the magnetic-field variation and corresponding to the flux-creep regime, comes out in the stability domain of the Bean critical model [177]. In the flux-creep regime the relation between the current density J and the electric field E is strongly nonlinear, and as a consequence the value of σ , i.e., the slope of the J - E curve, strongly depends on the electric field. In this situation, the flux jumping

4. Vortex instabilities driven by microwave fields

takes place on a background of a resistive state with a conductivity that strongly depends on the external magnetic-field ramp rate. For the flux-creep regime the conductivity is given by the formula

$$\sigma = \sigma(E) = \frac{\partial J}{\partial E} = \frac{J_1}{E}, \quad (4.2)$$

where J_1 determines the slope of the J - E curve and $J_1 \ll J_c$. It has been estimated that $\sigma(E) > 10^3$ A/cm² [177]. From this reckoning it follows that the conductivity σ that determines the flux-jump dynamics for the magnetization experiments is very high and so does the dimensionless ratio τ . Thus, the scenario of a flux jump for these experiments corresponds to the limiting case when $\tau \gg 1$ and the rapid heating stage takes place on the background of a frozen-in magnetic flux. Under certain conditions a flux jump is preceded by a series of magnetothermal oscillations [177], which have been observed for both low-temperature [222, 223] and high-temperature superconductors [224]. Theoretically, such oscillations were considered for a flux jump developing in the flux-flow regime [225], where the J - E curve is linear and σ is electric-field independent. High values of $\sigma(E)$ significantly affect the flux dynamics and therefore the magnetothermal oscillations.

In the simple case of a plate of type-2 superconductor located in an external magnetic field \mathbf{H} directed along the z axis, with a shielding current flowing along the y axis and determined by the J - E curve as $\mathbf{J} = J(T, E) \mathbf{E}/E$, and the magnetic induction $\mathbf{B}(x) = \mu_0 \mathbf{H}$ (which decreases by moving further into the sample), the coupling of the Maxwell equations to the heat diffusion,

$$\nabla \times \mathbf{B} = \mu_0 \mathbf{J}, \quad (4.3)$$

$$\nabla \times \mathbf{E} = -\frac{\partial \mathbf{B}}{\partial t}, \quad (4.4)$$

$$C \frac{\partial T}{\partial t} = \kappa \nabla^2 T + \mathbf{J} \cdot \mathbf{E}, \quad (4.5)$$

leads to an explicit form of the stability criterion for the critical state [177]:

$$\frac{\mu_0 H^2}{CJ} \left| \frac{\partial J}{\partial T} \right| > \mu_0 \sigma(E) \frac{\kappa}{C} + 1. \quad (4.6)$$

4. Vortex instabilities driven by microwave fields

Usually, $J/|\frac{\partial J}{\partial T}| \sim T_c$. The left-hand side of this equation contains the ratio of the characteristic magnetic energy $\mu_0 H^2$ to the characteristic thermal energy CT_c , while the right-hand side includes two terms that are responsible for two stabilization mechanisms. The first includes the heat conductivity and the differential conductivity, $\sigma(E) = \partial J/\partial E$. It is obvious that the greater the heat conductivity is, the more efficient the process of heat removal from the heated region and the more stable the superconducting state. The role of differential conductivity can be understood as follow. The density of the superconducting current decreases with heating, and the magnetic flux moves and leads to the appearance of an electric field. An increase in the electric field leads to an increase in the current density, $\partial J/\partial E > 0$, which in turn partly compensates the decrease in the current caused by heating. This is the so-called *dynamic stabilization mode*. If the first term is small compared to unity, a second mechanism, the so-called *adiabatic stabilization*, intervenes. If the ratio of the characteristic magnetic energy $\mu_0 H^2$ to the characteristic thermal energy $\sim CT_c$ is small, no flux jumps arise.

4.2.2 Dendritic instability

The described picture of the development of TEMI correctly characterizes many experimental facts, but by no means all of them. As it was mentioned in the previous section, numerous MOI experiments show that TEMI can lead to the appearance of a branching (dendritic) structure of the magnetic-flux distribution below a certain threshold temperature, $T_{th} < T_c$. Such a phenomenon is especially frequent in thin films placed in a perpendicular magnetic field. The dendritic instability develops as follows (Fig. 4.1). As the external field increases, the magnetic flux penetrates the sample. In small fields, the front of this magnetic flux is smooth. Suddenly, finger-like outbreaks of vortices into the bulk of the sample appear at the front [Fig. 4.1(a)], as if *grass* started to grow near the edge of the penetrating flux. Next, separate dendrites (*trees*) start appearing in a stronger external field [Fig. 4.1(b)]. With a further increase of the field, the number of dendrites gets greater and greater [Fig. 4.1(c)]. Gradually, the entire sample becomes filled by the *forest* of dendrites, and the distribution of the magnetic field takes a typical fractal form [Fig. 4.1(d)]. The dendritic instability occurs

4. Vortex instabilities driven by microwave fields

in a limited range of applied fields, $H_1^{th} \leq H \leq H_2^{th}$, where H_1^{th} and H_2^{th} are the so-called lower and upper threshold fields, respectively [see upper right-hand corner of panels (b) and (d) in Fig. 4.1], which depend on the width of the sample [200]. Additionally, it was shown that the formation of this kind of instability is a stochastic process, i.e., the exact nucleation site of the next dendrite, the field interval between two consecutive events, and the final shape of the dendritic structure are non-reproducible [200]. Finally, the degree of branching of the dendrites, sometimes represented by their fractal dimensionality and size, vary with temperature [226] and the magnetic field [190].

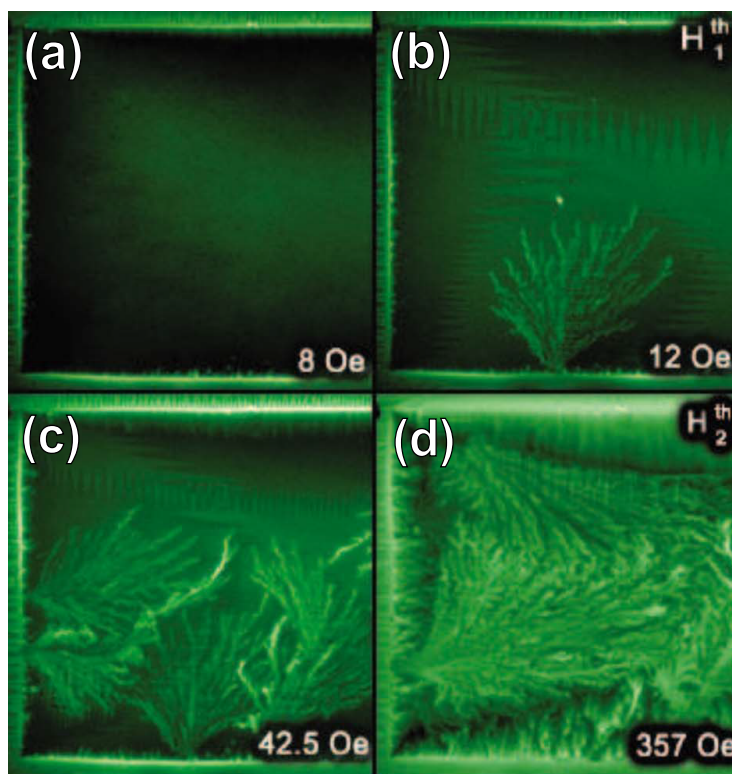


Figure 4.1: Magnetic-optical images of the development of a dendritic instability in a NbN film at $T = 4$ K. The lighter regions correspond to a greater magnetic field strength. Only the lower left-hand side of the sample is shown; its length is 2.4 mm. In the lower right-hand corner of each image, the applied magnetic field strength is indicated [190].

This behavior seems to contradict the *classical* concepts of TEMI. Indeed, be-

4. Vortex instabilities driven by microwave fields

cause heat conductivity suppresses the development of such an instability, the small transverse size of a dendrite appears to favor the fast removal of heat from its channel. Consequently, a thermal fluctuation of a large spatial scale should develop faster than a narrow dendrite. But a detailed analysis of experimental data unambiguously indicates the thermal nature of the appearance of a dendritic structure (see [200] and references therein). Certainly, this follows from direct measurements of temperature in dendrite channels using a thermal image. It is also supported by the fact that such a structure arises only in the region of low temperatures, where the heat capacity of the material is small, and from the good agreement between the experimental results and the theoretical estimation that treats a dendrite as a consequence of local TEMI [227, 228]. A dendritic spatial structure arises upon the development of a flux jump if the background electric field in a superconductor produced by an external regular source or by a random action exceeds some critical value E_c , which depends on the geometry of the sample. We note that because of the effect of the geometrical factor, the value of E_c for films ($\approx 4 \times 10^{-4}$ V/m) is less than for bulk samples (0.1 V/m). Correspondingly, the development of the dendritic instability is more probable in films.

The physical reason for the growth of a dendritic structure in superconductors can be understood from the following considerations. If a perturbed region extended in the direction transverse to the current vector appears in the sample, then the current cannot bypass this region, flows through it and heats it up. If the electric field E produced by an external source is sufficiently larger than E_c , then the heating of the perturbed region exceeds the heat removal and leads to the nucleation of a dendrite. The characteristic threshold flux penetration depth of the dendrite $l^* \sim (\kappa/|E\partial J/\partial T|)^{1/2}$, is determined by the balance between the heating and the heat removal [227]. The threshold field is then related to l^* as $H^{th} \sim \operatorname{arccosh}[w/(w-l^*)]$, where w is the half-width of the sample [227]. For the instability to develop, l^* should be positive, finite and smaller than w ; otherwise when l^* approaches w , H^{th} diverges and the dendritic avalanches vanish. In films, the rate of growth of a dendrite is determined by electromagnetic processes in the space surrounding the film and can reach giant magnitudes, 10^5 m/s and larger [49, 229].

4.3 Vortex dynamics under Sweeping Microwave Mode

In this section, we test the capability and sensibility of the low-temperature MW probe described in section 3.4.3 for characterizing vortex dynamics in three different thin film superconductors: $\text{La}_{1.82}\text{Sr}_{0.18}\text{CuO}_4$, Pb with a square antidot array, and MgB_2 . Instead of the gradual relaxation of the flux gradient that is observed in the absence of microwaves, non-monotonic features in the MW frequency-dependent magnetic moment response in the form of jumps, negative peaks, ripples and small steps at discrete frequency values under different dc magnetic fields, temperatures and MW nominal powers have been observed. The presence of these frequency-triggered anomalies is interpreted as nucleation of instabilities that change the smooth critical-state flux propagation.

4.3.1 Frequency-driven instability: $\text{La}_{1.82}\text{Sr}_{0.18}\text{CuO}_4$

Figure 4.2 presents the temporal evolution in logarithmic scale of the magnetic moment of $\text{La}_{1.82}\text{Sr}_{0.18}\text{CuO}_4$ recorded at $P = 15$ dBm ($\simeq 32$ mW), for $T = 18.0$ K and $H_{\text{dc}} = 50$ Oe [panel (a)], and for $T = 22.0$ K and $H_{\text{dc}} = 500$ Oe [panel (b)]. It is observed that the MW-free curve draws a conventional monotonous relaxation [open squares in Fig. 4.2(a)], meanwhile the response obtained under continuous radiation starts describing a smooth behavior until it is interrupted by a sharp dip at $f = 0.72$ GHz which is followed by a sudden jump and the final recovery of a new relaxation stretch [panel (a)]. By enhancing further the temperature ($T = 22.0$ K) and the dc magnetic field ($H_{\text{dc}} = 500$ Oe), only discontinuities in the form of negative peaks that span a few frequency values are registered [panel (b)].

Figure 4.3 shows the magnetic moment of the $\text{La}_{1.82}\text{Sr}_{0.18}\text{CuO}_4$ sample, that of the substrate SrTiO_3 alone and the difference of both signals as a function of MW frequency recorded under the same experimental conditions, $T = 20.0$ K, $H_{\text{dc}} = 50$ Oe, and $P = 15$ dBm. In the substrate signal (solid line) only a paramagnetic contribution in the form of a background noise that shifts the superconducting

4. Vortex instabilities driven by microwave fields

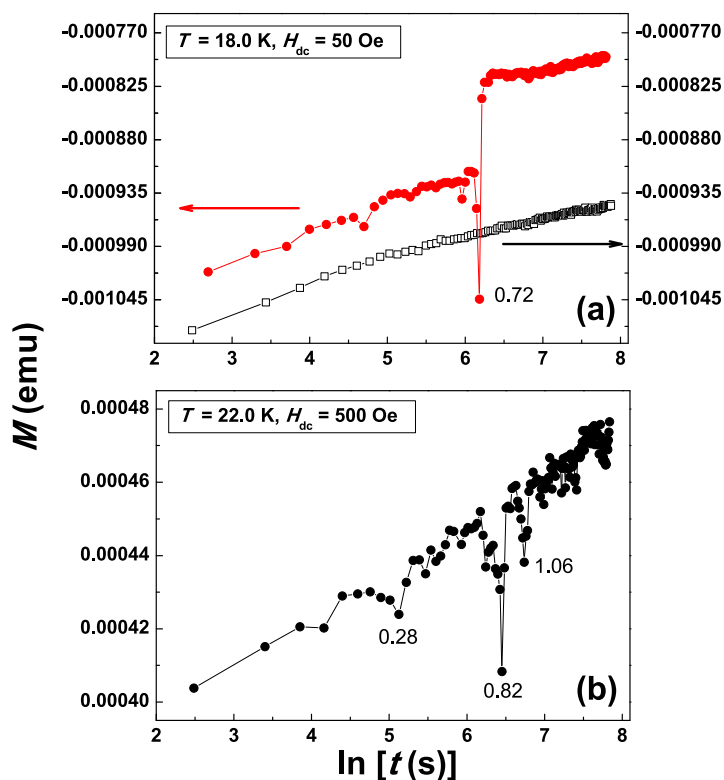


Figure 4.2: Temporal evolution in logarithmic scale of the magnetic moment registered as a function of microwave frequency and time when $\text{La}_{1.82}\text{Sr}_{0.18}\text{CuO}_4$ was irradiated with microwaves of $P = 15$ dBm ($\simeq 32$ mW) for $T = 18.0$ K and $H_{dc} = 50$ Oe [panel (a)], and $T = 22.0$ K and $H_{dc} = 500$ Oe [panel (b)]. The MW-free temporal evolution (open squares) is included in panel (a). The labels correspond to frequency values in GHz units.

4. Vortex instabilities driven by microwave fields

signal is registered. These results suggest that we can exclude the possibility of any substrate contribution to the magnetic moment and surmise that the response when the MW frequency is swept should come solely from the superconducting thin film. Similar paramagnetic signal has been obtained when performing identical measurements with the sample in the normal state.

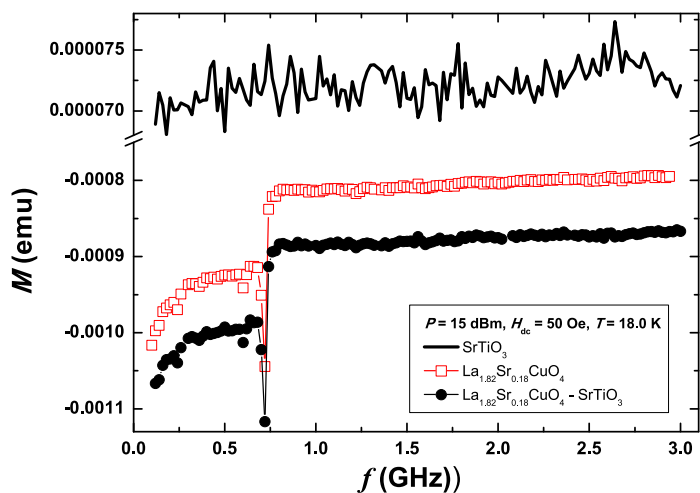


Figure 4.3: Magnetic moment registered as a function of microwave frequency when the $\text{La}_{1.82}\text{Sr}_{0.18}\text{CuO}_4$ sample (open squares) and the substrate SrTiO_3 alone (solid line), were irradiated with microwaves of $P = 15$ dBm for $H_{\text{dc}} = 50$ Oe at $T = 20.0$ K. The difference of both signals (closed circles) is included.

Figure 4.4 pictures the magnetic moment of $\text{La}_{1.82}\text{Sr}_{0.18}\text{CuO}_4$ as a function of the MW frequency recorded at $T = 18.0$ K for $P = 15$ dBm, after a zfc process while f was decreasing from 3.00 GHz to 0.10 GHz under $H_{\text{dc}} = 100$ Oe [panel (a)], and in remnant mode after the sample was first fc under $H_{\text{dc}} = 100$ Oe whilst f was swept from 3.00 GHz to 0.10 GHz [panel (b)]. It is observed that the response registered when the frequency is swept in backward way [panel (a)] is, in general, similar to those reported in forward direction [Figs. 4.2 and 4.3]. In this case, the flux profile evolves monotonously until a sudden peak appears $f = 0.96$ GHz and then the curve regains a new, almost flat, relaxation stage. A small mismatch in the frequency value at which the peak emerges as compared with the value at which appears in the forward way (see Fig. 4.2) is also registered. In the case

4. Vortex instabilities driven by microwave fields

when a fc process is first performed, the signal decreases in a smooth way up to a considerable jump which starts at $f = 0.82$ GHz and prolongs during several frequency values. Afterwards, a new nearly even stage is achieved. Here, the f value at which the irregularity occurs is also shifted with respect to the value for increasing frequency.

These results clearly suggest that the irregularities that come into view in the frequency-dependent magnetic moment curve are related with changes in the vortex dynamics when the MW frequency is continuously swept and they do not result from experimental artifacts. In the next, we study the behavior of these anomalies as a function of T , H_{dc} and P .

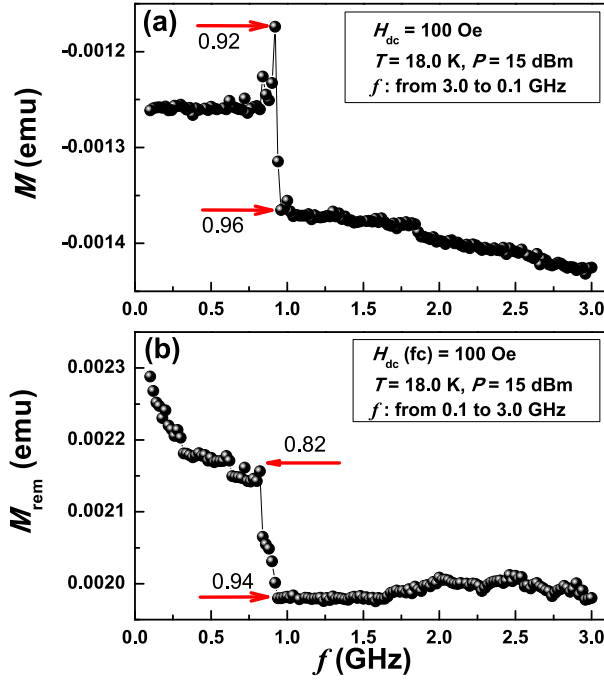


Figure 4.4: Magnetic moment registered as a function of microwave frequency when $\text{La}_{1.82}\text{Sr}_{0.18}\text{CuO}_4$ was irradiated with microwaves of $P = 15$ dBm at $T = 18.0$ K in a decreasing way from $f = 3.0$ GHz to 0.1 GHz [panel (a)], and in remnant mode after a fc process ($H_{\text{dc}} = 100$ Oe) [panel (a)]. The labels correspond to frequency values in GHz units.

Figure 4.5 shows the magnetic moment of $\text{La}_{1.82}\text{Sr}_{0.18}\text{CuO}_4$ recorded as a func-

4. Vortex instabilities driven by microwave fields

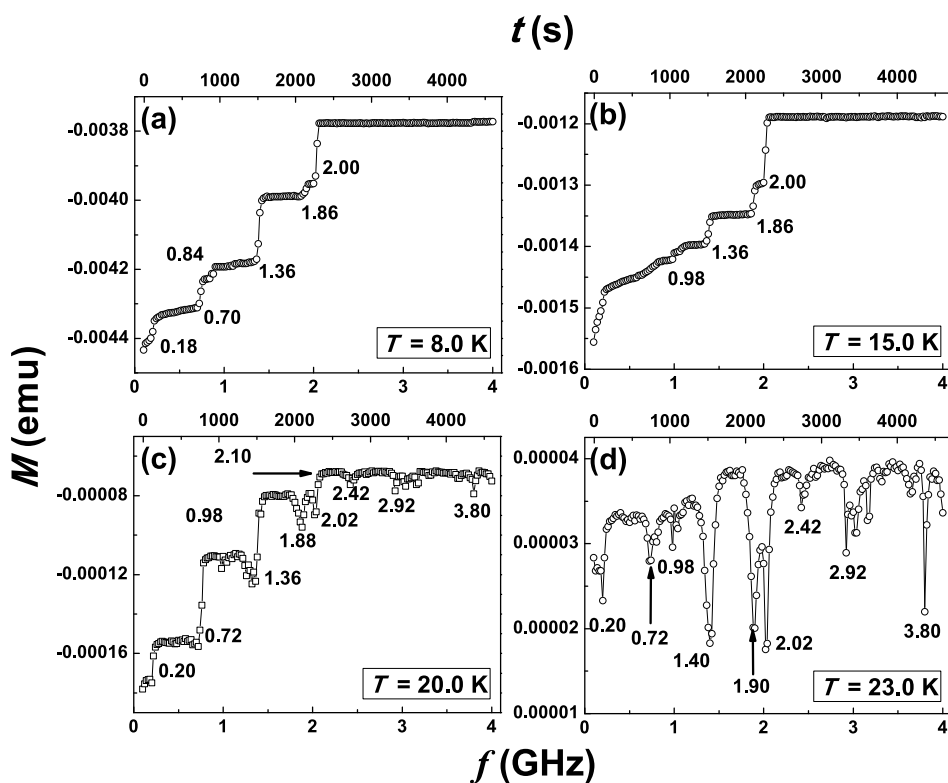


Figure 4.5: Magnetic moment registered as a function of microwave frequency and time when $\text{La}_{1.82}\text{Sr}_{0.18}\text{CuO}_4$ was irradiated with microwaves of $P = 10$ dBm (10 mW) for $H_{\text{dc}} = 50$ Oe at different system temperature values: $T = 8.0$ K (a), 15.0 K (b), 20.0 K (c), and 23.0 K (d). The labels correspond to frequency values in GHz units.

4. Vortex instabilities driven by microwave fields

tion of the MW frequency and time at $H_{\text{dc}} = 50$ Oe and $P = 10$ dBm (10 mW), for different temperature values: $T = 8.0$ K [panel (a)], 15.0 K [panel (b)], 20.0 K [panel (c)], and 23.0 K [panel (d)]. The curves display an unusual feature, namely, a staircase-like response with different irregularities at certain discrete frequency values. Significant jumps are registered at $f = 1.36$ and 2.00 GHz for $T = 8.0$ K [panel (a)], while an appreciable jump occurs at $f = 2.00$ GHz for $T = 15.0$ K [panel (b)]. At $T = 20.0$ K [panel (c)], the jumps are preceded by small dips, whereas notable jumps appear at $f = 0.72$ and 1.36 GHz, and negative peaks are reported from $f = 1.88$ GHz up to 3.80 GHz. At $T = 23.0$ K [panel (d)], only negative peaks are detected at frequency values comparable with those highlighted in panel (c). Additionally, for the lowest T values [panels (a) and (b)] the slope between jumps tends to an almost even stage above $f \simeq 1.00$ GHz and a plateau-like response is reported after the last jump has taken place at $f = 2.00$ GHz. At $T = 20.0$ K the plateau is disrupted by shallow negative peaks detected beyond $f \simeq 2.10$ GHz [panel (c)], while such behavior is registered in the entire range of frequencies at $T = 23.0$ K [panel (d)]. Regarding the jumps at certain f values at all temperatures but 23.0 K, it appears that their height is a decreasing function of T , whereas the occurrence of the peaks is noticeable only at the two highest T values. Finally, a minor mismatch of the order of 0.20 GHz in the f values at which the jumps take place comes into view as T increases.

Figure 4.6 illustrates the magnetic moment of $\text{La}_{1.82}\text{Sr}_{0.18}\text{CuO}_4$ recorded as a function of the MW frequency at $T = 8.0$ K and $H_{\text{dc}} = 50$ Oe for three different nominal MW powers, $P = 10$ dBm (10 mW, open squares), 15 dBm ($\simeq 32$ mW, solid squares) and 20 dBm (100 mW, open circles). All three curves present a staircase-like response and those obtained at $P = 15$ and 20 dBm deviate significantly from the one corresponding to $P = 10$ dBm. The jumps are observed to arise around similar values of f but with different heights for different P . Significant jumps are registered at $f = 0.72$ and 1.84 GHz for $P = 15$ dBm, while such jumps appear at $f = 0.18$ and 0.98 GHz for $P = 20$ dBm. Interestingly, the last notable jump that rises at $f = 2.00$ GHz for $P = 10$ dBm appears shifted to low f as P is enhanced, namely, $f = 1.84$ GHz ($P = 15$ dBm) and $f = 0.98$ GHz ($P = 20$ dBm). Finally, all curves show a plateau-like behavior after the last jump has occurred at $f = 2.00$ GHz.

4. Vortex instabilities driven by microwave fields

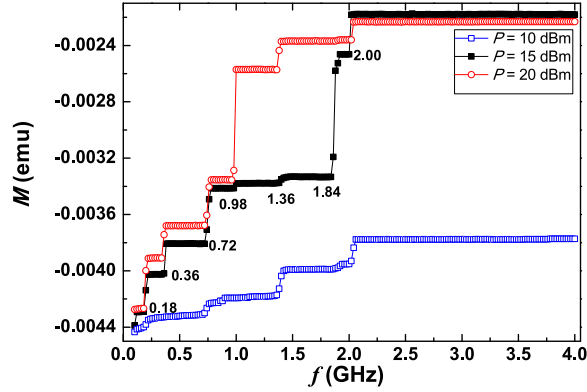


Figure 4.6: Magnetic moment of $\text{La}_{1.82}\text{Sr}_{0.18}\text{CuO}_4$ registered as a function of microwave frequency at $T = 8.0$ K and $H_{\text{dc}} = 50$ Oe, when it is irradiated with different microwave powers: $P = 10$ (10 mW, open squares), 15 dBm ($\simeq 32$ mW, solid squares), and 20 dBm (100 mW, open circles). The labels correspond to frequency values in GHz units.

Figure 4.7 depicts the magnetic moment of $\text{La}_{1.82}\text{Sr}_{0.18}\text{CuO}_4$ recorded as a function of the MW frequency at $T = 20.0$ K and $P = 15$ dBm, for different values of the dc magnetic field, $H_{\text{dc}} = 750$ Oe and 1 kOe [panel (a)], and $H_{\text{dc}} = 2$ kOe, 5 kOe and 10 kOe [panel (b)]. To make the behavior of these curves more comprehensible, they have been shifted upward from 1 to 10 kOe by 2 , 4 , 2.5 and 7.5×10^{-4} emu, severally. A parabolic-like response with a subtle staircase-like feature superimposed is observed until a sudden negative peak takes place at $f = 0.78$ GHz for all H_{dc} values. Thenceforth the curves evolve disrupted by shallow peaks, either in the same parabolic way at the lowest fields [panel (a)], or in a nearly plateau-like response at the highest ones [panel (b)]. The peaks become more pronounced as H_{dc} is increased up to 2 kOe, after which they start to decline. As an illustration, the negative peak at $f = 0.78$ GHz grows from $H_{\text{dc}} = 750$ Oe until it becomes maximum at $H_{\text{dc}} = 2$ kOe, and afterwards it starts to decay. The jumps at $f = 0.28$ and 0.40 GHz are preceded by small dips and turn into shallow negative peaks with the enhancement of H_{dc} , in analogy with the behavior registered for $f = 0.20$ and 0.72 GHz as T increases from 20.0 to 23.0 K [Figs. 4.5(c) and (d)]. It is worth mentioning that the difference of frequencies

4. Vortex instabilities driven by microwave fields

at which the main jumps or the negative peaks appear in the figures presented here is related rather with experimental artifacts associated with the soldering procedure of the rf-coil terminals to the semi-rigid coaxial cable than with the sample response.

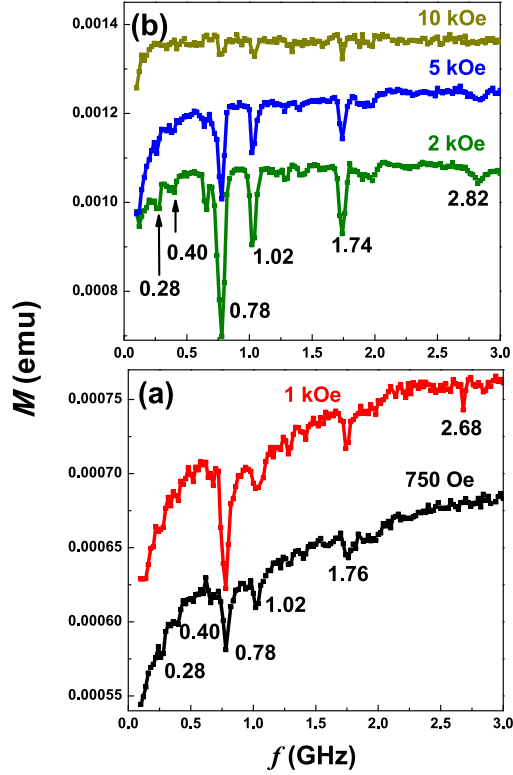


Figure 4.7: Magnetic moment registered as a function of microwave frequency when $\text{La}_{1.82}\text{Sr}_{0.18}\text{CuO}_4$ was irradiated with microwaves of $P = 15$ dBm at $T = 22$ K for different values of H_{dc} : (a) 750 Oe and 1 kOe; (b) 2 kOe, 5 kOe and 10 kOe. The upper curve in panel (a) and those in panel (b) have been rearranged and shifted upward for clarity. The labels correspond to frequency values in GHz units.

4.3.2 Frequency-driven instability: patterned Pb

Figure 4.8 plots the magnetic moment response recorded after every MW frequency step for the sample of Pb with a square antidot array at $T = 4.00$ K and

4. Vortex instabilities driven by microwave fields

$H_{\text{dc}} = 10$ Oe, for different P values: 0 dBm (1.0 mW) [panel (a)], 10 dBm ($\simeq 10.0$ mW) [panel (b)], 15 dBm ($\simeq 32.0$ mW) [panel (c)], and 20 dBm (0.1 W) [panel (d)]. The curves in this figure can be considered to reflect the time evolution of the magnetic flux inside the sample as the frequency changes, and present several remarkable issues as compared with the smooth vortex penetration that usually appears in a MW-free magnetic moment relaxation [230].

First, a plateau-like behavior and jumps that extend over certain frequency values appear in all panels. Second, the height of the jumps increases, in general, either as P grows for a certain frequency or as f rises for a certain P value. In fact, three small jumps are distinguished below $f = 1.00$ GHz and two relatively significant ones are registered at $f = 1.84$ and 1.98 GHz at the lowest power [panel (a)]. Relevant jumps are observed at $f = 0.92$, 1.84 and 1.98 GHz for $P = 10$ dBm [panel (b)] and at $f = 0.92$ and 1.06 GHz for $P = 15$ dBm [panel (c)], while they appear only below $f = 1.00$ GHz, at 0.70 and 0.92 GHz, for $P = 20$ dBm [panel (d)]. Third, the number of significant jumps depends on P . As an example, four jumps appear at $f = 0.70$, 0.92 , 1.06 , and 1.84 GHz for $P = 15$ dBm [panel (c)], whereas only two are realized at $f = 0.70$ and 0.92 GHz for $P = 20$ dBm [panel (d)]. Thus, the jumps tend to disappear at high frequency with the enhancement of P . Finally, a transition to the normal state ($M = 0$) occurs for the highest values of P at frequencies close to 2.00 GHz [panel (c)] and 1.00 GHz [panel (d)]. It is worthwhile noting that the magnetic moment response is, in general, similar when it is recorded while increasing or decreasing the frequency (not shown here), although the heights of the jumps that appear at similar frequency values in both cases are slightly different, whereas the plateaus appear independently of the sweeping direction.

4.3.3 Frequency-driven instability: MgB_2

Figure 4.9 illustrates the time evolution of the MW-free magnetic moment obtained for MgB_2 at $T = 18.0$ K and $H_{\text{dc}} = 25$ Oe. This curve evidences a smooth vortex penetration, as it is usual in non-irradiated superconducting samples.

Figure 4.10 pictures the magnetic moment of MgB_2 registered as a function of

4. Vortex instabilities driven by microwave fields

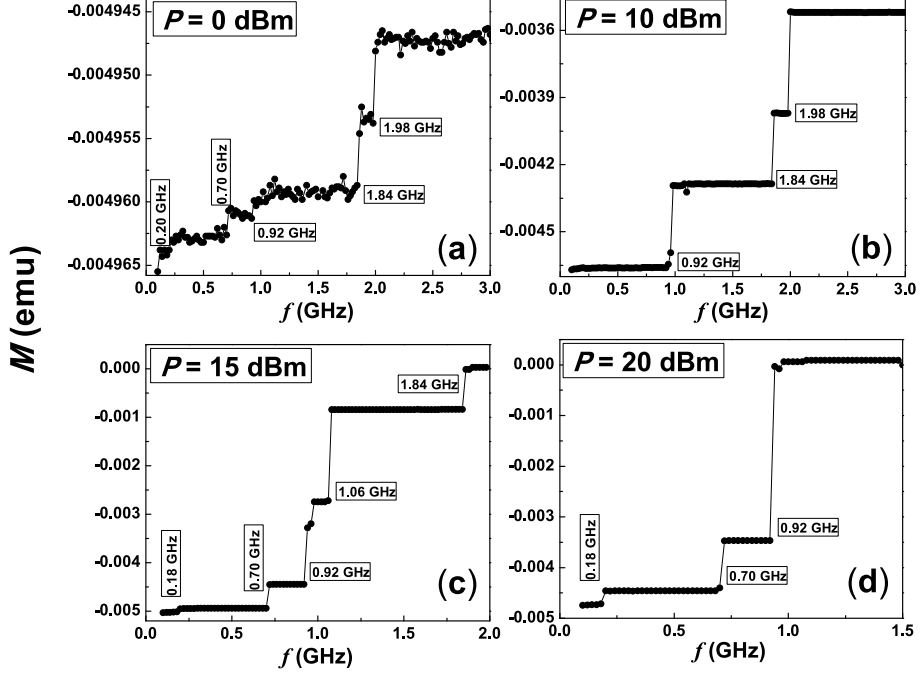


Figure 4.8: Magnetic moment registered as a function of microwave frequency at $T = 4.0$ K and $H_{\text{dc}} = 10$ Oe when the sample of patterned Pb was irradiated with different values of nominal power: $P = 0$ dBm (a), 10 dBm (b), 15 dBm (c), and 20 dBm (d).

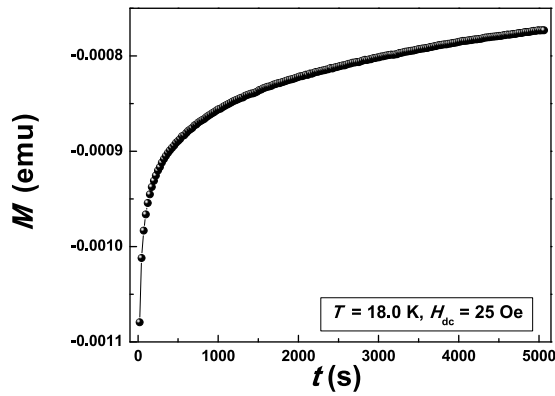


Figure 4.9: Time-dependent microwave-free magnetic moment recorded for MgB_2 at $T = 18.0$ K and $H_{\text{dc}} = 25$ Oe.

4. Vortex instabilities driven by microwave fields

the MW frequency and time at $P = -5$ dBm ($\simeq 0.3$ mW) under $H_{\text{dc}} = 100$ Oe for two different T values, 16.0 K and 17.0 K [panel (a)], and under $H_{\text{dc}} = 250$ Oe at the same temperatures [panel (b)]. It is found that the smooth evolution of the magnetic moment in a parabolic-like way, as the one plotted in Fig. 4.9, is disrupted by a ripple-like behavior that appears from $f = 1.76$ GHz on for $T = 16.0$ K and $H_{\text{dc}} = 100$ Oe [upper curve, panel (a)], while for $T = 17.0$ K, the onset of the ripples is shifted to higher frequency value, namely from $f = 2.66$ GHz on for the same H_{dc} [lower curve, panel (a)]. In both cases, the ripples become diffused as the frequency increases. Less pronounced ripples at similar f values and a sudden change in the slope of the magnetization curve at $f = 3.28$ GHz are reported in the upper curve of panel (b) at $T = 16.0$ K and $H_{\text{dc}} = 250$ Oe, whereas in the lower curve of panel (b) only a less steep slope at $f = 2.54$ GHz in the monotonous response is reported at $T = 17.0$ K. In these plots, it is noticed that by changing the system temperature in 1 K (from 16.0 to 17.0 K) at $H_{\text{dc}} = 100$ Oe, the value of f at which the first ripple comes to light is delayed, at the same time that the onset of the change in the slope of the magnetization curves at $H_{\text{dc}} = 250$ Oe is anticipated. By augmenting T or H_{dc} further, only a gradual relaxation of the flux gradient was registered (not shown here).

Similar results are reported in Fig. 4.11, where the magnetic moment is presented as a function of the MW frequency at $P = 0$ dBm (1.0 mW) for the same T values as the ones used above, 16.0 K [panel (a)] and 17.0 K [panel (b)], under $H_{\text{dc}} = 25$ and 100 Oe (upper and lower curves in all panels, respectively). Panel (a) shows that the ripple-like behavior sets in at $f = 1.94$ and 2.14 GHz for $H_{\text{dc}} = 25$ Oe (upper curve) and 100 Oe (lower curve), severally. In panel (b), the ripples are shown from $f = 2.52$ GHz on for $H_{\text{dc}} = 25$ Oe (upper curve), and from $f = 2.94$ GHz on for $H_{\text{dc}} = 100$ Oe (lower curve). Here, when the system temperature rises 1 K (from 16.0 to 17.0 K), the value of f at which the first ripple manifests is delayed for both magnetic fields. Comparing these results with the previous ones, we see that this delay is also observed varying the nominal MW power (from -5 to 0 dBm) at identical T for $H_{\text{dc}} = 100$ Oe. Therefore, it appears that the rise of the ripples at these two nominal MW powers is a function of the system temperature, so that an enhancement in T implies an increase in the frequency

4. Vortex instabilities driven by microwave fields

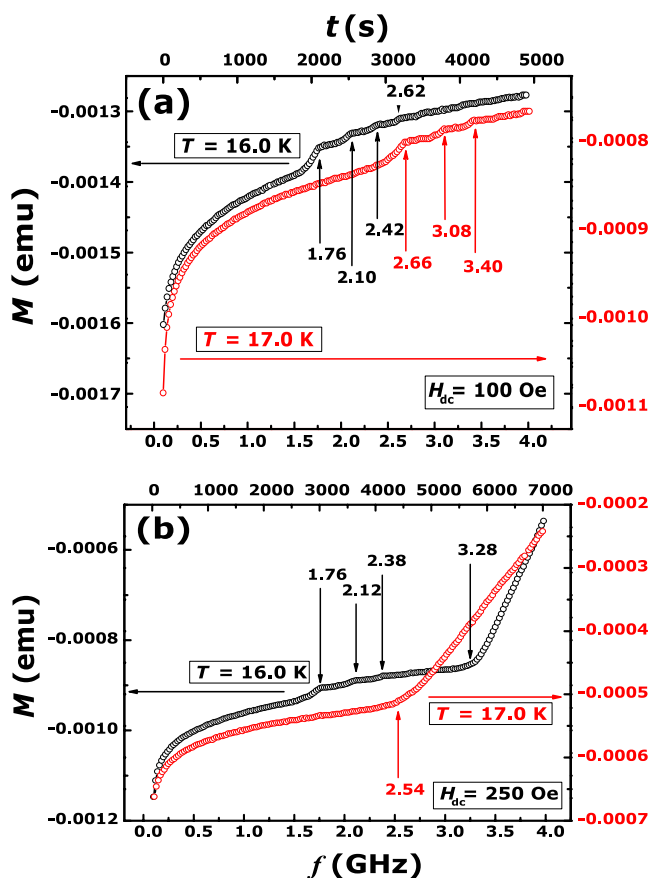


Figure 4.10: Magnetic moment registered as a function of microwave frequency and time when MgB_2 was irradiated with microwaves of $P = -5$ dBm for $H_{dc} = 100$ Oe at two different system temperature values, $T = 16.0$ K (upper curve) and $T = 17.0$ K (lower curve) (a), and for $H_{dc} = 250$ Oe at identical temperatures (b). The labels correspond to frequency values in GHz units.

4. Vortex instabilities driven by microwave fields

at which the ripples first come into sight. The delay seems to be conditioned by the magnetic field in a similar way.

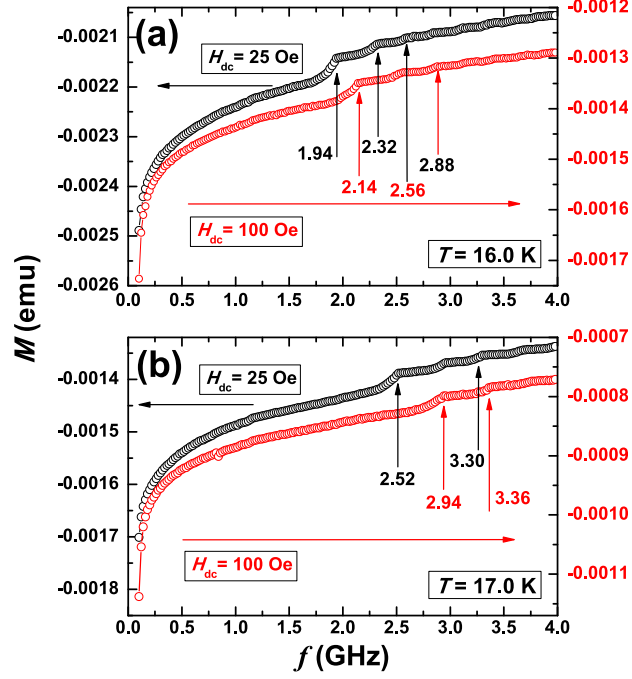


Figure 4.11: Magnetic moment registered as a function of microwave frequency when MgB_2 was irradiated with microwaves of $P = 0$ dBm at two different system temperatures, $T = 16.0$ K [panel(a)] and 17.0 K [panel(b)], for $H_{\text{dc}} = 25$ Oe and 100 Oe (upper and lower curves, respectively). The labels correspond to frequency values in GHz units.

Figure 4.12 shows the magnetic moment of MgB_2 registered as a function of the MW frequency at $P = 5$ dBm ($\simeq 3.2$ mW) for three different temperature values, $T = 16.0$ K [panel (a)], $T = 17.0$ K [panel (b)] and $T = 19.0$ K [panel (c)], under $H_{\text{dc}} = 25$ and 100 Oe (upper and lower curves in all panels, respectively). In panel (a), the magnetic moment follows a parabolic-like response as f increases until it is modified by small steps that appear at $f = 1.02$ GHz and extend up to 2.10 GHz for $H_{\text{dc}} = 25$ Oe (upper curve), and up to 1.90 GHz for $H_{\text{dc}} = 100$ Oe (lower curve), after which a smooth behavior is observed. Steps at similar f values and an additional variation of the slope at $f = 3.34$ GHz are registered

4. Vortex instabilities driven by microwave fields

at $T = 17.0$ K [panel (b)] for $H_{\text{dc}} = 25$ Oe (upper curve), while extra steps appear from $f \simeq 2.54$ GHz for $H_{\text{dc}} = 100$ Oe (lower curve). By enhancing the system temperature up to 19.0 K [panel (c)], the onset of the steps shifts to lower frequency values ($f = 0.78$ GHz), and a small dip precedes each step from 1.96 GHz on for $H_{\text{dc}} = 25$ Oe (upper curve), whereas small negative peaks are reported from 1.04 GHz on for $H_{\text{dc}} = 100$ Oe (lower curve). Moreover, at this temperature an almost flat response ensues after every step for both magnetic field intensities. By comparing these results with those plotted in Figs. 4.10 and 4.11, a change from ripple- to step-like response and the appearance of dips before the steps are verified. Moreover, contrary to the upward shift observed in Figs. 4.8 and 4.9 as either T or H_{dc} increase, the frequency values at which the irregularities come forth remain mostly invariant in Fig. 4.12, independently of changes in T and H_{dc} .

Figure 4.13 presents the magnetic moment of MgB_2 registered as a function of the MW frequency at $P = 10$ dBm (10.0 mW) for three different temperature values, $T = 16.0$ K [panel (a)], 17.0 K [panel (b)] and 19.0 K [panel (c)], under $H_{\text{dc}} = 25$ and 100 Oe (upper and lower curves in all panels, respectively). In the upper curve of panel (a), the parabolic-like response is first disrupted by a small step at $f = 0.78$ GHz and afterward it is altered by two significant jumps at $f = 1.02$ and 1.12 GHz, while a final small jump occurs at $f = 1.94$ GHz. Such notable jumps also occur in the lower curve of the same panel at identical f values, while a shallow negative peak appears at $f = 2.12$ GHz. In both curves, every step or jump is followed by a flat section, and a plateau-like response is observed after f is further enhanced beyond 2.12 GHz. In panel (b), the main jumps happen at similar frequency values for $H_{\text{dc}} = 25$ Oe (upper curve), and for $H_{\text{dc}} = 100$ Oe (lower curve). In this case, a new jump appears at $f = 2.12$ GHz for the lower field and turns into a small step for the higher one, and shallow negative peaks emerge at $f = 1.02$ and 1.94 GHz under $H_{\text{dc}} = 100$ Oe. In panel (c), the jumps rise in a less significant way at $f = 1.02$ and 1.12 GHz for $H_{\text{dc}} = 25$ Oe (upper curve) and 100 Oe (lower curve), respectively, and only small deviations are observed at higher frequency values. Similarly to the effect already discussed in Fig. 4.12, the frequencies at which the steps, the negative peaks and the jumps

4. Vortex instabilities driven by microwave fields

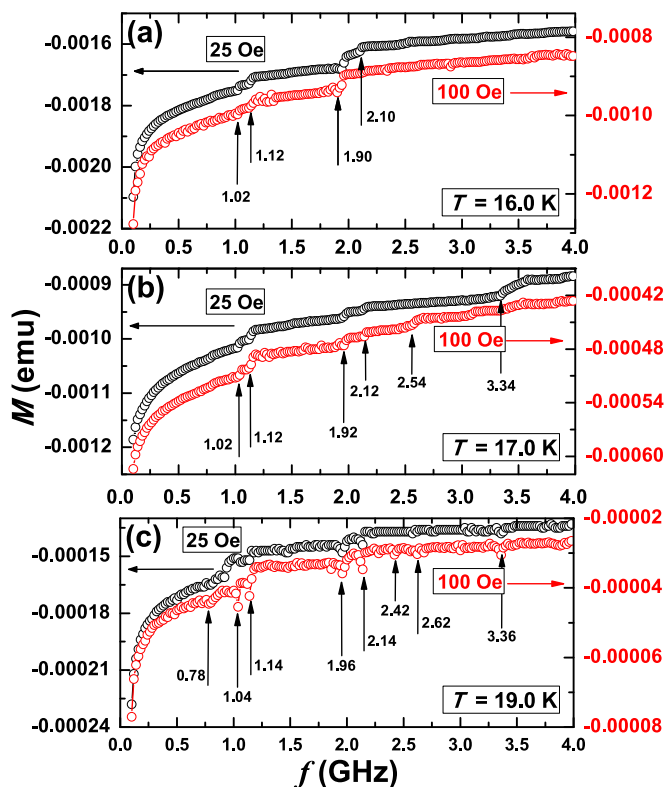


Figure 4.12: Magnetic moment registered as a function of microwave frequency when MgB_2 was irradiated with microwaves of $P = 5$ dBm at three different system temperature values, $T = 16.0$ K [panel (a)], 17.0 K [panel (b)] and 19.0 K [panel (c)], for $H_{dc} = 25$ and 100 Oe [upper and lower curves in all panels, respectively]. The labels correspond to frequency values in GHz units.

4. Vortex instabilities driven by microwave fields

come into view remain almost invariant when T or H_{dc} change. As T or H_{dc} are further enhanced, the steps and jumps become insignificant and only very shallow negative peaks, as the ones observed in Fig. 4.12, are reported (not shown here).

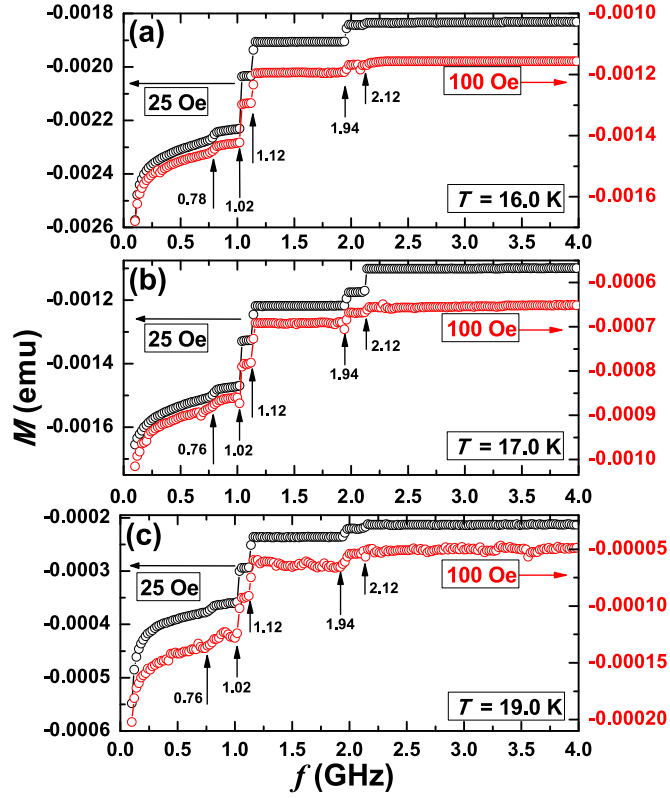


Figure 4.13: Magnetic moment registered as a function of microwave frequency when MgB_2 was irradiated with microwaves of $P = 10$ dBm at three different system temperature values, $T = 16.0$ K [panel (a)], 17.0 K [panel (b)] and 19.0 K [panel (c)] for $H_{\text{dc}} = 25$ and 100 Oe [upper and lower curves in both panels, respectively]. The labels correspond to frequency values in GHz units.

4.3.4 Microwave-frequency-driven vortex instabilities

In order to elucidate the mechanism that causes the irregularities to occur in the frequency-dependent magnetic moment curves, we first bear in mind the char-

4. Vortex instabilities driven by microwave fields

acteristics of the cs resonant structure and the MW energy density associated with the resonance modes. The frequency-swept spectra acquired in continuous mode, $|S_{11}(f)|$, for each sample (see for instance Fig. 3.9), exhibited resonant peaks at similar frequency values at which the anomalies have been reported. At each resonant frequency, f_0 , a significant amount of MW energy is fed into the cs (the MW power transmitted to the coil may be expected to increase at f_0 as a result of the cancellation of the reactive part of the intrinsic electric parameters of the resonant circuit [138]) and standing electromagnetic waves form and remain a certain time. The decay time of the energy stored at each mode [131] $1/\eta = Q/(2\pi f_0)$, has been estimated to range from 15 to 26 ns. These values, which are considerably smaller than the approximately 24 s it takes to register each M point, have been obtained considering that Q , calculated for various f_0 , varies between 30 and 500. This energy, which is expected to be in part dissipated at the surface of the copper coil and hence heat the cs, and in part absorbed by the sample, can be surmised to act as an external perturbation on the flux density gradient described by the Bean model [109] and modify the magnetic moment response accordingly.

There are two factors that hinder to establish with exactness the value of each energy fraction. The first is related with the complexity to set up with precision what quantity of MW power reaches the coil and what amount of heat energy is transferred to the thermal bath at each resonant mode. The second one is associated with the intricacy to establish the MW heating due to the highly nonlinear temperature dependence of the thermal parameters of the superconducting film and the substrate [51, 200, 227] as well as the particularities of the magnetic-field dependence of these parameters [231]. Nevertheless, despite these two conditions the observation of a MW-heating-induced breakdown of superconductivity at $P = 2$ dBm in MW reflection spectrometry experiments by using an analogous setup [232] suggests that a small increase of the sample temperature, T_s , is possible in the present situation even if heating effects are small. It is worthwhile recalling (see subsection 3.4.6 and cited references) that heating effects in superconducting thin films in the MW range under continuous and pulsed mode at different applied MW power fosters the downward shift of f_0 and the variation of Q as a function of P . Additionally, different effective MW powers absorbed by the sample, P_{eff} ,

4. Vortex instabilities driven by microwave fields

which depend on Q for the same incident P , have been obtained in real time under continuous mode [170, 233]. Another factor that leads to the same effect on f_0 and Q is the strong nonlinear behavior of the surface resistance as a function of P in HDC [170, 176, 234, 235, 236, 237], whose origin has been suggested to be vortex motion [234, 238] and local Joule heating [170, 176], among others.

The second consideration is the constriction imposed by the thin-film geometry on the flux penetration and the current distribution exposed in section 2.3, namely the weakened screening capacity, the large effective penetration depth, the less effectively screened local field around a vortex, and the long range repulsive interaction between vortices. All these factors facilitate the rise of a non-linear diffusion of the vortices from the edges toward the center of a thin film shape sample when a small fluctuation of the thermal forces, which depend on the temperature and the vortex density, may lead to strong fluctuations of the vortex positions at the border.

The third factor to keep in mind is the development of sudden bursts of flux penetration. As it was pointed out above (see section 4.1), all samples under study are susceptible to develop flux-jumping processes. Moreover, the existence of non-local electrodynamics in thin films [239] causes a considerable reduction in τ as compared to its bulk value [240],

$$\tau_f = \tau(th/\kappa)^{1/2}. \quad (4.7)$$

Here h is the heat transfer coefficient of the sample. This factor favors the nucleation of TEMI under the adiabatic heating approach ($\tau \ll 1$). It is worth mentioning that due to the strong influence of the cooling condition on the range of the flux jumps occurrence [47], and because of the lack of extensive experiments considering the critical state instability on thin film samples made of $\text{La}_{1.82}\text{Sr}_{0.18}\text{CuO}_4$ as compared with those of Pb and MgB_2 , our measurements were performed in a wide range of temperature ($0.30 < T/T_c < 0.85$) for the first case, whilst they were carried out at $T/T_c \simeq 0.55$ for patterned Pb. For MgB_2 the working temperature was above T_{th} ($T/T_c > 0.50$), where TEMI is expected not to be observed.

4. Vortex instabilities driven by microwave fields

Therefore, based on these considerations we can assume that the irregularities shown in the frequency-dependent magnetic moment response are associated with the presence of instabilities in the gradual penetration of the magnetic flux triggered by the MW energy density partially dissipated in the form of heat and partially absorbed by the sample at some specific resonant modes. Such instabilities would lead to different behaviors that could be associated with the development of different flux dynamics, from steady (ripples and small steps) to fast vortex diffusion or microavalanches (jumps). The different responses may be explained as follow. When the cs reaches one of its characteristic resonant frequencies, the energy stored inside is enhanced and the vortex configuration is thence perturbed. As a consequence, a significant amount of magnetic flux is suddenly induced to diffuse towards the sample center resulting in a jump-like response in the magnetic moment. This instability could result from the depinning of those vortices trapped at the sample edge driven by the energy of the resonance mode. As the input frequency keeps increasing and the resonance is left behind, the energy density in the setup should become smaller and a new nearly static stage akin to the previous one would be achieved after the jump.

On the basis of the first consideration pointed out above, we can assume that the perturbations driven at different f_0 values depend on the changes in real time of the characteristics of the resonant mode induced by MW heating and MW power losses. As a consequence, the features of the magnetic moment response at these discrete frequency values under different fixed parameters, including T , H_{dc} and P , would be conditioned by these deviations. This assumption could clarify the shift of the relevant jump to lower f values in $\text{La}_{1.82}\text{Sr}_{0.18}\text{CuO}_4$ (Fig. 4.6) and patterned Pb (Fig. 4.8), as P increases, as well as the different features (ripples, steps and jumps) and the delay in the onset of ripples as a function of T and P that appear in MgB_2 (see Figs. 4.10 – 4.13).

The almost flat phases between anomalies and the plateau-like behavior could be related with the existence of a metastable vortex state which would result from either a dynamic equilibrium, which sets up when a perturbation is balanced by relaxation and heat diffusion, or a frozen magnetic flux profile that settles after the MW-frequency-induced event terminates. In the particular case of Pb, the presence of a nanosized antidot lattice leads to effective vortex trapping [24], so

4. Vortex instabilities driven by microwave fields

that the flux movement in the sample is seriously conditioned by the artificial pinning structure. Actually, since the applied dc magnetic field ($H_{\text{dc}} = 10.0$ Oe) is close to the first matching field ($H_1 = 9.2$ Oe), we may expect that most of the vortices are initially locked in the antidots or in interstitial sites as the frequency starts to increase. Thus, we can surmise that only a few vortices move throughout the sample before and after a resonance is matched, and thus the sample magnetization remains mostly invariant and a plateau-like behavior is recorded. In addition to the factors referred before, we suggest that the nucleation of this vortex instability should depend also on the intensity of the applied magnetic field. In fact, for high H_{dc} the small distance between vortices should permit the formation of a rigid flux lattice which would result very stable against an external perturbation, whereas for low H_{dc} , when the flux lattice is rather loose, the disturbance would become effective and the vortex runaway would be activated. The former case (high H_{dc}) can contribute to explain the deviations reported for $\text{La}_{1.82}\text{Sr}_{0.18}\text{CuO}_4$ in Fig. 4.7, and the latter one (low H_{dc}) would help to describe the irregularities in the flux penetration observed in Fig. 4.5 and 4.6.

To give an explanation of the different features of the induced breakaway in the relaxing magnetic moment as a function of T and P , some temperature-dependent parameters can provide a useful hint for $\text{La}_{1.82}\text{Sr}_{0.18}\text{CuO}_4$ and Pb . The appearance of jumps up to $T/T_c \simeq 0.74$ [Figs. 4.5 and 4.6] and for $T/T_c \simeq 0.56$ (Fig. 4.8) would be favored by both the high local J_c and the small values of κ and h at these temperatures [200, 227]. The heat produced by the MW-driven vortex motion would thus propagate faster than the heat conduction to the outside, the superconductivity would become locally suppressed and easy paths for the penetration of additional magnetic flux would be created. As for MgB_2 , we propose that the onset and the details of the instabilities are conditioned by the magnitude of the input MW power and the values of the temperature. Indeed, the gradual relaxation process observed at $T = 16.0$ and 17.0 K for the lowest P (-5 and 0 dBm) is only slightly disturbed and a ripple-like response is registered at certain frequency modes [Figs. 4.10(a) and 4.11]. The presence of a linear growth of the relaxation above $f = 2.50$ GHz at these temperatures for $H_{\text{dc}} = 250$ Oe [Fig. 4.10(b)] might be related with sample heating proportional to the frequency (eddy current heating). By rising P (5 dBm), the intensity of the perturbation

4. Vortex instabilities driven by microwave fields

is enhanced and the ripple-like instabilities turn into steps (Fig. 4.12). Finally, by increasing P further (10 dBm), the intensity of the MW-induced disturbance becomes more important and a jump-wise response develops (Fig. 4.13). In this case, the presence of such flux instability seems to be driven by a normal hot spot generated by the MW perturbation. Actually, it has been demonstrated that by rising the temperature locally it has been possible to induce a vortex depinning at the sample edge that results in a fast flux diffusion toward the center of the sample [60].

The presence of dips preceding the jumps in $\text{La}_{1.82}\text{Sr}_{0.18}\text{CuO}_4$ near T_c [Figs. 4.2(a), 4.3, and 4.5(c)] or in MgB_2 well below T_c at the highest P values [Figs. 4.12(c) and 4.13], could reveal the occurrence of flux magnetic motion in the opposite direction to the fast vortex diffusion in the interval of time before the vortex instability takes place. These dips, reported previously both in shielding and flux-trapping regimes [241], have been proven to be connected with the existence of a nonlinear Meissner effect, which results from the bending of the flux magnetic lines around the film and the presence of a high surface barrier, and allow superconductors to persist in a metastable state [242, 243]. In this state, the superconducting order parameter near the sample surface reduces as H_{dc} increases, and this facilitates the accumulation of magnetic flux in the near-edge layer [244]. As it was mentioned in section 2.3, thin films of finite size are characterized by the occurrence of a strong local magnetic field at the sample edge [245]. Thus, under this scenario we surmise that a frequency-induced vortex depinning process takes place in $\text{La}_{1.82}\text{Sr}_{0.18}\text{CuO}_4$ close to T_c [Figs. 4.2(b) and 4.5(b)] or under high H_{dc} (Fig. 4.7). At this stage the magnetic flux expelled from the near-edge layer dominates over the flow of vortices that penetrate the sample and therefore negative peaks develop. The height of these peaks is determined by the competition of these two flows. The creation of such response could also be favored by the aforementioned strong repulsive vortex-vortex interaction that exists in thin-film geometry.

In order to examine the role of the resonant structure formed by the cs in the nucleation of the flux instability we will explore the significance of the MW electric (E_{MW}) and magnetic (H_{MW}) fields at the resonant modes of interest. By using the helical approach previously suggested (see subsection 3.4.6) an estimation

4. Vortex instabilities driven by microwave fields

on the order of 10^2 – 10^3 V/m for the parallel and perpendicular components of E_{MW} at the edge of the cs is obtained by considering reference values for P (10 dBm), Q (50) and f_0 (0.78, 1.00, 1.36 and 2.00 GHz). Such figure is considerably higher than the background field induced by the magnetic-field variation in the flux-creep regime ($E_0 = 10^{-4}$ V/m) [211] and the electric field at full magnetic flux penetration in the Bean model ($E_p = 10^{-2}$ V/m) [245], and is akin to the number calculated for the local enhancement of the electric field due to microavalanches [229]. This extra E_{MW} field contributes to increment ρ_f due to the proportionality between these two magnitudes [246], giving as a consequence a decrease of τ , which in turn favors a positive feedback effect and the fulfillment of the adiabatic heating approximation for flux jump occurrence. Using again the helical approach, the components of H_{MW} were calculated to range between 50 and 100 mOe, a value which is similar to the amplitude of the rf magnetic field needed to induce vortex depinning and trigger flux avalanches in Pb superconducting films [60]. Such H_{MW} field can thus contribute to drive the metastable vortices located at the near-edge layer into an unstable state either by changing the penetration rate at which the magnetic flux invades the sample or by shaking vortices back and forth. Since the vortex instability becomes very sensitive to external parameters near the stable-unstable phase boundary, we can conjecture that a small change in an external parameter, as E_{MW} and H_{MW} , becomes critical for fast vortex diffusion to develop.

Finally, as it was exposed in section 4.2, the conventional theory of TEMI predicts uniform flux jumps where the flux front is essentially flat, i.e. the spatial extension of the instability region tends to be maximal since small-scale perturbations are stabilized by thermal diffusion. Moreover, it was pointed out in the same section that the dendritic instability of the vortex matter in thin superconducting films placed in a perpendicular magnetic field is a generic phenomenon which has been modeled in the framework of the nonlocal nonlinear magnetic flux diffusion coupled to thermal diffusion in thin films [200, 227, 240]. The thermal origin of such sample-spanning dendritic structure has been confirmed both experimentally [192, 219, 247, 248] and theoretically [58, 200, 227, 228, 240], and the existence of a large critical background electric field, $E_c \approx 10^{-1}$ V/m, for the development of this kind of instability has been shown [200, 227, 228]. Therefore, despite all

the data presented here could support the suggestion that the frequency-induced instability found could emerge in nonuniform flux distribution, additional experiments that allow the visualization of the spatial distribution of the magnetic flux before and after the breakdown, and provide insight to the time-resolved behavior of flux propagation, are required to give extended information about the results exposed here.

4.4 Vortex dynamics under pulsed microwave mode

In this section, we present studies of flux penetration in the dynamic case by registering at low temperature the temporal variation of the magnetization when a static dc magnetic field plus a single MW pulse is applied. The output voltage signals of the magnetometer used to perform the experiments show the existence of flux instabilities in the magnetic moment response of superconductor thin films made of $\text{La}_{1.82}\text{Sr}_{0.18}\text{CuO}_4$ and MgB_2 . The characteristic macroscopic avalanche-like signature in the form of a significant variation in the sample magnetization which occurs below certain threshold values of thermodynamic variables and MW parameters has been registered. On the other hand, by using this technique we have tried to avoid the important drawback in interpreting the vortex avalanche phenomenon by performing conventional magnetometry, that is to say the pause time before each magnetization data point is recorded. Actually, although during this time the magnetic field remains unchanged, the flux inside the superconductor continues evolving as a relaxation process, causing additional heating. Part of this heat is removed by the coolant, while the remainder compels the temperature of the superconductor to increase, and this may lead to the occurrence of an avalanche.

4.4.1 Avalanche-like vortex penetration: $\text{La}_{1.82}\text{Sr}_{0.18}\text{CuO}_4$

The temporal resolution measurements of the voltage generated by vortex motion when single MW pulses are applied at fixed values of H_{dc} and T was first performed on $\text{La}_{1.82}\text{Sr}_{0.18}\text{CuO}_4$ superconducting thin films. The temporal variation

4. Vortex instabilities driven by microwave fields

of the output voltage signal, $\Delta V(t)$, was collected from the rf-SQUID through a Signal Recovery Pre-Amp 1 Hz High Pass Filter (model 5113) with a temporal resolution of 0.1 ms during 200 ms, after either a zfc or fc process at constant value of MW frequency ($f = 0.90$ GHz), at different fixed values of H_{dc} , T , and MW perturbation sensing parameters (t_{pulse} and P), and plotted in the time domain scale of the oscilloscope (see Fig. 3.6). No differences in $\Delta V(t)$ were observed when the MW pulse was applied after either a zfc or a fc protocol, in good agreement with earlier reports on avalanche-like flux penetration in zfc mode in the magnetization isotherms, $M(H_{\text{dc}})$, in single crystals of $\text{La}_{2-x}\text{Sr}_x\text{CuO}_4$ [52, 208], and other superconductors [48, 189, 192, 194], or those performed in the remnant state by MOI [49, 202].

4.4.1.1 Magnetic field dependence

Figure 4.14 represents the temporal variation of the output voltage signal, ΔV , when MW pulses of $P = 15$ dBm ($\simeq 32$ mW) and $t_{\text{pulse}} = 15$ ms are applied at $T = 2.50$ K for different values of H_{dc} , from 50 to 350 Oe [panel (a)] and from 400 to 700 Oe [panel (b)]. Panels (c) and (d) show magnifications of the low-time range (0–100 ms) data of panels (a) and (b), respectively. The corresponding pulsed square wave is plotted in all panels as a reference (solid line).

$\Delta V(t)$ shows different stages which extend beyond the MW pulse duration. For the lowest value of the magnetic field, $H_{\text{dc}} = 50$ Oe [lowermost curve in panels (a) and (c)], four sections are distinguished. In the first one, before the application of the MW pulse, a flat behavior is observed. In the second one, a deviation from the initial null value appears as a small slope, which changes to a parabolic-like response in the third section, until a maximum, named here as ΔV_{total} , is reached. In the end, a plateau is achieved in the fourth section. At $H_{\text{dc}} = 100$ Oe, five different phases [labeled 1 to 5 for the second curve to bottom in panel (c)] can be identified. The initial, constant value of phase 1 is followed here in phase 2 by a more pronounced slope as compared with that described for $H_{\text{dc}} = 50$ Oe. Then, in phase 3 the signal grows noticeably during a short time interval in a steep, jump-like way up to a certain value, from now on defined as ΔV_{fast} , above which a new less conspicuous slope develops in phase 4. Finally, after ΔV_{total} as

4. Vortex instabilities driven by microwave fields

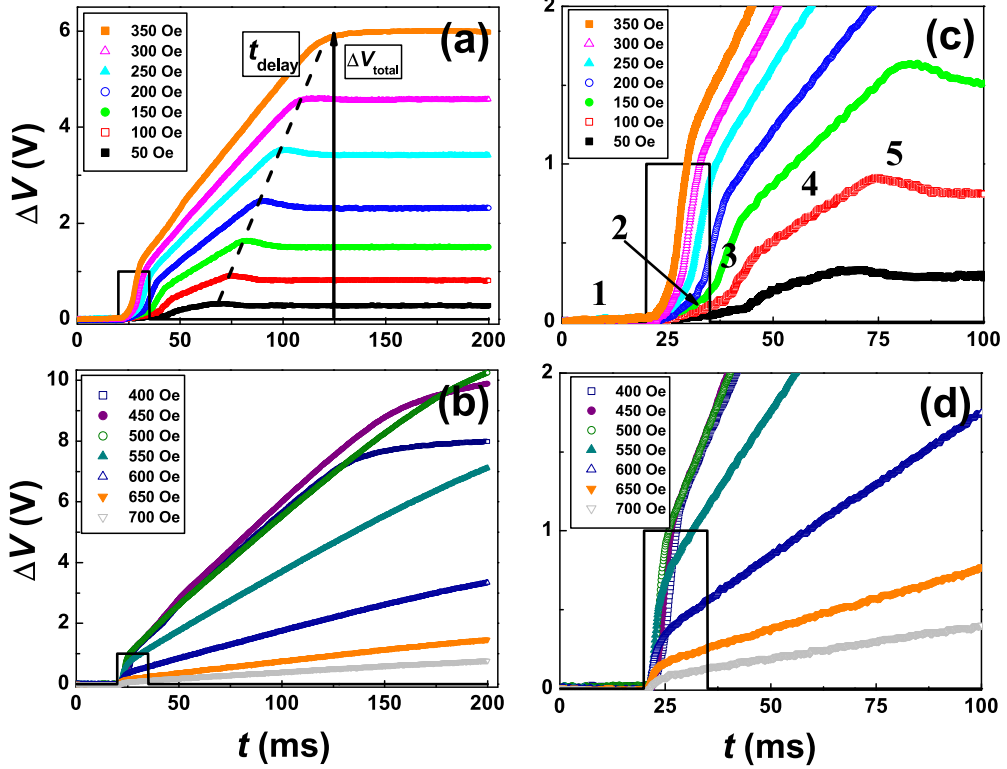


Figure 4.14: Time evolution of the rf-SQUID output voltage signal variation, $\Delta V(t)$, of $\text{La}_{1.82}\text{Sr}_{0.18}\text{CuO}_4$ when MW pulses of $P = 15$ dBm and $t_{\text{pulse}} = 15$ ms are applied at $T = 2.50$ K for different values of H_{dc} , from 50 to 350 Oe [panel (a)] and from 400 to 700 Oe [panel (b)]. Panels (c) and (d) show magnifications of the low-time data for panels (a) and (b), respectively (see legends for details). The corresponding pulsed square wave is shown in all panels as a reference (solid line).

4. Vortex instabilities driven by microwave fields

defined for $H_{\text{dc}} = 50$ Oe is overtaken, a smooth behavior is shown in phase 5. The presence of these five phases is observed in all curves as the magnetic field increases up to $H_{\text{dc}} = 500$ Oe, although the slopes become more prominent and result in higher values for both ΔV_{fast} and ΔV_{total} [panels (c) and (d)]. Furthermore, the occurrence of ΔV_{total} is delayed in a linear way as H_{dc} increases [see panel (a)]. Between $H_{\text{dc}} = 500$ and 700 Oe [panels (b) and (d)], $\Delta V(t)$ describes only two phases: the low-time fast one and a second stage with a slope that increases in a monotonous way and prolongs for most of the duration of the measurement. In this magnetic field regime, both ΔV_{fast} and the steepness of the curves decrease as H_{dc} increases. It is worth mentioning here that the existence of a small hump as $\Delta V(t)$ reaches its maximum value at the lowest magnetic fields (up to 250 Oe, approximately), is related rather with the filtering process than with the sample response.

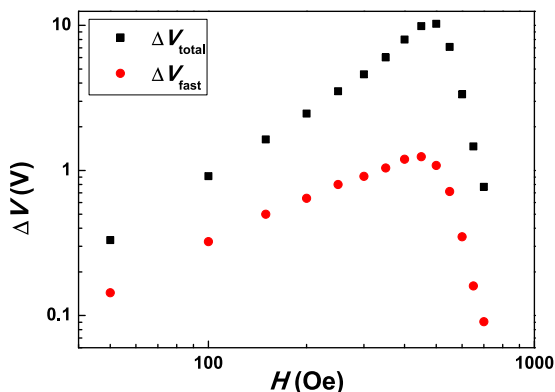


Figure 4.15: Magnetic-field dependence of the fast and total rf-SQUID output voltage signal variations, ΔV_{fast} (solid dots) and ΔV_{total} (solid squares), respectively, of $\text{La}_{1.82}\text{Sr}_{0.18}\text{CuO}_4$ at $T = 2.50$ K under MW pulses of $P = 15$ dBm and $t_{\text{pulse}} = 15$ ms.

The magnetic field dependence of the characteristic values of the output signal is depicted in logarithmic scale in Fig. 4.15. Here, ΔV_{total} (solid squares) increases up to $H_{\text{dc}} = 500$ Oe, where the curve reaches a maximum value of ~ 10.26 V, and eventually decreases rapidly down to ~ 0.77 V at $H_{\text{dc}} = 700$ Oe. For the highest fields, since ΔV_{total} is not observed in our temporal scale, we have chosen as a reference the maximum value of $\Delta V(t)$ measured at each magnetic field.

4. Vortex instabilities driven by microwave fields

As H_{dc} is further enhanced, no variation in $\Delta V(t)$ is observed, evidencing that there is an upper threshold field at which the MW-pulse-induced change in the flux penetration terminates. Additionally, Fig. 4.15 plots ΔV_{fast} (solid dots) as a function of the magnetic field. Similarly to ΔV_{total} , ΔV_{fast} grows nearly straight from ~ 0.14 V at $H_{\text{dc}} = 50$ Oe to ~ 1.25 V at $H_{\text{dc}} = 500$ Oe, and then drops suddenly to ~ 0.10 V at $H_{\text{dc}} = 700$ Oe.

4.4.1.2 Temperature dependence

Panel (a) in Fig. 4.16 presents the time dependence of ΔV for different values of temperature, from 2.00 K to 6.00 K, when MW pulses of $P = 15$ dBm and $t_{\text{pulse}} = 15$ ms are applied at $H_{\text{dc}} = 200$ Oe. At the lowest temperatures (2.00 K and 2.50 K), only a small monotonous growth, that reaches a small value of ΔV_{total} as defined in Fig. 4.14, is distinguished after the pulse application. From 3.00 K to 5.00 K, three phases can be told apart. The initial flat one before the pulse is followed by a second phase that achieves ΔV_{fast} , as described in Fig. 4.14, with a slope that increases with temperature. After ΔV_{total} is attained, a small decrement followed by a large plateau is obtained. At $T = 5.50$ K, the value of ΔV_{fast} is smaller than those shown at lower temperatures and a new phase that rises in a parabolic-like way is observed until ΔV_{total} is achieved at around 150 ms. Finally, at $T = 6.00$ K only a flat behavior is found.

The temperature dependence of ΔV_{total} (solid squares) and ΔV_{fast} (solid dots) is shown in panel (b) of this figure. ΔV_{total} increases from around $T = 3.00$ K up to a maximum at $T = 5.50$ K, and then decreases rapidly and disappears at around $T = 6.00$ K, indicating the existence of an upper threshold value of temperature at which the MW-pulse-induced fast flux front ceases. On the other hand, ΔV_{fast} grows as ΔV_{total} does, until it reaches a maximum at around $T = 4.50$ – 5.00 K and then decreases in an almost linear way down to $T = 6.00$ K. The filter effect on the voltage signal, as it was observed in Fig. 4.14, appears here in the temperature range between 2.00 K and 4.50 K.

4. Vortex instabilities driven by microwave fields

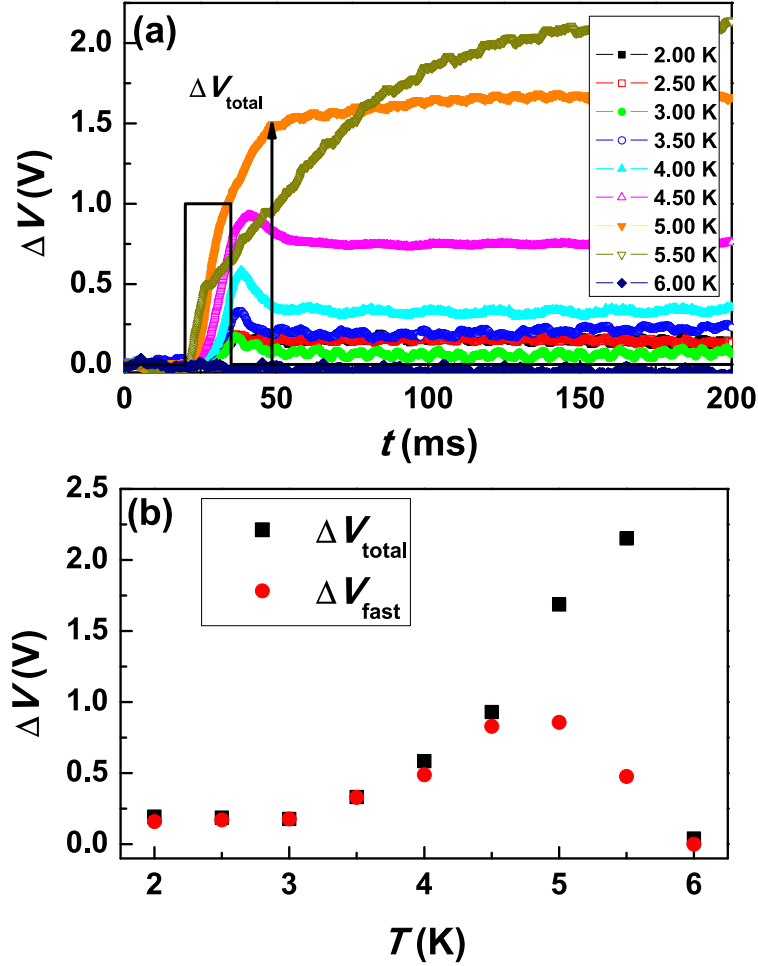


Figure 4.16: (a) Temporal dependence of the rf-SQUID output voltage signal variation, $\Delta V(t)$, of $\text{La}_{1.82}\text{Sr}_{0.18}\text{CuO}_4$ when MW pulses of $P = 15$ dBm and $t_{\text{pulse}} = 15$ ms are applied at $H_{\text{dc}} = 200$ Oe, for different values of temperature from 2.00 K to 6.00 K (see legend for details). The corresponding pulsed square wave is shown as a reference (solid line). (b) Temperature dependence of the fast and total rf-SQUID output voltage signal variation, ΔV_{fast} (solid dots) and ΔV_{total} (solid squares), respectively, as defined in panel (a).

4.4.1.3 Pulse duration dependence

Panel (a) in Fig. 4.17 shows the dependence of ΔV_{total} (solid squares) and ΔV_{fast} (solid dots), on t_{pulse} , for MW pulses of $P = 15$ dBm applied at $T = 2.50$ K and $H_{\text{dc}} = 200$ Oe. The behavior of $\Delta V(t)$ for $t_{\text{pulse}} = 25$ ms, which presents the different flux penetration phases as shown in Fig. 4.14 for different H_{dc} values, is plotted as an example in panel (b) of this plot. The maximum variation in the sample magnetization increases almost in a linear way with the enhancement of t_{pulse} from ~ 3 ms to ~ 40 ms, and then starts to decline and finishes at around 60 ms, demonstrating that the MW-pulse-induced instability depends also on the duration of the pulse. On the other hand, ΔV_{fast} [phase 3 in panel (b)] reaches a maximum slightly before 10 ms and then remains almost constant up to about 35 ms, when it starts to decrease slowly and finally vanishes at around 60 ms. As it is observed in panel (b), ΔV_{fast} is followed by a long relaxation process until a maximum in the voltage variation is achieved.

4.4.1.4 Power dependence

Panel (a) in Fig. 4.18 plots the time dependence of ΔV for different values of nominal power, from 9 dBm ($\simeq 8$ mW, lowermost curve) to 19 dBm ($\simeq 80$ mW, uppermost curve) in steps of 0.5 dBm, when MW pulses of $t_{\text{pulse}} = 15$ ms are applied at $H_{\text{dc}} = 500$ Oe and $T = 2.50$ K. The corresponding pulsed square wave is plotted as a reference (dashed line).

The behavior of the $\Delta V(t)$ curves is similar, in general, to that shown in panel (a) of Fig. 4.14: a flat initial phase previous to the pulse is followed by a smooth slope, after which a jump-like phase takes place until a new stage with a reduced slope appears, and a maximum that leads to a final plateau is reached. In this plot, ΔV_{total} seems to be completed relatively earlier with the enhancement of P for the lowest powers up to around $P = 10$ dBm (10 mW). Above this power value, ΔV_{total} is fulfilled with a considerable delay. Here, the effect of the filter on the voltage response as it was defined in Fig. 4.14 is significant for $P \simeq 10.5$ –15.5 dBm (around 11–35 mW). Panel (b) in this figure shows in semilogarithmic scale the nominal power dependence of ΔV_{total} as defined in panel (a), for $H_{\text{dc}} = 200$ Oe (solid dots) and $H_{\text{dc}} = 500$ Oe (solid squares). In accordance with the results

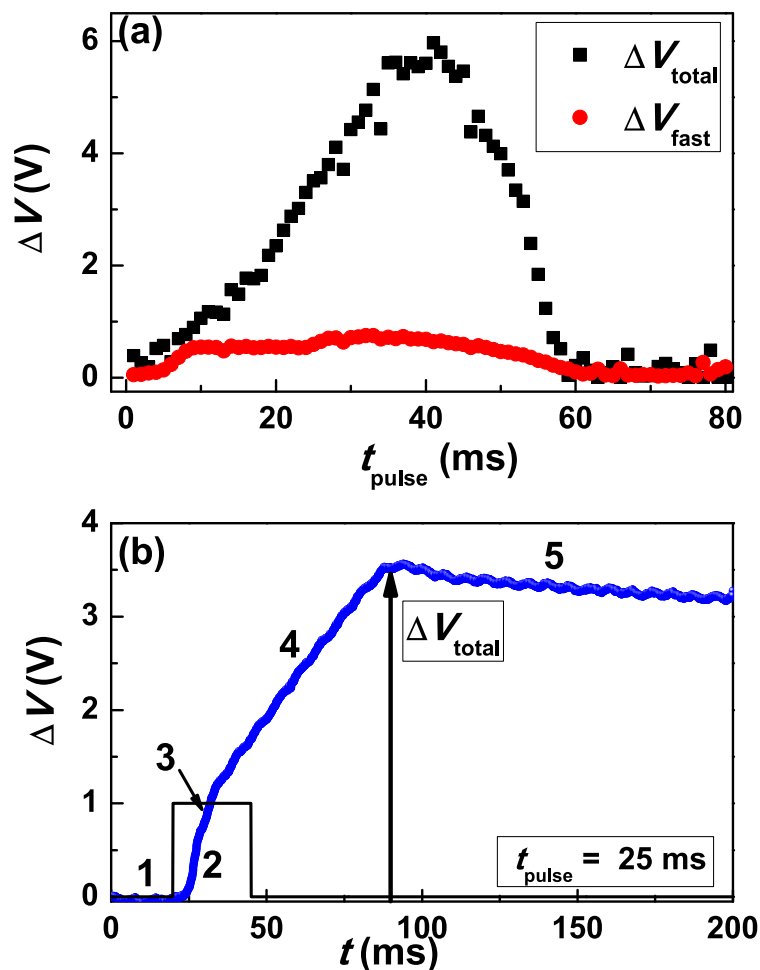


Figure 4.17: (a) Pulse duration dependence of the fast and total rf-SQUID output voltage signal variation, ΔV_{fast} (solid dots) and ΔV_{total} (solid squares), respectively, of $\text{La}_{1.82}\text{Sr}_{0.18}\text{CuO}_4$ for MW pulses of $P = 15$ dBm, at $T = 2.50$ K and $H_{\text{dc}} = 200$ Oe. (b) Temporal dependence of the voltage signal variation, $\Delta V(t)$, generated at $t_{\text{pulse}} = 25$ ms. The corresponding pulsed square wave is shown as a reference (solid line).

4. Vortex instabilities driven by microwave fields

obtained in Fig. 4.14 for $P = 15$ dBm, now the value of ΔV_{total} for $H_{\text{dc}} = 500$ Oe is larger than that for $H_{\text{dc}} = 200$ Oe at any P value. In both cases, as P increases, ΔV_{total} grows to achieve a maximum around $P = 15\text{--}16$ dBm ($\simeq 32\text{--}40$ mW), after which it stays almost constant for $H_{\text{dc}} = 200$ Oe, whereas it shows a short growth until a new smooth regime appears for $H_{\text{dc}} = 500$ Oe. Since the power received by the sample is reduced in 30 dB with respect to the input nominal power by the losses in the cable and connectors, it seems reasonable that the MW-pulse-induced fast flux movement does not appear until a significant value of P is realized.

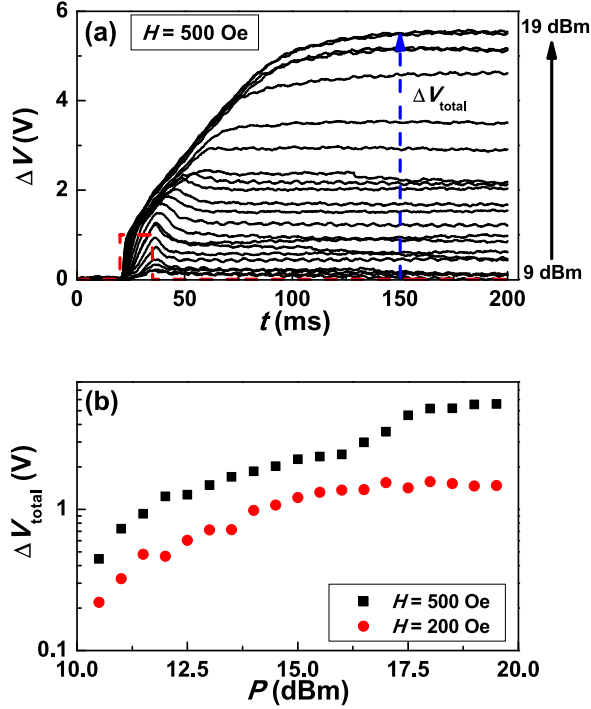


Figure 4.18: (a) Temporal dependence of the rf-SQUID output voltage signal variation, $\Delta V(t)$, of $\text{La}_{1.82}\text{Sr}_{0.18}\text{CuO}_4$ when MW pulses of $t_{\text{pulse}} = 15$ ms and different nominal powers, from 9 dBm (lowermost curve) to 19 dBm (uppermost curve), are applied at $H_{\text{dc}} = 500$ Oe and $T = 2.50$ K. (b) Nominal power dependence of the total rf-SQUID output voltage signal variation as defined in panel (a), ΔV_{total} , for $H_{\text{dc}} = 200$ Oe (solid dots) and $H_{\text{dc}} = 500$ Oe (solid squares).

4.4.1.5 MW-pulse-induced instabilities: $\text{La}_{1.82}\text{Sr}_{0.18}\text{CuO}_4$

Since $\Delta V(t)$ actually reflects the temporal variation of the sample magnetization, we can associate the MW-pulse-induced voltage signal with the time-resolved behavior of the flux penetration which occurs in different phases. Thus the smooth phase before the pulse is applied can be ascribed in all figures shown in this section to a slow and steady vortex diffusion which follows the Bean-like profile. By applying a MW pulse, the initial profile is perturbed so that a rapid flux front is induced and a new phase appears. This flux motion increases the local temperature, reducing therefore the critical current density and triggering further vortex motion. This feedback produces an enhancement of the amount of vortices that enter the sample rapidly, and leads to the achievement of ΔV_{fast} . This MW-assisted flux penetration is extended in a subsequent phase, but this happens at reduced velocity as the vortices move through the sample, and finally ceases at ΔV_{total} . Two different effects, namely intrinsic pinning and heat transfer from the film to the substrate and the coolant, could be behind the reduction in the vortex propagation.

Moreover, we cannot rule out the contribution that may come from the flux creep effect in this rather long phase and the delay to reach ΔV_{total} as the magnetic field [see Fig. 4.14(a)], the temperature [see Fig. 4.16(a)], or the power increase [see Fig. 4.18(a)]. As a matter of fact, the flux creep would change the flux profile inside the sample and thus the shape of $\Delta V(t)$. Finally, the flat response observed in the last phase could be referred either to gradual vortex propagation, with a slower dynamics with respect to the fast flux penetration, or to the existence of a magnetic field profile which remains frozen once the flux stops spreading. More information about this apparently smooth magnetic variation should be obtained from MOI, where the spatial distribution of vortices at this stage could be captured with high time resolution.

Our measurements show that the slopes of the different sections in the $\Delta V(t)$ curves change with the magnetic field (Fig. 4.14), the temperature [Fig. 4.16(a)], the pulse duration [Fig. 4.17(b)], and the power [Fig. 4.18(a)]. As H_{dc} is enhanced from 50 Oe up to 500 Oe, the slopes get more pronounced and ΔV_{total} increases suggesting that a higher density of vortices is driven from the edge towards the

4. Vortex instabilities driven by microwave fields

center of the sample with the rise of the magnetic field. The reduction of ΔV_{fast} , and consequently of the slope of $\Delta V(t)$, above $H_{\text{dc}} = 500$ Oe implies that the MW-pulse-assisted flux motion becomes less effective at these intensities.

Similarly, as T increases from 3.00 K to 5.00 K, the slopes become significant meaning that there is a range of intermediate temperatures at which the fast vortex motion could be MW-pulse-assisted. A comparable behavior has been also registered for the $\Delta V(t)$ curves acquired for values of t_{pulse} between 10 ms and 45 ms. Not surprisingly, the range of fast flux occurrence appears conditioned by the duration of the pulse since as t_{pulse} increases, so it does the excitation time that is needed to maintain this assisted motion. Nevertheless, the existence of a maximum value in t_{pulse} suggests that once it is reached, a further enhancement of the pulse duration will imply a longer time for the sample to transfer the heat to the environment giving as a consequence a reduction in the rapid flux penetration. We cannot rule out either the contribution to this diminution that may come from the relaxation of the magnetic moment of the sample.

4.4.2 Avalanche-like vortex penetration: MgB_2

In this section, we expose the results of flux penetration under dynamic conditions performed on thin superconducting films made of MgB_2 . The time-dependence of the output voltage signal, $\Delta V(t)$, was obtained with the experimental pulsed mode setup but without the High Pass Filter (see Fig. 3.6), with a time resolution of 0.5 ms, during 1000 ms after either a zfc and fc mode, at constant values of $f = 1.94$ GHz and $P = 15$ dBm, at different fixed values of H_{dc} (from 0 to 700 Oe), in the temperature range $T = 2.00\text{--}20.00$ K, and for different values of t_{pulse} in the range 100–600 ms.

4.4.2.1 Temperature and pulse duration dependences

Figure 4.19 shows examples of the jumps registered in the output voltage signal from the rf-SQUID as a function of time, $\Delta V(t)$, after a zfc mode for different values of temperature (from 3.00 to 6.50 K), and $H_{\text{dc}} = 20$ Oe, when pulsed square waves of $t_{\text{pulse}} = 100$ and 600 ms [dashed lines in panels (a) and (b), respectively] were applied. The height of the jump, that is the total variation of ΔV (named

4. Vortex instabilities driven by microwave fields

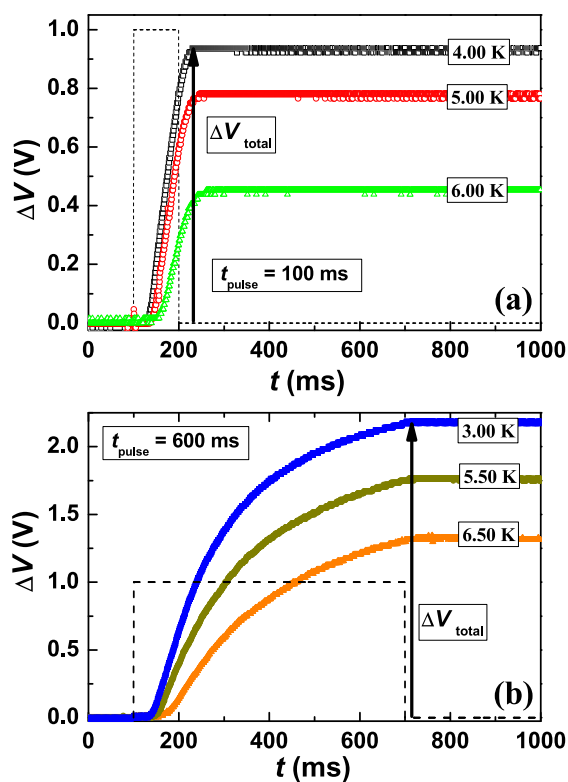


Figure 4.19: Time dependence of the rf-SQUID output signal variation, ΔV , of MgB₂ obtained at $H_{\text{dc}} = 20$ Oe applying single MW pulses with $P = 15$ dBm, $f = 1.94$ GHz and either $t_{\text{pulse}} = 100$ ms at $T = 4.00, 5.00$ and 6.00 K (from top to bottom) [panel (a)], or $t_{\text{pulse}} = 600$ ms at $T = 3.00, 5.50$ and 6.50 K (from top to bottom) [panel (b)], together with the corresponding pulsed square waves (dashed lines in both panels).

4. Vortex instabilities driven by microwave fields

here as ΔV_{total}), and the time it takes to occur are irreproducible under the same initial measurement conditions suggesting that the jumps emerge in a stochastic way. The height and the shape of the jump are observed to depend on the temperature and the duration of the pulse, namely the highest jumps occur at the lowest T for both t_{pulse} values [see the uppermost curves in panels (a) and (b)]. Fig. 4.20 presents the 10-times-averaged ΔV_{total} as a function of temperature at $H_{\text{dc}} = 20$ Oe, under MW pulses with different values of t_{pulse} from 100 to 600 ms in steps of 100 ms. By comparing the different curves, ΔV_{total} is found to depend increasingly on t_{pulse} , so that the longer the pulse duration the larger the induced jump. For all t_{pulse} values, ΔV_{total} increases in a non-monotonous way with temperature up to 4.00–4.50 K, after which it decreases gradually. The appearance here of a peak more or less at the same temperature for the different values of t_{pulse} suggests that the pulse-induced voltage has a non thermal origin. The dependence on temperature, however, could be conditioned by other parameters such as the heat transfer from the thin film to the substrate and the coolant [200], the local critical current density [45, 200], and the vortex dynamics [45]. Finally, the presence of the jumps beyond $T_{th} = 10.00$ K (the upper threshold temperature for the formation of TEMI in thin films made of MgB₂), is in agreement with the possibility for observing flux jumping above 12.00 K [213].

4.4.2.2 Magnetic field and pulse duration dependencies

Figure 4.21 plots the magnetic field dependence of the 20-times-averaged ΔV_{total} at $T = 2.00$ K when a single MW pulse of $t_{\text{pulse}} = 200$ ms is applied. The presence of abrupt jumps appears here to be conditioned by the intensity of the magnetic field: ΔV_{total} increases considerably up to approximately 200 Oe, after which it keeps almost constant until $H_{\text{dc}} = 610$ Oe, where a sharp decrease leads it to vanish at $H_{\text{dc}} = 650$ Oe. Apart from the non-monotonous behavior, these results reveal two interesting features: first, the jumps induced by the MW pulse are more significant in the range around 150–600 Oe and, second, there is an upper threshold magnetic field above which the jump activity terminates.

Similar behaviors are observed in Fig. 4.22, where the magnetic field dependence

4. Vortex instabilities driven by microwave fields

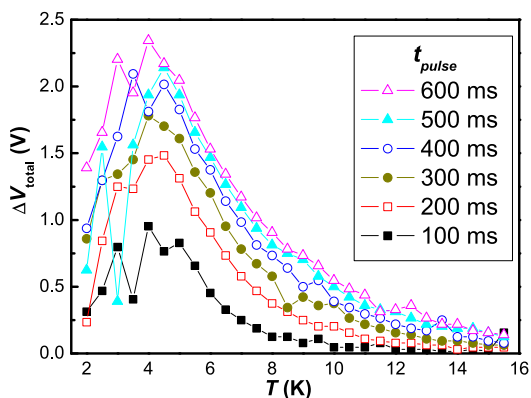


Figure 4.20: Temperature dependence of the total averaged rf-SQUID output signal variation, ΔV_{total} , of MgB₂ obtained at $H_{\text{dc}} = 20$ Oe applying single MW pulses of $P = 15$ dBm and $f = 1.94$ GHz, with different t_{pulse} values ranging from 100 ms to 600 ms in steps of 100 ms (see legend for details).

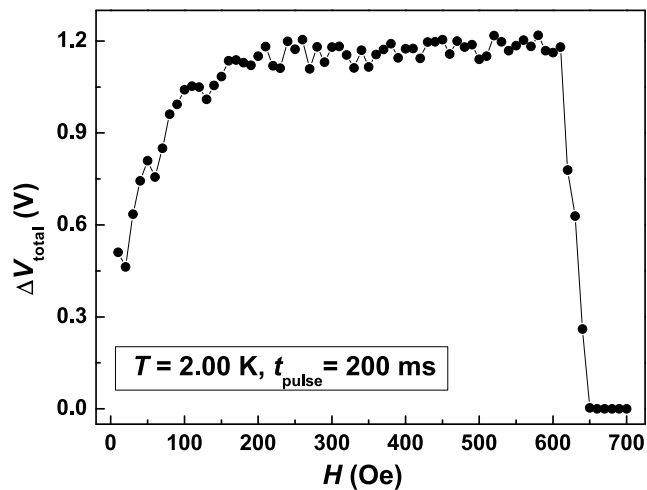


Figure 4.21: Magnetic field dependence of the total averaged rf-SQUID output signal variation, ΔV_{total} , of MgB₂ for MW pulses of $P = 15$ dBm, $f = 1.94$ GHz, and $t_{\text{pulse}} = 200$ ms at $T = 2.00$ K.

4. Vortex instabilities driven by microwave fields

of ΔV_{total} is plotted for $T = 2.00$ K at different values of t_{pulse} from 100 to 600 ms in steps of 100 ms. Moreover, the jumps increase with t_{pulse} up to 400 ms, while afterward their values become comparable. This fact and the results obtained in Fig. 4.20 suggest the existence of an upper threshold value for t_{pulse} at which the jump induced by the MW pulse starts to be less effective. This could be related with the time for heat transferring which is expected to increase with the enhancement of t_{pulse} .

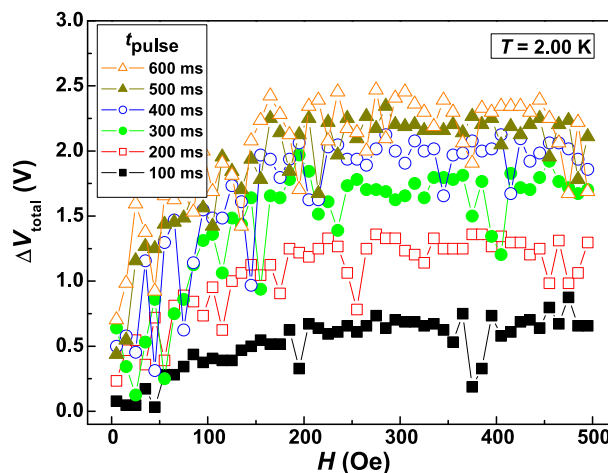


Figure 4.22: Magnetic field dependence of the total averaged rf-SQUID output signal variation, ΔV_{total} , of MgB_2 for MW pulses of $P = 15$ dBm, $f = 1.94$ GHz, at $T = 2.00$ K for different values of t_{pulse} from 100 ms (lowermost curve) to 600 ms (uppermost curve) in steps of 100 ms (see legend for details).

4.4.2.3 MW-pulse-induced instabilities: MgB_2

By considering the same relation described in subsection 4.4.1.5 for $\text{La}_{1.82}\text{Sr}_{0.18}\text{CuO}_4$ between ΔV and the variation of the sample magnetization, we associate the occurrence of stochastic-like jump in the time evolution of ΔV to a breakdown of the smooth critical-state distribution and the development of a fast flux diffusion, while the region where $\Delta V(t)$ stays constant is considered as a phase of gradual

4. Vortex instabilities driven by microwave fields

vortex distribution. Actually, the fact that $\Delta V(t)$ does not change substantially after the jump suggests that the flux structure triggered by the MW pulse may remain frozen inside the sample.

Figure 4.19 shows that the slope of the curves becomes less abrupt as the temperature increases and eventually changes to a parabolic-like shape for $t_{\text{pulse}} = 600$ ms at all T values [see panel (b)]. If we define as Δt the time interval elapsed between the onset of the jump and the achievement of ΔV_{total} , then the variation rates of the jump at $t_{\text{pulse}} = 100$ ms are $\Delta V_{\text{total}}/\Delta t = 9.34, 7.08$ and 5.06 V/ms for $T = 4.00, 5.00$ and 6.00 K, respectively, while the values at $t_{\text{pulse}} = 600$ ms are $\Delta V_{\text{total}}/\Delta t = 3.30, 2.83$ and 2.33 V/ms for $T = 3.00, 5.50$ and 6.50 K, respectively. These data indicate that for both t_{pulse} values the jump develops faster at the lowest temperatures, being the variation rate the largest for the smallest t_{pulse} value. $\Delta V_{\text{total}}/\Delta t$ is even noticeably reduced in the parabolic-like case as compared with the jump-like behavior. Finally, the ignition of the jump changes with temperature, that is to say the higher the temperature the longer the delay with respect to the pulse initiation. It is worth mentioning here that the average size of ΔV_{total} was the same when the MW pulse was applied after either a zfc or a fc mode. These findings are in agreement with previous results on abrupt flux penetration after a zfc process [53, 54, 55, 56, 57, 58, 194, 200, 208] or in the remnant state [202, 207].

Finally, the presence of instabilities in the vortex penetration process induced by the MW pulse, seems to be similar to those fluctuations observed in the magnetization measurements. In fact, the remnant part of the magnetization curves obtained without MW pulses in zfc mode and for temperatures between 2.00 and 5.00 K in steps of 0.50 K (see Fig. 4.23), shows the presence of noticeable noise around zero magnetic field which is commonly ascribed to the formation of a dendritic flux avalanche in thin films made of MgB_2 [53, 54, 55]. These fluctuations have been also observed as branched flux penetration in space-resolved magnetic measurements [55, 57, 58, 200, 201, 202]. Likewise, it has been shown that in films of MgB_2 , vortex instabilities can be easier triggered by a transport current pulse than by varying the magnetic field [202]. In the present situation, the MW-pulse-induced vortex instability seems to be originated by an additional kinetic energy which changes the smooth density profile.

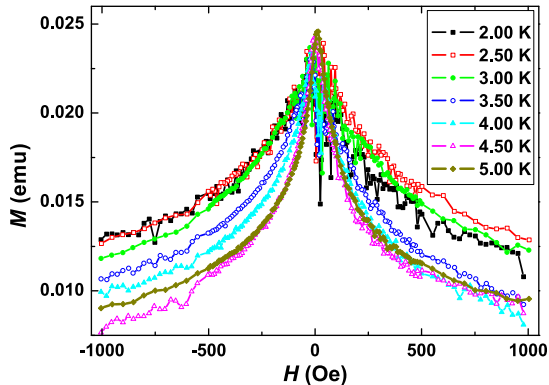


Figure 4.23: Remnant part of MW-free isothermal magnetic hysteresis cycles measured after the MgB₂ sample has been zero-field-cooled from the normal state down to temperatures that lies in the range from 2.00 to 5.00 K in steps of 0.50 K (see legend for details).

4.4.3 Vortex instabilities driven by pulsed microwave fields

The existence of recurrent MW-pulse-induced jumps in the temporal evolution of the output voltage signal, $\Delta V(t)$, of two kinds of thin films as a function of T , H , t_{pulse} and P , and below certain values of all these magnitudes but the input nominal power, allows us to attribute the jump-like behavior in the variation of the magnetization to the nucleation of a TEMI induced by the single MW pulse, similar to those triggered by nanosecond laser [50], transport current [202] pulses or the flux shaking provided by rf currents in resonators made of superconducting materials [215].

In order to shed light on the origin of such MW-pulse-induced fast flux diffusion we will consider the possible contribution to the development of TEMI from the electric and magnetic MW fields, E_{MW} and H_{MW} respectively, created at the edge of the thin film by the coil when the MW pulse is applied. It is worthwhile noting that it has been theoretically demonstrated [200, 227], and experimentally confirmed in magnetic field ramp [53, 55, 57, 58, 62, 194] and laser pulse [49, 50, 207] measurements that the background electric field plays an important role in the nucleation of a highly nonuniform flux distribution.

4. Vortex instabilities driven by microwave fields

By considering the rf-coil modeling exposed in subsection 3.4.6, the electric and magnetic fields created by the MW pulse in the coil at the border of the thin film have been found to be $E_{\text{MW}} \simeq 34$ V/m and $H_{\text{MW}} \simeq 2.0$ mOe, and $E_{\text{MW}} \sim 840$ V/m and $H_{\text{MW}} \sim 4.8$ mOe, for the $\text{La}_{1.82}\text{Sr}_{0.18}\text{CuO}_4$ and MgB_2 samples, respectively. In the former the following experimental data have been considered: $f = 0.9$ GHz, $\varepsilon_r = 300$ for the dielectric constant of the SrTiO_3 substrate, $P = 0.01$ mW ($\simeq -20$ dBm) for the effective incident power at the coil, and $Q = 100$. In the latter, $f = 1.94$ GHz, $\varepsilon_r = 9.2$ for the dielectric constant of the sapphire (Al_2O_3) substrate, $P = 0.03$ mW ($\simeq -15$ dBm), and $Q = 100$. In both cases the small value and the lack of uniformity of H_{MW} inside the coil (due to its limited length with respect to the sample size) enable us to disregard at first glance any effect this field maybe have. Nevertheless, the value obtained for E_{MW} (which is much higher than the value $E_p = 10^{-2}$ V/m, mentioned above), results significant for the ignition of the flux bursts. In fact, a value of around 1 V/m has been reported for the maximum electric field during the ignition of avalanche-like behavior [229]. Therefore, we can state that there is an additional electric field originated by the MW pulse at the edge of the sample that contributes considerably to the existing background electric field making the latter to increase enough to favor the nucleation of avalanche-like vortex penetration.

Finally, we recall that the occurrence of TEMI for a bulk under adiabatic condition is defined by Eq.(4.1). By considering that the electric field in Eqs. 4.4 and 4.5 accounts for a resistive flux flow state and a low-resistive flux creep state [240], the magnetic diffusivity can be expressed in term of ρ_f , resulting in a strongly reduces of the ratio of the thermal and magnetic diffusivity

$$\tau_f = \frac{\mu_0 \sqrt{th\kappa}}{C\rho_f}. \quad (4.8)$$

Here, the expression of τ_f for thin-film geometry has been considered (see Eq.(4.7) in subsection 4.3.4). It is noteworthy that since there are not relevant differences in κ and C among diverse MgB_2 samples [249], ρ_f turns out to be the key parameter for the fulfillment of such condition. In the case of $\text{La}_{1.82}\text{Sr}_{0.18}\text{CuO}_4$, both the heat transfer conditions and the flux creep effects play an important role in the development of the vortex instability. Since the dynamics of the flux

jumps is governed by τ , the contribution from the flux flow resistivity (which in turn increases as the electrical field does) in order to fulfill the appearance of flux jumps under adiabatic approximation ($\tau \ll 1$) becomes relevant.

4.5 Summary

We have performed studies on the influence of MW frequency radiation on the relaxation of the magnetic moment in $\text{La}_{1.82}\text{Sr}_{0.18}\text{CuO}_4$, Pb with a composite antidot lattice and MgB_2 superconducting thin films under sweeping and pulsed mode. In the first set of experiments carried out with the three samples, the MW frequency- and time-dependent magnetic response show irregularities in the form of ripples, small steps, jumps and negative peaks at certain thermal-dependent characteristic resonant modes under different dc magnetic fields, temperatures and microwave nominal powers. These frequency-triggered anomalies are interpreted as nucleation of instabilities in the relaxation of the flux profile. In the case of MgB_2 , ripples and small steps appear at the lowest P values, whilst the jump-wise anomalies seem to happen only at the highest P values. For $\text{La}_{1.82}\text{Sr}_{0.18}\text{CuO}_4$ the jumps are suggested to be ruled by thermal-dependent parameters as the critical current density, the thermal conductivity and the heat transfer coefficient. Additionally, the jumps appear conditioned by the magnetic field regime. In the case of Pb, besides the parameters mentioned, the jump-like response is conditioned by the presence of nanoscale defects (antidots). The existence of negative peaks either at temperatures close to T_c or for high H_{dc} are suggested to appear as a consequence of a change of the direction of the vortex diffusion in the near-edge layer with a strong flux concentration. Flux depinning at the sample edge is proposed to contribute in the development of such jumps and negative peaks. The frequency-triggered anomalies are shown in a rather wide temperature range in $\text{La}_{1.82}\text{Sr}_{0.18}\text{CuO}_4$ while they emerge in a short range over the threshold temperature for the nucleation of fast flux dynamics in MgB_2 . In the case of the Pb thin film with an engineered periodic antidot array, the experiments were performed in the range of temperature where flux jumping had been previously registered $T/T_c \leq 0.83$.

In the second set of experiments, we have studied the temporal evolution of the

4. Vortex instabilities driven by microwave fields

flux penetration in $\text{La}_{1.82}\text{Sr}_{0.18}\text{CuO}_4$ and MgB_2 when single MW pulses are applied as a perturbation source, by registering the output voltage signal from an rf-SQUID magnetometer. MW-pulse-induced avalanche-type flux penetration is observed in the form of a jump-like behavior, below threshold values for the dc magnetic field, temperature and pulse duration. These jumps appear in a stochastic way in the case of MgB_2 . The evolution of the shape and height of the output signal is suggested to be influenced by flux creep phenomena, heat transfer and pulse duration which act as stabilization factors against vortex bursts.

The induced vortex instabilities in both cases are suggested to be of MW electric field origin, similarly to the flux jumping induced by the background electric field predicted and observed during magnetic-field-swept or laser pulse measurements, which in turn favors the fulfillment of the adiabatic condition by increasing the flux flow resistivity. The role of the MW magnetic field has been estimated to be relevant for the first set of experiments but it appears less significant in the second one. The contribution from the MW energy density fed into the setup via MW heating that enhances the sample temperature is considered under the continuously sweeping mode although it is assumed to be reduced, but not discarded, in the pulsed mode scenario. Thin-film geometry appears as an important condition for the development of the instabilities in both cases. The experimental approach and the results presented here may also be relevant for the studies of vortex instabilities in other superconducting films. It is worth remarking that the data reading capability of the pulsed mode technique used here is comparable to that of the magnetization measurements performed to detect thermomagnetic instability by ramping the magnetic field. In order to have a full scenario and a complete interpretation of the observed phenomena in terms of the thermomagnetic model, further high-temporal resolution MOI measurements combined with the technique used here are suggested.

Chapter 5

Commensurability effects in ac and microwave power reflection mode experiments

5.1 Introduction

The applicability of type-2 superconductors in conventional active and passive MW thin-film superconducting devices require the suppression of dissipative processes originated by vortex motion, which leads to increased low-frequency noise and bit error rate, and reduced sensitivity, quality factor and power handling capability. Ordered arrays of pinning centers in superconductors give the key building blocks to reduce the losses associated with vortex motion and provide a versatile experimental testing field since it is possible to control the separation between vortices and pinning sites by simply varying the external magnetic field. Additionally, by changing the temperature, the characteristic length scales relevant in pinning interactions are modified and a large diversity of regimes can be obtained.

Among the micro- and nanosize objects used as pinning centers, much interest is generated by arrays of completely etched holes (antidots, with sizes much larger than ξ), which have been demonstrated to trap magnetic flux very effectively [22, 250, 251, 252, 253, 254, 255, 256, 257, 258, 259, 260, 261, 262, 263, 264,

5. Commensurability effects in ac and microwave power reflection mode experiments

265, 266, 267]. The interaction of the vortex lattice with such a regular array results in a wide range of commensurability effects at low magnetic fields and for temperatures close to T_c for integer or fractional numbers of flux quanta per pinning site. These features have been reported in an extensive number of publications where various measurement techniques such as dc magnetometry [265, 266], transport [257, 260, 261], ac susceptometry [251, 253, 254, 256, 260, 261], and direct imaging [250, 252, 258, 259, 264] have been used. Periodic array of holes in superconducting films show other interesting effects as the existence of multi-quantum vortices in holes [265, 266, 267] and vortices in interstitial positions [260, 266, 267]. The promising applicability of these engineered periodical systems in the reduction of noise in high- T_c SQUIDs [268], single flux quantum logic [269], vortex diodes [270, 271], and microwave, spintronic and fluxonic functionalities [272, 273, 274] have fostered the development of alternatives to the lithographic patterning based on templates formed by self-assembly of nanostructures [275, 276, 277, 278, 279, 280, 281, 282, 283].

Different regimes of vortex dynamics in superconducting lead films with arrays of either antidots [251, 253, 254, 256] or partially etched holes (the so-called blind holes) [253], have been investigated by using ac susceptibility techniques and varying either the ac perturbation sensing parameters (H_{ac} and f_{ac}) or the thermodynamic variables (H_{dc} and T) [251, 253, 254, 255, 256, 260, 261, 262]. These low- H_{ac} measurements in the kHz frequency range have proven to be successful and sensitive to probe the effective pinning potential without modifying the vortex distribution, making easier a direct correlation between the vortex lattice configuration and the observed dynamical response. Studies of superconductors in the MW and rf ranges, which are useful for the realization of low-loss electronic devices, yield important details about electromagnetic screening and dissipative processes and offer a way to verify theoretical models for vortex pinning and motion [284, 285, 286].

In this chapter, we give first a brief description of the commensurability effects that emerge in nanostructured materials. Then, we establish the main characteristics of patterned thin superconducting Pb films. Afterwards, we report on experimental results obtained with this sample measuring ac magnetic susceptibility under MW irradiation and MW power reflection techniques. The former set

5. Commensurability effects in ac and microwave power reflection mode experiments

of measurements shows that the commensurability effects related to the matching of the vortex lattice parameter and the antidot array spacing are strongly dependent on the values of the frequency and nominal power of the MW radiation. Such effects at integer and fractional matching field values have been observed as peaks in the magnetic field dependence of the MW backward reflection coefficient for different values of temperature, frequency and power. These peaks appear as a result of the contribution of the vortex dynamics to the reflected signal at the matching fields and their observation depends on the values of the MW power supplied to the sample.

5.2 Commensurability effects

Since pinning is crucial to obtain materials with high critical currents, a big effort has been devoted to increase pinning by means of artificial methods. The most striking results were obtained by high-energy heavy-ion irradiation which created a track of amorphous material along the ions path with radius around 50 Å suitable to pin vortices in HDC as $\text{YBa}_2\text{Cu}_3\text{O}_7$ where $\xi \sim 15$ Å [287, 288]. However, these defects are randomly distributed and have different pinning energies [289]. These topological and energetic dispersion can be reduced to minimum levels by using recent submicrometer lithographic techniques based on electron-beams which allow one to build artificial pinning centers in a nanometer scale [21, 22, 23]. With this technique it is possible to control the size and the type of the pinning sites together with the spatial distribution.

Artificial pinning centers arranged periodically give rise to commensurability phenomena between the vortex lattice and the periodic pinning potential. The stable vortex configuration, reproducing the symmetry of the pinning array, causes a local enhancement of the sample magnetization $M(H)$ and the critical current $I_c(H)$. These pronounced maxima, the so-called matching features, occur at integer multiples of the first matching field $H_n = nH_1 = n\Phi_0/S$, that is defined as the field at which the density of Φ_0 -vortices equals the density of pinning sites. S is the area of the unit cell of the antidot lattice. Furthermore, also rational multiples of the first matching field, namely $H_{p/q}$, where p and q are integers, can produce a reduced mobility of the vortex lattice. It is worthwhile mentioning

5. Commensurability effects in ac and microwave power reflection mode experiments

that matching effects are typically observed at temperatures close to T_c . This can be attributed to the divergence of $\lambda(T)$ at temperatures close to the critical one, leading to a stronger vortex-vortex interaction. Additionally, commensurability features due to the periodic pinning array are progressively masked by the intrinsic pinning as temperature is decreased.

The first observation of matching phenomena in a periodic pinning potential was reported as peaks in the critical current density at well-defined field values when studies on the interaction of the vortex lattice with a one-dimensional periodic thickness modulation of an Al film were performed [290]. A few years later experiments on two-dimensional pinning arrays of holes (antidots) were performed [291, 292]. The configurations of diverse flux line lattices under different fields have been directly visualized by Lorentz microscopy [264], magnetic force microscopy [293, 294], scanning Hall probe microscopy [273, 295, 296], and Bitter decoration [263].

An important intrinsic property of an artificial array of pinning sites is the maximum number of flux quanta than can be trapped in one site. This so-called saturation number, n_s , depends on the ratio between the size of the pinning site and the coherence length [103, 297, 298, 299]. For fields $H > n_s H_1$, incoming vortices will appear as flux lines repelled into the interstitial region between the antidots, resulting in the coexistence of two sub-systems: (*i*) multi-quanta fluxoids localized at the antidot sites, and (*ii*) weakly pinned, single-quantum vortices or *interstitial flux lines*. These interstitial vortices are much more mobile than vortices trapped into the pinning sites, thus resulting in a sharp decrease of the critical current at $H = n_s H_1$. However, this composite lattice containing a mixture of interstitial vortices and vortex trapped by the antidots can still be stable. This stability is due to the strong repulsion between interstitial vortices and those vortices inside the saturated antidots, and it is known as *caging* effect [298].

5.3 Patterned thin Pb film

Figure 5.1 shows an atomic force microscopy (AFM) image of a $5 \times 5 \mu\text{m}^2$ surface of a Ge(5 nm)/Pb(50 nm)/Ge(20 nm) thin film with an array of submicrometer antidots [253]. The antidot array is a square lattice of square holes of side length

5. Commensurability effects in ac and microwave power reflection mode experiments

$b = 0.8 \mu\text{m}$ and period $d = 1.5 \mu\text{m}$, that gives a value for the first matching field, $H_1 = 9.2 \text{ Oe}$, that is, the smallest integer value of H_{dc} at which commensurability between the antidot array spacing and the vortex lattice parameter is to be observed.

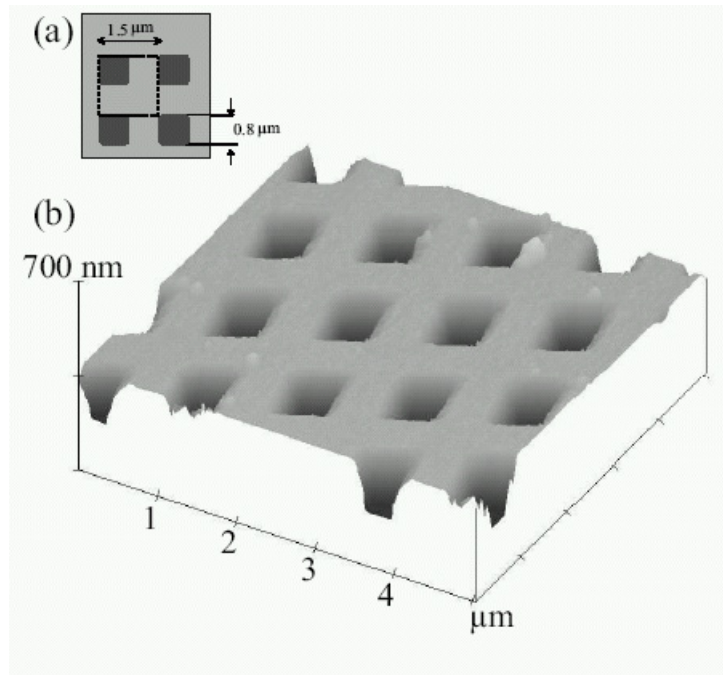


Figure 5.1: Layout of the Pb film with a composite array of square antidots. (a) Schematic representation of a unit cell of the antidot array. (b) Atomic force microscopy image of $5 \times 5 \mu\text{m}$ area of the composite antidot array [253].

For the sake of simplicity, we will estimate here the maximum vortex occupation of each antidot, n_s . This is obtained by using the expression [299] that gives this magnitude for an insulating cylindrical cavity in a type-2 superconductor, $n_s(T) = D/4\xi(T)$, where D is the antidot diameter and $\xi(T) = \xi(0)(1 - T/T_c)^{-1/2}$ is the temperature-dependent coherence length. In our case D may be approximated by the size of the square-shaped hole, b , so that by considering the value of $T_c = 7.20 \text{ K}$ quoted before and $\xi(0) \sim 33 \pm 1 \text{ nm}$, as determined for samples similar to the one used here [251, 254, 255, 256], we can estimate $n_s \simeq 1$ at all relevant temperatures in our experiments. This means that each hole can trap

5. Commensurability effects in ac and microwave power reflection mode experiments

one single flux quantum at the most and thus a multiquanta vortex lattice cannot be observed in our sample.

It is also worth mentioning that Pb, which in bulk shape is a type-I superconductor with a Ginzburg-Landau parameter [300] $\kappa_b \sim 0.30$ ($< 1/\sqrt{2}$) near T_c , becomes type-2 in thin film form as a result of the reduced dimensionality [301]. Additionally, it has to be taken into account that the penetration depth results increased due to the small thickness of the sample and the disorder created by the presence of impurities or antidots (see section 2.3.2). All these effects result in $\kappa_f \sim 1$ ($> 1/\sqrt{2}$).

5.4 ac magnetic susceptibility under MW irradiation

Figure 5.2 presents the in-phase, χ' , and out-of-phase, χ'' , components of the ac susceptibility, $\chi = \chi' + i\chi''$, measured at $H_{ac} = 236$ mOe and $f_{ac} = 829.65$ Hz as a function of a reduced dc magnetic field defined as $h_{dc} \equiv H_{dc}/H_1$, after the sample had been submitted to a zfc process from the normal state down to $T = 7.00$ K ($t \equiv T/T_c = 0.972$) and has been subsequently irradiated with $P = 0, 5, \text{ and } 12.5$ dBm (1.0, 3.2 and 17.8 mW, respectively), and $f = 0.92$ and 1.98 GHz. In all cases, H_{dc} was swept from -50.0 to 50.0 Oe in steps of 0.1 Oe, with a characteristic time delay of 100 s before the first data point was taken. Data obtained at $T = 7.00$ K and $T = 7.10$ K in the absence of radiation, following the same magnetic protocol, are plotted as a reference. These MW-free results follow the common behavior for χ in a superconductor: as h_{dc} increases, χ' and χ'' tend to zero, and actually vanish at $h_{dc} \simeq 4.5$ for $T = 7.10$ K, while still keep a very small but non-zero value for $T = 7.00$ K at the maximum magnetic field intensity used in our experiments, $h_{dc} \simeq 7.0$. This is in full agreement with the values of $H_{c2}(T)$ corresponding to these temperatures, that can be estimated using Eq. (2.23). If we substitute the values of T_c and $\xi(0)$ quoted above, we obtain $H_{c2}(7.10 \text{ K}) \simeq 42.0$ Oe and $H_{c2}(7.00 \text{ K}) \simeq 84.0$ Oe, which correspond respectively to $h_{dc} \simeq 4.6$ and $h_{dc} \simeq 9.1$.

5. Commensurability effects in ac and microwave power reflection mode experiments

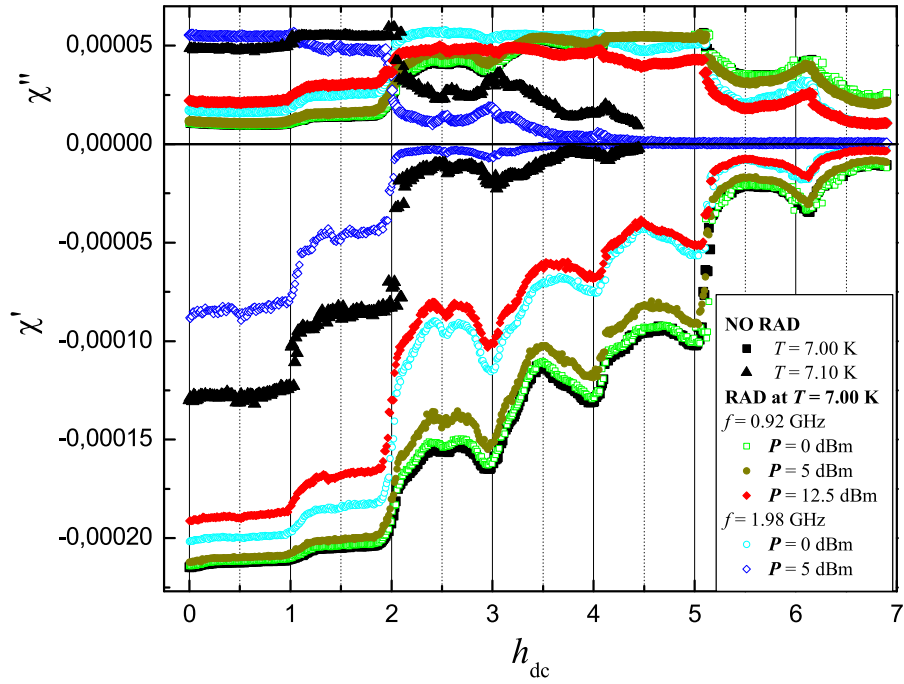


Figure 5.2: ac susceptibility, $\chi = \chi' + i\chi''$, as a function of the reduced dc magnetic field, h_{dc} , when the system temperature is $T = 7.00$ K, the ac parameters are $H_{\text{ac}} = 236$ mOe and $f_{\text{ac}} = 829.65$ Hz, and the patterned Pb sample is irradiated either with frequency $f = 0.92$ GHz and nominal MW powers $P = 0$ dBm (1 mW, open squares), $P = 5$ dBm ($\simeq 3.2$ mW, solid circles), and $P = 12.5$ dBm ($\simeq 18$ mW, solid rhombuses), or with $f = 1.98$ GHz and $P = 0$ dBm (open circles), and $P = 5$ dBm (open rhombuses). Data obtained at $T = 7.00$ K (solid squares) and $T = 7.10$ K (solid upward triangles) in the same conditions without microwave radiation are plotted as a reference.

5. Commensurability effects in ac and microwave power reflection mode experiments

Characteristic effects at integer (1 to 6) and half-integer ($1/2$, $3/2$, $5/2$) values of h_{dc} are additionally observed in all curves as changes, namely steps and peaks, both in χ' , that is the efficiency to screen out the sample from external perturbations, and χ'' , that is the dissipation associated with such perturbations. This behavior is a signature of commensurability effects between the vortex lattice parameter and the antidot array spacing, and is related to the presence of trapped vortex states and the occurrence of different dynamic regimes as a result of the competition between the pinning forces of the periodic antidot array and the interaction within the elastic vortex system [112, 251, 253, 254, 256, 257, 260, 261, 266]. Bearing in mind that each hole can trap one single flux quantum at the most, the considerable variation of χ' to less negative values (screening reduction) at $h_{\text{dc}} = 2$, coinciding with an increase in χ'' (dissipation enhancement), should reflect a change in the nature of the mechanism of vortex pinning [256]: for $h_{\text{dc}} < 2$, pinning should be ruled by the interaction of vortices with antidots, while at $h_{\text{dc}} = 2$, a transition to a weak pinning scenario where vortex-vortex interaction becomes dominant would take place. The existence of weakly pinned interstitial vortices would result then energetically favorable for $h_{\text{dc}} > 2$ as a consequence of collective effects. The vortex-pinning and vortex-vortex interaction will be considered in depth in the next section.

Fig. 6.2 shows that the effect of the application of MWs at $T = 7.00$ K with respect to the results obtained without radiation at the same temperature (solid squares) is to reduce the screening and to enhance the dissipation by increasing either P or f . In particular, for $h_{\text{dc}} < 2$, the departure of the χ' curves obtained at $f = 0.92$ GHz with respect to the curve without radiation is noticeable only at the highest power applied ($P = 12.5$ dBm), for which it becomes even larger for $2 < h_{\text{dc}} < 5$, while it is again less important for $h_{\text{dc}} > 5$. A similar behavior is observed at $f = 1.98$ GHz for $P = 0$ dBm and $P = 5$ dBm, for which a substantial variation in χ' with respect to the MW-free curve is registered particularly for $2 < h_{\text{dc}} < 5$. At this frequency a transition to the normal state at $h_{\text{dc}} \simeq 4$ is obtained for $P = 5$ dBm, similarly to what happens to the curve without radiation at $T = 7.10$ K.

The same figure shows that the minima exhibited by χ'' at commensurate values of $h_{\text{dc}} < 5$ turn into maxima at $h_{\text{dc}} \geq 5$ for all curves but the one obtained at

5. Commensurability effects in ac and microwave power reflection mode experiments

$P = 5$ dBm and $f = 1.98$ GHz, for which only maxima are actually observed in the whole range up to $h_{\text{dc}} = 4$, beyond which the curve tends to vanish. This behavior, that had been previously reported [253, 254, 256] for measurements performed close to T_c on similar samples for different values of H_{ac} , can be explained considering the expressions of χ' and χ'' in the framework of the Bean model for a strip [302]:

$$\chi' = (-1/h_{\text{ac}}) \tanh h_{\text{ac}} \quad (5.1)$$

$$\chi'' = (-1/h_{\text{ac}}) \tanh h_{\text{ac}} + (2/h_{\text{ac}}) \tanh(h_{\text{ac}}/2) \quad (5.2)$$

Here $h_{\text{ac}} \equiv H_{\text{ac}}/H_p$. As it was shown in subsection 2.3.4, the field for full flux penetration, H_p , is a function of the critical current density, J_c , which is a decreasing function of H_{dc} [254]. According to this model, in the asymptotic limits both components are related by $\chi'' \propto (1 - |\chi'|)$ for $h_{\text{ac}} \ll 1$, and $\chi'' \propto |\chi'|^{2/3}$ for $h_{\text{ac}} \gg 1$ [254, 302]. As a result, as H_{dc} increases, J_c decreases and, correspondingly, H_p changes with respect to the constant value of H_{ac} used in our experiments [254]. Thus a transition occurs from a regime, at $h_{\text{ac}} \ll 1$, where the dissipation is reduced when the screening is enhanced at commensurate values of h_{dc} (hence the minima both in χ' and χ''), into another regime, at $h_{\text{ac}} \gg 1$, where the dissipation reproduces the behavior of the screening (hence the occurrence of maxima in χ'' while χ' keeps showing minima).

In order to shed light on the role played by the MW radiation in these measurements, Fig. 6.3 presents the nominal MW power dependence of χ obtained at $T = 7.00$ K and $H_{\text{dc}} = 5$ Oe by sweeping P from -20.0 to 15.0 dBm (from $10 \mu\text{W}$ to 32 mW, approximately) in steps of 0.1 dBm, for the two f values specified before. No significant effects are found between -20.0 and 5.0 dBm for $f = 0.92$ GHz, whereas a reduction in the upper limit of this range to -5.0 dBm and a substantial suppression of χ' between 0.0 and 5.0 dBm are observed for $f = 1.98$ GHz. The behavior of both curves, which recalls the usual thermal dependence of χ observed in MW-free measurements, is in full agreement with the results plotted in Fig. 6.2, where all the curves at $f = 0.92$ GHz and the curve at $f = 1.98$ GHz and $P = 0$ dBm lie close to the curve obtained at $T = 7.00$ K without radiation, and only the curve at $f = 1.98$ GHz and $P = 5$ dBm lies slightly closer to the abscissa axis than the MW-free curve obtained at $T = 7.10$ K. This layout

5. Commensurability effects in ac and microwave power reflection mode experiments

suggests that the effect of MWs at certain f and P values could be related with some heat dissipation and a slight enhancement of the actual sample temperature, T_s .

Thus, although χ measurements as a function of the MW power do not imply a direct definition of T_s at each value of P , a rough estimate of its variation with respect to the data obtained at $T = 7.00$ K without radiation can be obtained. To do so, the total variation of χ' between 7.00 K and 7.10 K observed in Fig. 6.2 was taken as a reference, and effective T_s values for the other curves were estimated by interpolation. We found an enhancement of about 10 mK in the antidot pinning regime ($h_{dc} < 2$) and 25 mK in the interstitial pinning regime ($h_{dc} > 2$) for $f = 0.92$ GHz and $P = 12.5$ dBm, and a variation of about 100 mK at $h_{dc} < 2$ for $f = 1.98$ GHz and $P = 5$ dBm. Accordingly, in spite of the heating effect which might result from the application of MWs, T_s did not seem to increase enough as to take the sample into the normal state. Nonetheless, a full set of parameters comprising the thermal conductivity and heat capacity of the superconducting thin film together with its thermal coupling to the substrate, and the environmental helium gas, should be considered to perform a proper computation of thermal effects induced on the sample by the MW radiation.

To finish with the analysis of these results, it is worth mentioning that the ac response studied here was measured in the so-called linear or Campbell regime that dominates at low H_{ac} values [251, 253, 254, 256, 262]. In this case, the ac perturbation would cause a vortex oscillation inside the pinning sites that should not alter the initial vortex configuration established by H_{dc} , and then a response characterized by a H_{ac} -independent χ' and a very small χ'' should be expected. A transition to a more dissipative state with a H_{ac} -dependent screening (critical state regime) is mainly determined by the ac perturbation capability to shake the vortices strongly enough to drive them out the pinning centers. If we apply the common criterion that establishes the onset of nonlinearity at a dissipation threshold of $\chi'' = 0.05$ [253] to our results, we find that a linear ac response is guaranteed for the low H_{ac} value (236 mOe) used here (see the maximum values of χ'' in Figs. 5.2 and 5.3).

5. Commensurability effects in ac and microwave power reflection mode experiments

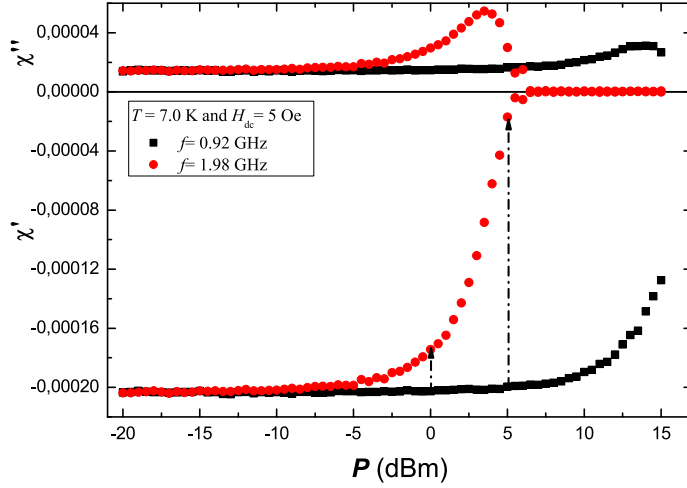


Figure 5.3: ac susceptibility of the patterned Pb film, $\chi = \chi' + i\chi''$, as a function of the nominal MW power, P , when the MW frequency is either $f = 0.92$ GHz or $f = 1.98$ GHz, the system temperature is $T = 7.00$ K, the dc magnetic field is $H_{dc} = 5$ Oe, and the ac parameters are $H_{ac} = 236$ mOe and $f_{ac} = 829.65$ Hz.

5.5 Magnetic field-dependent power reflection

5.5.1 MW power reflection as a function of temperature and frequency

Figure 5.4 plots the difference of the modulus of the MW complex reflection coefficient when the sample is in the superconducting state and its value in the normal state, $\Delta S_{11} \equiv S_{11} - S_{11,N}$, as a function of h_{dc} , for $P = -10$ dBm (0.1 mW) and $f = 2.01$ GHz, at temperatures between 6.80 and 7.08 K [panel (a)] and between 7.10 and 7.20 K [panel (b)], when H_{dc} is swept from -50.00 to 50.00 Oe in steps of 0.05 Oe using the external sourcemeter. Similar results are displayed in Figs. 5.5 and 5.6 for $f = 3.98$ and 1.86 GHz at temperatures between 6.90 and 7.15 K, and 7.00 and 7.17 K, respectively. Since all curves are largely symmetrical around $h_{dc} = 0$, from now on we will focus on the description of the behavior at positive h_{dc} values.

Above T_c or beyond the upper critical field, $H_{c2}(T)$, the backward reflection coefficient does not vary significantly, meaning that $S_{11,N}$ is practically independent

5. Commensurability effects in ac and microwave power reflection mode experiments

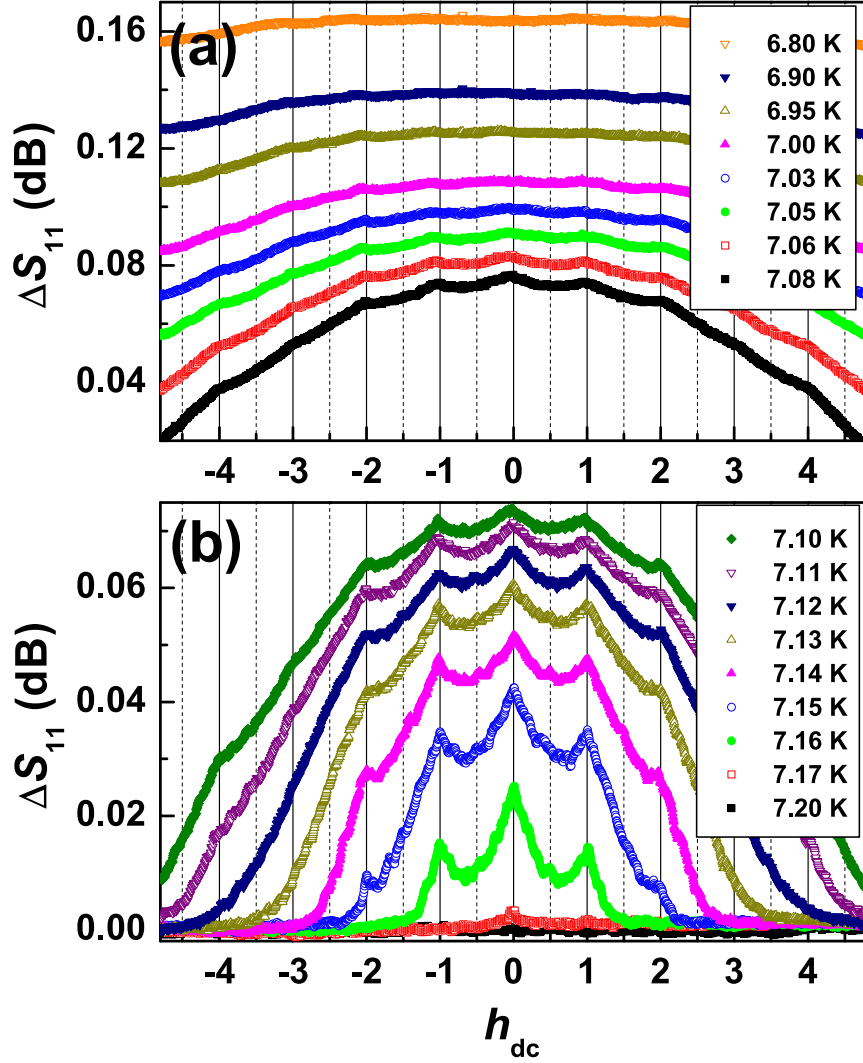


Figure 5.4: Difference of the amplitude of the MW power reflection coefficient in the superconducting state and its value in the normal state, ΔS_{11} , as a function of the reduced dc magnetic field h_{dc} , when the patterned Pb sample is irradiated with microwaves of $P = -10$ dBm (0.1 mW) and $f = 2.01$ GHz. Panel (a) shows the curves obtained for system temperatures from $T = 6.80$ K (uppermost curve) to $T = 7.08$ K (lowermost curve), and panel (b) shows the curves obtained from $T = 7.10$ K (uppermost curve) to $T = 7.20$ K (lowermost curve).

5. Commensurability effects in ac and microwave power reflection mode experiments

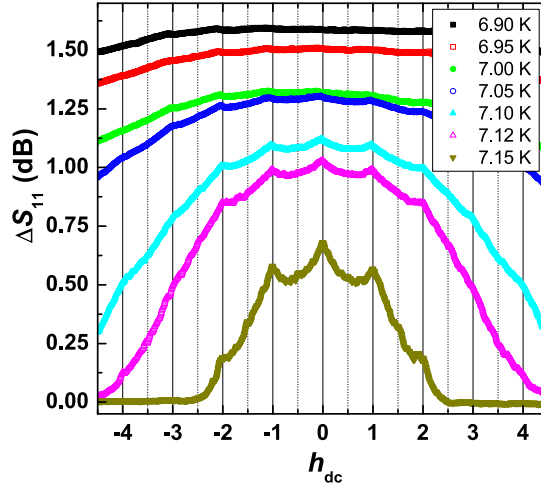


Figure 5.5: Difference of the amplitude of the MW power reflection coefficient in the superconducting state and its value in the normal state, ΔS_{11} , as a function of the reduced dc magnetic field h_{dc} , when the patterned Pb sample is irradiated with microwaves of $P = -10$ dBm (0.1 mW) and $f = 3.98$ GHz, for system temperatures from $T = 6.90$ K (uppermost curve) to $T = 7.15$ K (lowermost curve).

of h_{dc} . The invariance of this contribution enables us to take it as a reference for the signal obtained in the superconducting state and to consider therefore $\Delta S_{11}(h_{dc}) \sim 0$ to hold whenever the sample is normal. As T decreases below T_c and the sample becomes superconductor, ΔS_{11} increases and tends to a quasi-parabolic behavior at the lowest temperatures [see uppermost curves in Figs. 5.4(a), 5.5 and 5.6]. At each T value, the maximum signal appears at $h_{dc} = 0$, after which ΔS_{11} decreases in a strongly non-monotonic way as h_{dc} increases and finally vanishes when the sample is driven normal by the magnetic field. Irregularities appear as a collection of peaks for integer values of h_{dc} up to 4 at temperatures as low as 6.80 K [see Fig. 5.4(a)], and also for half-integer values (1/2 and 3/2) at $T > 7.10$ K [see Fig. 5.4(b) and lowermost curves in Figs. 5.5 and 5.6]. Although the largest temperature below T_c at which ΔS_{11} is non-zero here is $T = 7.17$ K ($t = 0.996$), only a single shallow peak for $h_{dc} = 1$ is observed at such temperature, since the first matching field ($H_1 = 9.2$ Oe) is very close to $H_{c2}(7.17 \text{ K}) \simeq 12.6$ Oe [$h_{c2}(7.17 \text{ K}) \simeq 1.37$].

5. Commensurability effects in ac and microwave power reflection mode experiments

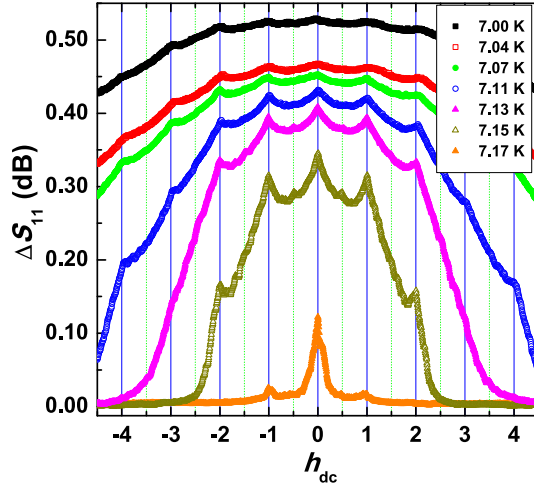


Figure 5.6: Difference of the amplitude of the MW power reflection coefficient in the superconducting state and its value in the normal state, ΔS_{11} , as a function of the reduced dc magnetic field h_{dc} , when the patterned Pb sample is irradiated with microwaves of $P = -10$ dBm (0.1 mW) and $f = 1.86$ GHz, for system temperatures from $T = 7.00$ K (uppermost curve) to $T = 7.17$ K (lowermost curve).

5.5.2 Commensurability effects in MW reflection spectrometry

The magnetic field-dependent power reflection results strongly suggest the presence of commensurability effects between the vortex lattice and the antidot array and show interesting features:

1. The matching peaks which disrupt the monotonous decrease of ΔS_{11} as h_{dc} increases, appear most significant for $h_{dc} = 1$ in the curves obtained close to T_c , unless for $T = 7.17$ K [see the lowermost curves in Figs. 5.4(b) and 5.6].
2. The peaks remain down to T relatively far below T_c ($t \simeq 0.94$ – 0.96), when they become shallow and diffuse [see the uppermost curves in Figs. 5.4(a), 5.5 and 5.6].
3. The variations between the main peaks at $h_{dc} = 0$ are important near T_c and decrease as the temperature lowers. As an example, an approximate

5. Commensurability effects in ac and microwave power reflection mode experiments

relative deviation of a 60% when the system temperature varies just 0.01 K (between $T = 7.15$ K and $T = 7.16$ K) is reported in Fig. 5.4(b). This suggests that the reflection measurements performed here are quite sensitive to any variation that may originate from changes in the system temperature.

4. Finally, it is worth pointing out that the difference of values obtained in ΔS_{11} for the three frequencies investigated ($f = 2.01, 3.98$ and 1.98 GHz) is related with the characteristics (height and full width at half maximum) of each resonant peak rather than with the precise frequency values.

In order to give an explanation of the mechanisms that may be responsible for the results obtained, a series of remarks are worth being made:

1. The behavior of the reflected signal results from changes in the characteristics of the selected resonant frequencies of the cs induced by the variation of the sample properties as the magnetic field and the temperature are modified.
2. The signal picked up by the cs probe, and consequently S_{11} , contains different contributions, arising basically from the screening properties and the vortex dynamics of the sample embedded in the coil.
3. The thermal and magnetic effects on the coil characteristics (impedance, inductance, dimensions...) are the same when the measurements of $S_{11}(h_{dc})$ are performed with the sample in the superconducting and normal states. Hence, by calculating $\Delta S_{11}(h_{dc})$ as defined before, the contribution of such effects is removed.
4. The application of a perpendicular magnetic field on type-2 superconductors leads to energy dissipation due to vortex motion and consequently to critical current reduction. Nevertheless, it has been shown that thin superconducting films with a periodic array of antidots show a more confined movement of vortices at the matching fields, which results in local minimum resistance [257], maximum critical current [254, 257] and high screening in the ac response [253, 254].

5. Commensurability effects in ac and microwave power reflection mode experiments

5. On the basis of the strong pinning that exists in patterned thin films we may ignore flux creep phenomena close to T_c [303].

Considering these aspects and taking the expressions that follow from the two-fluid model for superconductors [69] for the complex conductivity, $\sigma = \sigma_1 - j\sigma_2$, and the London penetration depth, $\lambda_L^2 = 1/(\omega\mu\sigma_2)$, where $\omega = 2\pi f$ is the angular frequency and μ is the magnetic permeability of the material, we will first discuss how the sample properties contribute to S_{11} as a function of the temperature and the magnetic field, and then we will focus on the peaks that appear at different matching fields. When the sample is normal, λ_L is infinite and the current carriers (defined by $\sigma_N = \sigma_1$) have no effect on the field penetration. In this case, the sample contribution to the reflected signal is ruled only by σ_1 , which does not depend on the external magnetic field. As a consequence, no changes in the characteristics of the resonant frequency of the cs are induced as the magnetic field is swept, and thence $S_{11,N}$ has to be constant as a function of h_{dc} .

As the temperature goes down below T_c , the electron pair contribution to σ becomes progressively relevant via σ_2 . This results in the reduction of the penetration depth and the stored magnetic field inside the patterned thin film, and accordingly in the decrement of the reactive part of the surface impedance, $X_s = \omega\mu\lambda_L$ [130]. The diminution of λ_L implies a change in the volume created by the electromagnetic modes in the cavity formed by the cs and therefore produces a deviation in the characteristics of its resonant frequency. This is observed as an enhancement of the reflected signal with respect to that obtained in the normal state, as a result of which S_{11} departs from constant values and gets higher as the temperature lowers. Actually, in a cavity resonator partly or entirely formed by a superconductor, any temperature variation modifies λ_L and induces changes in X_s that show up as shifts in the resonant frequency [130, 131]. As the external magnetic field is gradually increased beyond the lower critical field and the sample is driven into the mixed state, a continuous entrance of vortices through the border towards the center of the sample is assisted by surface screening currents. This motion leads to dissipation due to relaxation processes of normal quasiparticles in the vortex core [284, 285, 286]. As a matter of fact, the presence of normal carriers in the sample contributes to enhance the surface resistance, $R_s = (\sigma_1\omega^2\mu^2\lambda_L^3)/2$, via σ_1 . The reduction of the superconducting

5. Commensurability effects in ac and microwave power reflection mode experiments

area inside the sample and the rise of R_s with the increase of the magnetic field come about as a monotonous overall decay in the $S_{11}(h_{dc})$ curves from $h_{dc} = 0$ to $h_{dc} \simeq h_{c2}$, meaning that vortices contribute to bring the reflected signal down to the one obtained in the normal state. We can thus say that significant changes happen in the resonant frequency of the cs as h_{dc} augments, in accordance with previous works in MW resonators made of superconducting materials where the rise of the magnetic field induces the characteristic frequency to broaden and shift down [129, 133, 134, 135]. At $h_{dc} = 0$, there are not vortices and the only contribution to the reflected signal is that from λ_L , which leads to the occurrence of a maximum in $S_{11}(h_{dc} = 0)$ at each temperature.

The presence of antidots changes this scenario, since now it is energetically favorable that vortices locate in regions of reduced superconductivity. Moreover, the motion of vortices in an array of periodic pinning centers generates a complex picture due to the existence of different pinning potentials, particularly for $h_{dc} > 1$, where interstitially caged vortices coexist with those strongly locked in the antidots. In order to have an image of this new situation, we consider first the above estimated maximum vortex occupation of each antidot, $n_s \simeq 1$. Second, the penetration depth is enhanced by the presence of antidots according to the expression 2.50 given in section 2.3.2. Finally, the vortex dynamics can be described by a phenomenological balance equation of the local forces [304, 305], $\eta \partial \mathbf{u} / \partial t = \mathbf{F}_{vp} + \mathbf{F}_{vv}$, where η is the vortex viscosity, \mathbf{u} is the vortex velocity, \mathbf{F}_{vp} is the pinning force due to the trapping of the vortex by an antidot, and \mathbf{F}_{vv} is the vortex-vortex repulsive interaction. In this equation we have not considered the inertial term, since the mass per unit length of the vortex is negligible [306]; the thermal noise force, since high stability of the system temperature is guaranteed by the experimental equipment; and the Lorentz force related to the gradient of the magnetic induction, due to the constant profile described in the multiterrace critical state [250, 307]. The two right-hand side terms, which depend strongly on the applied magnetic field, describe the conservative part of the dynamics and contribute to the formation of a highly ordered vortex lattice, particularly at matching fields. The left-hand side describes the effects of a nonconservative environment presenting dissipation.

Let us start with $h_{dc} = 1$, when the density of vortices equals that of the antidot

5. Commensurability effects in ac and microwave power reflection mode experiments

array. In this case, vortex-vortex interaction is prevented by the high symmetry of the vortex lattice and vortices stay locked in the antidots. For this reason, the density of moving vortices, n_v , is strongly reduced, and this forces lower dissipation. As a consequence, the reflected signal increases and a peak is thus observed in $\Delta S_{11}(h_{dc} = 1)$. This peak is most pronounced close to T_c because the penetration depth is larger at these temperatures and this makes the trapping of vortices more effective [308]. Indeed, for MW resonators made of patterned samples, the reduced vortex motion at the matching fields has been identified as a decrease in the shift of the resonant frequency [134, 137] with respect to the shift detected in resonators made of plain samples [135]. As T goes down, this peak becomes less conspicuous since the ΔS_{11} curve is modified as the penetration depth declines. Additionally, at low temperature other phenomena such as the growth of the intrinsic pinning strength and the increase of self-field effects [281] become relevant with respect to the pinning by antidots.

The observation in Figs. 5.4(b), 5.5 and 5.6 of shallower peaks at $h_{dc} = 1/2$ and $3/2$, as compared to those registered at $h_{dc} = 1$, suggests that vortex motion contributes to the reduction of the reflected signal at these matching fields via dissipation. At $h_{dc} = 1/2$, vortices are expected to occupy every other pinning site in both orthogonal in-plane directions forming a square lattice of side length $d\sqrt{2}$ [264]. In this situation, vortex-vortex interaction does not cancel out, though it seems to be too feeble as to provide for long-range order because the vortex lattice parameter is larger than that at $h_{dc} = 1$. From a lower vortex density with respect to the antidot density it follows that additional vortices can move amidst the pinned ones, resulting in a dissipative contribution as long as they get not trapped by empty sites. At $h_{dc} = 3/2$, extra vortices would enter every other interstice and would thus occupy just half these sites [264]. In such arrangement, interstitial vortices can jump to next empty sites across the vortices pinned at the antidots and this causes significant dissipation. The resulting vortex-vortex interaction could be in this case the origin of short-lived metastable vortex states at the interstitial sites. Thus, the shallow peaks in ΔS_{11} at these matching fields would result from two kinds of vortex dynamics that would both lead to dissipative flux motion, being vortex pinning and vortex-vortex interaction the dominant mechanism at $h_{dc} = 1/2$ and $h_{dc} = 3/2$, respectively. A different behavior is ob-

5. Commensurability effects in ac and microwave power reflection mode experiments

served at $h_{\text{dc}} \geq 2$, where sharp peaks are found again. Specifically, additional vortices would occupy all the interstitial positions at $h_{\text{dc}} = 2$, caged through the interaction with the vortices strongly pinned at the antidots, forming a square lattice of side length $d/\sqrt{2}$ [264]. Strong vortex-vortex interaction and an ordered vortex configuration imposed by the pinning array is then expected, resulting in a considerable diminution of the dissipative and reactive contributions to the reflected signal, and therefore in a sudden enhancement of ΔS_{11} .

5.5.3 MW power reflection as a function of MW power

In order to determine the thermal limitations of the experimental setup and to evaluate the possible influence of MW heating effects on the sample properties, we have measured the dependence of S_{11} on h_{dc} for different values of P , at fixed f and T . Fig. 5.7 depicts the curves obtained for measurements performed from -13 to 2 dBm (0.05 to 1.58 mW), at $f = 1.86$ GHz and $T = 7.05$ K ($t = 0.979$), when H_{dc} is swept from -100.00 to 100.00 Oe in steps of 0.05 Oe. Similar results have been obtained in Fig. 5.8 which shows the curves obtained for measurements performed at values of P from -20 to 0 dBm (0.01 to 1.00 mW), when H_{dc} is swept from -50.00 to 50.00 Oe in steps of 0.05 Oe at $f = 2.01$ GHz and $T = 7.10$ K ($t = 0.986$), while a magnification in the range between -7 and -1 dBm (0.20 to 0.80 mW) is plotted in panel (b) in this same figure.

The results show that the observation of commensurability phenomena under MW radiation depends on the power supplied to the coil. Higher-order matching effects up to $h_{\text{dc}} = 4$ and 6 are registered for values of P from 0.01 to 0.25 mW [top curves in Fig. 5.8(a)], and for values of P from 0.05 to 0.20 mW [top curves in Fig. 5.7], respectively. Peaks at fractional h_{dc} values ($1/2, 3/2, \dots$) become evident only for values of P from 0.20 to 0.80 mW for $T = 7.10$ K [Fig. 5.8(b)], and from $P = 0.70$ to 0.85 mW for $T = 7.05$ K [lowermost curves in Fig. 5.7]. For $P = 1.00$ mW, the whole $S_{11}(h_{\text{dc}})$ curve collapses to zero and commensurability effects are no longer detected at $T = 7.10$ K. A similar scenario is obtained for $P = 1.58$ mW at $T = 7.05$ K. By comparing these results with those plotted in Figs. 5.4, 5.5 and 5.6, we find that increasing P produces the same effect as if the actual sample temperature, T_s , would gradually grow up to T_c . This means that the MW fields

5. Commensurability effects in ac and microwave power reflection mode experiments

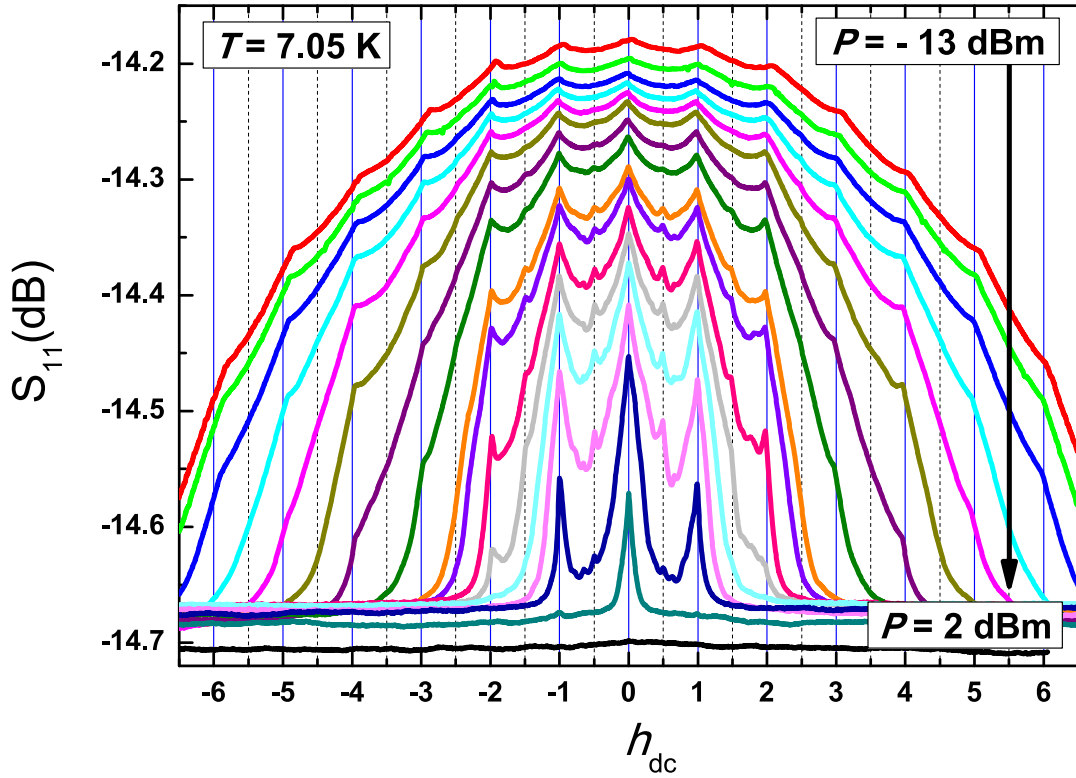


Figure 5.7: Amplitude of the microwave power reflection coefficient in the superconducting state, S_{11} , as a function of the reduced dc magnetic field h_{dc} , when the system temperature is $T = 7.05$ K and the patterned Pb sample is irradiated with microwaves of frequency $f = 1.86$ GHz and nominal power from $P = -13$ dBm (0.05 mW; uppermost curve) to $P = 2$ dBm (1.58 mW; lowermost curve).

5. Commensurability effects in ac and microwave power reflection mode experiments

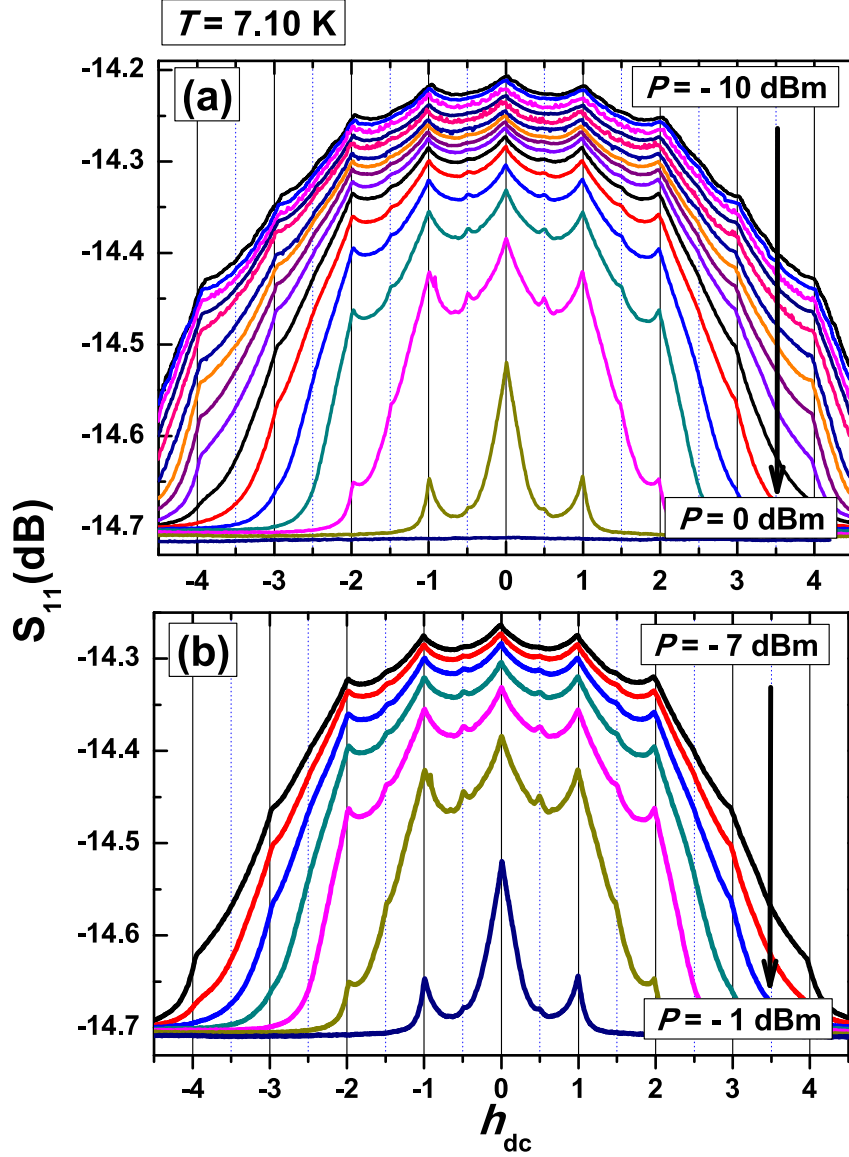


Figure 5.8: Amplitude of the microwave power reflection coefficient in the superconducting state, S_{11} , as a function of the reduced dc magnetic field h_{dc} , when the system temperature is $T = 7.10$ K and the patterned Pb sample is irradiated with microwaves of frequency $f = 2.01$ GHz. Panel (a) shows the results obtained with nominal powers from $P = -20$ dBm (0.01 mW; uppermost curve) to $P = -10$ dBm (0.10 mW) in steps of 2 dBm, and from $P = -10$ dBm to 0 dBm (1.00 mW; lowermost curve) in steps of 1 dBm, while panel (b) shows a magnification of the curves from $P = -7$ dBm (0.20 mW; uppermost curve) to -1 dBm (0.80 mW; lowermost curve).

5. Commensurability effects in ac and microwave power reflection mode experiments

induced in the coil could also dissipate heat and this would contribute to raise T_s . Nevertheless, the fact that the sample is normal in the whole h_{dc} range only for the largest value of P suggests that MW heating is low enough to allow for the observation of matching effects in the most part of the P range. This could be favored by the fact that some heat should be actually removed from the sample by the substrate and the environmental helium, resulting in a low increase of T_s .

5.6 Summary

ac magnetic susceptibility and power reflection methods have been used to investigate the vortex dynamics in a thin film of superconducting Pb containing a periodic square array of antidots which act as artificial pinning centers. Measurements performed close to T_c when dc and MW magnetic fields are applied, for different values of the MW frequency and power, show commensurability effects in the form of steps in the ac susceptibility at low integer multiples of the first matching field which evidence an antidot-dominated pinning regime, and sharp peaks at higher integer values which support the presence of vortices pinned at interstitial positions. Commensurability appears here conditioned by the values of either the power or the frequency applied to the coil. The main effect of the radiation is the reduction of the screening and the enhancement of the dissipation due probably to sample heating.

Commensurability effects have been observed in the form of peaks in the power reflected signal registered from the resonant coil sample setup as a function of the magnetic field at different fixed values of temperature, MW power and frequency. By considering the thin film and antidot corrections to the penetration depth, the two-fluid model and the phenomenology of the vortex dynamics, and neglecting the thermal fluctuations and the Lorentz force, it has been possible to correlate in a dissipative and reactive scenario, the superconducting properties and the occurrence of peaks at the matching fields in the backward signal. Vortex-pinning and vortex-vortex interactions, which favor the geometrical matching between the vortex lattice and the antidot array, are suggested to remain competitive against vortex drift during the sweeping of the magnetic field for integer h_{dc} , but lead to dissipative flux motion at half-integer. The thermal limitations of the experimen-

5. Commensurability effects in ac and microwave power reflection mode experiments

tal setup have been studied and a dissipation of heat from the coil, that would contribute to increase the sample temperature, has been found at the highest MW power.

By comparing the two techniques applied, it is observed that the ac susceptibility allows to cover a wide range of dynamic regimes at a passive linear scenario and to describe the vortex-antidot and vortex-vortex interactions under MW radiation in terms of screening and dissipation processes, while the power reflection method permits to visualize the commensurability phenomenon between the vortex lattice and the periodic pinning potential, to consider the interactions involved in the framework of the two-fluid model, namely the complex conductivity concepts, and to correlate the shielding and losses with the surface resistance and surface impedance.

Finally, the results demonstrate the sensitivity, reproducibility and validity of the techniques used. They may also be relevant for providing a new insight into the vortex associated losses and a new tool for the characterization and further study of the commensurability effects in engineered periodical systems.

Chapter 6

Conclusions

This thesis is a study of the application of a low-temperature microwave probe formed by a multi-turn coil with a sample located in its core, for the investigation of vortex dynamics in thin film superconductors under different microwave techniques.

The first set of experiments focused in the study of the vortex stability under a microwave frequency sweep (sweeping mode) and the application of microwave pulses (pulsed mode) at different values of the thermodynamics variables (temperature and dc magnetic field) and microwave perturbation sensing parameters (frequency, nominal power and pulse duration). The magnetic moment response subject to the sweeping mode in thin films made of $\text{La}_{1.82}\text{Sr}_{0.18}\text{CuO}_4$, patterned Pb and MgB_2 evidences the presence of instabilities in the vortex penetration. These anomalies appear in the temporal- and frequency-dependent magnetic moment curves at certain frequency values forming ripples, small steps, jumps, and negative peaks. In all cases, these frequency-assisted vortex instabilities appear conditioned by a thermal dependence of the characteristic resonant mode. This dependence is associated with the amount of microwave heating energy that is transferred to the probe at each resonant frequency and would result in a heating of the superconducting thin films. To establish with exactness the value of this energy is a challenge due to the complexity of the parameters involved (effective microwave power, amount of heat dissipated in the thermal bath, temperature dependence of the thermal parameters of the superconducting film and substrate, power-dependent microwave properties, etc.), but it also suggests interesting ex-

periments to be performed since they would provide a complete characterization of the layout. This in turn would contribute to set a consistent relationship between the characteristics of the excitation and those of vortex dynamics. The irregularities in the case of MgB_2 seem to have a dependence on the applied power. Ripples and small steps appear at the lowest values of power, while a jump-like behavior comes into view at the highest one. The appearance of such anomalies beyond the threshold temperature value at which the vortex instabilities are expected to be observed, result an interesting phenomenon needs further studies. The studies of vortex instabilities in samples made of $\text{La}_{2-x}\text{Sr}_x\text{CuO}_4$ have been limited, to our best knowledge, to a single crystal. Thus, the presence of irregularities in thin films of this superconducting system sustains the criterion that such phenomenon is a generic feature of the thin-film geometry. In the case of $\text{La}_{1.82}\text{Sr}_{0.18}\text{CuO}_4$, the frequency-triggered anomalies are displayed in a wide range of temperature, as jump-like (for low values of temperature and dc magnetic fields) or as negative peaks (for temperatures close to T_c and high dc magnetic fields). The irregularities are surmised to be constrained by the thermal-dependent parameters in the former case, and by the fluctuation of the vortex motion in the near-edge layer in the latter one. Finally, for patterned Pb, the frequency-driven vortex instabilities emerge in a sea of semi- or full-confined vortices where the vortex-hole and vortex-vortex interactions could act to stabilize the sample magnetization. An interesting question related with the synchronization between the vortex motion and the values of the excitation frequency emerges here. Vortex-jump synchronization could be reached via the electromagnetic interaction with an external resonant circuit causing in such way the generation of electromagnetic radiation. Studies of the time development of the magnetization under pulsed mode manifest the presence of avalanche-like vortex penetration. This change in the gradual penetration of magnetic flux is shown in the form of a jump-like response for values of dc magnetic field, temperature and pulse duration lower than some threshold numbers. Different regimes of flux diffusion are reported in the temporal evolution of the rf-SQUID output signal variation when single microwave pulses are applied as a function of dc magnetic field, temperature, pulse duration and power in the $\text{La}_{1.82}\text{Sr}_{0.18}\text{CuO}_4$. In this case, the presence of a regular fast flux motion is identified as the nucleation of thermoelectromagnetic instabilities

induced by the microwave pulse. Similar features in the form of abrupt discontinuities in the variation of the voltage signal from the magnetometer below certain temperature and dc magnetic field values have been registered in MgB₂.

The frequency-driven vortex instabilities and the avalanche-like response are surmised to be favored by the thin-film geometry and the presence of antidots in the case of Pb. The model proposed for the microwave probe gives a survey of the spatial configurations of the electric and magnetic fields inside the resonant system, which turns to be significant at the edge of the coil. On the basis of these results, the development of vortex instabilities in this set of experiments appears to be assisted by the contributions of these microwave electric and magnetic fields at the resonant mode. Lastly, more insight into the observed phenomena could be obtained by using visualization techniques such as scanning Hall probe microscopy and magneto-optical imaging, which have been demonstrated to be useful to display changes in the flux propagation in superconducting thin films.

The third set of measurements is centered in the investigation of commensurability effects in patterned Pb under ac susceptibility and microwave power reflection spectrometry. The in-phase (shielding) and out-of-phase (dissipation) components of the ac susceptibility under continuous radiation at different resonant modes and microwave power show maxima and minima, respectively, at integer and half-integer values of the matching fields. Different dynamics regimes that result from the interplay of the periodic pinning sites and the vortex system are identified. By comparing the irradiated with the microwave-free curves, a clear shift of the first (reduction of the screening and enhancement of the dissipation) with respect to the second is observed at different frequency and power values. The effect of the microwave heating is confirmed by registering the ac magnetic susceptibility as a function of the microwave power at the values of the resonant frequency used. Here, the curves show a thermal dependence behavior that characterizes the microwave-free ac susceptibility measurements.

The magnetic field dependence of the backward reflection coefficient registered for values of temperature from $T/T_c = 0.995$ down to 0.944, and at different fixed values of the resonant frequency, show the presence of commensurability effects between the vortex lattice parameter and the antidot array spacing. The signature of this commensurability is observed in the form of peaks at integer

and fractional matching fields. The influence of the microwave heating effects on the sample has been confirmed by performing these measurements for different values of power at fixed values of frequency and temperature. Here, with the enhancement of the power, the curves behave in a similar way as if the sample temperature is gradually enhanced up to T_c . The presence of these peaks is explained by considering the contribution of the vortex dynamics to the reflected signal at the matching fields. A correlation between the high screening in the ac response and the peaks in the reflected signal at the matching fields has been established under the framework of the two-fluid model for the complex conductivity, and the concepts of surface resistance and surface impedance for superconductors. The power reflection measurements performed here show a high sensitivity to any variation that originates from changes in the system temperature. Finally, it appears interesting to extend the use of this technique to other patterned thin superconducting systems, particularly to those where commensurability effects have been registered for temperature far enough from T_c ($T/T_c = 0.87$) and dc magnetic fields as high as 1 tesla.

To conclude, the low-temperature microwave probe designed to be used in a rf-SQUID magnetometer has proven to be a simple and practical microwave layout for performing vortex dynamics studies in thin superconducting films under different microwave techniques. The resonant structure appears to disturb significantly the gradual penetration of the magnetic flux under sweeping and pulsed mode, while it results sensitive to register the variation in the vortex dynamics in patterned films. We are currently improving the setup and performing study under sweeping and pulsed mode in superconducting tantalum nitride (TaN) and niobium nitrate (NbN) thin films.

Abstract

Introducció

La superconductivitat es caracteritza per una resistència zero a camps magnètics continus, per una quasi completa expulsió dels camps magnètics des de l'interior de la mostra (estat Meissner o diamagnètic), i per ser un efecte macroscòpic quàntic que sorgeix de la naturalesa mecanicoquàntica de l'estat correlacionat dels electrons superconductors. Aquest estat particular de la matèria està limitat per tres paràmetres crítics: la temperatura T_c , el camp magnètic H_c , i la densitat de corrent J_c . Un cop s'han traspasat uns d'aquests valors, el material superconductor torna al seu estat normal. El descobriment de la superconductivitat en òxids de coure dopat amb forats amb alta T_c de fins a 134 K, va suposar un pas molt significatiu tant pel que fa a la temperatura de transició i les propietats d'aquests nous materials com pel que fa a la seva utilització tecnològica. El fet de disposar d'una baixa dissipació de potència, una profunditat de penetració independent de la freqüència, una sobtada transició entre l'estat superconductor i l'estat normal, i un règim de temperatura de treball més assequible (per sobre la temperatura de líquidació del nitrogen, 77 K), conjuntament amb alts valors de J_c , proporcionen bons fonaments per considerar la implementació i realització d'aquests materials en dispositius de radiofreqüència d'alt rendiment i de microones basats en superconductors. Actualment, a causa de la seva baixa resistència superficial, molts materials superconductors han començat a substituir els metalls normals en el muntatge de dispositius electrònics de baixes pèrdues com filtres, antenes, ressonadors, etc. A més, la naturalesa no dispersiva dels superconductors els fan adequats per a la seva utilització en sistemes de microones sense fils i comunicació en

satèl·lits. La llista d'aplicacions inclou cables de transmissió elèctrica, motors, generadors, limitadors de corrent, sistemes superconductors d'emmagatzemament d'energia magnètica, sistemes de transport per levitació magnètica superconductora (Maglev), imatge en el rang del Terahertz, i computació d'alta velocitat, entre d'altres.

La majoria de materials superconductors, inclosos els d'alta T_c , amb interès tecnològic són superconductors tipus-2, els quals són penetrats pel flux magnètic en forma de quàntums de flux magnètic o vòrtexs a partir d'un camp magnètic crític inferior (10^{-2} tesles) fins a un de superior (10^2 tesles) on el material esdevé normal i els camps magnètics penetren uniformement la mostra. La visió clàssica d'aquest estat mixt considera que els vòrtexs formen una xarxa rígida. En aquests nous materials l'escala nanomètrica del cor dels vòrtexs (longitud de coherència petita) i l'escala mesoscòpica associada als corrents que circulen al seu voltant (longitud de penetració alta), juntament amb el fet que la interacció amb els defectes (energia d'ancoratge) i l'energia tèrmica (alta T_c) són totes dues comparables, fa que es generi una dinàmica de vòrtexs molt rica i diferent a la xarxa rígida. Aquest aspecte resulta rellevant des del punt de vista de les aplicacions, ja que per obtenir corrents crítics elevats s'ha d'ancorar els vòrtexs en una fase sòlida. Una forma d'ancorar-los ha estat el confinament en defectes columnars creats per la irradiació d'ions pesants, el que ha resultat en un increment significatiu de J_c . A l'actualitat, la combinació de les tècniques de creixement de capes primes amb la litografia micromètrica ha obert la possibilitat de fabricar superconductors nanoestructurats i objectes ultra-prims amb geometries molt ben definides a escales macroscòpiques. Això ha permès crear centres periòdics d'ancoratge, com per exemple forats amb dimensions nanomètriques. Capes primes de materials superconductors de baixa i alta T_c , amb formacions regulars de centres d'ancoratge mostren màxims periòdics del corrent crític a camps magnètics (matching fields) on la densitat de vòrtexs commensura amb la densitat de la xarxa de centres d'ancoratge. Una alternativa a la litografia ha estat l'ús de mem-

branes d'òxid d'alumini anoditzat com a substrat per a la deposició de capes primes de superconductors de baixa T_c . Aquesta nova tècnica permet observar increments periòdics de J_c en un rang de temperatura allunyat de T_c i amb camps magnètics de l'ordre de la tesla.

Uns dels materials que crida l'atenció per les seves bones propietats superconductores és l'aliatge MgB_2 , que presenta una $T_c = 39$ K, la qual duplica gairebé els 23 K en els quals s'havia establitzat el progrés de la T_c en els aliatges intermetàl·lics en el descobriment de la superconductivitat d'alta temperatura. A més, l'existència de dos paràmetres d'ordre superconductor gairebé independents en aquest nou material fa que s'obrin nous tòpics fonamentals d'investigació com la de l'estat semi-Meissner, efectes Josephson intrínsecs, o la d'un nou tipus de superconductivitat, l'anomenada 1.5.

A banda de la mobilitat dels vòrtexs, els materials superconductors poden, sota certes condicions, desenvolupar una inestabilitat termoelectromagnètica. Aquest fenomen consisteix en una propagació abrupta d'una interfície superconductor-normal, que deixa darrere una sendera de material sobreescalfat. Aquesta interfície es precipita a una gran profunditat del material tractant d'establir l'estat d'energia més baixa, per al qual la distribució del flux magnètic és pla a tot arreu. Aquest inestabilitat dels vòrtexs constitueix una limitació molt important sobre el valor de J_c i un seriós inconvenient en la utilització dels materials superconductors a camps magnètics alts i el desenvolupament potencial de dispositius basats en aquests materials.

L'objectiu d'aquesta tesi és estudiar la dinàmica de vòrtexs en diverses capes primes superconductores de tipus-2. En particular, explorem la resposta del moment magnètic en temps real a camps continus i polsats de microones. A més, estudiem els efectes de commensurabilitat mitjançant mesures de susceptibilitat magnètica en presència de camps de microones, i fent servir també espectrometria de reflexió de microones.

Tècniques experimentals

Les mostres utilitzades en aquesta tesi són mostres de capes primes superconductores fetes de $\text{La}_{1.82}\text{Sr}_{0.18}\text{CuO}_4$, Pb amb una formació periòdica micro-forats o antidots i MgB_2 . Les dimensions i T_c d'aquestes mostres són, respectivament, $3 \times 3 \text{ mm}^2$ i 200 nm de gruix i 27 K, $6 \times 4 \text{ mm}^2$ i 50 nm de gruix i 7.20 K, i $3 \times 3 \text{ mm}^2$ i 200 nm de gruix i 30 K. Les mesures dels moments magnètics i de la susceptibilitat magnètica es van realitzar amb l'ajuda d'un magnetòmetre MPMS basat en un dispositiu rf-SQUID, que permet mesurar moment magnètic amb una resolució de 10^{-8} emu i aplicar camps magnètics fins a ± 5 T dins del rang de temperatura entre 1.8 i 350 K. Aquest mateix equip es va utilitzar per obtenir la magnetització de la mostra en funció del temps en el rang dels mil·lisegons. La sonda de baixa temperatura de microones està formada per un cable coaxial semi-rígid (d'uns 2 metres de llargada), el qual acaba en una bobina de múltiples voltes amb la mostra localitzada al seu nucli (CS). Aquesta bobina està formada per un solenoide de 10 voltes i 1.55 mil·límetres de longitud fet amb cable de coure de 99.9% de puresa i de 0.1 mm de gruix. El bobinat s'ha fet sobre una palleta de plàstic buida, d'una secció transversal de 12 mm^2 . El CS s'ha introduït dins del magnetòmetre en el centre de l'imant superconductor. L'orientació de la mostra respecte al camp magnètic continu es perpendicular. Entre el CS i el conductor central de línia de transmissió s'ha deixat una distància d'uns 15 cm per evitar contribucions del cable coaxial a les mesures de magnetització. El cable coaxial rígid es va connectar als diferents equips de microones depenent de la tècnica utilitzada, mitjançant un cable coaxial flexible de 72 cm de llargada. El muntatge de la sonda de baixes temperatures no permet realitzar un calibratge sencer a les temperatures de treball. Malgrat tot, s'ha pogut filtrar el senyal reflectit pel cable coaxial flexible. La potència de microones, registrada a temperatura ambient, dóna uns valors inferiors en quatre ordres de magnitud al de la potència nominal a la sortida del generador.

El registrament de la resposta del moment magnètic en funció de la

frequència es va realitzar refredant des de l'estat normal a camp zero la mostra encastada en la bobina fins a la temperatura de treball per sota de T_c . Seguidament es va establir un camp magnètic continu i a continuació, deixant fixos tant la temperatura com el camp magnètic, es va fer un escombratge de la freqüència des de 0.10 fins a 4.00 GHz en passos de 0.02 GHz. El moment magnètic es va registrar a cada pas de freqüència. El temps de mesura de cada punt va ser d'uns 24 segons i la taxa d'escombratge va ser de 0.8 MHz. En acabar l'escombratge, es va apagar el camp magnètic i la mostra es va escalfar per sobre T_c . Idèntiques mesures a les fetes amb la mostra es van realitzar amb la mostra en estat normal i amb el substrat dins la bobina. Això va permetre descartar les contribucions del ressonador i el substrat sobre la mesura feta amb la mostra.

Les mesures de magnetització sota camps polsats de microones es van realitzar deixant fix el CS a la regió central del magnetòmetre. Per tal de garantir l'estabilitat temporal del camp magnètic durant el procés de mesura, es va operar l'imant superconductor amb una font externa. Les mesures es van realitzar després d'un procés de refredament en camp zero o bé després d'un refredament aplicant un camp magnètic. L'evolució temporal de la magnetització es va registrar prenent el senyal de voltatge de sortida des de l'SQUID, en passos de 0.5 o 0.1 mil·lisegons durant 200 o 100 mil·lisegons, respectivament amb diferents valors fixos de camp magnètic, de temperatura i dels paràmetres de microones pertorbatius (duració del pols, freqüència i potència). Per tal de certificar la presència de processos estocàstics, cada mesura es va realitzar diverses vegades sota les mateixes condicions experimentals inicials. Les dades d'aquestes mesures es van mitjanar.

Per tal de realitzar mesures de la potència reflectida en funció del camp magnètic continu a una temperatura fixa determinada, primerament es va col·locar el CS al centre del magnetòmetre. Posteriorment, es va escollir una freqüència ressonant. A continuació, es va refredar el CS en camp zero fins a la temperatura de treball. Després, al mateix

temps que es va realitzar un escombrat del camp magnètic continu amb ajuda d'una font externa en passos de 25 o 50 mOe, es va irradiar de forma contínua a una potència seleccionada, i es va enregistrar el senyal de la potència reflectida a cada pas del camp magnètic. Adicionalment, per tal d'establir les limitacions tèrmiques de la sonda i la possible influència de l'escalfament de microones sobre el CS, es van realitzar mesures de la potència reflectida en funció del camp magnètic continu a diferents valors de potència.

Finalment, per caracteritzar l'estructura ressonant formada pel CS, s'ha proposat un model teòric basat en el ressonador helicoïdal. El model reproduïx amb molta fidelitat, dintre d'un marge petit d'error, els valors de la freqüència ressonant registrats amb la mostra de Pb. A més, el model permet obtenir la distribució espacial dels camps elèctrics i magnètics de microones dins de l'estructura ressonant. Aquests camps apareixen pràcticament homogenis i considerablement petits en una àrea extensa de la bobina, tret de la regió a la vora del CS.

Inestabilitat dels vòrtexs induïda pels camps de microones

L'estudi de la dinàmica de vòrtexs sota l'escombrat de freqüència es va dur a terme en les tres mostres esmentades anteriorment.

L'evolució temporal del moment magnètic en funció de la freqüència de microones es diferencia significativament de la mateixa evolució obtinguda sense irradiació. La relaxació monòtona convencional és interrompuda per la presència d'irregularitats en forma de salts, pics negatius, ondulacions i petits passos. Aquestes anomalies apareixen a cert valor de la freqüència de microones i a diferents valors de les variables termodinàmiques (temperatura i camp magnètic continu) i dels paràmetres d'excitació de microones (potència i freqüència). En el cas de la mostra de $\text{La}_{1.82}\text{Sr}_{0.18}\text{CuO}_4$, els salts apareixen més aviat a baixes temperatures. A mesura que augmenta la temperatura el salts es transformen en pics negatius. Aquesta mateixa resposta s'observa per a mesures fetes a camps magnètics continus alts. Les

mesures fetes amb la mateixa mostra per a valors fixos de la temperatura i del camp magnètic continu per a diferents valors de potència presenten salts de diferents altures, més o menys per al mateixos valors de freqüència. La presència d'aquestes irregularitats no depèn ni de la direcció d'escombratge de la freqüència (de manera creixent o decreixent), ni de la història tèrmica o magnètica abans o durant el procés d'escombratge (refredament en camp magnètic zero o refredament en presència de camp magnètic). Resulta interessant que la presència d'irregularitats en aquesta mostra és visible en un marge ample de temperatura. En el cas de la mostra de Pb amb una formació periòdica de microforats, les mesures d'escombratge de la freqüència es van fer per a uns valors fixos de temperatura i camp magnètic continu i a diferents valors de potència de microones. Aquí la resposta del moment magnètic presenta un comportament en forma d'escala, amb regions planes interrompudes per salts a diferents valors de la freqüència. La dinàmica de vòrtexs en aquest cas està determinada per la presència dels centres periòdics d'ancoratge, els quals afavoreixen la formació d'una estructura metaestable un cop cessa la pertorbació de la freqüència ressonant. A la mostra de MgB_2 , la penetració suau dels vòrtexs és interrompuda per petites ondulacions que apareixen desplaçades si les mesures es realitzen a diferents valors de temperatura i camps magnètics continus. A mida que la s'incrementa potència, en lloc d'ondulacions apareixen petits salts. Al màxim valor de potència aplicada, les corbes de relaxació són interrompudes per salts. En aquest darrer cas el salts són seguits d'un comportament pla. En aquesta mena de mostra, el comportament del moment magnètic apareix condicionat pel valor de la potència de microones, però també per la temperatura límit a la qual s'observa el fenomen d'inestabilitat termo-electromagnètica dels vòrtexs.

La presència d'irregularitats en la resposta del moment magnètic en funció de la freqüència apareix determinada per la freqüència ressonant del CS. L'energia de les microones a la freqüència ressonant és significativa i pot contribuir de dues formes a la resposta magnètica:

una part pot escalfar la mostra (escalfament de microones), i l'altra part pot resultar absorbida per la mostra. Establir aquestes parts resulta complicat a causa de la dificultat d'establir la quantitat d'energia que arriba al CS, o que es transfereix al sistema refrigerant, i per les dependències tèrmica i magnètica de certs paràmetres del superconductor i del substrat. Malgrat tot, no es pot descartar un petit escalfament de la mostra. Altres aspectes que poden afavorir l'aparició d'aquestes irregularitats són la geometria de la capa fina i la contribució dels camps elèctrics i magnètics de microones. Aquests últims resulten significatius a la vora de la regió mostra-bobina i poden ajudar a activar inestabilitats termo-electromagnètiques dels vòrtexs. Particularment, la contribució del camp elèctric pot facilitar el desenvolupament d'aquesta mena d'inestabilitat en condicions adiabàtiques.

El registre de la variació temporal de la magnetització sota la influència d'un pols de microones es va dur a terme en les mostres de $\text{La}_{1.82}\text{Sr}_{0.18}\text{CuO}_4$ i MgB_2 . A la primera s'identifiquen diferents règims de penetració dels vòrtexs en funció del camp magnètic continu, la temperatura, la durada del pols i la potència. Les corbes d'evolució temporal de la variació de la magnetització mostren clarament un règim de ràpida difusió dels vòrtexs. Aquest règim existeixen dins d'un marge de valors del camp magnètic continu, la temperatura, i la durada del pols. A més, aquestes corbes presenten valors de màxima difusió en funció d'aquests mateixos paràmetres. Una resposta similar en forma de canvis significatius en l'evolució de la magnetització s'observa per al cas del MgB_2 . Aquí, les corbes mostren anomalies que persisteixen en un rang definit de camp magnètic continu i de temperatura. La presència d'aquestes inestabilitats disparades pels pols sembla que resulten de la contribució dels camps elèctrics i magnètics de microones i de la geometria de capa prima.

Efectes de commensurabilitat en experiments de susceptibilitat magnètica i potència reflectida de microones

Les mesures dels components de la susceptibilitat magnètica en funció del camp magnètic continu irradiat amb diferents valors de potència i freqüència de microones mostren els característics efectes de commensurabilitat per a múltiples enters i fraccionaris dels camps de coincidència (matching). La presència en aquestes corbes de passos i pics evidencia el confinament dels vòrtexs a aquests valors i l'aparició de diferents règims dinàmics. Aquests règims resulten de la competició entre les forces d'ancoratge de la formació periòdica de forats i la interacció del sistema elàstic de vòrtexs. La regió amb passos és identificada com la zona on l'ancoratge és dominat per la interacció entre els vòrtexs i els forats, mentre que la regió de pics s'associa a la zona on la interacció entre vòrtexs es fa dominant. Les corbes a diferents valors de freqüència i potència mostra que l'augment de qualsevol d'aquest dos paràmetres resulta en la reducció de l'apantallament i l'increment de la dissipació. Aquest efecte va ser confirmat realitzant mesures de les components de la susceptibilitat magnètica en funció de la potència als diferents valors de la freqüència de microones. En realitat, el comportament d'aquestes dues components és igual al que s'obté per a mesures de les mateixes components en funció de la temperatura. Tot això confirma que l'efecte de la radiació és l'augment de la temperatura de la mostra.

Les corbes del mòdul del coeficient de reflexió de microones en funció del camp magnètic continu a una potència i freqüència de microones fixes, mesurades a diferents valors de temperatura, mostren clarament els efectes de commensurabilitat. L'empremta d'aquest efecte es mostra en forma de pics a valors enters i fraccionaris dels camps de coincidència. Aquest pics són significatius a temperatures properes a T_c i es van difuminant a mida que la temperatura augmenta. Malgrat tot, els efectes de commensurabilitat s'observen a temperatures relativament allunyades de T_c . Aquest comportament es va detectar per a idèntiques mesures realitzades amb diferents valors de la freqüència ressonant. La tendència que segueixen les corbes del coeficient de reflexió fora dels valors dels camps de coincidència és

suau i monòtona. L'observació dels pics a les corbes del coeficient de reflexió apareix com a resultat de la contribució de la dinàmica de vòrtexs al senyal reflectit als camps de coincidència. La presència d'aquest pics es pot explicar considerant els conceptes de la conductivitat complexa del model de dos fluids, la longitud de penetració de London i les forces que descriuen la dinàmica de vòrtexs en l'equació de balanç fenomenològic. Quan la densitat de vòrtexs iguala la de forats, la densitat de vòrtexs que es mouen es redueix i, com a conseqüència, les forces dissipatives són més petites. Això resulta en un augment de la contribució dels parells de Cooper via σ_2 a la conductivitat complexa per a temperatures per sota de T_c i, com a resultat, en un decreixement de la longitud de penetració. Conseqüentment, la quantitat de camp magnètic emmagatzemat dins la mostra i la part reactiva de la impedància superficial es redueixen. La disminució de la profunditat de penetració comporta un canvi en el volum creat per les ones electromagnètiques dins la cavitat ressonant formada pel CS i, per tant, produeix una desviació en les característiques de la freqüència ressonant, la qual es reflecteix en un augment del senyal de reflectit. Una desviació del camp magnètic respecte als valors de coincidència provoca el moviment de vòrtexs. Aquest moviment comporta una dissipació a causa dels processos de relaxació de les quasi-partícules normals que existeixen dins el nucli del vòrtex. Cal dir que la presència de portadors normals de càrrega a la mostra contribueix a l'augment de la resistència superficial via σ_2 . Així doncs, la reducció de l'àrea superconductora dins de la mostra i l'increment de la resistència superficial a mesura que s'incrementa el camp magnètic comporta un decaïment monòton del senyal reflectit fins que es fa nul quan el camp arriba al camp crític superior. A camps fraccionaris de coincidència, els pics esdevenen poc profunds com a conseqüència d'una major mobilitat dels vòrtexs i, per tant, de l'augment de la dissipació.

Finalment, les limitacions tèrmiques de la sonda experimental han estat testades fent mesures del coeficient de reflexió en funció del camp

magnètic continu a diferents valors de la potència de microones, per a valors fixos de temperatura. Els resultats mostren que el fenomen de la commensurabilitat enregistrat mitjançant les variacions del coeficient de reflexió depèn de la potència aportada a la bobina. Amb l'increment de la potència, les corbes descriuen un comportament com el que s'observaria si la temperatura de la mostra s'incrementés, arribant a col·lapsar-se per al valor més alt de potència utilitzada.

Conclusions

La sonda de microones de baixa temperatura dissenyada per ser utilitzada en un magnetòmetre rf-SQUID ha demostrat ser un dispositiu de microones simple i pràctic per realitzar estudis de la dinàmica de vòrtexs en mostres de capes primes superconductores. L'estructura ressonant apareix com una font de pertorbació en el procés gradual de penetració dels vòrtexs quan es duu a terme un escombratge de la freqüència amb les variables termodinàmiques i la potència de radiació de microones fixes. Aquest mateix resultat s'observa quan es registra l'evolució temporal de la magnetització sota l'aplicació de pols de microones. El sistema ressonant resulta sensible al registrament d'efectes de commensurabilitat en presència de centres periòdics d'ancoratge. Per acabar, aquest enfocament experimental i els resultats presentats aquí també poden ser rellevants per realitzar estudis de dinàmica de vòrtexs en altres sistemes de capes primes superconductores. L'ús conjunt d'altres tècniques, com pot ser la imatge magnetoòptica, poden resultar de molta utilitat per revelar la distribució espacial del flux magnètic abans, durant i després de la inestabilitat dels vòrtexs.

Appendix A: ac magnetic susceptibility

A magnetic susceptibility measurement is based on the Meissner effect which predicts the expulsion of the magnetic field from a superconductor in its superconducting state. The ac susceptibility is a measure of a sample magnetization and is defined as

$$\chi = M/H_{dc}, \quad (1)$$

where M is the magnetization and H_{dc} is the applied dc magnetic field. When an ac magnetic field, $H_{ac} = h_0 \cos \omega t$, is applied the magnetization of the sample will change in time and the susceptibility can be written as

$$\chi = dM/dH_{ac}. \quad (2)$$

A phase difference ϕ can occur between the magnetization and the applied field, due to certain relaxation processes in the material:

$$M_{ac} = M_0 \cos(\omega t) \cos \phi + M_0 \sin(\omega t) \sin \phi = \chi' h_0 \cos(\omega t) + \chi'' h_0 \sin(\omega t) \quad (3)$$

where,

$$\chi' = \frac{M_0 \cos \phi}{h_0}, \quad (4)$$

$$\chi'' = \frac{M_0 \sin \phi}{h_0}. \quad (5)$$

This can be written in the complex notation as

$$M_{ac} = \chi h_0 \exp(i\omega t) \quad (6)$$

$$\chi = \chi' + i\chi'' \quad (7)$$

The in-phase component χ' gives a quantitative expression for the amount of flux penetration into the sample. For a complete Meissner expulsion (in the superconducting state of the sample) $\chi' = -1$, whereas for full penetration (in the normal state) $\chi' = 0$. The out-of-phase component χ'' is proportional to the energy losses in the sample.

As the temperature increases towards T_c , the lower critical field, H_{c1} , is exceeded and flux lines and bulk shielding currents start penetrating the sample. The losses in the sample rise and reach a maximum at T_{max} when the flux lines fully penetrate the material, $H_*(T_{max}) = H_{ac}$. As the temperature increase beyond T_c , the shielding currents recede and the losses drop to zero again. A peak in χ'' is observed and χ' decreases to zero.

In the Bean model, no frequency dependence of the susceptibility is predicted. However, at high frequency (> 100 kHz) a logarithmic variation of the transition temperature as a function of frequency has been observed in ac susceptibility measurements. This effect has been explained by the theory of Anderson and Kim, based on flux creep. In our experiments we only used frequencies below 100 kHz, which is too low to see flux creep effects.

Bibliography

- [1] J.G. Bednorz, and K.A. Müller, Z. Phys. B: Condens. Matter **64**, 189 (1986). [1](#), [9](#)
- [2] A. A. Abrikosov, Sov. Phys. JETP **5**, 1174 (1957). [1](#), [8](#), [14](#), [15](#), [20](#)
- [3] Y. Tanaka, M. Akiya, H. Ishii, A. Saito, and S. Ohshima, IEEE Trans. Appl. Superconduct. **23**, 6384702 (2013). [2](#)
- [4] M.J. Lancaster, *Passive Microwave Device Applications of High Temperature Superconductors*, **ch. 1**, Cambridge University Press, Cambridge, 1997. [2](#), [33](#), [34](#)
- [5] M.P. Paranthaman, T.A.L. Stan, Q. Jia, C. Cantoni, and S.H. Wee, Supercond. Sci. Technol. **27**, 022002 (2014). [2](#)
- [6] A. Palau, E. Bartolomé, A. Llordés, T. Puig, and X. Obradors, Supercond. Sci. Technol. **24**, 125010 (2011). [2](#)
- [7] C. Li, H. Li, X. Zhang, Ch.Li, L. Sun, Q. Zhang, J. Wang, Y. Bian, and Y. He, J. Supercond. Novel Magn. **26**, 1843 (2013). [2](#)
- [8] M. Nisenoff, Proc. IEEE MTT-S International Microwave Symposium Digest, paper WE1F-2 (2011). [2](#), [3](#)
- [9] S. Anders, M.G. Blamire, F.-Im. Buchholz, D.-G. Crété, R. Cristiano, P. Febvre, L. Fritzsche, A. Herr, E. Il'ichev, J. Kohlmann, J. Kunert, H.-G. Meyer, J. Niemeyer, T. Ortlev, H. Rogalla, T. Schurig, M. Siegel, R. Stolz,

-
- E. Tarte, H. J.M. ter Brake, H. Toepfer, J.-C. Villegier, A.M. Zagoskin, and A.B. Zorin, *Physica C* **470**, 2079 (2010). [2](#)
- [10] C.P. Foley, and H. Hilgenkamp, *Supercond. Sci. Technol.* **22**, 064001 (2009). [2](#)
- [11] S.K. Remillard, and S. Cordone, *J. Supercond. Novel Magn.* **19**, 523 (2006). [2](#)
- [12] A.V. Velichko, M.J. Lancaster, and A. Porch, *Supercond. Sci. Technol.* **18**, R24 (2005). [2](#), [50](#)
- [13] M. Hein, *High-Temperature Superconductor Thin Films at Microwave Frequencies*, ch. 6, Springer Tracts in Modern Physics, vol. 155, Springer, Berlin, 1999. [2](#)
- [14] M.J. Lancaster, *Passive Microwave Device Applications of High Temperature Superconductors*, **ch. 5–8**, Cambridge University Press, Cambridge, 1997. [2](#)
- [15] J. Wosik, L.-M. Xie, and R. Grabovickic, *Supercond. Sci. Technol.* **22**, 1050003 (2009). [2](#)
- [16] M. Hein, T. Kaiser, and G. Müller, *Phys. Rev. B* **61**, 640 (2000). [2](#)
- [17] S. Nishijima, S. Eckroad, A. Marian, K. Choi, W.S. Kim, M. Terai, Z. Deng, J. Zheng, J. Wang, K. Umemoto, J. Du, P. Febvre, S. Keenan, O. Mukhanov, L.D. Cooley, C.P. Foley, W.V. Hassenzahl, and M. Izumi, *Supercond. Sci. Technol.* **26**, 113001 (2013). [3](#)
- [18] L. Civale, A.D. Marwick, T.K. Worthington, M.A. Kirk, J.R. Thompson, L. Krusin-Elbaum, Y. Sun, J.R. Clem, and F. Holtzberg, *Phys. Rev. Lett.* **67**, 648 (1991). [3](#)
- [19] P. Martinoli, O. Daldini, C. Leemann, and B. Van den Brandt, *Phys. Rev. Lett.* **36**, 382 (1976) [3](#)

-
- [20] D.A. Glocker and S.I. Shah (eds.), *Handbook of Thin Film Process Technology*, Institute of Physics Publishing, Bristol, 1998. [3](#)
- [21] J.I. Martín, Y. Jaccard, A. Hoffmann, J. Nogués, J.M. George, J.L. Vicent, and I.K. Schuller, *J. Appl. Phys.* **84**, 411 (1998). [3](#), [116](#)
- [22] A. Castellanos, R. Wördenweber, G. Ockenfuss, A. v.d. Hart, and K. Keck, *Appl. Phys. Lett.* **71**, 962 (1997). [3](#), [114](#), [116](#)
- [23] V.V. Moshchalkov, L. Gielen, M. Baert, V. Metlushko, G. Neuttiens, C. Strunk, V. Bruyndoncx, X. Qiu, M. Dhallé, K. Temst, C. Potter, R. Jonckheere, L. Stockman, M. Van Bael, C. Van Haesendonck, and Y. Bruynseraede, *Physica Scripta* **T55**, 168 (1994). [3](#), [116](#)
- [24] Victor V. Moshchalkov and Joachim Fritzsche, *Nanostructured Superconductors*, World Scientific Publishing Co. Pte. Ltd. Singapore, 2011. [3](#), [16](#), [17](#), [18](#), [21](#), [22](#), [65](#), [90](#)
- [25] V.V. Moshchalkov, R. Wördenweber, and M. Lang, *Nanoscience and Engineering in Superconductivity*, Berlin: Springer, 2010. [3](#), [65](#)
- [26] U. Welp, X.L. Xiao, V. Novosad, and V.K. Vlasko-Vlasov, *Phys. Rev. B* **71**, 014505 (2005). [3](#)
- [27] W.K. Kwok, Z.L. Xiao, U. Welp, A. Rydh, V. Vlasko-Vlasov, and V. Novosad, *Physica C* **412**, 347 (2004). [3](#)
- [28] J.W. Sinclair, Y.L. Zuev, C. Cantoni, S.H. Wee, C. Varanasi, J.R. Thompson, and D.K. Christen, *Supercond. Sci. Technol.* **25**, 115003 (2012). [3](#)
- [29] C. Buzea, and T. Yamashita, *Supercond. Sci. Technol.* **14**, R115 (2011). [3](#)
- [30] A. Gurevich, S. Patnaik, V. Braccini, K.H. Kim, C. Mielke, X. Song, L.D. Cooley, S.D. Bu, D.M. Kim, J.H. Choi, L.J. Belenky, J. Giencke, M.K. Lee, W. Tian, X.Q. Pan, A. Siri, E.E. Hellstrom, C.B. Eom, and D.C. Larbalestier, *Supercond. Sci. Technol.* **17**, 278 (2004). [3](#)

-
- [31] H.J. Kim, W.N. Kang, E.M. Choi, M.S. Kim, K.H.P. Kim, and S.I. Lee, Phys. Rev. Lett. **87**, 087002 (2001). [3](#)
- [32] G. Ghigo, D. Botta, A. Chiodoni, L. Gozzelino, R. Gerbaldo, F. Laviano, E. Mezzetti, E. Monticone, and C. Portesi, Phys. Rev. B **71**, 214522 (2005). [3](#)
- [33] J. Nagamatsu, N. Nakagawa, T. Muranaka, Y. Zenitani, and J. Akimitsu, Nature (London) **410**, 63 (2001). [3](#), [9](#)
- [34] H.J. Choi, D. Roundy, H. Sun, M.L. Cohen, and S.G. Louie, Nature (London) **418**, 758 (2002). [3](#)
- [35] S. Souma, Y. Machida, T. Sato, T. Takahashi, H. Matsui, S.-C. Wang, H. Ding, A. Kaminski, J.C. Campuzano, S. Sasaki, and K. Kadowaki, Nature **423**, 65 (2003). [3](#)
- [36] F. Bouquet, R.A. Fisher, N.E. Phillips, D.G. Hinks, and J.D. Jorgensen, Phys. Rev. Lett. **87**, 047001 (2001). [3](#)
- [37] E. Babaev, and J.M. Speight, Phys. Rev. B **72**, 180502(R) (2005). [3](#), [17](#)
- [38] E. Babaev, and N.W. Ashcroft, Nature Phys. **3**, 530 (2007). [4](#)
- [39] L.F. Chibotaru, V.H. Dao, and A. Ceulemans, Europhys. Lett. **78**, 47001 (2007). [4](#)
- [40] G. Blumberg, A. Mialitsin, B.S. Dennis, M.V. Klein, N.D. Zhigadlo, and J. Karpinski, Phys. Rev. Lett. **99**, 227002 (2007). [4](#)
- [41] E. Babaev, L.D. Faddeev, and A.J. Niemi, Phys. Rev. B **65**, 100512(R) (2002). [4](#)
- [42] Y. Tanaka, Supercond. Sci. Technol. **28**, 034002 (2015). [4](#)
- [43] E.H. Brandt, and M.P. Das, J. Supercond. Nov. Magn. **24**, 57 (2011). [4](#), [16](#)
- [44] V.V. Moshchalkov, M. Menghini, T. Nishio, Q.H. Chen, A.V. Silhanek, V.H. Dao, L.F. Chibotaru, N.D. Zhigadlo, J. Karpinski, Phys. Rev. Lett. **102** 117001 (2009). [4](#), [9](#), [15](#)

-
- [45] M. Tinkham, *Introduction to Superconductivity*, McGraw Hill Inc., New York, 1996. [4](#), [10](#), [11](#), [13](#), [14](#), [19](#), [20](#), [23](#), [24](#), [28](#), [106](#)
- [46] M. Baziljevich, E. Baruch-El, T.H. Johansen, and Y. Yeshurun, *Appl. Phys. Lett.* **105**, 012602 (2014). [4](#), [64](#), [65](#)
- [47] A. Nabisiałek, A. Wisniewski, V.V. Chabanenko, S.V. Vasiliev, T.V. Tsvetkov, and F. Pérez-Rodríguez, *Supercond. Sci. Technol.* **25**, 035005 (2012). [4](#), [64](#), [65](#), [89](#)
- [48] A. Nabisiałek, M. Niewczas, H. Dabkowska, A. Dabkowski, J.P. Castellán, and B.D. Gaulin, *Phys. Rev. B* **67**, 024518 (2003). [4](#), [64](#), [65](#), [95](#)
- [49] U. Bolz, B. Biehler, D. Schmidt, B.-U. Runge, and P. Leiderer, *Europhys. Lett.* **64**, 517 (2003). [4](#), [64](#), [71](#), [95](#), [110](#)
- [50] P. Leiderer, J. Boneberg, P. Brüll, V. Bujok, and S. Herminghaus, *Phys. Rev. Lett.* **71**, 2646 (1993). [4](#), [64](#), [65](#), [110](#)
- [51] M.E. McHenry, H.S. Lessure, M.P. Maley, J.Y. Coulter, I. Tanaka, and H. Kojima, *Physica C* **190**, 403 (1992). [4](#), [64](#), [65](#), [88](#)
- [52] M.E. McHenry, S. Simizu, H.S. Lessure, M.P. Maley, J.Y. Coulter, I. Tanaka, and H. Kojima, *Phys. Rev. B* **44**, 7614 (1991). [4](#), [64](#), [65](#), [95](#)
- [53] J.Y. Lee, H.J. Lee, M.H. Jung, S.I. Lee, E.M. Choi, and W.N. Kang, *J. Appl. Phys.* **107**, 013902 (2010). [4](#), [64](#), [65](#), [109](#), [110](#)
- [54] J.Y. Lee, H.J. Lee, S.I. Lee, C.G. Zhuang, Y.Z. Wang, Q.R. Feng, Z.Z. Gan, X.X. Xi, E.M. Choi, J.H. Cho, and Y.H. Jo, *J. Appl. Phys.* **105**, 083904 (2009). [4](#), [64](#), [65](#), [109](#)
- [55] E.M. Choi, H.S. Lee, J.Y. Lee, S.I. Lee, Å.A.F. Olsen, V.V. Yurchenko, D.V. Shantsev, T.H. Johansen, H.J. Kim, and M.H. Cho, *Appl. Phys. Lett.* **91**, 042507 (2007). [4](#), [64](#), [65](#), [109](#), [110](#)
- [56] J. Albrecht, A.T. Matveev, J. Stremper, H.-U. Habermeier, D.V. Shantsev, Y.M. Galperin, and T.H. Johansen, *Phys. Rev. Lett.* **98**, 117001 (2007). [4](#), [64](#), [65](#), [109](#)

-
- [57] F.L. Barkov, D.V. Shantsev, T.H. Johansen, P.E. Goa, W.N. Kang, H.J. Kim, E.M. Choi, and S.I. Lee, Phys. Rev. B **67**, 064513 (2003). [64](#), [65](#), [109](#), [110](#)
- [58] T.H. Johansen, M. Baziljevich, D.V. Shantsev, P.E. Goa, Y.M. Galperin, W.N. Kang, H.J. Kim, E.M. Choi, M.-S. Kim, and S.I. Lee, Europhys. Lett. **59**, 599 (2002). [4](#), [64](#), [65](#), [93](#), [109](#), [110](#)
- [59] C. Tien, E.V. Charnaya, D.Y. Xing, A.L. Pirozerskii, Yu.A. Kumzerov, Y.S. Ciou, and M.K. Lee, Phys. Rev. B **83**, 014502 (2011). [4](#), [65](#)
- [60] A.A. Awad, F.G. Aliev, G.W. Ataklti, A. Silhanek, V.V. Moshchalkov, Y.M. Galperin, and V. Vinokur, Phys. Rev. B **84**, 224511 (2011). [4](#), [64](#), [65](#), [92](#), [93](#)
- [61] D.G. Gheorghe, M. Menghini, R.J. Wijngaarden, S. Raedts, A.V. Silhanek and V.V. Moshchalkov, Physica C **437–438**, 69 (2006). [4](#), [65](#)
- [62] M. Menghini, R.J. Wijngaarden, A.V. Silhanek, S. Raedts, and V.V. Moshchalkov, Phys. Rev. B **71**, 104506 (2005). [4](#), [64](#), [65](#), [110](#)
- [63] A.V. Silhanek, S. Raedts, and V. V. Moshchalkov, Phys. Rev. B. **70**, 144504 (2004). [4](#), [64](#), [65](#)
- [64] H.A. Radovan, and R.J. Zieve, Phys. Rev. B **68**, 224509 (2003). [4](#), [65](#)
- [65] P.W. Anderson, Science **235**, 1196 (1987). [4](#)
- [66] A. García-Santiago, F. Sánchez, M. Varela, and J. Tejada, Appl. Phys. Lett. **77**, 2900 (2000). [5](#)
- [67] H. Kammerlingh Onnes, Leiden Comm. **120b**, **122b**, **124c** (1911). [7](#)
- [68] W. Meissner and R. Ochsenfeld, Naturwissenschaften **21**, 787 (1933). [7](#)
- [69] C.J. Gorter, and H.B.G. Casimir, Phys. Z. **35**, 963 (1934). [8](#), [33](#), [129](#)
- [70] F. London and H. London, Proc. Roy. Soc. London **A149**, 71 (1935). [8](#), [18](#), [33](#)

-
- [71] F. London, *Superfluids*, vol. 1 John Wiley and Sons (1950). 8
- [72] E. Maxwell, Phys. Rev. **78**, 477 (1950). 8
- [73] C.A. Reynolds, B. Serin, W.H. Wright, and L.B. Nesbitt, Phys. Rev. **78**, 487 (1950). 8
- [74] H. Fröhlich, Phys. Rev. **79**, 845 (1950). 8
- [75] J. Bardeen, Revs. Modern Phys. **23**, 261 (1951). 8
- [76] V.L. Ginzburg and L.D. Landau, Zh. Experim. i Theor. Fiz. **20**, 1064 (1950). 8
- [77] L.D. Landau, Zh. Ekperim. i theor. Fiz. **7**, 371 (1937). 8
- [78] A.P. Pippard, Proc. R. Soc. London, **A216**, 547 (1953). 8
- [79] W.S. Corak, B.B. Goodman, C.B. Satterthwaite, and A. Wexler, Phys. Rev. **96**, 1442 (1956). 8
- [80] J. Bardeen, L.N. Cooper, and J.R. Schrieffer, Phys. Rev. **108**, 1175 (1957). 9
- [81] N.N. Bogoliubov, Sov. Phys. JETP **7**, 41 (1958); Sov. Phys. JETP **7**, 51 (1958). 9
- [82] L.P. Gor'kov, Sov. Phys. JETP **9**, 1364 (1959). 9
- [83] B.D. Josephson, Phys. Lett. **1**, 251 (1962). 9
- [84] C.W. Chu, L.Z. Deng, and B. Lv, Physica C **514**, 290 (2015). 9
- [85] A.D. Huxley, Physica C **514**, 368 (2015). 9
- [86] Y. Kamihara, H. Hiramatsu, M. Hirano, and H. Hosono, J. Am. Chem. Soc. **130**, 3296 (2008). 9
- [87] A.A. Abrikosov, *Fundamentals of the Theory of Metals*, North-Holland, Amsterdam, 1988. 12

-
- [88] P.G. de Gennes, *Superconductivity of Metals and Alloys*, Benjamin, New York, 1966. [12](#), [19](#), [20](#), [28](#)
- [89] V.V. Schmidt, *The Physics of Superconductors*, Cambridge University Press, Cambridge, 1995. [13](#)
- [90] V.V. Metlushko, L.E. DeLong, V.V. Moshchalkov, and Y. Bruynseraede, *Physica C* **391**, 196 (2003). [13](#)
- [91] I. Lukyanchuk, V.M. Vinokur, A. Rydh, R. Xie, M.V. Milosevic, U. Welp, M. Zach, Z.L. Xiao, G.W. Crabtree, S.J. Bending, F.M. Peeters, W.K. Kwok, *Nat. Phys.***11**, 21 (2015). [15](#)
- [92] E. Babaev, J. Carlstrom, J. Garaud, M. Silaev, J.M. Speight, *Physica C* **479**, 2 (2012). [15](#)
- [93] E.H. Brandt, and S. Zhou, *Physics* **2**, 22 (2009). [15](#)
- [94] R.P. Huebener, *Magnetic Flux Structures of Superconductors*, Springer-Verlag, New York, 1990. [16](#), [20](#)
- [95] E.H. Brandt, and U. Essmann, *phys. stat. sol.(b)* **144**, 13 (1987). [16](#)
- [96] D.K. Christen, F. Tasset, S. Spooner, and H.A. Mook *Phys. Rev. B* **15**, 4506 (1977). [16](#)
- [97] T. Nishio, V.H. Dao, Q. Chen, L.F. Chibotaru, K. Kadowaki, and V.V. Moshchalkov, *Phys. Rev. B* **81**, 020506 (2010). [17](#)
- [98] C.P. Poole, H.A. Farach Jr., and R.J. Creswick, *Superconductivity*, Academic Press, San Diego, 1995. [19](#)
- [99] E.H. Brandt, *Phys. Rev. B* **34**, 6514 (1984). [20](#)
- [100] Y.B. Kim, and M.J. Stephen, *Superconductivity*, Marcel Dekker, New York, 1969. [23](#)
- [101] D.M. Gaitonde and T.V. Ramakrishnan, *Phys. Rev. B* **56**, 11951 (1997). [23](#)

-
- [102] Y.B. Kim, C.F. Hempstead, and A.R. Strnad, Phys. Rev. Lett. **9**, 309 (1962). [24](#)
- [103] A. Buzdin, and D. Feiberg, Physica C **256**, 303 (1996). [25](#), [29](#), [117](#)
- [104] G. Carneiro, Phys. Rev. B **69**, 214504 (2004). [25](#)
- [105] M.V. Milošević, S.V. Yampolskii, and F.M. Peeters, Phys. Rev. B **66**, 174519 (2002). [25](#)
- [106] M.V. Milošević, S.V. Yampolskii, and F.M. Peeters, Low Temp. Phys. **130**, 321 (2003). [25](#)
- [107] M. Tinkham, Phys. Rev. **129**, 2413 (1963); Rev. Mod. Phys. **36**, 268 (1964). [26](#)
- [108] A.M. Campbell and J.E. Evetts, Adv. Phys. **21**, 199 (1972). [26](#)
- [109] C.P. Bean. Phys. Rev. Lett. **8**, 250 (1962). [26](#), [27](#), [30](#), [88](#)
- [110] E. Altshuler, and T.H. Johansen, Rev. Mod. Phys. **76**, 471 (2004). [27](#)
- [111] J. Pearl, Appl. Phys. Lett. **5**, 65 (1964). [28](#)
- [112] V.V. Moshchalkov, M. Baert, V.V. Metlushko, E. Rosseel, M.J. Van Bael, K. Temst, Y. Bruynseraede, and R. Jonckheere, Phys. Rev. B **57**, 3615 (1996). [29](#), [121](#)
- [113] A. Wahl, V. Hardy, J. Provost, Ch. Simon, and A. Buzdin, Physica C **250**, 163 (1995). [29](#)
- [114] R.M. Araujo-Moreira, C. Navau, and A. Sanchez, Phys. Rev. B **61**, 634 (2000). [29](#)
- [115] A.L. Fetter, and P.C. Hohenberg, Phys. Rev. **159**, 159 (1967). [30](#)
- [116] W.T. Norris, J. Phys. D **3**, 489 (1970). [30](#)
- [117] P.N. Mikheenko, and Yu.E. Kuzovlev, Physica C **204**, 229 (1993). [30](#)

-
- [118] J.R. Clem, and A. Sanchez, Phys. Rev. B **50**, 9355, (1994). [30](#)
- [119] E.H. Brandt, Phys. Rev. B **58**, 6506 (1998). [30](#), [31](#)
- [120] D.S. Shantsev, Y.M. Galperin, and T.H. Johansen, Phys. Rev. B **61**, 9699 (1993). [30](#)
- [121] E. Zeldov, J.R. Clem, M. McElfresh, and M. Darwin, Phys. Rev. B **49**, 9802 (1994). [31](#)
- [122] Sophie Raedts, *Vortex dynamics in type-II superconductors with a periodic pinning array*, PhD thesis, Katholieke Universiteit Leuven, 2004. [32](#), [43](#)
- [123] M. Hein, *High-Temperature Superconductor Thin Films at Microwave Frequencies*, ch. 1, Springer Tracts in Modern Physics, vol. 155, Springer, Berlin, 1999. [34](#), [38](#)
- [124] Liesbet Weckhuysen, *High magnetic field study of the transport properties of under- and overdoped $La_{2-x}Sr_xCuO_4$ epitaxial thin films*, PhD thesis, Katholieke Universiteit Leuven, 2002. [40](#)
- [125] M. Gregor, R. Mičunek, T. Plecenik, T. Roch, A. Lugstein, E. Bertagnolli, I. Vávra, M. Štefečka, M. Kubinec, M. Leporis, V. Gašparík, P. Kúš, and A. Plecenik, Physica C **468**, 785 (2008). [45](#), [46](#)
- [126] R. Mičunek, A. Plecenik, P. Kúš, M. Zahoran, M. Tomášek, T. Plecenik, M. Gregor, M. Štefečka, V. Jacko, J. Greguš, B. Grančič, M. Kubinec, and M. Mahel', Physica C **435**, 78 (2006). [45](#)
- [127] P. Chaddah, S.T. Herbert, D. Stroud, and J.C. Garland, Physica C **159**, 570 (1989). [48](#)
- [128] O. Klein, S. Donovan, M. Dressel, and G. Grüner, Int. J. Infrared and Millimeter Waves **14**, 2423 (1993); S. Donovan, O. Klein, M. Dressel, K. Holczer, and G. Grüner, Int. J. Infrared and Millimeter Waves **14**, 2459 (1993); M. Dressel, O. Klein, S. Donovan, and G. Grüner, Int. J. Infrared and Millimeter Waves **14**, 2489 (1993). [50](#)

-
- [129] R.J. Ormeno, D.C. Morgan, D.M. Broun, S.F. Lee, and J.R. Waldram, *Rev. Sci. Instrum.* **68**, 2121 (1997). [50](#), [130](#)
- [130] M.J. Lancaster, *Passive Microwave Device Applications of High Temperature Superconductors*, **ch. 3**, Cambridge University Press, Cambridge, 1997. [50](#), [129](#)
- [131] M. Hein, *High-Temperature Superconductor Thin Films at Microwave Frequencies*, Springer Tracts in Modern Physics, vol. 155, **ch. 2**, Springer, Berlin, 1999. [50](#), [88](#), [129](#)
- [132] P.J. Petersan, and S.M. Anlage, *J. Appl. Phys.* **84**, 3392 (1998). [50](#), [60](#)
- [133] D. Görlitz, D. Dölling, and J. Kötzler, *Rev. Sci. Instrum.* **75**, 1243 (2004). [50](#), [51](#), [130](#)
- [134] C. Song, T.W. Heitmann, M.P. DeFeo, K. Yu, R. McDermott, M. Neeley, J.M. Martinis, and B.L.T. Plourde, *Phys. Rev. B* **79**, 174512 (2009). [50](#), [130](#), [131](#)
- [135] C. Song, M.P. DeFeo, K. Yu, and B.L.T. Plourde, *Appl. Phys. Lett.* **95**, 232501 (2009). [50](#), [130](#), [131](#)
- [136] P.J. de Visser, J.J.A. Baselmans, S.J.C. Yates, P. Diener, A. Endo, and T.M. Klapwijk, *Appl. Phys. Lett.* **100**, 162601 (2012). [50](#)
- [137] D. Bothner, T. Gaber, M. Kemmler, D. Koelle, R. Kleiner, S. Wünsch, and M. Siegel, *Phys. Rev. B* **86**, 014517 (2012). [50](#), [131](#)
- [138] D. Pozar, *Microwave Engineering*, 3rd ed. (Wiley and Sons, New York, 2005). [50](#), [60](#), [88](#)
- [139] M. Golosovsky, M. Tsindlekht, and D. Davidov, *Supercon. Sci. Technol.* **9**, 1 (1996). [50](#)
- [140] C.J. van der Beek, V.B. Geshkenbein, and V.M. Vinokur, *Phys. Rev. B* **48**, 3393 (1993). [50](#)

-
- [141] M.W. Coffey, and J.R. Clem, Phys. Rev. Lett. **67**, 386 (1991); Phys. Rev. B **46**, 11757 (1992). [50](#)
- [142] E.H. Brandt, Phys. Rev. Lett. **67**, 2219 (1991); Physica C **185-189**, 270 (1991). [50](#)
- [143] N.-C. Yeh, Phys. Rev. B **43**, 523 (1991). [50](#)
- [144] R.C. Taber, Rev. Sci. Instrum. **61**, 2200 (1990). [51](#)
- [145] V.V. Talanov, L.V. Mercaldo, S.M. Anlage, and J.H. Claassen, Rev. Sci. Instrum. **71**, 2136 (2000). [51](#)
- [146] L. Hao, and J.C. Gallop, IEEE Trans. Appl. Supercond. **9**, 1944 (1999). [51](#)
- [147] S. Tonegawa, K. Hashimoto, K. Ikada, Y.-H. Lin, H. Shishido, Y. Haga, T.D. Matsuda, E. Yamamoto, Y. Onuki, H. Ikeda, Y. Matsuda, and T. Shibauchi, Phys. Rev. Lett. **109**, 036401 (2012). [51](#)
- [148] P.J. Turner, D.M. Broun, S. Kamal, M.E. Hayden, J.S. Bobowski, R. Harris, D.C. Morgan, J.S. Preston, D.A. Bonn, and W.N. Hardy, Rev. Sci. Instrum. **75**, 124 (2004). [51](#)
- [149] P.J. Turner, R. Harris, S. Kamal, M.E. Hayden, D.M. Broun, D.C. Morgan, A. Hosseini, P. Dosanjh, G.K. Mullins, J.S. Preston, R. Liang, D.A. Bonn, and W.N. Hardy, Phys. Rev. Lett. **90**, 237005 (2003). [51](#)
- [150] J.C. Booth, D.H. Wu, and S.M. Anlage, Rev. Sci. Instrum. **65**, 2082 (1994). [51](#)
- [151] J.C. Booth, D.H. Wu, S.B. Qadri, E.F. Skelton, M.S. Osofsky, A. Piqué, and S.M. Anlage, Phys. Rev. Lett. **77**, 4438 (1996). [51](#)
- [152] N. Tosoratti, R. Fastampa, M. Guira, V. Lenzi, S. Sarti, and E. Silva, IEEE Trans. Appl. Superconductivity **11**, 3028, (2001). [51](#)
- [153] M. Scheffler, and M. Dressel, Rev. Sci. Instrum. **76**, 074702 (2005). [51](#)
- [154] C. Song, and T.G. Castner, Phys. Rev. B **72**, 085204 (2005). [51](#)

-
- [155] R.J. Deri, Rev. Sci. Instrum. **57**, 82 (1986). [51](#)
- [156] M.S. Dilorio, A.C. Anderson, and B.-Y. Tsaur, Phys. Rev. B **38**, 7019 (1988). [51](#)
- [157] D.E. Oates, A.C. Anderson, and P.M. Mankiewich, J. Supercond. **3**, 251 (1990). [51](#)
- [158] N. Belk, D.E. Oates, D.A. Feld, G. Dresselhaus, and M.S. Dresselhaus, Phys. Rev. B **53**, 3459 (1996). [51](#)
- [159] The use of dBm units here has nothing to do with attenuation of the microwave signal, but it is just a common way to express power in microwave measurements as $P(\text{dBm}) = 10 \log [P(\text{mW})/1 \text{ mW}]$. [52](#)
- [160] *Agilent Technologies*, Santa Clara, CA; 85056A 2.4 mm calibration kit: short, open and 50 Ω loads. [54](#)
- [161] *Agilent Technologies*, Santa Clara, CA; 8510C Network Analyzer System. [54](#)
- [162] *Agilent Technologies*, Santa Clara, CA; HP83651B Synthesized Sweep Generator, 45 MHz - 20 GHz. [54](#)
- [163] *Agilent Technologies*, Santa Clara, CA; E4433B ESG Series Signal Generator. [54](#)
- [164] *Agilent Technologies*, Santa Clara, CA; 3320A-20 MHz Waveform Generator. [56](#)
- [165] *Keithley Instruments Inc.*, Cleveland, OH; 2400 Series. [56](#)
- [166] *Agilent Technologies*, Santa Clara, CA; 54621A model. [57](#)
- [167] *Agilent Technologies*, Santa Clara, CA; E8361A PNA Series. [58](#)
- [168] P.-de-J. Cuadra-Solís, A. Fernández-Martínez, J.M. Hernández, A. García-Santiago, J. Vanacken, and V.V. Moschchalkov, Rev. Sci. Instrum. **86**, 064701 (15). [60](#)

-
- [169] K.L. Corum and J.F. Corum, *Microwave Review* **7**, 36 (2001). [60](#)
- [170] J. Kermorvant, C.J. van der Beek, J.-C. Mage, B. Marcilhac, Y. Lemaitre, J. Briatico, R. Bernard, and J. Villegas, *J. Appl. Phys.* **106**, 023912 (2009). [62](#), [89](#)
- [171] B. Abdo, E. Segev, O. Shtempluck, and E. Buks, *Phys. Rev. B* **73**, 134513 (2006). [62](#)
- [172] L.F. Cohen, A L. Cowie, A. Purnell, N A. Lindop, S. Thiess, and J C. Gallop, *Supercond. Sci. Technol.* **15**, 559 (2002). [62](#)
- [173] M. Hein, *High-Temperature Superconductor Thin Films at Microwave Frequencies*, Springer Tracts in Modern Physics, vol.155, **ch. 3** and **4**, Springer, Berlin, 1999. [62](#)
- [174] A.A. Pukhov, *Supercond. Sci. Technol.* **12**, 102 (1999). [62](#)
- [175] A.A. Pukhov, *Supercond. Sci. Technol.* **10**, 82 (1997). [62](#)
- [176] J. Wosik, L.M. Xie, K. Nesteruk, D. Li, J H. Miller, and S. Long, *J. Supercond.* **10**, 97 (1997). [62](#), [89](#)
- [177] R.G. Mints, and A.L. Rakhmanov, *Rev. Mod. Phys.* **53**, 551 (1981). [63](#), [67](#), [68](#)
- [178] A. Wallraff, D.I. Schuster, A. Blais, L. Frunzio, R.S. Huang, J. Majer, S. Kumar, S.M. Girvin, and R.J. Schoelkopf, *Nature* **431**, 162 (2004). [64](#)
- [179] F. Najafi, F. Marsili, E. Dauler, R.J. Molnar, and K.K. Berggren, *Appl. Phys. Lett.* **100**, 152602 (2012) [64](#)
- [180] M. Hofherr, D. Rall, K. Ilin, M. Siegel, A. Semenov, H.-W. Hubers, and N.A. Gippius, *J. Appl. Phys.* **108**, 014507 (2010) [64](#)
- [181] J. Gao, J. Zmuidzinas, B.A. Mazin, H.G. LeDuc, and P.K. Day, *Appl. Phys. Lett.* **90**, 102507 (2007). [64](#)

-
- [182] P.K. Day, H.G. LeDuc, B.A. Mazin, A. Vayonakis, and J. Zmuidzinas, *Nature (London)*, **425**, 817 (2003). [64](#)
- [183] E.A. Tholén, A. Ergül, E.M. Doherty, F.M. Weber, F. Grégis, and D.B. Haviland, *Appl. Phys. Lett.* **90**, 253509 (2007). [64](#)
- [184] M. Metcalfe, E. Boaknin, V. Manucharyan, R. Vijay, I. Siddiqi, C. Rigetti, L. Frunzio, R.J. Schoelkopf, and M.H. Devoret, *Phys. Rev. B* **76**, 174516 (2007). [64](#)
- [185] Ch. Jooss, J. Albrecht, H. Kuhn, S. Leonhardt, and H. Kronmü, *Rep. Prog. Phys.* **65**, 651 (2002). [64](#)
- [186] M.R. Koblischka, and R.J. Wijngaarden, *Supercond. Sci. Technol.* **8**, 199 (1995). [64](#)
- [187] M.S. Welling, R.J. Westerwaal, W. Lohstroh, and R.J. Wijngaarden, *Physica C* **411**, 11 (2004). [64](#)
- [188] C.A. Durán, P.L. Gammel, R.E. Miller, and D.J. Bishop, *Phys. Rev. B* **52**, 75 (1995). [64](#)
- [189] I.A. Rudnev, S.V. Antonenko, D.V. Shantsev, T.H. Johansen, and A.E. Primenko, *Cryogenics* **43**, 663 (2003). [64](#), [95](#)
- [190] V.V. Yurchenko, D.V. Shantsev, T.H. Johansen, M.R. Nevala, I.J. Maasilta, K. Senapati, and R.C. Budhani, *Phy. Rev. B* **76**, 092504 (2007). [64](#), [70](#)
- [191] I.A. Rudnev, D.V. Shantsev, T.H. Johansen, and A.E. Primenko, *Appl. Phys. Lett.* **87**, 042502 (2005). [64](#)
- [192] E.M. Choi, H.-S. Lee, H.J. Kim, B. Kang, S.-I. Lee, A.A.F. Olsen, and D.V. Shantsev, T.H. Johansen, *Appl. Phys. Lett.* **87**, 152501 (2005). [64](#), [93](#), [95](#)
- [193] D.V. Shantsev, P.E. Goa, F.L. Barkov, T.H. Johansen, W.N. Kang, and S.I. Lee, *Supercond. Sci. Technol.* **16**, 566 (2003). [64](#)

-
- [194] Z.W. Zhao, S.L. Li, Y.M. Ni, H.P. Yang, Z.Y. Liu, H.H. Wen, W.N. Kang, H.J. Kim, E.M. Choi, and S.I. Lee, Phys. Rev. B **65**, 064512 (2002). [64](#), [95](#), [109](#), [110](#)
- [195] S.C. Wimbush, B. Holzapfel, and Ch. Jooss, J. Appl. Phys. **96**, 3589 (2004). [64](#)
- [196] M. Motta, F. Colauto, W.A. Ortiz, J. Fritzsche, J. Cuppens, W. Gillijns, V.V. Moshchalkov, T.H. Johansen, A. Sanchez and A.V. Silhanek, Appl. Phys. Lett., **102**, 212601 (2013). [64](#), [66](#)
- [197] F. Colauto, M. Motta, A. Palau, M.G. Blamire, T.H. Johansen, and W.A. Ortiz, IEEE Trans. Appl. Supercond. **25**, 7500704 (2015). [64](#)
- [198] F. Colauto, E.J. Patiño, M.G. Blamire, and W.A. Ortiz, Supercond. Sci. Technol. **21**, 045018 (2008). [64](#)
- [199] F. Colauto, E.M. Choi, J.Y. Lee, S.I. Lee, V.V. Yurchenko, T.H. Johansen, and W.A. Ortiz, Supercond. Sci. Technol. **20**, L48 (2007). [64](#)
- [200] D.V. Denisov, D.V. Shantsev, Y.M. Galperin, E.M. Choi, H.S. Lee, S.I. Lee, A.V. Bobyl, P.E. Goa, A.A.F. Olsen, and T.H. Johansen, Phys. Rev. Lett. **97**, 077002 (2006). [64](#), [66](#), [70](#), [71](#), [88](#), [91](#), [93](#), [106](#), [109](#), [110](#)
- [201] E. Altshuler, T.H. Johansen, Y. Paltiel, P. Jin, K.E. Bassler, O. Ramos, Q.Y. Chen, G.F. Reiter, E. Zeldov, and C.W. Chu, Phys. Rev. B **70**, 140505(R) (2004). [64](#), [109](#)
- [202] A.V. Bobyl, D.V. Shantsev, T.H. Johansen, W.N. Kang, H.J. Kim, E.M. Choi, and S.I. Lee, Appl. Phys. Lett. **80**, 4588 (2002). [64](#), [95](#), [109](#), [110](#)
- [203] A. Nabisławek, and M. Niewczas, Physica C **436**, 43 (2006). [64](#), [65](#)
- [204] M. Motta, F. Colauto, R. Zadorosny, T.H. Johansen, R.B. Dinner, M.G. Blamire, G.W. Ataklti, V.V. Moshchalkov, A.V. Silhanek, and W.A. Ortiz, Phys. Rev. B. **84**, 214529 (2011). [64](#)

-
- [205] M. Motta, F. Colauto, T.H. Johansen, R.B. Dinner, M.G. Blamire, G.W. Ataklti, V.V. Moshchalkov, A.V. Silhanek, and W.A. Ortiz, *Physica C* **479**, 134 (2012). [64](#)
- [206] P.S. Swartz, and C.P. Bean, *J. Appl. Phys.* **39**, 4991 (1968). [64](#)
- [207] U. Bolz, J. Eisenmenger, J. Schiessling, B. U. Runge, and P. Leiderer, *Phys. B* **284**, 757 (2000). [64](#), [65](#), [109](#), [110](#)
- [208] V. V. Chabanenko, A. I. D'yachenko, M. V. Zalutskii, V. F. Rusakov, H. Szymczak, S. Piechota, and A. Nabialek, *J. Appl. Phys.* **88**, 5875 (2000). [64](#), [95](#), [109](#)
- [209] V. V. Chabanenko, A. I. D'yachenko, A.V. Chabanenko, H. Szymczak, S. Piechota, A. Nabiałek, and N. D. Dung, *J. Appl. Phys.* **83**, 7324 (1998). [64](#), [65](#)
- [210] V. V. Chabanenko, A. I. D'yachenko, A.V. Chabanenko, M. V. Zalutsky, H. Szymczak, S. Piechota, and A. Nabialek, *Supercond. Sci. Technol.* **11**, 1181 (1998). [64](#), [65](#)
- [211] R. G. Mints, *Phys. Rev. B* **53**, 12311 (1996). [64](#), [65](#), [93](#)
- [212] S. L. Wipf, *Cryogenics* **31**, 936 (1992). [64](#)
- [213] S. Treiber, C. Stahl, G. Schütz, and J. Albrecht, *Supercond. Sci. Technol.* **25**, 65010 (2012). [65](#), [106](#)
- [214] G. Ghigo, R. Gerbaldo, L. Gozzelino, F. Laviano, G. Lopardo, E. Monticone, C. Portesi, and E. Mezzetti, *Appl. Phys. Lett.* **94**, 052505 (2009). [65](#)
- [215] G. Ghigo, F. Laviano, L. Gozzelino, R. Gerbaldo, and E. Mezzetti, E. Monticone and C. Portesi, *J. Appl. Phys.* **102**, 113901 (2007). [65](#), [110](#)
- [216] D. Bothner, C. Clauss, E. Koroknay, M. Kemmler, T. Gaber, M. Jetter, M. Scheffler, P. Michler, M. Dressel, D. Koelle and R. Kleiner, *Appl. Phys. Lett.* **100**, 012601 (2012). [65](#)

-
- [217] P. Selders and R. Wördenweber, *IEEE Trans. Appl. Supercond.* **11**, 928 (2001). [65](#)
- [218] E.-M. Choi, V. V. Yurchenko, T. H. Johansen, H.-S. Lee, J. Y. Lee, W. N. Kang and S.-I. Lee, *Supercond. Sci. Technol.* **22**, 015011 (2009). [65](#)
- [219] M. Baziljevich, A. Bobyl, D. Shantsev, E. Altshuler, T. Johansen, and S. Lee, *Physica C* **369**, 93 (2002). [65](#), [93](#)
- [220] V.V. Yurchenko, K. Ilin, J.M. Meckbach, M. Siegel, A.J. Qviller, Y.M. Galperin and T.H. Johansen, *Appl. Phys. Lett.* **102**, 252601 (2013). [66](#)
- [221] F. Colauto, J.I. Vestgård, A.M.H. de Andrade, A A M. Oliveira, W A. Ortiz and T H. Johansen, *Appl. Phys. Lett.* **103**, 032604 (2013). [66](#)
- [222] N H. Zebouni, A. Venkataram, G.N. Rao, C.G. Grenier, and J.M. Reynolds, *Phys. Rev.* **13**, 606 (1964). [68](#)
- [223] J. Chikaba, *Cryogenics* **10**, 306 (1970). [68](#)
- [224] L. Legrand, I. Rosenman, Ch. Simon, and G. Collin, *Physica C* **211**, 239 (1993). [68](#)
- [225] R.G. Mints, *JETP Lett.* **27**, 417 (1978). [68](#)
- [226] J.I. Vestgård, D.V. Shantsev, Y.M. Galperin, and T.H. Johansen, *Phys. Rev. B* **84**, 054537 (2011). [70](#)
- [227] D.V. Denisov, A.L. Rakhmanov, D.V. Shantsev, Y.M. Galperin, and T.H. Johansen, *Phys. Rev. B* **73**, 014512 (2006). [71](#), [88](#), [91](#), [93](#), [110](#)
- [228] A.L. Rakhmanov, D.V. Shantsev, Y.M. Galperin, and T.H. Johansen, *Phys. Rev. B* **70**, 224502 (2004). [71](#), [93](#)
- [229] J.I. Vestgård, D.V. Shantsev, Y.M. Galperin, and T.H. Johansen, *Sci. Rep.* **2**, 886 (2012). [71](#), [93](#), [111](#)
- [230] Y. Yeshurun, A.P. Malozemoff, and A. Shaulov, *Rev. Mod. Phys.* **68**, 911 (1996). [80](#)

-
- [231] V.V. Chabanenko, S.V. Vasiliev, A. Nabiałek, A.S. Shishmakov, F. Pérez-Rodríguez, V.F. Rusakov, A. Szewczyk, B.N. Kodess, M. Gutowska, J. Wieckowski and H. Szymczak, *Low Temp. Phys.* **39**, 329 (2013). [88](#)
- [232] P.-de-J. Cuadra-Solis, A. Garcia-Santiago, J.M. Hernandez, J. Tejada, J. Vanacken, and V.V. Moshchalkov, *Phys. Rev. B* **89**, 054517 (2014). [88](#)
- [233] S. Adam, L. Piraux, D. Lucot, and D. Mailly, *J. Appl. Phys.* **110**, 053919 (2011). [89](#)
- [234] P. Lahl, and R. Wördenweber, *J. Appl. Phys.* **97**, 113911 (2005). [89](#)
- [235] S. M. Anlage, W. Hu, C. P. Vlahacos, D. Steinhauer, B. J. Feenstra, S. K. Dutta, A. Thanawalla, and F. C. Wellstood, *J. Supercond.* **12**, 353 (1999). [89](#)
- [236] M. Hein, W. Diete, M. Getta, S. Hensen, T. Kaiser, G. Müller, H. Piel, and H. Schilk, *IEEE Trans. Appl. Supercond.* **7**, 1264 (1997). [89](#)
- [237] T.B. Samoilova, *Supercond. Sci. Technol.* **8**, 259 (1995). [89](#)
- [238] M.W. Coffey, and J.R. Clem, *Phys. Rev. Lett.* **67**, 386 (1991); *Phys. Rev. B* **46**, 11757 (1992). [89](#)
- [239] A. Gurevich, *Int. J. Mod. Phys. B* **94**, 1045 (1995). [89](#)
- [240] I.S. Aranson, A. Gurevich, M.S. Welling, R.J. Wijngaarden, V.K. Vlasko-Vlasov, V.M. Vinokur, and U. Welp, *Phys. Rev. Lett.* **94**, 037002 (2005). [89](#), [93](#), [111](#)
- [241] V.V. Chabanenko, V. Rusakov, V. Yampol'skii, S. Piechota, A. Nabialek, S. Vasiliev, and H. Szymczak, *cond-mat/0106379* (June 19, 2001). [92](#)
- [242] A.K. Geim, S.V. Dubonos, J.G.S. Lok, M. Henini, and J.C. Maan, *Nature (London)* **396**, 144 (1998). [92](#)
- [243] V.A. Schweigert, and P.M. Peeters, *Phys. Rev. Lett.* **83**, 2049 (1999). [92](#)

-
- [244] A.K. Geim, S.V. Dubonos, I.V. Grigorieva, K.S. Novoselov, F.M. Peeters, and V.A. Schweigert, *Nature (London)* 407, 55 (2000). [92](#)
- [245] E.H. Brandt, *Phys. Rev. B* 54, 4256 (1996); *Phys. Rev. B* **55**, 14513 (1997). [92](#), [93](#)
- [246] I.S. Aranson, A. Gurevich, and V.M. Vinokur, *Phys. Rev. Lett.* 87, 067003 (2001). [93](#)
- [247] C. Stahl, S. Treiber, G. Shütz, and J. Albrecht, *Supercond. Sci. Technol.* 26, 015007 (2013). [93](#)
- [248] E. Baruch-El, M. Baziljevich, T.H. Johansen, and Y. Yeshurun, *J. Supercond. Nov. Magn.* 28, 379 (2015). [93](#)
- [249] Z.X. Ye, Q. Li, Y.F. Hu, A.V. Pogrebnyakov, Y. Cui, X.X. Xi, J.M. Redwing and Qi Li, *Appl. Phys. Lett.* **85**, 5284 (2004). [111](#)
- [250] A.V. Silhanek, J. Gutierrez, R.B.G. Kramer, G.W. Ataklti, J. Van de Vondel, V.V. Moshchalkov, and A. Sanchez, *Phys. Rev. B* **83**, 024509 (2011). [114](#), [115](#), [130](#)
- [251] S. Raedts, A.V. Silhanek, V.V. Moshchalkov, J. Moonens, and L.H.A. Leunissen, *Phys. Rev. B* **73**, 174514 (2006). [114](#), [115](#), [118](#), [121](#), [123](#)
- [252] V.V. Yurchenko, R. Wördenweber, Yu.M. Galperin, D.V. Shantsev, J.I. Vestgård, and T.H. Johansen, *Physica C* **437–438**, 357 (2006). [114](#), [115](#)
- [253] S. Raedts, A.V. Silhanek, M.J. Van Bael, and V.V. Moshchalkov, *Phys. Rev. B* **70**, 024509 (2004). [114](#), [115](#), [117](#), [118](#), [121](#), [122](#), [123](#), [128](#)
- [254] A.V. Silhanek, S. Raedts, M.J. Van Bael, and V.V. Moshchalkov, *Phys. Rev. B* **70**, 054515 (2004). [114](#), [115](#), [118](#), [121](#), [122](#), [123](#), [128](#)
- [255] A.V. Silhanek, S. Raedts, M.J. Van Bael, and V.V. Moshchalkov, *Eur. Phys. J. B* **37**, 19 (2004). [114](#), [115](#), [118](#)
- [256] A.V. Silhanek, S. Raedts, M. Lange, and V.V. Moshchalkov, *Phys. Rev. B* **67**, 064502 (2003). [114](#), [115](#), [118](#), [121](#), [122](#), [123](#)

-
- [257] L. Van Look, B.Y. Zhu, R. Jonckheere, B.R. Zhao, Z.X. Zhao, and V.V. Moshchalkov, *Phys. Rev. B* **66**, 214511 (2002). [114](#), [115](#), [121](#), [128](#)
- [258] S.B. Field, S.S. James, J. Barentine, V. Metlushko, G. Crabtree, H. Shtrikman, B. Ilic, and S.R.J. Brueck, *Phys. Rev. Lett.* **88**, 067003 (2002). [114](#), [115](#)
- [259] A.N. Grigorenko, G.D. Howells, S.J. Bending, J. Bekaert, M.J. Van Bael, L. Van Look, V.V. Moshchalkov, Y. Bruynseraede, G. Borghs, I.I. Kaya, and R.A. Stradling, *Phys. Rev. B* **63**, 052504 (2001). [114](#), [115](#)
- [260] V. Metlushko, U. Welp, G.W. Crabtree, R. Osgood, S.D. Bader, L.E. DeLong, Z. Zhang, S.R.J. Brueck, B. Ilic, K. Chung, and P.J. Hesketh, *Phys. Rev. B* **60**, R12585 (1999). [114](#), [115](#), [121](#)
- [261] V. Metlushko, U. Welp, G.W. Crabtree, Z. Zhang, S.R.J. Brueck, B. Watkins, L.E. DeLong, B. Ilic, K. Chung, and P.J. Hesketh, *Phys. Rev. B* **59**, 603 (1999). [114](#), [115](#), [121](#)
- [262] G. Pasquini, L. Civale, H. Lanza, and G. Nieva, *Phys. Rev. B* **59**, 9627 (1999). [114](#), [115](#), [123](#)
- [263] A. Bezryadin, Yu. N. Ovchinnikov, and B. Pannetier, *Phys. Rev. B* **53**, 8553 (1996). [114](#), [117](#)
- [264] K. Harada, O. Kamimura, H. Kasai, T. Matsuda, A. Tonomura, and V.V. Moshchalkov, *Science* **274**, 1167 (1996). [114](#), [115](#), [117](#), [131](#), [132](#)
- [265] V.V. Moshchalkov, M. Baert, V.V. Metlushko, E. Rosseel, M.J. Van Bael, K. Temst, R. Jonckheere, and Y. Bruynseraede, *Phys. Rev. B* **54**, 7385 (1996). [115](#)
- [266] M. Baert, V.V. Metlushko, R. Jonckheere, V.V. Moshchalkov, and Y. Bruynseraede, *Phys. Rev. Lett.* **74**, 3269 (1995). [115](#), [121](#)
- [267] V.V. Metlushko, M. Baert, R. Jonckheere, V.V. Moshchalkov, and Y. Bruynseraede, *Solid State Commun.* **91**, 331 (1994). [115](#)

-
- [268] P. Selders and R. Wördenweber, *Appl. Phys. Lett.* **76**, 3277 (2000). [115](#)
- [269] T. Puig, E. Rosseel, M. Baert, M.J. Van Bael, V.V. Moshchalkov, and Y. Bruynseraede, *Appl. Phys. Lett.* **70**, 3155 (1997). [115](#)
- [270] C.C. de Souza Silva, J. Van de Vondel, B.Y. Zhu, M. Morelle, and V.V. Moshchalkov, *Phys. Rev. B* **73**, 014507 (2006). [115](#)
- [271] J.E. Villegas, S. Savel'ev, F. Nori, E.M. Gonzalez, J.V. Anguita, R. García, and J.L. Vicent, *Science* **302**, 1188 (2003). [115](#)
- [272] P. Lahl, and R. Wördenweber, *Appl. Phys. Lett.* **81**, 505 (2002). [115](#)
- [273] M.J. Van Bael, J. Bekaert, K. Temst, L. Van Look, V.V. Moshchalkov, Y. Bruynseraede, G.D. Howells, A.N. Grigorenko, S.J. Bending, and G. Borghs, *Phys. Rev. Lett.* **86**, 155 (2001). [115](#), [117](#)
- [274] L. Van Look, E. Rosseel, M.J. Van Bael, K. Temst, V.V. Moshchalkov, and Y. Bruynseraede, *Phys. Rev. B* **60**, R6998 (1999). [115](#)
- [275] P. Sabatino, C. Cirillo, G. Carapella, M. Trezza, and C. Attanasio, *J. Appl. Phys.* **108**, 053906 (2010). [115](#)
- [276] X. Hallet, M. Mátéfi-Tempfli, S. Michotte, L. Piraux, J. Vanacken, V.V. Moshchalkov, and S. Mátéfi-Tempfli, *Appl. Phys. Lett.* **95**, 252503 (2009). [115](#)
- [277] M. Trezza, C. Cirillo, S.L. Prischepa, and C. Attanasio, *Physica C* **470**, 957 (2009). [115](#)
- [278] C. Chilotte, D. Pérez Daroca, G. Paquini, V. Bekkeris, C.-P. Li, F. Casanova, J.E. Villegas, and I.K. Schuller, *Physica B* **404**, 2809 (2009). [115](#)
- [279] L. Horng, T. J. Yang, R. Cao, T. C. Wu, J. C. Lin, and J. C. Wu, *J. Appl. Phys.* **103**, 07C706 (2008). [115](#)
- [280] W. Vinckx, J. Vanacken, and V.V. Moshchalkov, *J. Appl. Phys.* **100**, 044307 (2006). [115](#)

-
- [281] A.A. Zhukov, E.T. Filby, M.A. Ghanem, P.N. Bartlett, and P.A.J. de Groot, *Physica C* **404**, 455 (2004). [115](#), [131](#)
- [282] A. A. Zhukov, P. A. J. de Groot, V. V. Moshchalkov, and B. Ilic, *Appl. Phys. Lett.* **83**, 4217 (2003). [115](#)
- [283] U. Welp, Z.L. Xiao, J.S. Jiang, V.K. Vlasko-Vlasov, S.D. Bader, G.W. Crabtree, J. Liang, H. Chik, and J.M. Xu, *Phys. Rev. B* **66**, 212507 (2002). [115](#)
- [284] M. Golosovsky, M. Tsindlekht, and D. Davidov, *Supercond. Sci. Technol.* **9**, 1 (1996). [115](#), [129](#)
- [285] M.W. Coffey and J.R. Clem, *Phys. Rev. Lett.* **67**, 386 (1991); *Phys. Rev. B* **45**, 9872 (1992). [115](#), [129](#)
- [286] E.H. Brandt, *Phys. Rev. Lett.* **67**, 2219 (1991); *Physica C* **195**, 1 (1992). [115](#), [129](#)
- [287] A.V. Silhanek, L. Civale, S. Candia, G. Nieva, G. Pasquini, and H. Lanza, *Phys. Rev. B* **59**, 13620 (1999). [116](#)
- [288] G. Blatter, M.V. Feigel'man, V.B. Geshkenbein, A.I. Larkin, and V.M. Vinokur, *Rev. Mod. Phys.* **66**, 1125 (1994). [116](#)
- [289] D. Niebieskikwiat, A.V. Silhanek, L. Civale, G. Nieva, P. Levy, and L. Krusin-Elbaum, *Phys. Rev. B* **63**, 144504 (2001). [116](#)
- [290] O. Daldini, P. Martinoli, J.L. Olson, and G. Berner, *Phys. Rev. Lett.* **32**, 218 (1974). [117](#)
- [291] A.T. Fiory, A.F. Hebard, and S. Somekh, *Appl. Phys. Lett.* **32**, 73 (1978). [117](#)
- [292] A.F. Hebard, A.T. Fiory, and S. Somekh, *IEEE Trans. Magn.* **1**, 589 (1977). [117](#)
- [293] A. Volodin, K. Temst, C. Van Haesendonck, and Y. Bruynseraede, *Physica C* **332**, 156 (2000). [117](#)

-
- [294] A. Volodin, K. Temst, C. Van Haesendonck, and Y. Bruynseraede, *Appl. Phys. Lett.* **73**, 1134 (1998). [117](#)
- [295] A.N. Grigorenko, S.J. Bending, M.J. Van Bael, M. Langge, V.V. Moshchalkov, H. Fangohr, and P.A.J. de Groot, *Phys. Rev. Lett.* **90**, 237001 (2003). [117](#)
- [296] S.J. Bending, G.D. Howells, A.N. Grigorenko, M.J. Van Bael, J. Bekaert, K. Temst, L. Van Look, V.V. Moshchalkov, Y. Bruynseraede, G. Borghs, and R.G. Humphreys, *Physica C* **332**, 20 (2000). [117](#)
- [297] H. Nordborg, and V.M. Vinokur, *Phys. Rev. B* **62**, 12408 (2000) [117](#)
- [298] I.B. Khalfin, and B. Ya Shapiro, *Physica C* **207**, 359 (1993). [117](#)
- [299] G.S. Mkrtchyan, and V.V Schmidt, *Zh. Eksp. Teor. Fiz.* **61**, 367 (1971) [*Sov. Phys. JETP* **34**, 195 (1972)]. [117](#), [118](#)
- [300] D.E. Farrell, B.C. Chandrasekhar, and H.V. Culbert, *Phys. Rev.* **177**, 694 (1969). [119](#)
- [301] G.J. Dolan, and J. Silcox, *Phys. Rev. Lett.* **30**, 603 (1973). [119](#)
- [302] Th. Herzog, H.A. Radovan, P. Ziemann, and E.H. Brandt, *Phys. Rev. B* **56**, 2871 (1997). [122](#)
- [303] E.H. Brandt, *Rep. Prog. Phys.* **58**, 1465 (1995). [129](#)
- [304] C.C. de Souza Silva, J.A. Aguiar, and V.V. Moshchalkov, *Phys. Rev. B* **68**, 134512 (2003). [130](#)
- [305] C. Reichhardt, C.J. Olson, and F. Nori, *Phys. Rev. B* **57**, 7937 (1998). [130](#)
- [306] D. Golubchik, E. Polturak, and G. Koren, *Phys. Rev. B* **85**, 060504(R) (2012). [130](#)
- [307] L.D. Cooley, and A.M. Grishin, *Phys. Rev. Lett.* **74**, 2788 (1995). [130](#)
- [308] A. Hoffmann, P. Prieto, and I.K. Schuller, *Phys. Rev. B* **61**, 6958 (2000). [131](#)

Publications and contributions

Publications

1. **DC and AC characterization of tantalum and niobium nitride superconducting thin films.**

P.-de-Jesús Cuadra-Solís, Antoni García-Santiago, Joan Manel Hernández, Saumyadip Chaudhuri, and Ilari J. Maasilta, in preparation.

2. **RF-susceptibility studies on $\text{La}_{1.82}\text{Sr}_{0.18}\text{CuO}_4$ superconducting thin films by using BD-oscillator techniques in low dc magnetic fields.**

P.-de-Jesús Cuadra-Solís, Antoni García-Santiago, Tom Wambecq, Johan Vanacken, and Victor V. Moshchalkov, in preparation.

3. **Microwave-frequency-driven vortex instability in superconducting thin films.**

Pedro-de-Jesús Cuadra-Solís, Antoni García-Santiago, Joan Manel Hernández, Javier Tejada, Johan Vanacken, V. Machkaoustan, and Victor V. Moshchalkov. *Submitted to Phys. Rev. B (2015).*

4. **A radio-frequency coil for the microwave characterization of vortex dynamics in thin film superconductors.**

Pedro-de-Jesús Cuadra-Solís, Antoni Fernández-Martínez, Joan Manel Hernández, Antoni García-Santiago, Johan Vanacken, and Victor V. Moshchalkov. *Rev. Sci. Instrum.* 86, 064701 (2015).

5. **Observation of commensurability effects in patterned thin superconducting Pb film using microwave reflection spectrometry.**

Pedro-de-Jesús Cuadra-Solís, Antoni García-Santiago, Joan Manel Hernández,

-
- Johan Vanacken, and Victor V. Moshchalkov. *Phys. Rev. B* **89**, 054517 (2014).
6. **Avalanche-like vortex penetration driven by pulsed microwave fields in an epitaxial LaSrCuO thin film.**
P.-de-J. Cuadra-Solís, J. M. Hernández, A. García-Santiago, J. Tejada, J. Vanacken, and V. V. Moshchalkov. *J. Appl. Phys.* **114**, 233902 (2013).
 7. **Vortex Avalanches Induced by Single High-Frequency Pulses in MgB₂ Films.**
P. de Jesús Cuadra-Solís, J. M. Hernández, A. García-Santiago, J. Tejada, J. Noskovic, A. Pidik, and M. Grajcar. *J. Supercond. Nov. Magn.* **24**, 395 (2011).
 8. **High-frequency vortex matching effects in Pb thin films with a periodic array of antidots.**
P. J. Cuadra-Solís, J. M. Hernández, A. García-Santiago, J. Tejada, J. Vanacken, and V. V. Moshchalkov. *Physica C* **468**, 777 (2008).
 9. **Magnetic moment relaxation studies by swept and pulsed microwave technique in LaSrCuO epitaxial thin film.**
P. J. Cuadra-Solís, J. M. Hernández, A. García-Santiago, J. Tejada, J. Vanacken, and V. V. Moshchalkov. *Physica C* **468**, 805 (2008).
 10. **Magnetic characterisation of La_{2-x}Sr_xCuO₄ at microwave frequencies.**
P. J. Cuadra-Solís, A. García-Santiago, J. Tejada, J. Vanacken, and V. V. Moshchalkov. *J. Phys. Chem. Solids* **67**, 419 (2006).
 11. **Study of the oxygen migration versus anneal in Co/AlO_x/Fe-FeO_y/Ti tunnel junctions.**
X. Batlle, P. J. Cuadra, Z. Zhang, S. Cardoso, and P.P. Freitas. *J. Magn. Mater.* **261**, L305 (2003).
 12. **Low-resistance spin-dependent tunnel junctions with HfAlO_x barriers for high-density recording-head application.**

J. Wang, P.P. Freitas, E. Snoeck, X. Battle, and J. Cuadra. *IEEE Trans. Magn.* **38**, 2703-2705 (2002).

13. **Low resistance spin-dependent tunnel junctions with ZrAlO_x barriers.**

J. Wang, P.P. Freitas, E. Snoeck, X. Battle, and J. Cuadra. *J. Appl. Phys.* **91**, 7463 (2002).

Conferences, workshop and seminary

1. P.-de-Jesús Cuadra-Solís, J.M. Hernández, A. García-Santiago, J. Tejada, J. Noskovic, A. Pidik, M. Grajcar, J. Vanacken and V.V. Moshchalkov. Vortex instability driven by microwave-induced non-equilibrium state in superconducting thin films. Contribution: poster. 8th. International Workshop on Nanomagnetism and Superconductivity. Coma-ruga, Spain. 1–5 July 2012.
2. P.-de-Jesús Cuadra-Solís, J.M. Hernández, A. García-Santiago, J. Tejada, J. Noskovic, A. Pidik, M. Grajcar, J. Vanacken and V.V. Moshchalkov. Microwave experiments in superconductivity thin films: vortex depinning, avalanche-like vortex penetration and commensurability effects. Contribution: oral. International Conference on Superconductivity and Magnetism (ICSM 2012), Kumburgaz (Istanbul), Turkey, 29.04–04.05.2012.
3. P.J. Cuadra-Solís, J.M. Hernández, A. García-Santiago, J. Tejada, J. Noskovic, A. Pidik, M. Gajcar, J. Vanacken and V.V. Moshchalkov: Switching Response of Superconducting Thin Films in Avalanche-like Vortex Penetration Triggered by Single Microwave Pulses. Contribution: poster. International Workshop on Mesoscopic Superconductivity and Vortex Imaging. Bath, U. K. 3–7 May 2011.
4. P.J. Cuadra-Solís, J.M. Hernández, A. García-Santiago, J. Tejada, J. Vanacken and V.V. Moshchalkov: Evidence of Thermomagnetic Instability Induced by Pulsed Microwave Fields in LaSrCuO Epitaxial Thin Films. Contribution: poster. International Conference on Superconductivity and Magnetism (SM2010): hybrid proximity nanostructures and intrinsic phenomena. Paestum, Italy. 5–11 September 2010.

-
5. P.J. Cuadra-Solís, J.M. Hernández, A. García-Santiago, J. Tejada, J. Noskovic, A. Pidik, and M. Gajcar. Vortex Dendritic Avalanches Induced by Microwave Pulses in MgB₂. Contribution: oral. International Conference on Superconductivity and Magnetism: ICSM 2010. Antalya, Turkey. 25–30 April 2010.
 6. P.J. Cuadra-Solís, J.M. Hernández, A. García-Santiago, J. Tejada, J. Noskovic, A. Pidik, and M. Gajcar. Vortex Dendritic Avalanches Induced by High Frequency Pulses in MgB₂. Contribution: poster. 5th International Workshop on Nanomagnetism and Superconductivity. Comarruga (Barcelona), Spain. 5–9 July 2009.
 7. P.J. Cuadra-Solís, J.M. Hernandez, A. García-Santiago, J. Tejada, J. Vanacken and V.V. Moshchalkov. Matching effects in superconductors. Contribution: oral. Department of Fundamental Physics: Seminars. Faculty of Physics. University of Barcelona. Barcelona. Spain. 2008.
 8. P.J. Cuadra-Solís, J.M. Hernández, A. García-Santiago, J. Tejada, J. Vancken and V.V. Moshchalkov. High-frequency commensurability effects in superconducting Pb thin films. Contribution: oral. International Workshop on Nanostructured Superconductor: from Fundamental to Applications. Freudenstadt–Lauterbad, Germany. 13–17 September 2008.
 9. P.J. Cuadra-Solís, J.M. Hernández, A. García-Santiago, J. Tejada, J. Vanacken and V.V. Moshchalkov. High-frequency vortex matching effects in Pb thin films with a periodic array of antidots. Contribution: poster. The 5th International Conference on Vortex Matter in Nanostructured Superconductors. Rhodes, Greece. 8–14 September 2007.
 10. P.J. Cuadra-Solís, J.M. Hernández, A. García-Santiago, J. Tejada, J. Vanacken and V.V. Moshchalkov. Magnetic moment relaxation studies by swept and pulsed microwave technique in LaSrCuO epitaxial thin film. Contribution: poster. The 5th International Conference on Vortex Matter in Nanostructured Superconductors. Rhodes, Greece. 8–14 September 2007.

11. P.J. Cuadra Solís, J.M. Hernández, A. García-Santiago and J. Tejada, J. Vanacken and V.V. Moshchalkov. Microwave frequency-dependent magnetic moment relaxation of $\text{La}_{1.82}\text{Sr}_{0.18}\text{CuO}_4$ epitaxial thin film. Contribution: poster. Conference on Nanoscale Superconductivity and Magnetism (NSM2006). A Satellite M2S-HTSC-VIII Conference in school format. Leuven, Belgium. 6–8 July 2006.
12. P.J. Cuadra Solís, J.M. Hernández, A. García-Santiago and J. Tejada, J. Vanacken and V.V. Moshchalkov. Microwave experiments in LaSrCuO thin films. Contribution: poster. The 4th National Meeting on Solid State Physics. Alicante, Spain. 1–3 February 2006.
13. P.J. Cuadra Solís, A. García-Santiago and J. Tejada, J. Vanacken and V.V. Moshchalkov. Magnetic Characterization of LSCO at microwave frequencies. Contribution: poster. Seventh International Conference on Spectroscopies in Novel Superconductors (SNS2004). Sitges, Spain. 11–16 July 2004.
14. P.J. Cuadra Solís, A. García-Santiago and J. Tejada, J. Vanacken and V. Moshchalkov. Magnetic Characterization of LSCO at microwave frequencies. Contribution: poster. Combined ESF-Vortex and ESF-PiShift Workshop on Nanostructured Superconductivity: from fundamental to applications. Bad Münstereifel, Germany. 15–19 May 2004.
15. X. Batlle, B.J. Hattink, P.J. Cuadra, A. Labarta, B.J. Jonsson-Akerman, R. Escudero, I.K. Schuller, Z. Zhang, S. Cardoso, P.P. Freitas. The X-ray photoelectron spectroscopy in the characterization of the isolated barrier in magnetic tunnel junctions. Contribution: poster. The 2th National Meeting on Solid State Physics. Calella de la Costa, Spain. 6–8 February 2002.
16. J. Wang, P.P. Freitas, E. Snoeck, X. Batlle, P.J. Cuadra. Low resistance spin-dependent tunnel junctions with ZrAlO_x barriers. Contribution: oral. The 46th Annual Conference on Magnetism and Magnetic Materials, Seattle, USA. 2001.

17. X. Batlle, P.J.Cuadra, Z. Zhang, S. Cardoso, P.P. Freitas. Enhanced thermal stability of magnetic tunnel junctions with FeO_x interface layers: oxygen migration to the barrier. Contribution: oral. The 46th Annual Conference on Magnetism and Magnetic Materials, Seattle, USA. 2001.

Curriculum Vitae

Personal data

Family and first name	Cuadra-Solís, Pedro de Jesús
Date and place of birth	December 13, 1964. Leon, Nicaragua
E-mail	jcuadra@ubxlab.com
Spoken Languages	English (fluent), Russian (fluent), Czech (fluent) Catalan (fluent) and Spanish (mother tongue)

Educational background

- M.Sc. Program in Physics and Theoretical Physics at Physics Faculty and Department of Theoretical Physics, Odessa State University, Odessa, Ukraine (former USSR). Sept. 1985–June 1990.
- Undergraduate research projects: The neutrinos in cosmological models (1988). Dielectrics permeability in non-homogenous suspension (1989).
- Master of Science in Physics and Mathematics Thesis: The Localization of Bose Excitation in High- T_c Superconductors. Advisor: Vladimir A. Fedorin. Odessa State University, Odessa, Ukraine (former USSR).
- Postgraduate program in Material Sciences (1996-97). Universitat Autònoma de Barcelona, Barcelona, Spain
- Postgraduate program in Advanced Physics (1999-2001). Universitat de Barcelona, Barcelona, Spain

Staying at research centers

- 2006. High frequency susceptibility measurements on low and high- T_c superconductors in a magnetic field. I3-EuroMagNet programme. Institute for Nanoscale Physics and Chemistry (INPAC). Pulsed Fields Group. Leuven, Belgium. 06-17 February.
- 2008. Acoustic transport of vortices in superconductors. Programm DAAD-Acciones Integradas. Paul-Drude-Institut für Festkörperelectronik. Berlin, Germany. 17-20 September.

Technique and equipment used

- Surface and interfaces analysis X-ray Photoelectron Spectroscopy (XPS). Analysis of surface oxidation states and interfaces in magnetic multilayer.
- Thermomagnetic measurements Magnetometer SQUID. Magnetic moment relaxation under low and high magnetic fields, magnetic moment under different thermodynamic conditions.
- Thermomagnetic measurements Magnetometer AC. Dynamical processes under different ac perturbation sensing parameter and thermodynamics variables.
- Microwave measurements. PNA Series Network Analyzer, ESG-D Series Signal Generator, 20 MHz Function/Arbitrary Wave Form Generator. Frequency-dependent magnetic moment relaxation under different thermodynamic conditions, temperature and magnetic dependence of the complex reflection coefficient S_{11} , and stochastic processes under pulsed fields.

Honor

- September 1984–June 1990. Grantee of the Department of Middle and High Education (Former USSR).

Professional data

- September 1991–August 2008. Full teacher at the CEIR-ARCO technical and vocational school. Vehicle technology specialization.

- September 2008–present. Full teacher at the Minister of Education. INS Esteve Terradas i Illa technical and vocational school. Vehicle technology specialization.
- September 2005–August 2008. Comenius partnership project. Innovation teaching methods: The cooperative learning approach as a participative methodology. Local coordinator at CEIR–ARCO technical and vocational school.
- September 2010–August 2012. Leonardo da Vinci Transfer of Innovation project. Teach, learn and Quality. Local coordinator at INS Esteve Terradas i Illa.
- August 2012–July 2014. Leonardo da Vinci partnership project. Knowledge, transferring and training. General international coordinator.
- August 2012–July 2014. Comenius partnership project. Quality at School. Local coordinator at INS Esteve Terradas i Illa.